

UNIVERSITY OF COPENHAGEN
FACULTY OF HEALTH AND MEDICAL SCIENCES

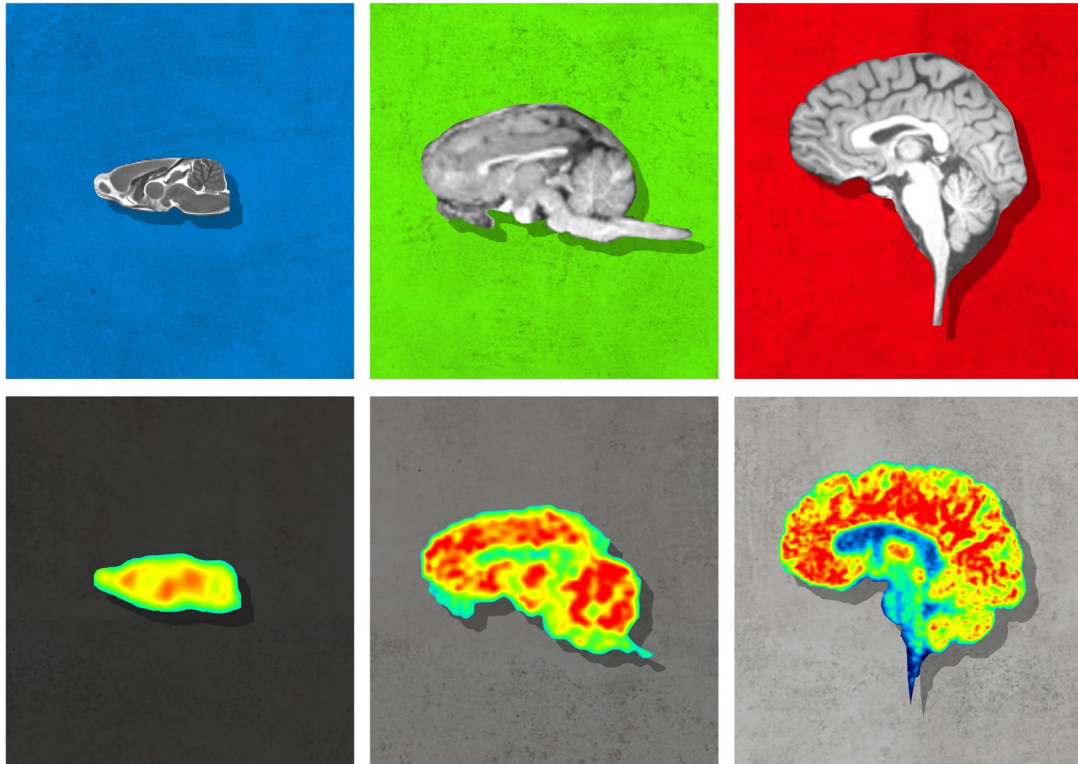


PhD Thesis

Nakul Ravi Raval

Translational Positron Emission Tomography

Animal Models and *In Vitro* Autoradiography for
Radioligand Development



This thesis has been submitted to the Graduate School of Health and Medical Sciences,
University of Copenhagen on February 14th, 2022

PhD thesis

Translational Positron Emission Tomography:

Animal Models and In vitro Autoradiography for Radioligand Development

by

Nakul Ravi Raval

Neurobiology Research Unit,
Copenhagen University Hospital Rigshospitalet

Faculty of Health and Medical Sciences,
University of Copenhagen

“Do or do not, there is no try.”

George Lucas

Yoda

The Star Wars Trilogy



Cover illustration: The cover image was a collaborative work of art by Kritika Kharbanda and me. It shows MRI (top) and [^{11}C]UCB-J PET (bottom) images from a rat, pig, and human (left, middle, and right). MR images either acquired for a study or training were acquired on NRU's 3T Prisma MR scanner except for the rat, which was acquired on a rodent scanner (kindly provided by Kristian Nygaard Mortensen to Mikael Palner). The Human MR image used was from my own brain, depicting the literal and figurative use in this thesis. Amazingly, every PET image came from the same, faithful, and beloved HRRT. The image of human PET was generously provided by Annette Johansen. I leave all other interpretations up to the viewer.

Title: Translational Positron Emission Tomography:
Animal Models and In Vitro Autoradiography for Radioligand Development

Author: Nakul Ravi Raval

Department: Neurobiology Research Unit,
Copenhagen University Hospital (Rigshospitalet), Denmark

Institution: Graduate School of Health and Medical Sciences,
University of Copenhagen, Denmark

Date of submission: February 14th, 2022

Date of defense: April 29th, 2022

Principal supervisor: Prof. Dr. Gitte Moos Knudsen,
Neurobiology Research Unit,
Copenhagen University Hospital (Rigshospitalet), Denmark

Co-supervisors: Dr. Mikael Palner
Neurobiology Research Unit,
Copenhagen University Hospital (Rigshospitalet), Denmark

Dr. Hanne Demant Hansen
Neurobiology Research Unit,
Copenhagen University Hospital (Rigshospitalet), Denmark

Dr. Louise Møller Jørgensen
Neurobiology Research Unit,
Copenhagen University Hospital (Rigshospitalet), Denmark

Dr. Stina Syvänen
Department of Public Health and Caring Science, Molecular Geriatrics
Uppsala University, Sweden

Dr. Pekka Kallunki
H. Lundbeck A/S, Denmark

Review committee: Dr. Birgitte Rahbek Kornum (chairperson)
Department of Neuroscience,
University of Copenhagen, Denmark

Dr. Anne M. Landau
Department of Clinical Medicine - Translational Neuropsychiatry Unit,
Aarhus University, Denmark

Prof. Dr. Kristina Herfert
Werner Siemens Imaging Center,
Eberhard Karls University of Tübingen, Germany

Preface

Three years of study in the Graduate Program in Neuroscience at the Department of Health and Medical Science, University of Copenhagen's culminated in this Ph.D. thesis. This work was conducted at the Neurobiology Research Unit, Copenhagen University Hospital (Rigshospitalet) under the primary supervision of Professor Dr. Gitte Moos Knudsen, and aid by Dr. Mikael Palner, Dr. Hanne Demant Hansen, Dr. Louise Møller Jørgensen, Dr. Stina Syvänen and Dr. Pekka Kallunki. It was made financially possible by European Union's Horizon 2020 research and innovation program (Marie Skłodowska-Curie grant agreement No. 813528) named PET-AlphSy. It was also partly funded by the Parkinsonforeningen, Denmark and NeuroPharm (Centre for Experimental Medicine Neuropharmacology).

The following manuscripts serve as the foundation for this thesis, and are addressed according to their roman numerals:

- Study I. **Raval N. R.**, Nasser, A., Madsen, C. A., Beschorner, N., Beaman, E. E., Juhl, M., Lehel, S., Palner, M., Svarer, C., Plavén-Sigray, P., Jørgensen, L. M., & Knudsen, G. M. (2022). An *in vivo* pig model for testing novel PET radioligands targeting cerebral protein aggregates. *Frontiers in Neuroscience (Brain Imaging Methods)*, 16:847074.
- Study II. **Raval, N. R.**, Madsen, C.A.*, Shalgunov, V.*, Nasser, A., Battisti, U.M., Beaman, E. E., Juhl, M., Jørgensen, L. M., Herth, M. M., Hansen, H. D., Plavén-Sigray, P., & Knudsen, G. M. Evaluation of the α -synuclein PET radiotracer (d₃)-[¹¹C]MODAG-001 in pigs. *Submitted*. BioRxiv (*: shared authorship)
- Study III. **Raval, N. R.***, Gudmundsen, F.*, Juhl, M., Andersen, I. V., Speth, N., Videbæk, A., Petersen, I. N., Mikkelsen, J. D., Fisher, P. M., Herth, M. M., Plavén-Sigray, P., Knudsen, G. M., & Palner, M. (2021). Synaptic Density and Neuronal Metabolic Function Measured by Positron Emission Tomography in the Unilateral 6-OHDA Rat Model of Parkinson's Disease. *Frontiers in Synaptic Neuroscience*, 13, 715811. (*: shared authorship)
- Study IV. **Raval, N. R.**, Johansen, A., Donovan, L. L., Ros, N. F., Ozenne, B., Hansen, H. D., & Knudsen, G. M. (2021). A Single Dose of Psilocybin Increases Synaptic Density and Decreases 5-HT_{2A} Receptor Density in the Pig Brain. *International Journal of Molecular Sciences*, 22(2), 835.
- Study V. **Raval, N. R.**, Madsen, C.A., Beaman, E. E., Olesen, M. V., Salvesen, V., Kaalund, S. S., Hansen, H. D., Aznar, S., & Knudsen, G. M. Decreased Cortical Presynaptic Density in Postmortem Parkinson's disease, Progressive Supranuclear Palsy and Multiple System Atrophy. *On going (Manuscript not attached)*.

The following publications and manuscripts are relevant to the work discussed in the thesis but are not included in it:

1. Shalgunov, V., Xiong, M., L'Estrade, E. T., **Raval, N. R.**, Andersen, I. V., Edgar, F. G., Speth, N. R., Baerentzen, S. L., Hansen, H. D., Donovan, L. L., Nasser, A., Peitersen, S. T., Kjaer, A., Knudsen, G. M., Syvänen, S., Palner, M., & Herth, M. M. (2020). Blocking of efflux transporters in rats improves translational validation of brain radioligands. *EJNMMI Research*, 10(1), 124.
2. Schain, M., Plavén-Sigra, P., Johansen, A., Donovan, L. L., **Raval, N. R.**, Nasser, A., Petersen, N. P., Hansen, H. D., Knudsen, G. M., Lammertsma, A. A., Ogden, T. R., & Svarer, C. (2022). Kinetic models for PET displacement studies. *Manuscript*.
3. Shalgunov, V*., van den Broek, S. L.*., Andersen, I. V., Vázquez, R. G., **Raval, N. R.**, Palner, M., Mori, Y., Schäfer, G., Beschoner, N., Nedergaard, M., Barz, M., Knudsen, G. M., Battisti, U. M., & Herth, M. M. (2022). Development of ¹⁸F-labeled tetrazines for pretargeted brain imaging. *Manuscript*.
(*: shared authorship)

Table of Contents

Preface.....	6
Summary	10
Dansk Resumé.....	12
Acknowledgments.....	15
Abbreviations	18
Background	22
Positron Emission Tomography	22
- Basic Principles of PET	22
- Applications of PET Imaging.....	24
- Static PET Quantification.....	25
- Dynamic PET Quantification.....	25
Autoradiography.....	28
- Receptor Binding Theory.....	28
- Practicalities in Autoradiography.....	29
Radioligand Development.....	31
- Target Identification and Radiochemistry	32
- <i>In Vitro</i> and Early <i>In Vivo</i> Evaluation	33
- <i>In Vivo</i> Evaluation in Large Animals	34
- Validation in Humans.....	36
Neurodegeneration and PET imaging	36
- α -synuclein PET Radioligand Development	38
- Animal Models with α -synuclein Aggregates	39
- Intracerebral Protein Injection Pig Model.....	40
Presynaptic Density Imaging	41
- Neurodegeneration and Synaptic Loss.....	42
- Psychedelic-Induced Neuroplasticity: Biochemical Mechanisms.....	43
Aims	47
Methods and Materials:.....	50
Study Designs.....	50
Surgical Procedure in Pigs	53

Surgical Procedure in Rats	54
PET Data Acquisition.....	54
PET Data Analysis	55
Autoradiography.....	56
Statistical Analysis	59
Data Availability Statement	60
Ethical Statements	60
Funding Acknowledgments	61
Results and Discussion:	64
Study I: Validation of Intracerebral Protein Injection Pig Model	64
- [¹¹ C]PIB TACs and Kinetic Modeling Parameters	64
- Autoradiographic Characterization of Injection Sites.....	66
Study II: Evaluation of (d ₃)-[¹¹ C]MODAG-001	66
- (d ₃)-[¹¹ C]MODAG-001 TACs and Kinetic Modeling Parameters	66
- (d ₃)-[¹¹ C]MODAG-001 metabolite and signal-to-noise ratio.....	68
Study III: Evaluation of [¹¹ C]UCB-J in 6-OHDA Rat Model	68
- [¹¹ C]UCB-J and [¹⁸ F]FDG PET Show Divergent Changes	68
- [¹¹ C]UCB-J PET vs [³ H]UCB-J Autoradiography	70
Study IV: Effects of a Single Psilocybin Dose in Pigs.....	71
- Increased SV2A and Decreased 5-HT _{2A} R Post-psilocybin in Pigs.....	71
Study V: Characterization of [³ H]UCB-J in Movement Disorders	72
- Binding Characteristics of [³ H]UCB-J in Postmortem Human Brain	72
- Changes in Neocortical SV2A in PD, PSP, and MSA	73
Experimental Limitations:.....	75
Conclusions and Future Perspective	80
References	83
Appendix	96
Study I	97
Study II.....	129
Study III.....	167
Study VI	195

Summary

Translational Positron Emission Tomography:

Animal Models and In Vitro Autoradiography for Radioligand Development

Positron emission tomography (PET) is an imaging technique where positron-emitting (e.g., ^{11}C or ^{18}F) radiolabelled tracers are used to assess concentrations of molecular targets. PET neuroimaging is the superior technique for investigating the brain *in vivo*, but it requires access to well-validated radiotracers. The development of appropriate radioligands is not easy, and in particular, the steps from *in vitro* to PET neuroimaging in humans often turn out unsuccessful. An intermediate step is the radiotracer assessment in animals. However, this step sometimes requires access to appropriate animal models, such as a model with misfolded pathological protein aggregates, as seen in several neurodegenerative diseases that are often associated with insufficient synaptogenesis.

This thesis has two aims. Aim I: To establish a pig model with intracerebral protein injection to assess novel radioligands. Aim II: *In vitro* and *in vivo* quantification of presynaptic density using the radioligand $^3\text{H}/^{11}\text{C}$ UCB-J for synaptic vesicular protein 2A (SV2A) in neurodegeneration and to assess the synaptoplastic potential of drugs.

In Study I, we establish a pig model with abnormal intracerebral protein aggregated and characterize this using ^{11}C PIB, a radioligand for amyloid- β with affinity to β -sheet structures like α -synuclein. We inject α -synuclein preformed fibrils (α -PFF), saline or post-mortem human brain homogenates from subjects with either dementia with Lewy bodies (DLB, pure α -synuclein pathology) or Alzheimer's disease (AD, pure amyloid- β and tau pathology). We confirm the expected increased binding of ^{11}C PIB in the AD-homogenate-injected and α -PFF-injected brain regions. In contrast, there is no specific ^{11}C PIB binding in the DLB-homogenate-injected or saline-injected regions. Post-mortem, the pig brains were investigated with ^3H PIB autoradiography and compared to the *in vivo* PET findings.

Study II evaluates and characterizes (d_3) - ^{11}C MODAG-001, a radioligand for misfolded α -synuclein, using the pig model developed in Study I. We find increased (d_3) - ^{11}C MODAG-001 binding in both α -PFF-injected and in AD-homogenate-injected brain regions, but not in DLB-homogenate-injected regions. We also demonstrate a dose-response PET signal in the α -PFF injected brain region and a good test-retest variability.

Study III measures presynaptic density using ^{11}C UCB-J and neuronal metabolic function using ^{18}F FDG in the unilateral dopaminergic lesioned rat model of Parkinson's disease. ^{11}C UCB-J and ^{18}F FDG PET revealed divergent regional changes in this rat model, especially in cortical regions not directly affected by the neurotoxin. We also compare *in vitro* ^3H UCB-J autoradiography with *in vivo* ^{11}C UCB-J PET in brains from the same animals and find a strong correlation between the two techniques.

In Study IV, we characterize three radioligands *in vitro* in the pig brain: ^3H UCB-J for presynaptic density and ^3H MDL100907/ ^3H Cimbi-36 for 5-HT $_{2A}$ R density. Next, we investigate if a single psychedelic dose of psilocybin changes presynaptic and 5-HT $_{2A}$ R density, which may play a role

in psilocybin's antidepressive effects. Compared to saline-treated pig brains, we find increased presynaptic density in the pig brains at one and seven days post-psilocybin treatment. We also find lower 5-HT_{2A}R density at one day but not seven days in the psilocybin-treated pig brains compared to saline-treated pig brains.

Finally, in Study V, we characterize [³H]UCB-J in post-mortem neurologically normal human brain sections. We measure the loss of cortical SV2A density in post-mortem human brain sections from patients with movement disorders like Parkinson's disease (PD), multiple system atrophy (MSA), and progressive supranuclear palsy (PSP) and compare them to the neurologically normal subjects. In PD, we find lower SV2A density in the frontal and temporal cortex. Lower SV2A density is seen in the frontal and parietal cortex in MSA. While, PSP patients show lower SV2A density in the frontal, temporal, parietal, and occipital cortex. We find no difference in white matter binding, supporting its use as a pseudo-reference region for these diseases.

Dansk Resumé

Translatiønnel Positron Emissions Tomografi:

Dyremodeller og In Vitro Autoradiografi til Udvikling af Radioligander

Positron emissions tomografi (PET) er en billeddannelsesteknik, hvor positron-emitterende (f.eks. ^{11}C eller ^{18}F) radiomærkede sporstoffer bruges til at bestemme koncentrationen af molekylære targets. PET billeddannelse er den overlegne teknik til undersøgelse af hjernen *in vivo*, dog kræver den velvaliderede sporstoffer. Udviklingen af velegnede radioligander er en kompliceret proces, bestående af mange trin, der især mislykkes i trinene fra *in vitro* forsøg til *in vivo* PET billeddannelse i mennesker. Et mellemliggende trin er evalueringen af radiosporstoffer i dyr. Imidlertid kræver dette trin som regel adgang til velegnede dyremodeller, eksempelvis modeller med patologisk misfoldede proteinaggregater, hvilket ses i flere neurodegenerative sygdomme som ofte er associeret med utilstrækkelig synaptogenese.

Denne afhandling har to overordnede målsætninger. Målsætning I: At etablere en grisemodel med intracerebral proteininjektion til evaluering af nye radioligander. Målsætning II: *In vitro* og *in vivo* kvantificering af præsynaptisk densitet, ved hjælp af radioliganden ^3H / ^{11}C UCB-J der binder til synaptisk vesikulært protein 2A (SV2A), i neurodegeneration, og til vurdering af det synaptoplastiske potentiale af lægemidler.

I studie I etableres en grisemodel med intracerebralt aggregeret protein, der karakteriseres ved hjælp af ^{11}C PIB, en radioligand for amyloid- β med affinitet for β -sheet strukturer såsom α -synuclein. Der injiceres enten α -synuclein fibriler (α -PFF), saltvand eller homogenater af post mortem hjernevæv fra patienter med enten Lewy-body demens (DLB, en ren α -synuclein-patologi) eller Alzheimers sygdom (AD, en ren amyloid- β - og taupatologi). Som forventet, fandt vi en øget binding af ^{11}C PIB i de hjerneregioner, hvor AD-homogenat og α -PFF var injiceret. I modsætning hertil, så vi ingen specifik ^{11}C PIB-binding i hjerneregioner injiceret med DLB-homogenat eller saltvand. Grisehjerneerne blev efterfølgende undersøgt post mortem ved brug af ^3H PIB autoradiografi og sammenlignet med fund fra *in vivo* PET-undersøgelserne.

I studie II evalueres og karakteriseres (d_3) - ^{11}C MODAG-001, en radioligand for misfoldet α -synuclein, ved brug af grisemodellen udviklet i studie I. Vi fandt øget (d_3) - ^{11}C MODAG-001-binding i både α -PFF- og i AD-homogenat-injicerede hjerneregioner, dog ikke i hjerneregioner injiceret med DLB-homogenat. Vi viser desuden et dosis-respons PET-signal i hjerneregioner injiceret med α -PFF og en god test-gentest-variabilitet.

I studie III undersøges præsynaptisk densitet ved brug af ^{11}C UCB-J og neuronal metabolisk funktion ved brug af ^{18}F FDG i en rottemodel for Parkinsons sygdom der indebærer unilateral dopaminerg læsion. ^{11}C UCB-J og ^{18}F FDG PET viste afvigende regionale ændringer i denne rottemodel, særligt i kortikale områder der ikke er direkte påvirket af neurotoksinet. Vi sammenligner ligeledes *in vitro* ^3H UCB-J autoradiografi med *in vivo* ^{11}C UCB-J PET i hjerner fra samme dyr og finder en stærk korrelation mellem de to teknikker.

I studie IV karakteriserer vi tre radioligander i grisehjernen *in vitro*: [³H]UCB-J til måling af præsynaptisk densitet og [³H]MDL100907 samt [³H]Cimbi-36 til måling af 5-HT_{2A}-R-densitet. Derefter undersøger vi, om en enkel psykedelisk dosis af psilocybin ændrer præsynaptisk- og 5-HT_{2A}-R-densitet, hvilket kan have betydning for de antidepressive effekter af psilocybin. Sammenlignet med saltvandsbehandlede grise finder vi øget præsynaptisk densitet både én- og syv dage efter behandling med psilocybin. Derudover finder vi lavere 5-HT_{2A}-R-densitet efter én, men ikke syv dage efter psilocybin behandling, sammenlignet med de saltvandsbehandlede grise.

Afslutningsvist karakteriserer vi i studie V [³H]UCB-J i vævssnit af post mortem hjernevæv fra neurologisk normale mennesker. Derudover måler vi den kortikale SV2A-densitet i vævssnit af post mortem hjernevæv fra patienter med bevægelsesforstyrrelser såsom Parkinsons sygdom (PD), multisystematrofi (MSA) og Progressiv supranukleær parese (PSP), og sammenligner med hjernevæv fra neurologisk normale mennesker. I PD-patienter finder vi en lavere SV2A-densitet i den frontale og temporale cortex, i MSA-patienter finder vi en lavere SV2A-densitet i den frontale og parietale cortex, mens i PSP-patienter finder vi en lavere SV2A-densitet i den frontale, temporale, parietale og occipitale cortex. Desuden finder vi ingen forskel i binding i hvid substans mellem patientgrupper, hvilket understøtter anvendelsen som en pseudo-referenceregion i førnævnte sygdomme.



Figure 0.1| A significant number of NRUsers captured in a digital photograph. This photograph was taken at the NRU day of 2021. Although several notable members are absent, this shows a major part of NRU. Everyone in this image is significant hence none are denoted with a *. Photograph credits: Peter Steen Jensen.

Acknowledgments

This Ph.D. thesis would not be what it is now without the help of numerous people. Gitte Moos Knudsen, my primary supervisor, advisor, and mentor, is the first person I'd like to thank. You have my gratitude for believing in me and allowing me to flourish under your guidance. I've been in awe of you from our first day of working together, and I doubt that will ever change. I aspire to be like you in every way.

Without the guidance of Mikael Palner, Hanne Deman Hansen, Louise Møller Jørgensen, Stina Syvänen, and Pekka Kallunki, this thesis would not have been possible. For someone to have five co-supervisors is an uncommon occurrence, but I am grateful for your assistance in every tiny and significant way. Mikael, I inspire to be a researcher like you. Hanne, you're just too awesome. Louise, the things that you taught me were so valuable. Stina, thank you for hosting me in Uppsala. I enjoyed all the fikas with you and group. Pekka, you're a genius. Thank you, R-wizard Pontus Plavén-Sigra, for everything you've taught me also for exposing me to kinftr and flæskesvær; it's impossible for me to express my gratitude sufficiently. Patrick Fisher, Claus Svarer, and Jens Holm Mikkelsen have also provided me with some sort of supervision at NRU. It was a pleasure to collaborate with you.

Dedicated to Birgit Tang, Dorthe Givard, Lone Freyr, and Peter Steen Jensen, the unsung heroes behind the scenes. Thank you for your patience with my zillion inquiries, many of which arrived at the same time—countless blessings to you, patient souls. Gerda Thomsen and Svitlana Olsen have also been regular sources of support for me.

To Lene Lundgaard Donovan, Annette Johansen, and Martin Schain of the “TACo” group: a heartfelt thank you! Lene, thank you for always letting me turn around and ask you the most ridiculous question. Martin, math and music are two subjects that I wish I could excel at, just like you. It's an honor to call you a friend and coworker, Annette. You guys are the best coworkers a person could wish for. Vibeke Dam is one of those special officemates. Thank you very much for the hugs; they brightened my day every time. To Clara, thank you for all the very long days in the HRRT basement and never hesitating to help out.

Thank you to everyone else at NRU who helped to make my time there feel like home. Throughout our time together, I intend to savor every moment of it. This list includes but is not limited to Agata Casado Sainz, Camilla Borgsted Larsen, Drummond McCulloch, Emily Eufaula Beaman, Giske Opheim, Maria Grzywacz, Martin Korsbak Madsen, Martin Nørgaard, Sara Marie Larsen, Sophia Armand, and Søren Vinther Larsen. Thank you, Maria and Clara, for helping me with the translation of the summary, as well; Neuroscience is easier than Danish. Thank you to William Dalseg Reith, Nidia Fernández Ros, Katrine Kiilerich, Nikolaj Speth, Burcu Azak Pazarlar, and Annemette

Ringsted for your contributions during mine and your time at NRU.

Sanjay Aripaka, a chef in the lab and in the kitchen, has been an enormous help to me. All the meals and lab assistance you provided were very appreciated! Also, thank you for proof reading the thesis. To Arafat Nasser, Morten Juhl, and Brice Ozenne, I would like to express my gratitude for your constant support over the past few years. Without your hard work and dedication, none of my initiatives would have been finished. To Natalie Beschorner, I want to express my gratitude for her tireless efforts on my behalf. My gratitude goes out to the team at the Department of Experimental Medicine team; this includes Charlotte Fink, Janie Jørgensen, Karsten Pharao Hammelev, and Stefania Embla Arnórsdóttir for all their hard work and dedication. Additional thanks to Bente Pakkenberg, Susana Aznar, Hans-Jørgen Jensen, and the Research Laboratory for Stereology and Neuroscience for their highly valuable contributions.

It is with great gratitude that I acknowledge Matthias Herth and his team at the Herth Lab. Matthias, thank you so much for your willingness and confidence. I'd want to thank Vladimir Shalgunov for his openness and enthusiasm; he has never rejected any of my demands. Additionally, I'd like to thank Ida Vang Andersen, Natasha Bedesi, Rocío García Vázquez, Sara Irene Lopes van den Broek, and Umberto Maria Battisti for their assistance (Amazing performance!). The radiochemistry unit's Jacob Madsen, Szabolcs Lehel, and Ida Neymann Petersen all played crucial roles in this thesis, and I owe them a debt of appreciation.

Thank you to everyone involved in PET-AlphaSy, especially the supervisors and Ph.D. students. Special thanks to Dag Sehlín, Eva Schlein, Mengfei Xiong, Sahar Roshanbin, Ran Sing Saw, and Ulla Kløve Jakobsen for their contributions. Thanks to Thomas Wünsche for being such a great friend. I'd like to express my heartfelt gratitude; you've saved my life.

To the people that are my most significant support, Anish Behere, Gavati Wad, Rashmi Dharia, and Varun Solanki. You have always been in my thoughts, no matter what day. I don't know who I would be without you guys. More important people whose role in my life can never change: Aniket Agarwal, Aryan Bendrey, Daksha Mutha, Gaurav Joshi, Kartik Mandot, Madhur Dutta, Mansing Athere, Raunak Deo, Tanveer Teranikar, and Tanvi Ghude. You folks are game-changers. To my Copenhagen friends, Aphroditi Panagiotopoulou, Kypros Venetis, and Vita Rehberger, your friendship meant a lot to me; I will cherish every moment of my time with you. To the friends because of whom my mental health was on the check, a huge thank you - Sayali Potdar, Shivani Natu, Vaidehi Patil, and Akshay Jakkali.

Thank you so much, Kritika Kharbanda, for shaping me into the person I am today. It's because of you that I've learned how to be a better researcher and person. If it wasn't for you, the long months indoors would have been devastating. Please accept my gratitude for the creative assistance you provided for each and every diagram in this thesis and the Adobe license. In addition, I'd like

to thank my support animal, Max, for making this journey a lot easier. Arjun Raval, the guy who sowed the seed of science in my head, is next on the list of people to thank. You're a genius (Bad Boys for Life!). In the metaphor that Arjun was science, Nischol Raval was medicine. It took me a long time to realize that medicine was more than just scooter rides and vitamin C tablets. Dr. Raval is the kindest human I've ever known, and for that, I'll be eternally thankful. Further, I would like to show my sincerest gratitude to the person I respect the most and who taught me that with perseverance anything is achievable, Hemant Bendrey. Sunita Raval and Ravi Raval are always at the top of the list. It's incredible how much you two believe in me. I got here because of the hard work and determination you instilled in me. The amount of time we've spent traveling has been extraordinary. You have always been there for me, whether it was tennis, medicine, dentistry, or science, and I appreciate that. Thank you for allowing me to express myself freely. Because of you, I am who I am today.

Nakul Ravi Raval
February 14th, 2022
Pune, India.

Abbreviations

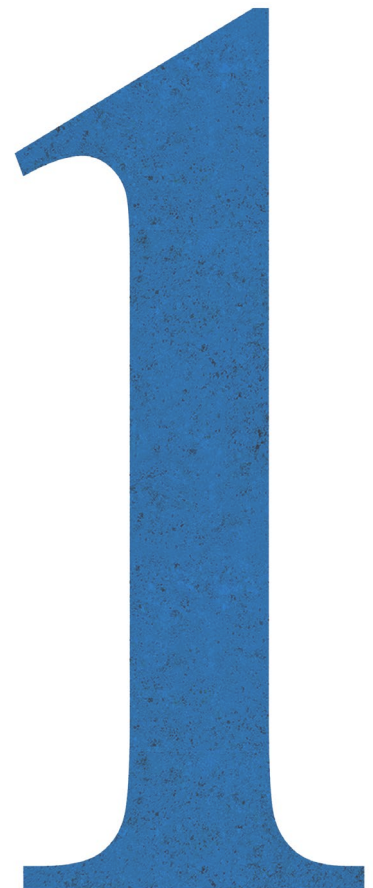
1/2TCM	One/Two-tissue compartment model
5-HT	5-hydroxytryptamine (5-HT)
6-OHDA	6-hydroxydopamine
A β	Amyloid-beta
AD	Alzheimer's disease
AIF	Arterial input function
ANOVA	One-way analysis of variance
ARRIVE	Animal research: reporting of <i>in vivo</i> experiments
BBB	Blood-brain barrier
B_{\max}	Total density (or concentration) of receptors
BP	Binding potential
BP_{ND}	Binding potential non-displaceable
BSA	Bovine serum albumin
CNS	Central nervous system
CSTC	Cortico-striato-thalamo-cortical
dH ₂ O	Deionised water
DLB	Dementia with Lewy bodies
FDG	Fluorodeoxyglucose
G	Birmingham gauge
GCI	Glial cell inclusions
GPCR	G-protein coupled receptor
HRRT	High-resolution research tomography
IDIF	Image derived input function
IHC	Immunohistochemistry
IM	Intramuscular
IP	(phosphor-)Image plates
IRF	Impulse response function
IV	Intravenous
K_{D}	Equilibrium dissociation constant
L	Ligand
LOR	Line of response
LR	Ligand-receptor complex
MFB	Medial forebrain bundle
mPFC	Medial Prefrontal cortex
MRI	Magnetic resonance imaging

MSA	Multiple system atrophy
NC	Neurologically healthy control
NFT	Neurofibrillary tangles
NHP	Non-human primates
NSB	Non-specific binding
P-gp	P-glycoprotein
PBS	Phosphate-buffered saline
PD	Parkinson's disease
PET	Positron emission tomography
PIB	Pittsburgh compound B
PSD-95	Postsynaptic density protein 95
PSP	Progressive supranuclear palsy
<i>R</i>	Receptor or protein binding site
R-HPLC	Radio-high performance liquid chromatography
ROI	Region of interest
SB	Specific Binding
SPECT	Single-photon emission tomography
SRTM	Simplified reference tissue model
SUV	Standardized uptake values
$t_{1/2}$	half-life
TAC	Time-activity curve
TB	Total binding
TE	Tissue equivalent
V_T	Total volume of distribution
WB_{NF}	Whole-brain normalization factor
WT	Wild type
α -PFF	α -synuclein reformed fibrils

Background

“The art of medicine is long, Hippocrates tells us, “and life is short; opportunity fleeting; the experiment perilous; judgment flawed.”

Siddhartha Mukherjee
The Emperor of All Maladies:
A Biography of Cancer



1. Background

1.1 Positron Emission Tomography

Positron emission tomography (PET) is a functional and molecular imaging technique that enables *in vivo* investigation of biochemical targets and physiological processes. PET allows the quantification of proteins like receptors and transporters, protein aggregates, enzymes, metabolism, neurotransmitter release, and blood flow. Molecular imaging is widely applied in the pharmaceutical industry and academic research to better understand human brain neurobiology and pathophysiology, information used to develop treatment strategies for central nervous system (CNS) illnesses. Performing a PET scan requires a molecule to be labeled with a radioactive isotope; this molecule usually has high affinity and specificity for a biological target of interest and is referred to as a radioligand or radiotracer (radioligand has a binding site while radiotracer may or may not). The radioligand is injected into the subject, and it spreads throughout the body, while the unstable isotope decays at a constant rate. This time-defined constant rate is called half-life ($t_{1/2}$). Carbon-11 ($[^{11}\text{C}]$) and Fluorine-18 ($[^{18}\text{F}]$) are short-lived (short $t_{1/2}$) positron-emitting radionuclides that are most commonly used in neuro-PET.

Table 1.1 shows the properties of other commonly used radionuclides. Metal-based and longer-lived radionuclides, e.g., Gallium-68, Zirconium-89, etc., have been used in research and clinical settings with cardiology and oncology (Zhang et al., 2011; Tanzey et al., 2018), but finding their “entry” into neuroimaging will be challenging. Hence, this thesis will mainly focus on $[^{11}\text{C}]$ - and $[^{18}\text{F}]$ -labeled radionuclides used and developed for neuro-PET.

1.1.1 Basic Principles of PET

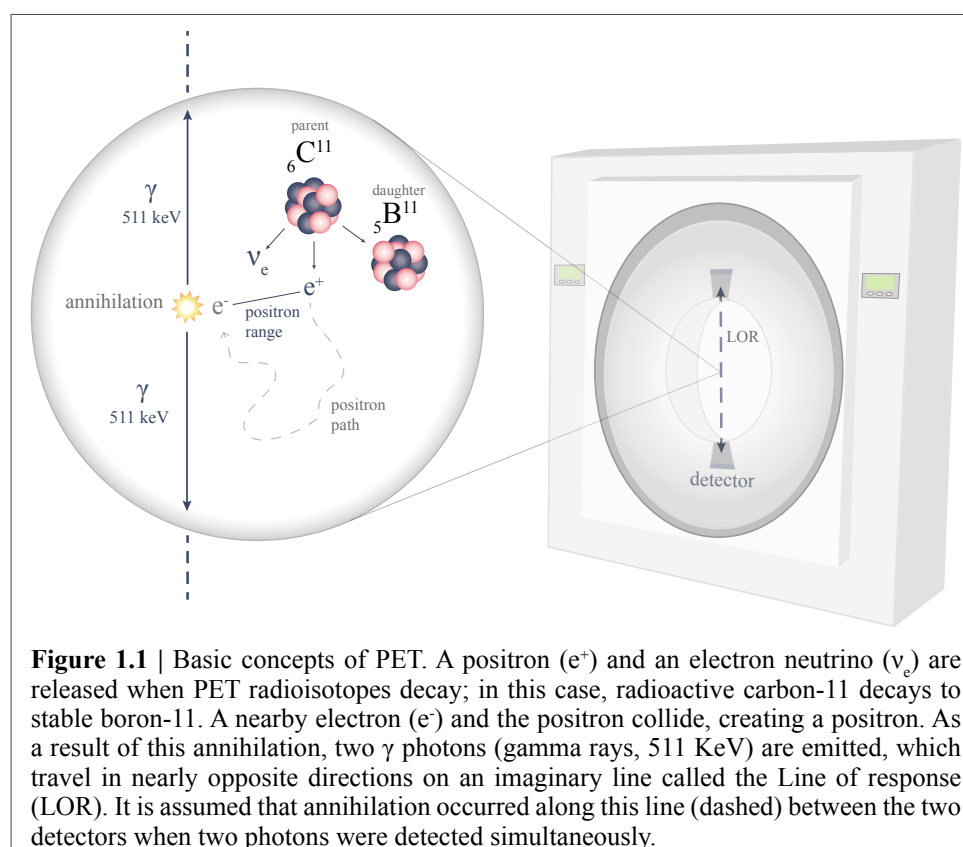
During a PET scan, the radioligand is typically injected as a bolus (single large dose) intravenously (IV) into the subject and distributed to the brain and

other organs via the bloodstream. When the radiolabeled isotope decays, a positron, and an electron neutrino (ν_e) are released from the nucleus of the atom. A positron is an antiparticle to electrons with the same mass and charge and has some kinetic energy (positron energy) after emission. Not all emitted positrons will have the same energy. However, the maximum positron energy of an isotope will define the maximum distance that the positron can travel (positron range) (Table 1.1) (Conti and Eriksson, 2016). This energy is lost by numerous collisions with electrons in neighboring tissues. The positron’s total or nearly complete loss of energy results in its merger with an electron, producing a short-lived element called positronium. The positronium eventually annihilates, converting its mass into two gamma (γ) photons of 511 keV emitted in opposite directions, separated by $180 \pm 0.25^\circ$ (Moses, 2011) (Figure 1.1).

Table 1.1 | Commonly used radionuclides and their half-lives and average positron energy. Modified from Conti & Eriksson, 2016.

Radionuclide	Half-life ($t_{1/2}$)	Max positron energy [MeV]	Max positron range in tissue [mm]
Carbon-11 (^{11}C)	20.4 min	0.96	4.2
Nitrogen-13 (^{13}N)	9.9 min	1.20	5.5
Oxygen-15 (^{15}O)	2.1 min	1.73	8.4
Fluorine-18 (^{18}F)	109.8 min	0.63	2.4
Copper-64 (^{64}Cu)	12.7 h	0.65	2.4
Gallium-68 (^{68}Ga)	68.3 min	1.90	2.9
Rubidium-82 (^{82}Rb)	1.26 min	3.37	5.9
Zirconium-89 (^{89}Zr)	78.4 h	0.90	3.8

The photons travel through the body and air before being detected by the PET system. The unique property of simultaneous emission of two photons serves as the foundation for detecting and localizing radioactive decay. The line of response (LOR) (Figure 1.1) is described as an imaginary line connecting the detectors, and radioactive decay is presumed to have occurred somewhere along that line. This revolutionary approach is known as coincidence detection (Phelps et al., 1975). A PET scanner circles the subject and is composed of a ring of detectors to detect the annihilation photons. It is possible to pinpoint the origin of the annihilation site using their position on the detection ring and the relative delay between their detection.



Radioactivity can then be located and quantified once annihilations are detected repeatedly over time, and substantial LORs are generated. A quantitative spatial estimate of the radioactivity's origin is possible by a highly sophisticated process known as reconstruction. This process generates a 3D PET image. The 3D PET image will represent the underlying mechanism impacting the target protein (e.g., binding to a receptor, utilization by a cell). Radioligand brain uptake and washout can be measured by acquiring radioactivity concentrations in time intervals known as "time frames." The length of each frame is governed by the preferred temporal resolution and the radionuclide's half-life. As a result, 3D PET images are converted to a dynamic 4D PET image, with the fourth dimension being time. A full PET scan typically contains 20–40 time frames of a 60–120 min scan duration, with a time resolution of several minutes (Sejnowski et al., 2014).

Regional time-activity curves (TAC) are produced by specifying a region of interest (ROI) across image elements, voxels (3D pixel), and calculating the average voxel values^{**}. PET has not only a poor temporal resolution but also a poor spatial resolution. This is due to the technical and physical limitations of the detector and the positron range. The low spatial resolution makes it difficult to delineate anatomical characteristics, making it challenging to accurately “draw” ROIs. Nevertheless, PET can be accompanied by other techniques with much higher spatial resolution, such as magnetic resonance imaging (MRI) and computed tomography (CT). These anatomical scans can then be used to create the desired ROIs, which can then show the temporal behavior of the radioligand.

PET’s sensitivity outweighs its lack of high temporal or spatial resolution. The sensitivity to quantify biochemical processes is unparalleled compared to the other techniques like MRI, or electroencephalogram (EEG). While an MRI system can identify and quantify concentrations in the millimolar (i.e., 10^{-3}M) range, PET has the sensitivity to detect concentrations in the picomolar range (i.e., 10^{-12}M) (Sharma et al., 2002). The specificity of the PET complements its sensitivity. Specificity is a property of the radioligand to bind to the target protein, with little to no off-target binding. Using a molecule with high specificity will dominate the signal indicating the availability of the target.

1.1.2 Applications of PET Imaging

PET is used in the clinical setting for differential diagnosis of different diseases within neurology, cardiology, and oncology. In pharmaceutical research, PET can be used in microdosing studies (Bergström et al., 2003) (i.e., radiolabeling the drug and measuring the distribution) and in occupancy (Takano et al., 2016) (i.e., measure the occupancy of the drug on a specific receptor) studies. PET radioligand development in the pharmaceutical industry is broadly explained in Section 1.3.

This thesis lies in the domain of general research. More specifically, it is in the field of neurobiology and neuropathology. Researchers can determine and answer several questions or hypotheses within the clinical and preclinical environment including:

1. Drug discovery:

- a. Pharmacodynamics, pharmacokinetics, and distribution of various novel drugs.
- b. A drug’s ability and extent to bind or block the target of interest.
- c. Characterize the degree of target occupancy associated with therapeutic effects (Madsen et al., 2019) or side effects (Farde et al., 1992).
- d. Calculate the appropriate drug dosage (Finnema et al., 2019).

2. Neurobiology:

- a. Quantification of neurotransmitter receptors and transporters (Beliveau et al., 2017).
- b. Occupancy by endogenous neurotransmitter release (Knudsen, 2009; Jørgensen et al., 2017) or depletion (Spies et al., 2015)
- c. Changes in target concentration before and after prolonged behavioral (Koepp et al., 1981) or pharmacological interventions (Dewey et al., 1993) or simply in healthy aging (Carson et al., 2018).

* ROIs are often referred to as a more accurate interpretation called the volume of interest (VOI), but the umbrella term ROI is used for this thesis.

3. Neuropathology:

- a. Used in psychiatric and neurological pathology to associate PET-derived outcomes with theoretical attributes like personality traits (Stenbæk et al., 2017; Madsen et al., 2020) or cognitive performance (Vernaleken et al., 2007).
- b. Quantify the difference of target protein in patient-control comparisons (Holmes et al., 2019; Matuskey et al., 2020; Chen et al., 2021).
- c. Quantify within-subject effects post-treatment and their association to reductions in symptoms (Kennedy et al., 2001; Cervenka et al., 2012).

To answer such questions, PET's outcomes need to be quantified for general comparison within the unit as well as for the general PET community for combination research. There are two major ways that PET data can be quantified, i) static PET quantification and ii) dynamic PET quantification.

1.1.3 Static PET Quantification

Static PET is the quantification of a single time frame, which is often scanned at a specific time following tracer injection. These are 3D PET images with spatial quantities embedded in individual voxels. The most common strategy to compare static images is to convert the radioactivity concentration from the PET scanner (C_{PET} , C stands for concentration) into standardized uptake values (SUV, units: g/mL). SUVs are PET quantifiers that are widely used in both research and clinical settings. As shown in Equation 1.1, it is the ratio of C_{PET} (example units: kBq/mL) and amount of administered dose (example units: MBq) divided by the bodyweight (example units: kg).

$$SUV = \frac{C_{PET}}{Dose/Weight} \quad \text{Equation 1.1}$$

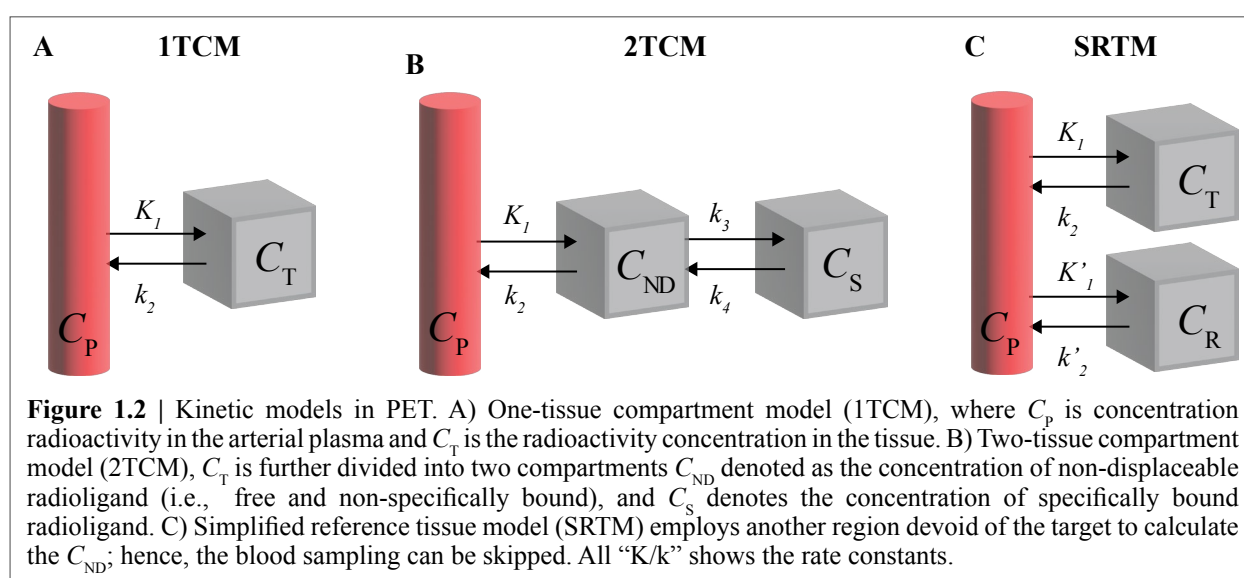
The dose and tissue radioactivity should be decay corrected to the same time point. The equation's divider indicates the average radioactivity concentration across the body, and so the SUV equals the region-to-whole-body radioactivity concentration ratio. SUVs quantification comes with some bias. These are introduced with differences in body weight, body composition, and time of injection (Keyes, 1995). Nevertheless, it continues to be used because dynamic imaging and blood collection are not required. In this thesis, SUV values have been used especially in Study III, we used these to compare lesioned vs. control tissue. Often, further normalization steps are required to confidently use these values (more details in Section 2.5). Another quantification often used in animal studies is the percentage-injected dose per gram (%ID/g). In small animals (*in vitro/ex vivo* studies), dissected tissue can be weighted, and the radioactivity measured. %ID/g is the percentage of injected dose and organ weight. PET results may be compared with *in vitro* results; hence, a 1 g/mL density is assumed, and C_{PET} values are converted to %ID/g.

1.1.4 Dynamic PET Quantification

Static quantification only shows the total radioactivity in the measured tissue. But, within the tissue, the radioligand can exist in different compartments or pools such as the blood in blood vessels, extracellular spaces, intracellular spaces, the target, or (unfortunately) non-specific targets. The ultimate goal of quantitative analysis of PET data is to develop a mathematical model that accurately characterizes

observed regional TACs and distinguishes radioligand concentrations in various compartments (Heurling et al., 2017) at equilibrium. Most models rely on the radioligand concentration in arterial plasma, since it is from where the radioligand is transferred to the brain.

Some of the radioactivity in the blood may be due to radiolabeled metabolites. These metabolites need to be corrected for. Multiple arterial blood samples over the scan duration are analyzed with a radio-high pressure liquid chromatography (R-HPLC). This allows the quantification of the parent radioligand in the plasma. R-HPLC separates the different compounds in a liquid sample based on their polarity. The radio detector in the R-HPLC helps quantify the compounds to calculate a metabolite-corrected arterial input function (AIF). Hence, PET data from the scanner is often complimented with blood and plasma data. This method of quantification is called *invasive kinetic modeling*.



Commonly used models are shown in Figure 1.2. Several different compartments are necessary to model the TAC. Kinetic modeling outcomes are always calculated at equilibrium (See Section 1.2.1). Although equilibrium is not reached via a bolus injection experiment, outcomes can be calculated using rate constants (Figure 1.2: K_1 , k_2 , k_3 , k_4). The rate constants describe the rate at which the transfer of the radioligand occurs between the different compartments. A set of differential equations with increasing complexity may be constructed using these rate constants. This would mathematically represent the exchange of radioligand between compartments. The differential equation for the one-tissue compartment model (1TCM) can be explained with:

$$\frac{dC_T(t)}{dt} = K_1 C_P(t) - k_2 C_T(t) \quad \text{Equation 1.2}$$

Solving the differential Equation 1.2 reveals that the C_T at a particular moment in time (on the TAC) can be characterized by the convolution of the AIF and the impulse response function (IRF). The IRF would describe the radioligand concentration over time if the radioligand delivery were instantaneous. In short, IRF expresses the radioligand efflux from the tissue. Hence, the TACs can be conceptualized as a result of a continuous series of tracer deliveries from the AIF, which flows out according to the

IRF (Matheson, 2018). Iteratively solving these convolution equations yields the rate constants, also called micro parameters, and the ratio of these rate constants provides the macro parameters.

For reversible tracers, full quantification methods produce two types of macro parameters: i) total volumes of distribution (V_T) and ii) binding potential (BP). V_T is defined as the amount of radioligand in the tissue volume, i.e., concentration, relative to plasma at equilibrium (Innis et al., 2007). For example, if radioactivity concentration in an ROI is 2 kBq/cm³ and the C_p is 1 kBq/mL, then the V_T is 2 mL/cm³, which means 2 mL of plasma would account for a volume of 1 cm³ in the brain. V_T is a sum of non-displaceable (V_{ND}) and specific (V_S) volume of distribution. For 1TCM,

$$V_T = \frac{K_1}{k_2} \quad \text{Equation 1.3}$$

BP refers to the specific binding of the radioligand to other reference concentrations. Specific binding is relatively easier to calculate *in vitro*; hence the concept of BP can also be explained in terms of *in vitro* binding, which is explained in Section 1.2.1. *In vivo*, different kinds of BP values can be calculated, depending on the reference concentration used. This thesis will focus on the non-displaceable compartment, hence BP_{ND} .

$$BP_{ND} = \frac{V_T - V_{ND}}{V_{ND}} \quad \text{Equation 1.4}$$

However, arterial blood sampling to determine an AIF can be uncomfortable for the participant and is resource-intensive in terms of instrumentation and labor. As a result, alternatives to blood sampling are desirable. Reference tissue kinetic modeling, such as the simplified reference tissue model 1 and 2 (SRTM1/2) (Lammertsma and Hume, 1996; Wu and Carson, 2002), do not require blood samples and provide estimates of BP_{ND} (for reversible tracers). SRTM is a simplification of the invasive kinetic models, when a region of the brain exhibits no or low specific binding. BP_{ND} can be estimated by using the reference tissue's TAC as input instead of the AIF. These models too are iteratively solved.

Nevertheless, these modeling strategies come with some caveats and assumptions. It is essential to abide by the assumption of SRTM for accurate and unbiased outcomes (Salinas et al., 2015). The assumptions of SRTM are:

1. No displaceable competent in the reference region.
2. 1TCM compartmental model must accurately describe the kinetics of the radioligand.
3. V_B (blood volume) contribution to the tissue must be negligible.
4. V_{ND} must be similar in the reference and the target region.

Apart from the iterative approach to calculate the micro parameters, a graphical method such as the Logan plot can also be applied (Logan et al., 1990, 1996). Linearization of the different kinetic models allow for applying linear least-squares fitting processes that are faster and ensure that the global minimum is reached. These models offer only the macro-parameters like V_T and BP_{ND} . This thesis performs two types of Logan graphical analysis: invasive Logan plot (with AIF) and non-

invasive Logan plot (with a reference region).

A different method for estimating V_T (and BP) is to provide the radioligand via a constant infusion, which maintains parent radioligand (accounting for radioactive decay) concentrations in the blood (Carson et al., 1997). Multiple brief scans can be performed to verify that steady radioactivity levels have been achieved. Once equilibrium is established, V_T can be determined directly from the ratio of tissue (C_T) to plasma (C_p) concentration. This is arguably also a static quantification method.

All of the kinetic models discussed here are approximate representations of biological processes. While such models may help estimate a biological target of interest, they cannot be guaranteed to produce precise or even meaningful outcomes (Plavén-Sigray, 2018). The fact that one model performed well in describing a radioligand in a species or condition does not imply that the same model will work for other radioligands, species, or conditions. All outcomes will also be subject to some degree of uncertainty, whether owing to biological variability, measurement error, or incorrect model assumptions. Thus, a V_T or BP_{ND} value does not represent the target's absolute binding, availability, or density but rather a likely value among a large number of possible values. Although there are strategies to account for this inherent uncertainty in PET outcome measurements, it is rarely recognized in the PET literature, let alone this thesis (Ogden and Tarpey, 2006).

1.2 Autoradiography

The specific binding of radioligands can be tested *in vitro* to quantify the distribution of its target protein in a technique called autoradiography (auto: “self” or “within”). Traditional quantification of proteins is done using antibodies either through western blot or enzyme-linked immunosorbent assays (ELISA). However, quantification of antibodies is often tricky and highly reliant on standards protein measurements. Autoradiography using a selective radioligand is more sensitive to the quantification of protein and its binding sites. While PET's sensitivity can potentially image at the picomolar range, autoradiography can measure at the femtomolar range (i.e., 10^{-15} M).

1.2.1 Receptor Binding Theory

The receptor binding theory was derived from Michaelis-Menten's work involving substrates and enzymes (Michaelis et al., 2011). This theory has dominated the field of biochemistry for centuries since its seminal introduction in 1913 (Srinivasan, 2021). In receptor binding assays, a radioactive ligand is used in place of a substrate, and the result is the ligand's binding to the receptor. This derives the law of mass action (Equation 1.5).

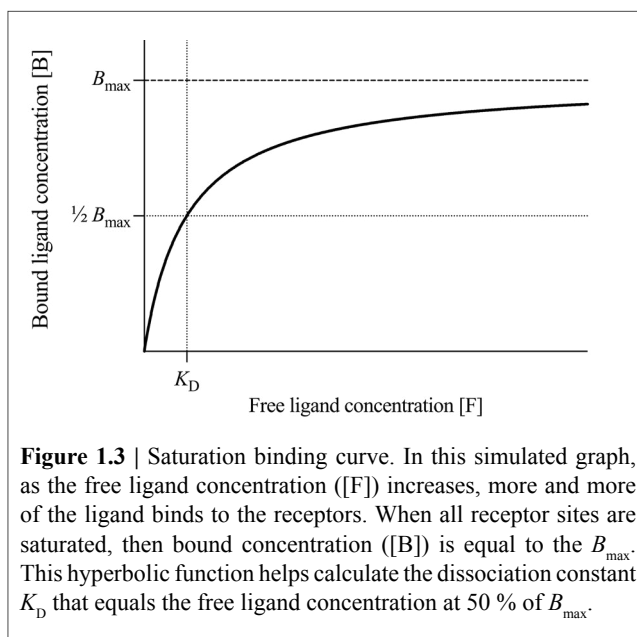


This is a reversible reaction; ligand (L) does not chemically bind to the receptor (R). This binding forms a ligand-receptor complex (LR). As a result, the ligand can “bind” (rate constant of association is k_{on}) and “unbind” (rate constant of dissociation is k_{off}) to the receptor. At equilibrium of the above reaction (Equation 1.3), the ratio of k_{off} and k_{on} is defined as equilibrium dissociation constant; K_D (unit: nM). The strength of the binding interaction (i.e. affinity) is the inverse of K_D . Hence, higher

the affinity of the ligand lower is the K_D value. Another important aspect of receptor binding assays is B_{\max} which refers to the total density or concentration of receptors in a tissue sample. The receptor binding theory leads to measuring the K_D and B_{\max} . The law of mass action can be solved (Maguire et al., 2012) and substituted to produce,

$$B = \frac{B_{\max} \times F}{K_D + F} \quad \text{Equation 1.6}$$

Where B is the concentration of the bound radioligand, F is the concentration of the free radioligand. In practice, both these values are known. B is the outcome measure of the assay, while F is the concentration that was used in the assay. This equation plotted as concentration of B vs. F is hyperbolic with a horizontal asymptote at B_{\max} (Figure 1.3). This means if enough F is used to saturate all receptors, B equals B_{\max} . The other critical point on this curve is the concentration of F at 50% of B_{\max} (Figure 1.3). When B equals 50% of B_{\max} ($B_{\max}/2$), Equation 1.6 can be solved to demonstrate $F = K_D$. In other words, K_D is the concentration of free ligand required to



saturate 50% of receptors. The ratio of B_{\max} and K_D is the BP (Equation 1.7) as defined by Mintun et al., 1984 (Mintun et al., 1984). This parameter is critical for *in vivo* imaging (Section 1.1.4) and is often overlooked during *in vitro* investigations.

$$BP = \frac{B_{\max}}{K_D} \quad \text{Equation 1.7}$$

1.2.2 Practicalities in Autoradiography

In vitro autoradiography (hence forward called only autoradiography) is best performed with long-lived radionuclide ^{125}I ($t_{1/2} = 59.4$ days), ^{14}C ($t_{1/2} = 5730$ years), ^{35}S ($t_{1/2} = 87.5$ days), ^{32}P ($t_{1/2} = 14.3$ days) and tritium (^3H , $t_{1/2} = 12.3$ years). Although, $[^{11}\text{C}]$ - and $[^{18}\text{F}]$ -labeled radioligands can be used, they may not be as feasible due to the number of productions that would be required. Tritium is the most utilized radionuclide for radiolabeling ligands due to its long half-life and low-energy β emission (18.5 KeV). The β particle can only travel a few mm within the tissue, which provides great spatial resolution with top-notch imaging systems providing a resolution of as little as 10 μm (Kuhar and Unnerstall, 1985; Polak and Wharton, 1993).

Sections having intact proteins or receptors can perfectly interact with the radioligand *in vitro*. These radioligands bind to the proteins, which then can be quantified. Radioligands often have some amount of non-specific binding (NSB) that needs to be accounted for. Hence, two adjacent sections undergo

autoradiography. One section undergoes total binding (TB), i.e., only the radioligand is incubated with the tissue section. The other section represents NSB, i.e., the radioligand is incubated with a 10,000-fold excess of an unlabeled competing ligand with high affinity to the target. This competing ligand ensures the occupancy of all target receptors. Thus, the radioligand's specific binding (SB) can be calculated by the Equation 1.8.

$$SB = TB - NSB \quad \text{Equation 1.8}$$

The unlabeled ligand should preferably have a different chemical structure than the radiolabeled ligand to ensure binding only to the target and not non-target binding sites (Manuel et al., 2015; Griem-Krey et al., 2019).

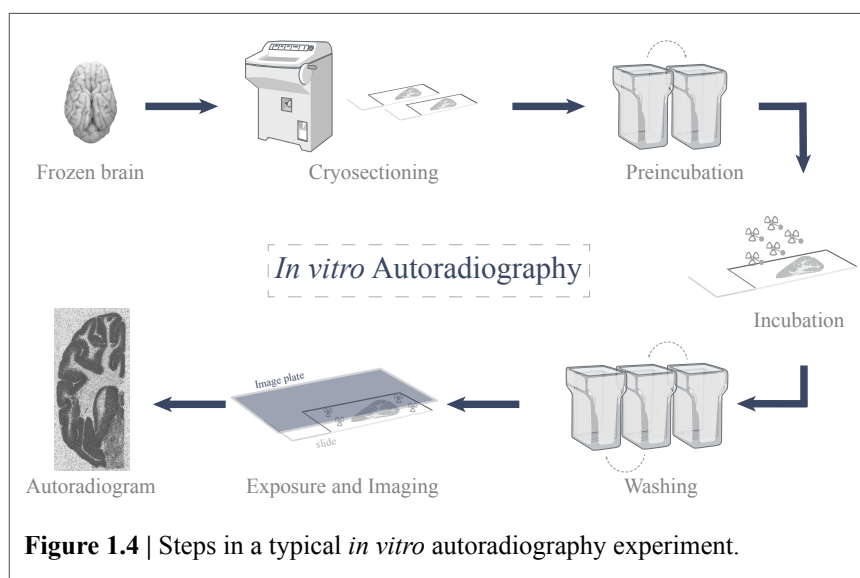
Autoradiography assays are frequently conducted in three different ways:

1. **Saturation assays:** Used to practically calculate the K_D and B_{max} . For this, an increasing concentration of the radioligand is added to different tissue sections with approximately the same concentration of the receptor (e.g., adjacent sections from the same tissue). The binding at equilibrium is measured and plotted against the radioligand concentration fitted with the non-linear model (Equation 1.8). Saturation binding assays have been used in Study I, IV, and V.
2. **Competition assays:** Autoradiography can also be used to determine the affinity of a competing cold compound. For this, the radioligand concentration is kept constant, while varying concentrations of the cold compound are used on different sections. Measured specific binding of the radioligand is plotted against the concentration of cold compound (as a function) (Maguire et al., 2012). Although not used in this thesis, competition assays are essential for *in vitro* evaluation during radioligand development (more details in Section 1.3.3).
3. **Group comparison:** Like with PET, autoradiography can be used to quantify the difference in target protein in patient-control (Study III and V) or drug treatment comparisons (Study IV). In this, the same concentrations of the radioligand are added to the sections of the different groups, binding is measured, and the outcomes are compared. Two types of comparison can be achieved: i) Total receptor density or B_{max} : when a concentration of $4-5 \times K_D$ is used ii) Binding potential or BP is measured, which combines K_D and B_{max} . This can be performed with radioligand concentrations lower than K_D . For instance, these assays can be used when the experimenter is confident that the variables do not change the affinity of the radioligand.

Radioactivity imaging has been traditionally performed using x-ray films. However, newer methods like the phosphor-image plates (IP) or gaseous detectors (Delayre et al., 2020) provide much higher sensitivity and resolution. IPs are semiflexible screens coated with photostimulable phosphor (BaFBr:Eu²⁺). The radioactive sections come in close contact with the screens. Ionizing radiation emitted from radionuclides converts Eu²⁺ to Eu³⁺, and the emitted electron is in turn trapped in bromine vacancies. When the IP is stimulated with light, bromine releases the trapped electrons, converting Eu³⁺ to “excited” Eu²⁺. This bromine stimulation is performed with red lasers to stimulate smaller regions precisely to provide high resolution. Excited Eu²⁺ stabilizes by emitting luminance that can

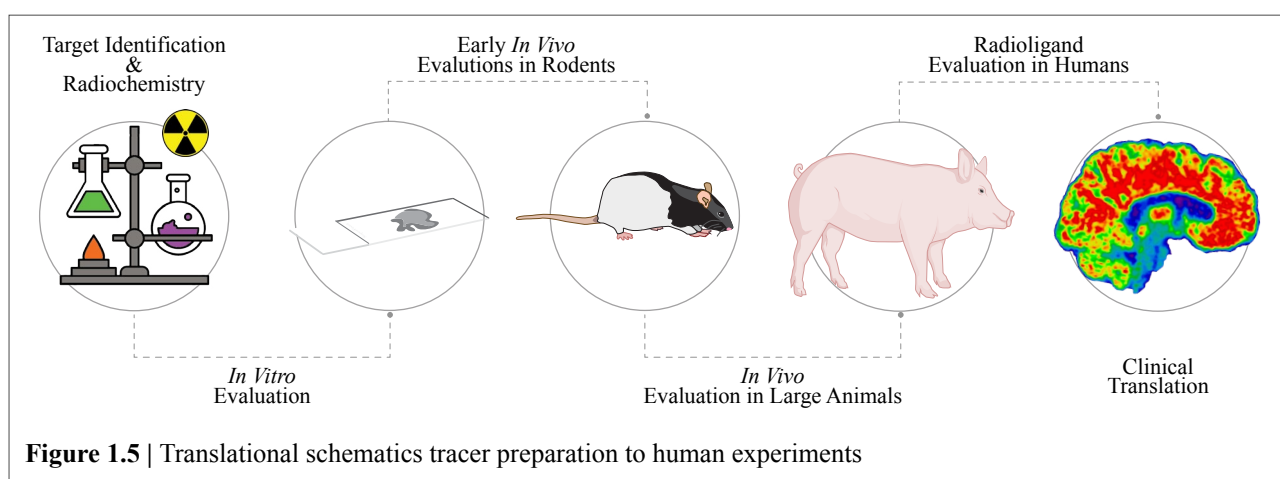
be picked up by photomultiplier tubes in the image-plate scanner and digitalized into a 16-bit image (i.e., every pixel has a greyscale between 0 and 65,536) (Amemiya and Miyahara, 1988; Kanekal et al., 1995).

The practical steps required for performing an autoradiography experiment are illustrated in Figure 1.4. When a novel radioligand is evaluated, numerous considerations and optimization are performed; see the methods section for more details.



1.3 Radioligand Development

Enzyme or receptor targeting was first performed on humans in 1939 using [¹³¹I]iodide (Brock et al., 2003). Since then, we have come a long way. In 2010, it was estimated that 2600 novel radioligands had been tested *in vitro* or *in vivo*, out of which 20% have been tested in humans (Eckelman, 2011). A PET radioligand must be developed prior to the drug development to evaluate therapeutic efficacies accurately. Radioligand development starts with target selection and radiochemistry, *in vitro* and *in vivo* testing, and finally, in-human testing (Figure 1.5).



It is imperative to mention that radioligand development is a very costly affair. Cost is associated with radiolabeling, animal studies, human studies, etc. There is tremendous cost in this multidisciplinary approach of radioligand development that involves chemists, biologist, physicist and mathematicians that are may be required at different steps and processes. The only way to reduce this financial burden is to produce optimum results in all stages without affecting the generated data quality. Keeping this in mind, all the steps explained below have intentions to produce high-quality data by reducing the number of experiments required to suggest the success of a radioligand confidently.

1.3.1 Target Identification and Radiochemistry

In the pre-genomic era, leads for target protein of interest were found through drug efficacy studies and *in vitro* experiments (genetic linkage of diseases or postmortem studies). In recent years, additional targets were identified due to gene mapping and sequencing (Eckelman, 2011). Although, the original route still exists and is highly relevant. Due to the advances in molecular biology, many targets of interest have surfaced. Most of the targets of interest within the CNS domain can be distinguished into distinct components, with some targets having a clear overlap between themselves. This includes, but is not limited to:

1. Single proteins that are potential drug targets hence imaged for occupancy, e.g., G-protein-coupled receptors (GPCR) like the 5-HT_{2A}R (Ettrup et al., 2014)
2. Single proteins that may not be drug targets but are relevant for differential diagnosis, e.g., dopamine transporter imaging for Parkinson's disease (PD) (Ziebell et al., 2012)
3. Protein aggregates imaging where the aggregates may be used as markers for disease progression, e.g., amyloid- β (A β) and tau imaging in AD (Ni and Nitsch, 2021).
4. Target proteins or enzymes (metabolism) that maybe help understand the neurobiology, e.g., tryptophan imaging for serotonin synthesis (Endepols et al., 2022)

Radiochemistry includes radionuclide manufacturing, radioligand design, radiolabelling, and radiopharmaceutical production. Once the molecules of interest are established, it is necessary to radiolabel them. The radionuclide commonly used in CNS imaging is produced in a cyclotron, a cyclic particle accelerator that produces high-energy proton or deuteron beams that can be recovered and utilized to bombard stable atoms like oxygen-18 and nitrogen-14 to yield [¹⁸F] and [¹¹C], respectively. Many common bench-top organic chemistry reactions are too slow or practically tricky to synthesize radioligand because of the short half-life of the radionuclides employed. The most popular PET radionuclides require robust chemical reactions that incorporate the radionuclide at a later stage, are fast and high-yielding, and require easy purification.

Finally, an essential aspect of PET imaging is the tracer dose of radioligands; to not tamper with the pharmacokinetics or pharmacology of the process being imaged. Due to the advances in PET radiochemistry, different classes of small molecules can be labeled with high molar activity. Molar activity is the amount of radioactivity per unit mole of the compound (Luurtsema et al., 2021). This

will essentially define the amount of radioactivity injected as a tracer. For [^{11}C]-labeled tracers, molar activity is typically in the range of 10–1000 GBq/ μmol are observed in practice (Thompson et al., 2020).

1.3.2 *In vitro* and Early *In vivo* Evaluation

The target and radioligand must meet the ideal imaging requirements as a pair. Usually, a library of molecules is created as potential radioligands. However, it would be a hassle and often troublesome to radiolabel each molecule of this library. Instead, one most promising ligand is chosen for radiolabeling. Once radiolabeled, this molecule will evaluate all the different entities in the library. Using this parent molecule, the affinities and selectivity of the entire library are evaluated using competition binding assays and other screening assays. Further, the lipophilicity of the radioligand is calculated theoretically as well as experimentally (logD). Other calculations like the CNS-multiparameter optimization (CNS-MPO) desirability may also be beneficial (Wager et al., 2016). These are the initial *in vitro* evaluation that are performed to choose a small batch of ligands from the library that show promise.

From the above tests, a few ligands move into *in vivo* studies. This batch of ligands is radiolabeled and commonly tested in rodents. This can be performed in mice and rats and include biodistribution, metabolism, and blocking experiments. Such assays are usually performed in wild-type (WT) animals but maybe also performed in disease rodent models. Some important criterias, method of evaluation and range are listed in Table 1.2.

Table 1.2 | Criterias for a successful radioligand (Honer et al., 2014; Zhang and Villalobos, 2017; McCluskey et al., 2020; Korat et al., 2021).

Property	Verification method	Therotical desirable range
Affinity	<i>In vitro</i> autoradiograophy and <i>in vivo</i> occupancy studies	$K_D < 10 \text{ nM}$ (dependant on B_{max})
Specificity	Binding assay, autoradiograophy and <i>in vivo</i> occupancy studies	50–100 fold selectivity $B_{\text{max}} : K_D > 10$
Radiolabeling	Chemical structure, radiolabeling site identification	RCY > 10% (activity yield > 500 MBq) MA > 50 GBq/ μmol 1–5% Occupancy at tracer dose
BBB penetration	Lipophilicity, P-gp w/o blocking	$1.0 < \log D < 3.0$ No active efflux
Kinetics	<i>In vivo</i> PET scanning	Early peak uptake SUV > 1.5 Reversible kinetics Medium-Fast washout
Metabolism	HPLC anlysis of blood and brain tissue	Rapid plasma clearance No/minimum BBB permeable radiometabolites
Signal-to-Noise ratio	Lipophilicity, <i>in vivo</i> PET scanning, and kinetic modeling,	$1.0 < \log D < 3.0$ Off-target binding > 500 nM No BBB permeable radiometabolites
Variability	Kinetic modeling	Low inter- and intra- subjected variability
Safety	Toxicology and dosimetry	Non-toxic

K_D : Dissociation constant
 B_{max} : total number of protein/ receptors
 MW: molecular weight
 RCY: radiochemical yield

MA: Molar activity
 logD: measure of lipophilicity
 SUV: standardized uptake values

An important criterion for a CNS radioligand is its permeability of the blood-brain barrier (BBB). This is a highly selective semipermeable barrier that prevents passive diffusion of circulating solutes from passing into the extracellular fluid of the CNS, serving as a defense mechanism. In some instances, the radioligands may also need to permeate the plasma membrane to reach intracellular targets. Many successful CNS radioligands with intracellular targets show that this is possible, e.g., monoamine oxidase A and B (Holland et al., 2013). Although many of the mechanisms contribute to BBB permeability, we thoroughly understand the effects of lipophilicity, which is likely the most important. An additional defense mechanism installed at the BBB is efflux transporters (Golden and Pollack, 2003). Molecules that are lipophilic and would theoretically pass through the brain microvasculature are restricted by efflux transport like P-glycoprotein (P-gp). To remove molecules that have passed the BBB, substrates of P-gp are pumped back into the lumen of the blood vessels. An extensive pipeline has been developed in our laboratory to screen radioligands for this property (Shalgunov et al., 2020) to reduce the risk of failure.

Another major reason for the failure of radioligands is the high NSB. NSB is influenced by two reasons: i) physiochemical property of the molecule, ii) *in vivo* metabolism. Lipophilicity is the most frequently used physiochemical property to predict brain uptake and NSB. High lipophilicity is required for the radioligand to enter the brain, but at the same time, if the lipophilicity is too high, the NSB of the molecule increases (Waterhouse, 2003; Honer et al., 2014). *In vivo* metabolism can also influence the background. Fast tissue clearance of the non-target bound radioligand is a desirable property. This will limit the tracer concentration in the non-displaceable component and reduce the background. If possible, having a radioligand with brain penetrating radio-metabolites should be avoided since the PET scanner cannot distinguish between radioactivity from the intact radioligand and radio-metabolites. If such radio-metabolites are present, strategies to reduce the metabolism can be applied, e.g., deuterium incorporation into the molecule (Klenner et al., 2021).

Additionally, kinetic modeling maybe performed and evaluated in these animals to quantify the radioligands. Such assays provide important information of the pharmacokinetics of the radioligand. Kinetic modeling is also performed with an image-derived input function (IDIF). This can replace traditional blood sampling, a major concern in rodents. TAC from an ROI in the heart is replaced as AIF. This, of course, needs to be validated by the traditional setting but maybe an advantageous strategy (Bertoglio et al., 2020).

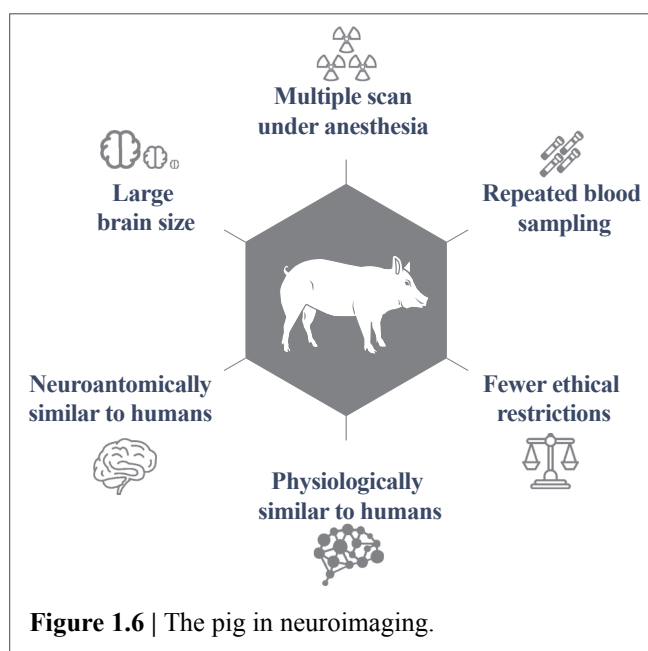
1.3.3 *In vivo* Evaluation in Large Animals

In vivo evaluation in rodent models comes with some disadvantages. The main disadvantage is that the radioligand's prediction of *in vivo* pharmacokinetics cannot be directly translated from rodents to humans. This is due to various reasons, which include differences in metabolism, more active P-gp efflux, other confrontation of the target protein, and poor blood sampling capabilities (an important attribute that has been thoroughly emphasized throughout the thesis). Nevertheless, large animals that are considered higher species may fill the void between human and laboratory animals. They can provide the same information as rodents but with much more confidence for accurate translation.

For this purpose, non-human primates (NHP) are often considered the “gold standard.” To date, Old World macaques and baboons (with some exceptions) are the primary NHP models used in functional neuroimaging studies. For PET studies, these animals have significant benefits over other laboratory animals. For example, NHPs have a long life span and can contribute tremendously to the evaluation of novel radioligand, especially for long-term longitudinal studies. They can remain under anesthesia for extended durations, which allows multiple scans with “easy” access to arterial blood samples making quantification more accurate and trustworthy. Additionally, some research shows NHPs have similar metabolism profiles to humans than any other animal species (Cherry and Gambhir, 2001; Howell and Murnane, 2011).

Although the NHP sounds like an ideal model for radioligand development, it is associated with high costs, less feasible, minimum opportunities for repeatability, and, not least, its use is associated with ethical concerns (Harding, 2017). It is getting more challenging to perform NHP studies with only a handful of laboratories that have access to them. Hence, non-conventional animals are being utilized for radioligand development. In Europe, the use of the pig (Vodička et al., 2005; Alstrup and Smith, 2012; Hoffe and Holahan, 2019) and cats (Kim et al., 2010) in biomedical research is on the rise.

We and others have utilized the pig extensively for radioligand development and evaluation purpose due to its strong predictive value for effective translation to humans (Parker et al., 2012; Ettrup et al., 2013; Hansen et al., 2014; Winterdahl et al., 2014; Donovan et al., 2020b). The use of domestic pigs may be a way to overcome most of the hurdles that NHP studies have. While being physiologically and anatomically similar to humans, young domestic pigs correspond adequately to benchmark requirements of molecular neuroimaging: they allow for performing multiple scans with ample arterial blood sampling (Alstrup and Smith, 2012), and it fits



the physical requirement of human scanners. Additionally, pigs have large brains and also fit well into the gantry of human scanners; the use of human scanners eliminates the need for dedicated preclinical imaging research systems. Finally, pig experiments have considerably fewer ethical restrictions than NHPs. Hence, with these advantages in mind (graphically demonstrated in Figure 1.6), the domestic pig is an excellent suitable intermediate between rodents and humans to characterize novel radioligands.

1.3.4 Validation in Humans

Once the radioligand shows satisfactory results *in vitro* and *in vivo*, it can be tested in humans. Unfortunately, it is not a straightforward task. A plethora of complex regulations govern PET studies. They pertain to toxicology, radiation exposure (dosimetry), manufacturing/production licenses, good manufacturing practices, the types of approvals required (which often vary according to the investigation's objective, the study population, and clinical trial status), and the approval and conduct of clinical studies themselves (Honer et al., 2014).

Typically, the first step in evaluating a new PET ligand in humans is to characterize its brain uptake and distribution in healthy control subjects. These investigations include dynamic PET scanning and arterial blood sampling with metabolite correction for kinetic modeling. The evaluations are usually started with a few baseline scans before performing more arduous experiments like blocking or test-retest scans. The experiment's data is often compared to preclinical data to understand the radioligand behavior. After these initial experiments, the radioligand can be used for its intended purpose.

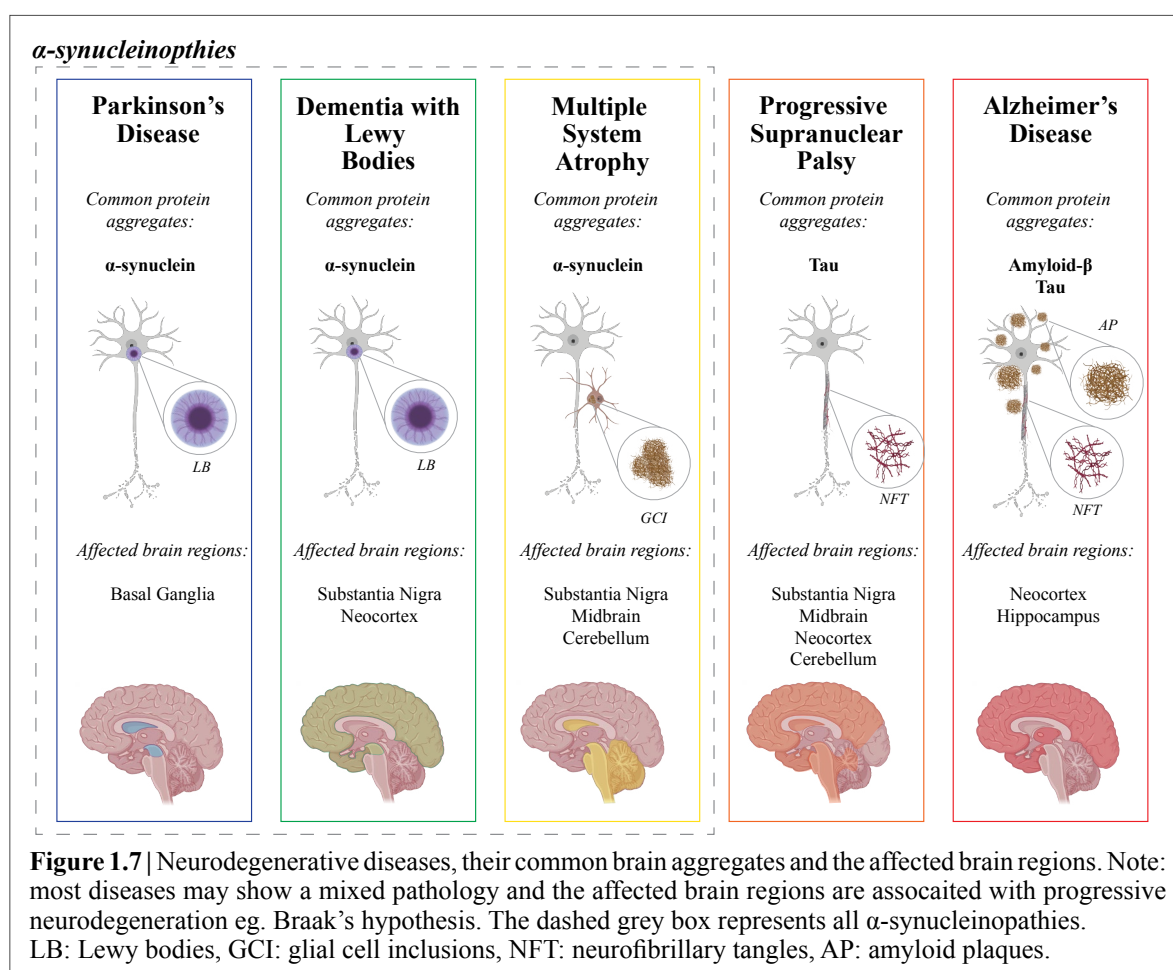
The section about PET, autoradiography and radioligand development sought to provide a reasonably concise overview of the processes involved in a research unit that deals with novel radioligands developed for the CNS. PET is one of the few non-invasive *in vivo* techniques that can directly assess pharmacology, pathology, and basic biology. The following section will focus on understanding PET's application for radioligand development and hypothesis evaluation within two major disciplines of neuroPET. This includes imaging protein aggregate (associated with neurodegenerative diseases) and synaptic density, sub-specialties that have dominated neuroPET research for the last decade.

1.4 Neurodegeneration and PET imaging

Neurodegeneration, in simple words, is the progressive loss of neurons. Such degeneration impairs brain function, resulting in a loss of cognitive function and limiting a person's ability to move. Neurodegenerative diseases consist of a variety of maladies, including Alzheimer's disease (AD), Parkinson's disease (PD), dementia with Lewy bodies (DLB), multiple system atrophy (MSA), progressive supranuclear palsy (PSP), frontotemporal dementia, multiple sclerosis, and Huntington's disease. Around fifty million individuals have Alzheimer's disease or other dementias worldwide, while another eight million individuals have Parkinson's disease or related disorders (James et al., 2018). This is a massive burden on society. Apart from being a devastating disease for the patient and their family members, these common neurodegenerative diseases cost society nearly one trillion dollars yearly (Breijyeh and Karaman, 2020). Despite decades of research, there are still numerous gaps in our understanding of how and why disease progression occurs, and many diseases remain incurable, with available treatments focusing exclusively on symptom management rather than reversing the underlying cause.

Although numerous neurodegenerative diseases exhibit a variety of clinical signs, it is now recognized that they have a common underlying pathophysiology. This includes toxicity associated with the aggregation and misfolding of proteins into β -sheet structures called fibrils. These proteins are A β in AD, tau in PSP and AD, and α -synuclein in PD, DLB, and MSA. As a result, these disorders are referred

to as proteinopathies. It is also essential to understand that these diseases are not predominantly related to only one of these proteins but may show mixed pathology. These proteins have a normal function in its healthy state but form insoluble fibril inclusions known as amyloid plaques, neurofibrillary tangles (NFT), and Lewy bodies/glia cell inclusions (GCI), which are predominantly composed of misfolded $A\beta$, tau, and α -synuclein, respectively (Pike et al., 1993; Kotzbauer et al., 2004; Maruyama et al., 2013) (Figure 1.7).



PET imaging in neurodegenerative diseases has been performed for the majority of developed CNS imaging radioligands. This includes neuronal metabolism, neuroreceptors, neurotransmitters, neuroinflammation, protein aggregates, and synaptic density. This thesis will focus on neuronal metabolism, protein aggregate, and synaptic density imaging further. Synaptic density imaging is introduced and explained in Section 1.5.

[^{18}F]fluorodeoxyglucose (FDG) is the radioligand used to evaluate brain metabolism. [^{18}F]FDG is the most established and frequently used radioligand across all domains of PET imaging, with its principal application in cancer (Zimmer and Luxen, 2012). [^{18}F]FDG's success lies in its simple strategy to target *in vivo* glucose metabolic pathway or glycolysis: first delivered into a cell and then phosphorylated similarly to glucose. However, unlike glucose that is further metabolized, [^{18}F]FDG will not be further metabolized due to the presence of the labeled fluorine isotope rather than the 2-OH

group (which is the next step in glycolysis). As a result, [^{18}F]FDG gets trapped within the cell. This metabolic entrapment accumulates different amounts of radioactivity within hypermetabolic (more entrapping) or hypometabolic cells (less entrapping). PET can visualize and quantify these fluctuations (Hoh, 2007). The degree of hypometabolism correlates with the progression of neurodegeneration, and changes in glucose metabolism can be used to predict the severity of disease progression in most neurodegenerative diseases (Mosconi, 2013; Meyer et al., 2017). Hence, often [^{18}F]FDG metabolism has been used as a surrogate for neural integrity or function. Nevertheless, [^{18}F]FDG is metabolized in both neurons and glial cells (astrocytes, microglia, and oligodendroglia), and it is sensitive to blood glucose levels, medication, and physical and sensory activity at the time of the PET scan.

Over the last two decades, a significant portion of the radioligand development efforts for imaging neurodegenerative diseases has been directed on aggregated protein deposits, which are pathological characteristics of these diseases. PET imaging of aggregated proteins enables improved diagnosis and treatment of these diseases. Additionally, it is a critical tool for drug development and advancing our understanding of the pathophysiological processes underlying disease progression. A variety of radioligands are developed for both A β and tau (Mathis et al., 2017).

Amyloid-PET has been an active field of research since the beginning of the 2000s. For A β , the most successful radioligand is [^{11}C]Pittsburgh Compound B (PIB). Although a non-selective radioligand with an affinity for other β -sheet structures, it has been used in several studies, and some cases are still used in the clinical setting (Klunk et al., 2004; Lockhart et al., 2007; Madsen et al., 2012). On the other hand, [^{18}F]florbetapir (Garber, 2012) and [^{18}F]florbetaben (Sabri et al., 2015) are next-generation radioligands that are more selective for A β and have also been approved by the FDA (US Food and Drug Association) for clinical imaging of A β in the diagnosis of AD.

Tau is another protein aggregate that has successful radioligands to quantify with PET. Two successful radioligands exist for *in vivo* tau imaging. [^{11}C]PBB3 is currently undergoing clinical trial (Rigney et al., 2021), while [^{18}F]flourtaucipir (previously known as [^{18}F]AV-1451/[^{18}F]T807)(Barthel, 2020) is already approved by the FDA for clinical use. Both the radioligands have been demonstrated to bind well to the tau fibrils seen in AD. Results indicate a positive association with clinical symptoms and the known development of tau deposition (Maruyama et al., 2013; Xia et al., 2013). However, some evidence suggests that [^{18}F]AV-1451 does not exhibit the same association in non-AD tauopathies such as PSP, putting doubt on its usage in these disorders (Gomez et al., 2016).

In contrast, efforts to develop a radioligand suited for imaging α -synuclein aggregates or inclusions have mostly failed (Korat et al., 2021). A PET radioligand specific for α -synuclein would be crucial in facilitating an earlier and more exact diagnosis, which would benefit both the patient and clinician and the development of effective treatments.

1.4.1 α -synuclein PET Radioligand Development

Alpha-synuclein is a ubiquitous protein found throughout the CNS. Normally, it can be found in the neocortex, hippocampus, substantia nigra, thalamus, and cerebellum and accounts for approximately 1% of cytosolic proteins in the brain (Iwai et al., 1995). The function of α -synuclein is still unknown,

but its presence in presynapses is thought to play some role in synaptic plasticity. It seems α -synuclein plays a vital role in dopaminergic neurons since the dopamine system is the most affected in PD and, in most instances, MSA and DLB.

Numerous attempts have been made to generate an appropriate radioligand for α -synuclein, and some radioligand appeared promising in rodents (Verdurand et al., 2018; Hooshyar Yousefi et al., 2019; Capotosti et al., 2020; Kaide et al., 2020; Kuebler et al., 2020; Ono et al., 2021; Uzuegbunam et al., 2022). Developing an α -synuclein radioligand is much more challenging than the A β and tau. The main reason for this is that the amount of α -synuclein aggregates are thought to be at least ten to fifty times lower than A β and tau aggregates (Bagchi et al., 2013; Mathis et al., 2017). These proteins can coexist in the diseased brain, making it further challenging (Eberling et al., 2013). Since the target concentration is so low, a molecule with a very high affinity must distinguish between the off-target binding and the specific signal.

The reliability and predictability of *in vitro* binding experiments are critical in developing any PET radiotracer and present a significant hurdle for α -synuclein tracer development (Korat et al., 2021). Binding assays for *in vitro* evaluation of radioligands use synthetic α -synuclein preformed fibrils (α -PFF). It has been hypothesized that structural differences in α -synuclein between patient-derived aggregates and α -PFF may explain why novel α -synuclein PET tracers have proven challenging to translate to clinical studies (Strohäker et al., 2019). This means that the conformation of the *in vitro* fibrils may not be the same as the *in vivo* pathological fibrils in disease brains. Such considerations also apply to the rodent models with α -synuclein depositions (Eberling et al., 2013), and hence their feasibility for screening novel radioligand is questioned.

Nevertheless, MODAG (Neuroscience Solutions, GmbH), in collaboration with the Werner Siemen's imaging center (Eberhard Karls University of Tübingen), recently showed promising results for an α -synuclein radioligand. [^{11}C]MODAG-001 or (d_3)-[^{11}C]MODAG-001 (Kuebler et al., 2020) was derived from the lead structure anle138b, a molecule with therapeutic potential in Parkinson's disease and multiple system atrophy mouse models due to its affinity for α -synuclein aggregates (Wagner et al., 2013; Heras-Garvin et al., 2019). Anle138b and its derivatives have been extensively studied *in vitro* and in rodents (Maurer et al., 2019; Kuebler et al., 2020). Due to its high affinity, good brain penetration, and capacity to detect α -PFF in a protein deposition rat model, (d_3)-[^{11}C]MODAG-001 showed the most promise as a possible radioligand for detecting α -synuclein. This radioligand is evaluated in pigs in Study II.

1.4.2 Animal Models with α -synuclein Aggregates

Most radioligands are often tested in WT animals, i.e., animals without a target region. Although these experiments provide helpful information about the pharmacokinetics of the radioligand, they fail to show affinity and signal-to-noise ratio. These are fundamental parameters that may decide the fate of the radioligand. Hence, animal models with α -synuclein depositions may be valuable tools for evaluating the radioligand.

Rodent animal models can be classified into transgenic, protein deposition, and viral vectors. Several

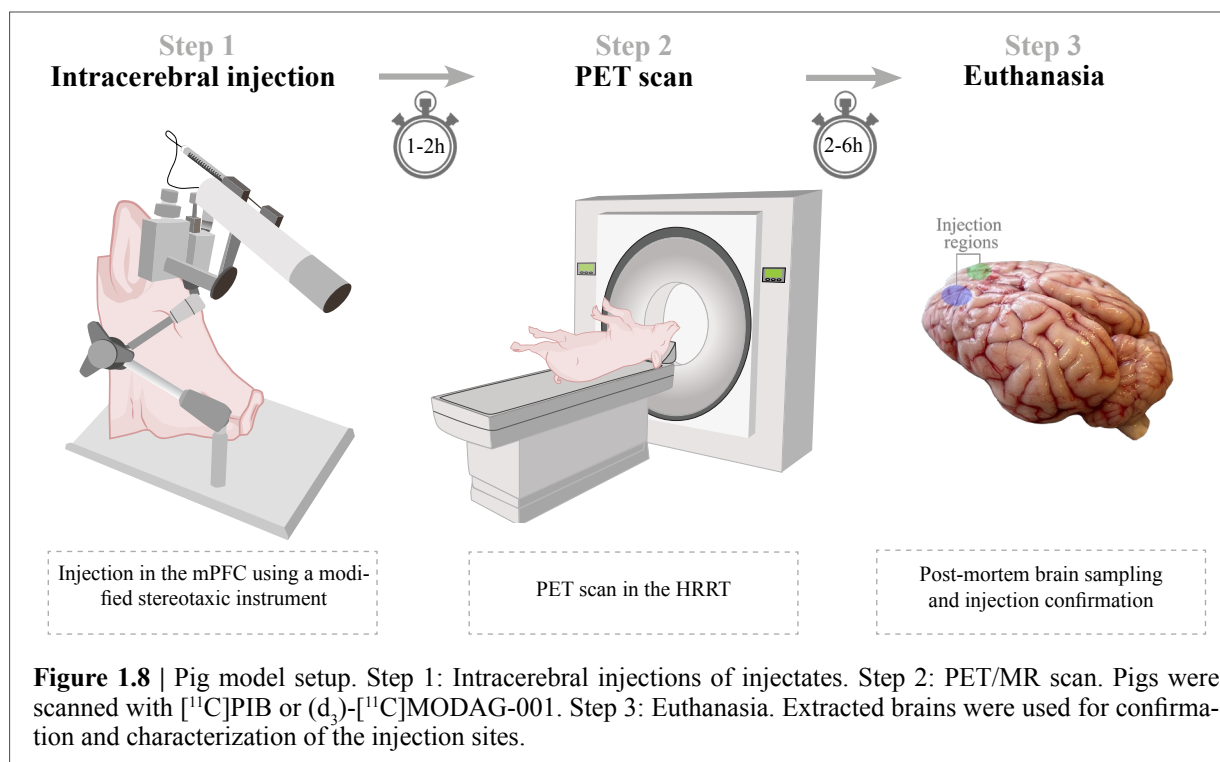
genetically modified rodent models are currently available (Visanji et al., 2016). These animals are often robust but need long durations to develop pathology (several months) and the high cost limits their use. For these reasons, the most frequently used rodent models are seeding with α -PFF, viral vectors, and a combination of viral vectors and α -PFF (Peelaerts et al., 2015; Thakur et al., 2017). The combination of a viral vector and α -PFFs demonstrated all the critical attributes of α -synucleinopathies. It was reported to speed the induction of α -synuclein aggregates to as little as ten days following α -PFF injection (Thakur et al., 2017). Verdurand et al. developed another simple, robust, and easy-to-implement model by injecting fibrils into the striatum of rats and PET imaging *in vivo* seven days after inoculation (Verdurand et al., 2018). Such an acute model was also used to evaluate (d₃)-[¹¹C] MODAG-001 (Kuebler et al., 2020).

The protein deposition (Recasens et al., 2014; Shimozawa et al., 2017) and viral vector models (Kirik et al., 2003; Eslamboli et al., 2007; Bourdenx et al., 2015; Yang et al., 2015; Koprach et al., 2016) have been used in NHPs as well. These can be valuable for radioligand development. Unfortunately, these models explained above are costly, ethically unavailable, difficult to maintain and require extended time to develop pathology. Hence as a substitute for these models, we propose a pig model where the α -synuclein protein either as homogenates or α -PFFs are intracerebrally injected and almost immediately PET scanned with a novel radioligand to test the binding properties in this injected region.

1.4.3 Intracerebral Protein Injection Pig Model

Despite its cumbersome name, the pig model proposed in this thesis serves as a simple technique of artificially creating a brain region with target protein (Study I and II). The intracerebral protein injection pig model is an acute, robust, and cheap model to enhance the efficacy of the pig as a more suitable model for radioligand development. This model is mainly developed for proteinopathies, but its application is not limited to it. This model is not meant to replace the highly valuable disease models, both rodents and larger animals. Instead, produce a more manageable addition, explicitly meant for radioligand development. For this, protein aggregates can be directly injected into the brain, the animal can then be PET scanned almost immediately, and the binding properties of the radioligand can be evaluated. The user can determine the choice and concentration of proteins to answer the specific question required, e.g., determine the minimum injectate concentration necessary for a signal. The model is tested with both α -PFFs as well as pathological human brain homogenates. The human brain pieces used to create the homogenates are thoroughly characterized *in vitro*. Hence, the exact human pathology can be verified. In this way, the hypothesized structural difference between human and *in vitro* fibrils can be overcome. This is a non-survival setup, i.e., the pig is anesthetized in the morning, undergoes intracerebral protein injections, PET scanned, and then euthanized at the end of the day. Consequently, the injectates are evaluated *in vitro* before the injection, *in vivo* after the injections, and again *in vitro* on postmortem tissue. This is especially advantageous in radioligand development. The outline of a single pig's surgery and PET scan is illustrated in Figure 1.8.

MR-guided stereotactic injections are standard practice for intracerebral injections (Glud et al.,



2011). However, this is a long and extensive methodology that involves surgically placing an MR visible probe, MR scan, localization, and injection. Apart from being time consuming, this process is costly, and labor-intensive. Instead, we try a different approach of minimally invasive surgery using a modified stereotaxic setup. The exact procedure is explained in more detail in Section 2.2. Since it did not matter where the artificial target region is created (as long as it is in the same region every time), we decided to use the medial prefrontal cortex (mPFC). In the past, Jørgensen et al. (Jørgensen et al., 2017) validated this region for microdialysis probe placement. We choose these specific coordinates because of a prominent gyrus in this region. This large gyrus reduces the chance of missing the injection site and injecting into a sulcus which may be easily “lost.” Once the setup was optimized, the method was much faster, and we were able to finish the surgery within 3–4 hours, which still provided time for the PET scans after. BBB leakage after intracerebral injection was one of our significant concerns, but we demonstrate that our minimally invasive surgery does not hamper the BBB (more in Section 3.1 and Study I). Although, most radioligands that have passed rodent studies may already have shown data about their BBB permeability.

1.5 Presynaptic Density Imaging

In the CNS, a neuron releases neurotransmitters into the synaptic cleft, which bind to and influence receptors on pre- and post-synaptic neurons through which these neurons communicate (Alberts et al., 2013). Synaptic vesicles (storage units for neurotransmitters) are critical to this process and are situated in the presynaptic. These synaptic vesicles are lined with different kinds of proteins and phospholipids (Südhof, 1999). A vesicular protein that is our target of interest is synaptic vesicle protein 2A (SV2A). It belongs to a family of proteins comprised of three isoforms: SV2A, SV2B,

and SV2C. SV2A (92.6 kDa) are transmembrane glycoproteins (742 amino acids) with 12 domains that are expressed in synaptic vesicles ubiquitously throughout the brain (Shi et al., 2011; Mendoza-Torreblanca et al., 2013; Bartholome et al., 2017; Heurling et al., 2019). In contrast, SV2B and SV2C have a considerably more restricted distribution (Bajjalieh et al., 1994). The precise physiological function of SV2A is unknown, but it is speculated essential for neurotransmitter release since SV2A knock-out (KO) mice die of severe seizures within three weeks of being born (Janz et al., 1999; Crowder et al., 2002).

For about two decades, SV2A has been investigated and is a significant milestone in presynaptic research. It was started from the discovery of Lynch et al., who showed that SV2A is the binding site for the first-in-class antiepileptic drug from UCB pharma, levetiracetam (Lynch et al., 2004). The evaluation and characterization of [¹¹C]UCB-J were performed in NHPs. In two major studies of *in vivo* PET and *in vitro* binding assays, the Yale PET group established [¹¹C]UCB-J imaging for presynaptic density imaging (Finnema et al., 2016; Nabulsi et al., 2016). In postmortem studies, they compared the regional uptake of [¹¹C]UCB-J to other more well-known synaptic markers like synaptophysin. They show strong co-localization of SV2A and synaptophysin in the grey matter while none to weak binding in the white matter region of centrum semiovale. The first practical application of SV2A PET was the preclinical evaluation of the newly developed antiepileptic drug, brivaracetam, which was the predecessor to levetiracetam (Nicolas et al., 2016).

Synaptic density can be measured using UCB-J (*in vitro* and *in vivo*), a foundational tool for determining whether synapses have decreased or increased. This biophysical and biochemical property of the brain to reorganize itself structurally, called structural neuroplasticity, is further explored in this thesis.

1.5.2 Neurodegeneration and Synaptic Loss

The prospect of [¹¹C]UCB-J to measure presynaptic loss has been performed in multiple *in vivo* studies worldwide from different PET centers. [¹¹C]UCB-J (or its derivatives) have been tested in neurodegenerative diseases like AD (Robinson et al., 2014; Mecca et al., 2020), PD (Matuskey et al., 2020), PSP (Holland et al., 2020; Mak et al., 2021), and DLB (Nicastro et al., 2020). It has also been used *in vitro* for autoradiography to measure presynaptic density in AD subjects (Metaxas et al., 2019). [¹¹C]UCB-J is not only used in clinical studies but its efficacy has been evaluated in rodent models of neurodegeneration (Bertoglio et al., 2020; Thomsen et al., 2021a, 2021b; Xiong et al., 2021).

Study III uses the unilateral 6-hydroxydopamine (6-OHDA) dopaminergic lesion rat model of Parkinson's disease. Experiments using constrained neural systems have formed a critical research technique for delving into the brain connection. PD subjects show an alteration in the dopamine system (Alexander, 2004). A wide range of neurotoxins are available, of which 6-OHDA targets the dopamine system explicitly; hence this is called a model for Parkinson's disease. The neurotoxin was injected in one hemisphere (ipsilateral) while the other hemisphere acted as control (contralateral). This hemispheric lesion is possible since ascending dopamine neurons are directed toward the ipsilateral hemisphere, although a minority (~5%) also project towards the contralateral hemisphere.

This model has two variants: i) partial lesion and ii) severe lesion (Breit et al., 2007). The partial lesion may represent the early stages of PD-related dopaminergic lesion. The 6-OHDA is intracerebrally injected into the striatum and causes a lesion in the nigrostriatal pathway (neurons connected between substantia nigra to the striatum). On the other hand, the severe model of 6-OHDA causes a total or subtotal lesion of the dopaminergic cells. For this, 6-OHDA is injected into the substantia nigra or (/ and) the medial forebrain bundle (MFB). The partial lesion was previously tested with [¹¹C]UCB-J (Binda et al., 2021; Thomsen et al., 2021b), while the severe lesion was tested in Study III. Minor changes that could be identified with [¹¹C]UCB-J in the regions outside the nigrostriatal pathway were expected.

In an ongoing study, the efficacy of [³H]UCB-J was also evaluated *in vitro* in neocortical regions of three neurodegenerative diseases, PD, PSP, and MSA. These are also identified as movement disorders since they initially (often primarily) affect movement, balance, and gait. Subcortical neurodegeneration, that has been shown *in vivo*, may correspond to the movement and balance disabilities in PD and PSP (Holland et al., 2020; Matuskey et al., 2020). However, other non-motor symptoms like cognitive impairment, pain, and depression, may be associated with neocortical neurodegeneration, which are not well characterized (Constantinescu et al., 2019; Mak et al., 2021). Further, a decrease in [¹¹C]UCB-J signal has been associated with tau and A β protein aggregates (Vanhaute et al., 2020; Coomans et al., 2021; O'Dell et al., 2021; Mecca et al., 2022). It would be interesting to see the effect of α -synuclein aggregates on presynaptic density. Since no radioligand is available for α -synuclein, currently quantification of α -synuclein can only be performed *in vitro*. Being a presynaptic protein, α -synuclein's effect on SV2A is very interesting to know for therapeutic as well as neuropathological purposes. Currently, [³H]UCB-J autoradiography is completed, while semiquantification of α -synuclein, tau and A β will be performed using immunohistochemical methodologies.

From all of the clinical and preclinical studies in neurodegenerative diseases, it is evident that presynaptic imaging is unlikely to enable pre-symptomatic diagnosis, but it is a promising tool for determining pathogenetic pathways, monitoring disease progression, and evaluating responsiveness to experimental treatments (Cai et al., 2019; Holland et al., 2020).

1.5.3 Psychedelic-Induced Neuroplasticity: Biochemical Mechanisms.

Humphrey Osmond coined the term “psychedelics” in 1957 (Osmond, 1957), describing a group of substances that had mind-manifesting effects. Preclinical (Catlow et al., 2013; de la Fuente Revenga et al., 2021; Hesselgrave et al., 2021; Shao et al., 2021) and clinical studies (Griffiths et al., 2016; Carhart-Harris et al., 2018, 2021; Davis et al., 2020) have shown that psychedelics may be therapeutic in treating disorders of the CNS such as major depressive disorder, post-traumatic stress disorder, and substance abuse (Carhart-Harris and Goodwin, 2017). The therapeutic effects of psychedelics are rapid and sustained, even after only a single dose (Ross et al., 2016). Currently, it is hard to understand how psilocybin has such a long and persistent effect. One explanation suggests that psilocybin facilitates a thorough interaction with the therapists, and it is this mystical-type effect (McCulloch et al., 2021) that

is therapeutic (Hartogsohn, 2018; Yaden and Griffiths, 2021). Although, this can often be subjective and hard to quantify. The other hypothesis suggests that psychedelics, including psilocybin, induced structural and functional neuroplasticity (Olson, 2022; Vollenweider and Smallridge, 2022). This is further hypothesized to be 5-HT_{2A}R mediated. 5-HT_{2A}R are GPCRs, i.e., upon agonist stimulation, the receptor can interact with G-protein resulting in various downstream effects depending on the type of G-protein.

Psychoactive effects of psychedelics are induced by activating 5-HT_{2A}R, particularly those on cortical pyramidal neurons, which are essential for a hallucinogenic experience (González-Maeso et al., 2007). The focus of psychedelics in this thesis is primarily psilocybin, a so-called classical psychedelic. Psilocybin can be found in ~200 types of fungi or mushrooms, therefore the common moniker “magic mushrooms” (Gartz, 1996).

Psilocybin is a psychedelic prodrug, i.e., it is only dephosphorylated to its active ingredient, psilocin, when ingested or injected into the body. Psilocin is an agonist of various 5-HT receptors, but the 5-HT_{2A}R is the most relevant because it is responsible for the psychedelic experience in humans and 5-HT_{2A}R-mediated behavior in animals (González-Maeso et al., 2007; Donovan et al., 2020a).

It has been previously shown that 5-HT_{2A}R and some other GPCRs exist in two states, a high-affinity state and a low-affinity state (López-Giménez et al., 2001; Song et al., 2005; Shalgunov et al., 2019). While antagonists have a single affinity for receptors, agonists have two affinities: high affinity for receptors coupled to G-proteins and low affinity for uncoupled receptors (López-Giménez et al., 2001) (Figure 1.9). The pharmacology of high-affinity receptors includes several distinct processes, including functional activation and receptor internalisation, leading to lysosomal degradation of the 5-HT_{2A}R (Berry et al., 1996; Gray and Roth, 2001). Functional activation is through the G_{o11}-protein pathway, which may play an essential role in cell growth (Goldsmith and Dhanasekaran, 2007; Wang et al., 2014). We hypothesize this to be the pathway through which psilocybin and other psychedelics may induce structural plasticity.

Structural neuroplasticity in brain regions associated with emotional processing, such as the hippocampus and PFC, may be critical in the pathophysiology of mood disorders such as major depressive disorder. Postmortem (Kang et al., 2012; Duric et al., 2013) and *in vivo* (Holmes et al., 2019) research on depressed patients have revealed a loss of synapses due to the down-regulation of

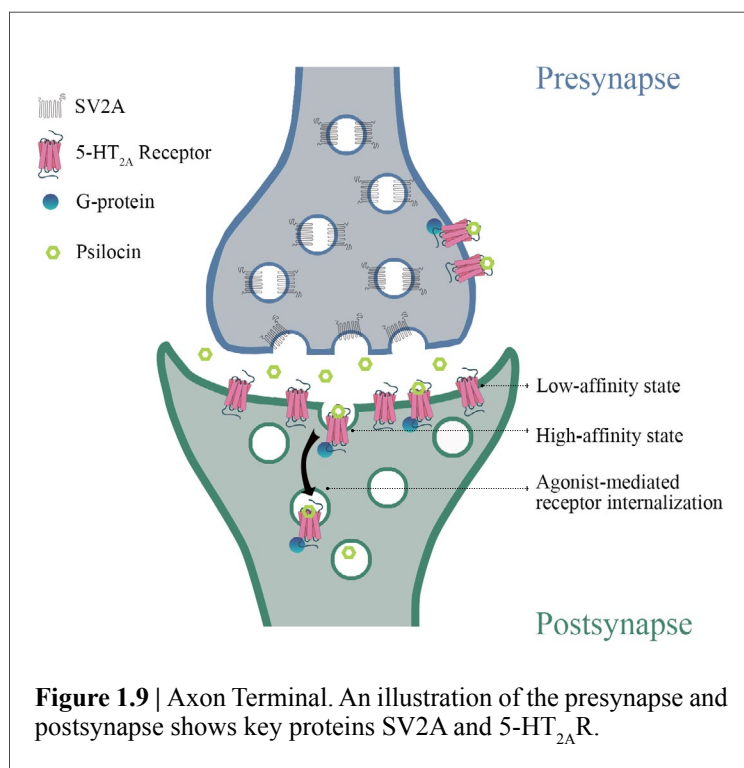


Figure 1.9 | Axon Terminal. An illustration of the presynapse and postsynapse shows key proteins SV2A and 5-HT_{2A}R.

synaptic proteins or genes. On the other hand, 5-HT_{2A} R gene and protein levels have been shown to be increased in depressed individuals (Shelton et al., 2009; Amidfar et al., 2017). Thus, a 5-HT_{2A} R mediated increase in synaptic density may be connected with psychedelics' possible antidepressant effects. Study IV explores these hypotheses using autoradiography for synaptic density (to see neuroplastic changes) and 5-HT_{2A} R autoradiography (to see the effects of psychedelics on them).

Aims

The research presented in this thesis can be divided into two broad aims, each of which was the subject of various studies with specific objectives.

AIM I

To establish a pig model with intracerebral protein injections that will help assess novel radioligands.

Objective 1:

To validate the intracerebral protein injection pig model using [¹¹C]PIB.

Objective 2:

To evaluate the novel α -synuclein radioligand, (d₃)-[¹¹C]MODAG-001 in the intracerebral protein injection pig model.

AIM II

To optimize, evaluate, and apply [¹¹C]UCB-J PET and [³H]UCB-J autoradiography for SV2A quantification as a marker for presynaptic density in preclinical settings.

Objective 1:

To compare the synaptic density and neuronal metabolic function in the unilateral 6-OHDA dopamine lesioned rat model of Parkinson's disease.

Objective 2:

To quantify presynaptic and 5-HT_{2A}R density in the pig brains after receiving a single dose of psilocybin.

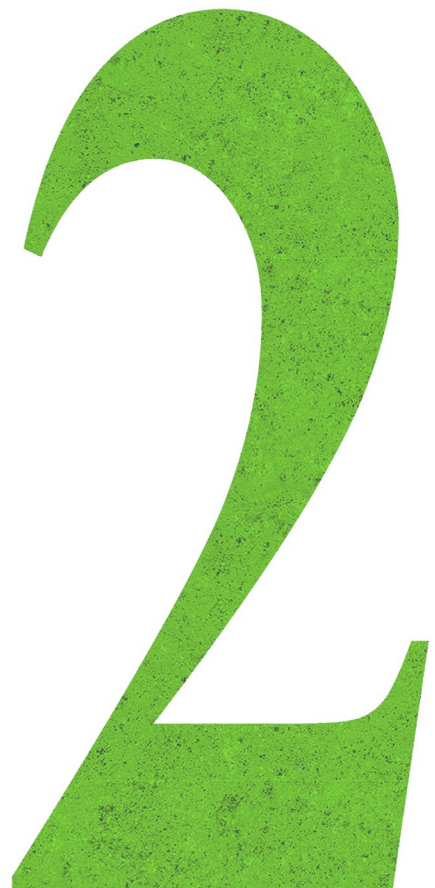
Objective 3:

To evaluate the neocortical presynaptic density in postmortem brains from PD, PSP, and MSA patients.

Methods & Materials

*“If you wish to make an apple pie from scratch, you must first
invent the universe.”*

Carl Sagan
Cosmos



2. Methods and Materials:

2.1 Study Designs

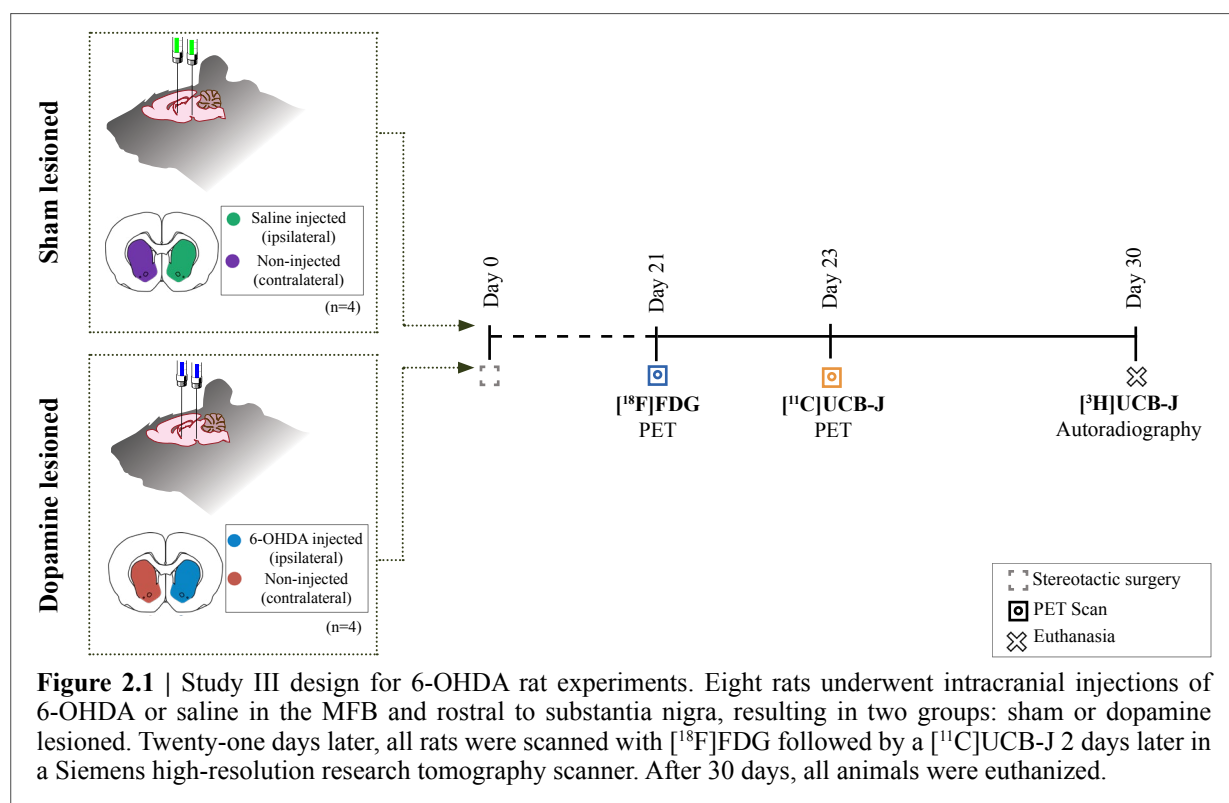
Study I and II: The intracerebral protein injection model was developed to evaluate novel radioligands. Eleven pigs were intracerebrally injected with α -PFF, AD human brain homogenate, DLB human brain homogenate, or saline (Table 2.1). A detailed description of the α -PFF and human brain used in these studies are provided in the supplementary of Study I (Raval et al., 2022b). The model was validated using [^{11}C]PIB, showing affinity to A β and α -PFF but not for the Lewy bodies (Klunk et al., 2004; Ye et al., 2008). Hence, saline and DLB homogenates acted as negative and positive control injections. Autoradiography was used to characterize the injected brain region. Once the model was validated (d_3)-[^{11}C]MODAG-001, a novel α -synuclein radioligand was tested in the model. In addition to testing (d_3)-[^{11}C]MODAG-001 in the different injections mentioned above, a test-retest scan and blocking experiment with its unlabeled counterpart was performed.

Table 2.1 | Overview of pigs used in Study I and Study II. Details of bodyweight, PET scans, intracerebral injection, and additional data availability are shown.

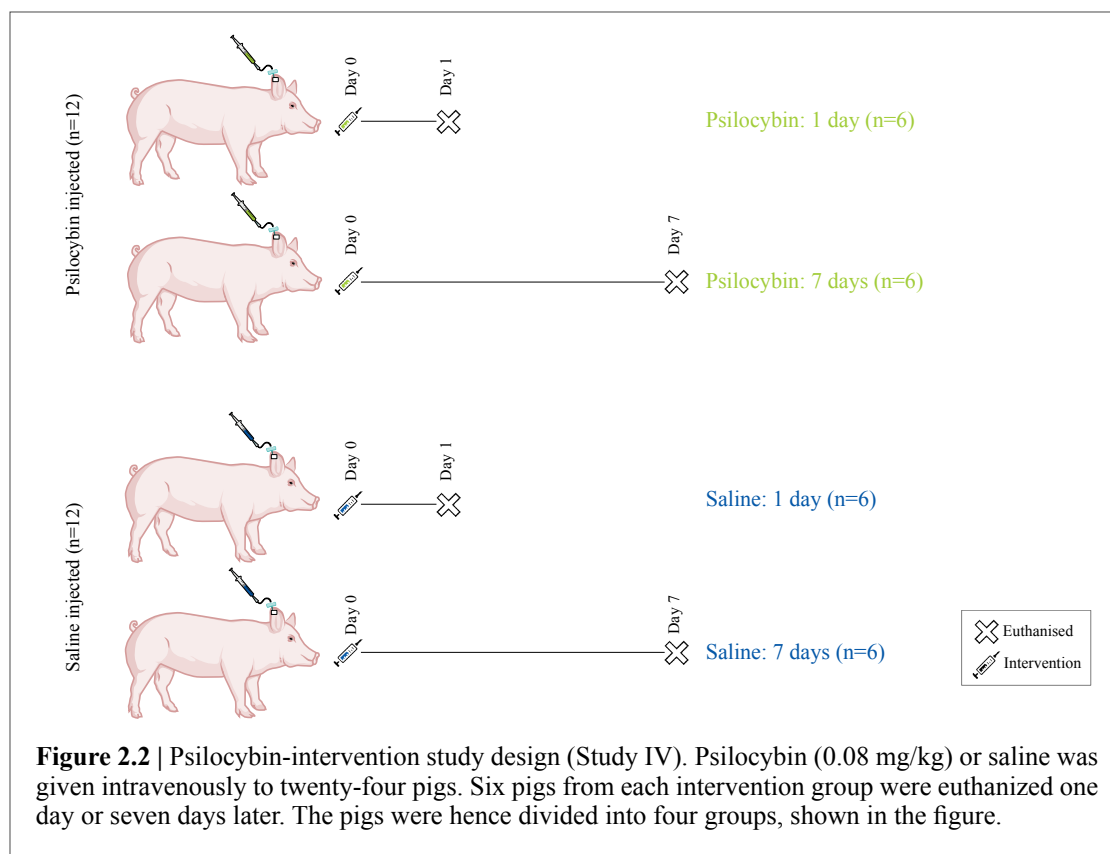
Study	PET scan	Pig no.	Weight (kg)	Left injection site	Right injection site	Additional data
Study I (Model Validation)	[^{11}C]PIB	1	28	160 μg α -PFF	160 μg α -PFF	Individual PF curve
		2	27	150 μg α -PFF	Saline	Individual PF curve
		3	25	Saline	160 μg α -PFF	Individual PF curve
		4	28	160 μg α -PFF	DLB homogenate	Individual PF curve
		5	31	DLB homogenate	AD homogenate	-
		6	28	DLB homogenate	AD homogenate	-
		7	27	Saline	AD homogenate	-
Study II (Novel radioligand)	(d_3)-[^{11}C]MODAG-001	8	28	DLB homogenate	150 μg α -PFF	-
		9	25	AD homogenate	150 μg α -PFF	-
		10	26	75 μg α -PFF	150 μg α -PFF	Test-retest
		11	29	75 μg α -PFF	150 μg α -PFF	Blocking study Brain R-HPLC

α -PFF: α -synuclein preformed fibrils (25 μL)
 Saline: physiological saline (25 μL)
 DLB-homogenate: DLB human brain homogenate (10%, 25 μL) [Braak stage II, n = 2 x2 regions, A β and tau -ve]
 AD-homogenate: AD human brain homogenate (10%, 25 μL) [Braak stage IV, n = 2 x2 regions, α -syn -ve]
 PF curve: individual parent fraction curve
 Blocking study: pretreatment of unlabeled MODAG-001 (1 mg/kg) dissolved in 19% dimethyl sulfoxide in saline
 Brain R-HPLC: brain radiometabolites measurement with radio-high performance liquid chromatography

Study III: Dynamic [^{11}C]UCB-J and static [^{18}F]FDG scans were performed in the severe unilateral 6-OHDA lesioned rat model to compare the two tracers in a specific neuronal circuit called the cortico-striato-thalamo-cortical (CSTC) circuit (Yuan et al., 2005; Blandini et al., 2008). In a total of eight female Long-Evans WT rats (~ 215 g, 10–11 weeks old), four were dopamine lesioned while four were sham lesioned. After the recovery period, the rats were PET scanned with the two radioligands. *In vivo* [^{11}C]UCB-J PET and *in vitro* [^3H]UCB-J autoradiography were also compared in the same animals (Raval et al., 2021a). An illustration of the study design is shown in Figure 2.1.



Study IV: This study is a pure autoradiography application. Pig brains were retrieved from previously published research in our group, where pigs received either psilocybin or saline (Donovan, 2020; Donovan et al., 2020a). Donovan et al. determined the psilocybin dose required to produce psychedelic effects comparable to humans. The amount was set to 0.08 mg/kg, which shows a 67% occupancy with [^{11}C]Cimbi-36, a 5-HT $_2\text{A}$ /2CR agonist radioligand. This occupancy of the 5-HT $_2\text{A}$ R can elicit a strong psychedelic effect in both humans and pigs (Madsen et al., 2019; Donovan et al., 2020a). Psilocybin or saline was injected IV through a long-term ear vein catheter in awake pigs, which were not under any form of external stress. A total of 24 pigs (~ 20 kg, 10–11 weeks old) received the interventions. Twelve pigs were euthanized one day after, while the remaining were euthanized seven days after. Pigs were divided into four groups based on intervention and termination day: Psilocybin: 1 day, Psilocybin: 7 days, Saline: 1 day, and Saline: 7 days (Raval et al., 2021b). In frozen brain sections, [^3H]UCB-J binding is used to measure SV2A density, while [^3H]Cimbi-36 (agonist) and [^3H]MDL100907 (antagonist) binding are used to measure 5-HT $_2\text{A}$ R density. Figure 2.2 shows the overall design of the study.



Study V: The final study on the thesis was also an autoradiography study. In this ongoing study, the ability of [³H]UCB-J was tested to determine, not so well-known, cortical neurodegeneration in movement disorders like PD, PSP, and MSA. Postmortem frozen brain sections from the frontal cortex, temporal cortex, parietal cortex, occipital cortex, and centrum semiovale were acquired from six PD patients, seven PSP patients, seven MSA patients, and seven neurologically healthy subjects (hereafter called controls [NC in figures]) (Table 2.2). First, the B_{\max} and K_D of [³H]UCB-J in postmortem human brain sections were determined. Then, [³H]UCB-J white matter and cortical binding are compared in the patients to neurologically healthy controls. Experiments currently on-going include quantification of protein aggregates and post-synaptic markers, e.g. postsynaptic density protein 95 (PSD-95)

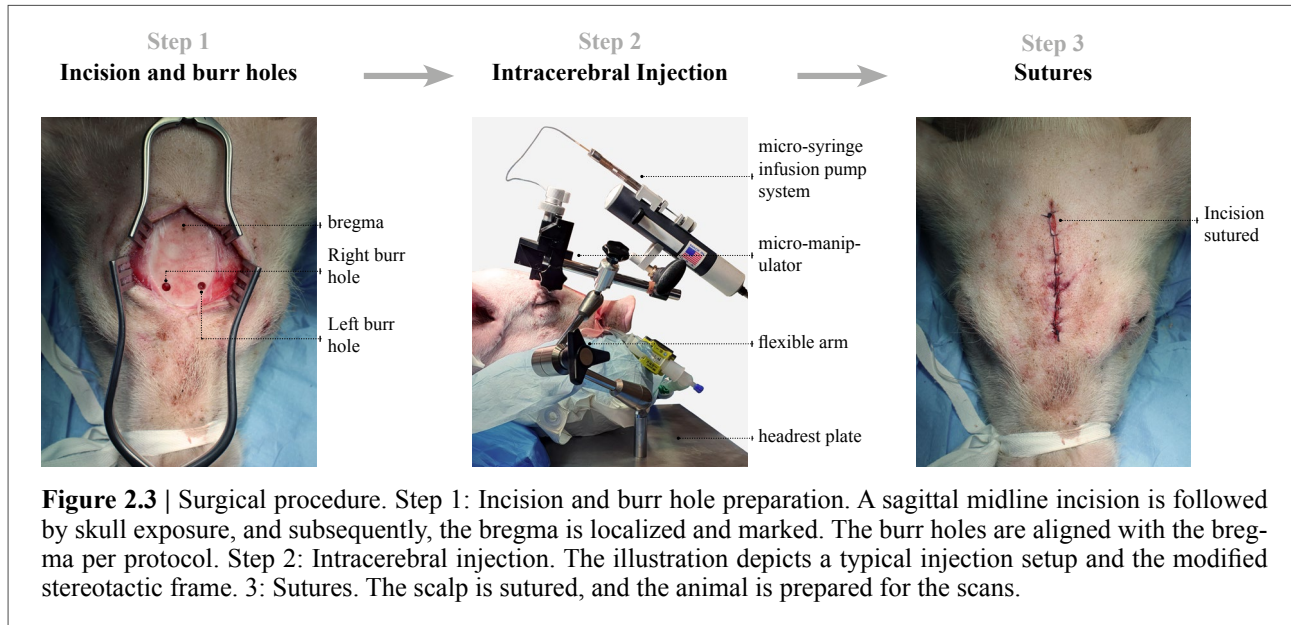
Table 2.2 | Summary of the disease and control groups in Study V.

Diagnosis	Sex (F/M)	Age at Onset (y)	Age at Death (y)	PMI (h)	Brain weight (g)
NC	6F/1M	NA	83.9 (11.3)	44.6 (29.2)	1131 (164)
PD	6M	65.5 (8.7)	76.2 (7.7)	57.0 (38.3)	1371 (140)
PSP	2F/5M	68.1 (5.2)	74.4 (5.3)	29.7 (21.7)	1242 (137)
MSA	5F/2M	59.1 (4.7)	65.1 (4.5)	28.9 (4.7)	1130 (172)

NC: Neurologically healthy controls, PD: Parkinson's Disease, PSP: Progressive Supranuclear Palsy, MSA: Multiple System Atrophy, PMI: Postmortem Interval, NA: Not Applicable.
Data shown as mean (SD).

2.2 Surgical Procedure in Pigs

For Study I and II, all pigs were injected with 25 μ L of the substrates in both hemispheres' mPFC. This technique was developed from another similar approach targeting the mPFC (Jørgensen et al., 2017, 2018).



Explaining the procedure in short, anesthesia was induced with Zoletil mixture intramuscular (IM) injection and maintained with 10-15 mg/kg/h propofol IV infusion; local anesthesia was instilled at the site was incisions (scalp and catheter placement). Fentanyl IV infusion was used to achieve analgesia. Using endotracheal intubation, ventilation was provided with 34% oxygen in normal air. The following were catheterized to obtain arterial and venous access: two femoral arteries, two superficial mammary veins, and two ear veins. The pigs' vital signs were constantly monitored during surgery and PET scan.

An in-house modified stereotactic instrument was designed for the intracerebral injections. This contained a head-rest plate, a flexible arm attached with a micro-manipulator, and a micro-syringe infusion pump system. As shown in Figure 2.3, the flexible arm allowed the micro-manipulator to be positioned and locked relative to the target entry site with a trajectory perpendicular to the skull. Two burr holes were placed bilaterally, 25 mm anterior and 8 mm lateral to bregma after midline incision and skull exposure. The injections were performed with a 250 μ L syringe and a 28 G blunt tip needle attached to the micromanipulator and microinfusion pump system. The needle was advanced 14 mm dorsally to the mPFC target point (8, 25, 14 mm in XYZ coordinates). The infusion was delivered over two steps (10 and 15 μ L, 1 mm apart) at 450 nL/min by a 7-minute pause before a slow withdrawal of the needle to avoid backflow. An absorbable hemostatic gelatin sponge was inserted into both burr holes and the incision sutured back. The animals were then transported to the scanner facilities.

2.3 Surgical Procedure in Rats

Conventional stereotactic procedure and apparatus (Fornari et al., 2012) was employed in Study III for the unilateral injection of 6-OHDA(2,5-Dihydroxytyramine hydrobromide) into the MFB and rostral substantia nigra to cause a severe dopaminergic lesion in one hemisphere. Since 6-OHDA also could cause damage to noradrenergic neurons, desmethylimipramine (25 mg/kg, intraperitoneal) was injected before the surgery. Desmethylimipramine, a norepinephrine reuptake inhibitor, has a neuroprotective effect on noradrenergic neurons and ensures a dopaminergic lesion with 6-OHDA (Esteban et al., 1999; Palner et al., 2011). Anesthesia was induced with 3% isoflurane and maintained with 1.2–1.8% isoflurane in oxygen. A dental micromotor and a round bur were used to drill two burr holes on one side of the skull (ipsilateral side, while the other is contralateral). Target regions were the MFB (coordinate: AP = 4.8 mm, ML = 1.7 mm, DV = 8 mm) and the rostral substantia nigra (coordinate: AP = 3.6 mm, ML = 2 mm, DV = 8.3 mm) (Raval et al., 2021a). Three μL of 2 $\mu\text{g}/\mu\text{L}$ 6-OHDA (Sigma-Aldrich, Sborg, Denmark) or saline were infused at the target with a speed of 151 nL/min followed by 7 min of pause before removal of the needle. This was performed with a 10 μL syringe with a 33 G needle. The incision was sutured back, and the rat was returned to its cage, starting a recovery period for 21 days.

2.4 PET Data Acquisition

All PET-scanned including the rats and pigs, were performed in a Siemens high-resolution research tomograph (HRRT) PET scanner (CPS Innovations/Siemens, Malvern, PA, USA). Radiochemical preparations were performed at the Department of Clinical Physiology, Nuclear Medicine & PET, Rigshospitalet. [^{11}C]methyl triflate preparation was used for [^{11}C]PIB (Raval et al., 2022b), while [^{11}C]methyl iodide preparation was used for (d_3)-[^{11}C]MODAG-001 (Raval et al., 2022a) and [^{11}C]UCB-J (Raval et al., 2021a). [^{18}F]FDG was obtained through in-house clinical production. A rotating point source ^{137}Cs (cesium) transmission scan was carried out before or after each PET emission scan (Keller et al., 2013). All raw PET data were reconstructed using the OP-3D-OSEM algorithm using a point-spread function modeling, 16 subsets, 10 iterations, and standard corrections (Sureau et al., 2008). Attenuation and scatter correction were performed using the transmission scan (Keller et al., 2017b). Time framing details are provided in the article (Raval et al., 2021a, 2022a, 2022b). Each time frame consisted of 256×256 voxels ($1.22 \times 1.22 \times 1.22$ mm in size) and 207 planes.

Tracers were administered IV through one of the superficial mammary veins at the start of the scan for the pigs. PET emission data were acquired: 90 min for [^{11}C]PIB (449 ± 35 MBq, 5 ± 4 μg) and 121 min for (d_3)-[^{11}C]MODAG-001 (323 ± 83 MBq, 6 ± 1 μg). Along with the PET data. Arterial blood sampling was performed. Two methods were used. 1) Automatic blood sampling was performed using an ABSS autosampler (Allogg Technology, Strängnäs, Sweden) during the first 15-20 min that provides whole blood radioactivity. 2) Manual blood sampling was performed at multiple time points throughout the scan. More manual samples were collected at the start of the scan, while the frequency was reduced over time. These samples were processed for different data acquisitions, including whole blood radioactivity, plasma radioactivity, and parent fraction curve using R-HPLC

(Gillings, 2009; Raval et al., 2022a, 2022b). All instruments used to measure radioactivity in the blood lab and the ABSS autosampler were cross-calibrated against the HRRT to provide comparative measurements. Pig 10 and Pig 11 received two scans of (d₃)-[¹¹C]MODAG-001. Pig 10 received a test-retest scan where the animal was scanned twice after the intracerebral injection. In Pig 11, a self-blocking experiment was performed with non-deuterated unlabelled MODAG-001 (1 mg/kg). This was dissolved in saline with 19% dimethyl sulfoxide and infused over 15 mins starting ~6 min before tracer injection. Pig 11 also received a third (d₃)-[¹¹C]MODAG-001 injection (180 MBq, 3.74 μg) and was euthanized 15 min post-tracer injection. R-HPLC was also performed in brain homogenate and plasma to see potential radio-metabolites crossing the BBB (Raval et al., 2022a).

For rat PET scans, isoflurane (3%) in oxygen was used to induce anesthesia. Rats were placed in a two × two in-house custom-made rat holder (called “The Rat Hotel”). This enabled the simultaneous full-body scanning of four rats with a single tracer production (Keller et al., 2017a). Before the [¹⁸F]FDG scan, the rats were fasted overnight. [¹⁸F]FDG was administered intraperitoneally at a dose of 25 ± 3 MBq on average. The rats were returned to their cage to achieve [¹⁸F]FDG uptake while awake. Then the rats were anesthetized (45 min post-injection), placed in the holder, and a PET emission data was obtained for 45 min. For [¹¹C]UCB-J, the tail veins were cannulated (BD Neoflon 25G, Stockholm, Sweden) before the scan. [¹¹C]UCB-J (20 ± 2 MBq, 0.04 ± 0.1 μg) was administered over 7–10 s through the tail vein catheter at the start of the scan. PET emission data was acquired for 60 min.

2.5 PET Data Analysis

Pig preprocessing was performed using an in-house developed code on MATLAB 9.5.0. To delineate the specific ROIs, the reconstructed PET data was parcelled in an automated fashion using a PET-MR pig brain atlas based on the Saikali MR atlas (Saikali et al., 2010), where the PET data is coregistered to a group of PET and MR data sets usually not from the same animal (Villadsen et al., 2017). Once coregistered, the parcellation is performed for the desired ROIs, and the TACs are generated. Regions used from the Saikali MR atlas include the neocortex, occipital cortex, temporal cortex, and cerebellum. In addition, two additional regions of the injection sites were added. These were hand-drawn on the atlas. ROIs were defined from an approximate injection site initially around the needle penetration site seen on the MRI. Positive immunohistochemistry (IHC) sections further optimized this from different injections. The region is about 0.32-0.35 cm³ (~ 250 voxels) and symmetrical in both hemispheres. Automatic delineation was visually inspected for all pig scans. Blood data was processed on Microsoft Excel. A complete PET data set included PET TACs, whole blood radioactivity, plasma radioactivity, and the parent fraction.

Kinfitr (v. 0.6.0) in RStudio (R, v. 4.0.2) was used to perform kinetic modeling for both [¹¹C]PIB and (d₃)-[¹¹C]MODAG-001 (Matheson, 2019; Tjerkaski et al., 2020). For [¹¹C]PIB, the Logan Graphical Analysis (Logan et al., 1990) was applied to the ROI TACs and metabolite corrected population-based AIF (Raval et al., 2022b) to estimate the V_T values. The optimal threshold time (t^*) for the Logan plot was calculated with kinfitr. It was set to 27.5 min (last 10 time frames) since it had the

least maximum percentage of variance and stable outcome parameter. SRTM2 with the occipital cortex as a reference region was used for reference tissue modeling to calculate BP_{ND} values (Wu and Carson, 2002). The average k_2 over R_1 ratio, i.e., k_2' , was calculated using the SRTM (Lammertsma and Hume, 1996). For (d₃)-[¹¹C]MODAG-001, the non-invasive Logan graphical analysis (Logan et al., 1996) was used to calculate BP_{ND} values with the occipital cortex as reference regions. Average k_2' was calculated from SRTM from high-binding regions (α -PFF injected region) (Lammertsma and Hume, 1996). The t^* of 23 min (last 15 time frames) was found optimum. To generate SUVs (g/mL) that are used for the graphical purpose, the regional radioactivity concentration (kBq/mL) was normalized to the administered dosage (MBq) and corrected for the animal weight (kg). PMOD 3.7 created and visualized representative summed PET images.

Preprocessing and kinetic modeling of the rat PET data was done with PMOD 3.7/3.0. Brains were cropped and coregistered to either a PET template ([¹⁸F]FDG) or MR template in standard space. ROI-atlas of the selected regions CSTC circuit regions from Schiffer's atlas (Schiffer et al., 2006) were applied to the PET scans, including anterior cingulate cortex, medial prefrontal cortex, motor cortex, nucleus accumbens, orbitofrontal cortex, striatum, thalamus, and ventral midbrain (a region covering both the ventral tegmental area and substantia nigra) (Raval et al., 2021a). All parcellation and co-registration were visually inspected post spatial transformation.

Since [¹⁸F]FDG was static, PET analyses were straightforward. The PET data were pooled into one large time frame. The radioactive in the ROIs (Bq/mL) was first converted to SUV. for this time frame. Then, a whole-brain normalization factor (WB_{NF}) was applied to each ROI (Raval et al., 2021a). This allows the comparison of signals between animals since it cancels effects such as tracer metabolism in blood and variations in brain uptake due to the intraperitoneally injections. For [¹¹C]UCB-J, TACs were generated from all ROIs. In addition, an ROI was delineated in the lumen of the heart's left ventricle (Raval et al., 2021a). This heart ROI was used as an IDIF, which acts as a surrogate AIF (Bertoglio et al., 2020). V_T values were calculated using the IDIF and the TACs using the 1TCM (Bertoglio et al., 2020; Raval et al., 2021a; Xiong et al., 2021).

2.6 Autoradiography

Autoradiography was performed on cryosection made on a cryostat mounted on Superfrost PlusTM microscope slides. Study I used coronal pig sections from the different injection sites for [³H]PIB autoradiography. Study III used coronal sections from around the striatum of dopamine and sham lesioned animals for [³H]UCB-J autoradiography. Study IV used sections from the PFC and the hippocampus of psilocybin or saline-treated animals for [³H]UCB-J, [³H]MDL100907, and [³H]Cimbi-36 autoradiography. Finally, Study V had sections from the frontal, temporal, parietal, and occipital cortex as well as centrum semiovale of all subjects for [³H]UCB-J autoradiography. Table 2.3 shows where the ligands were acquired or purchased from, the preincubation, incubation, washing, and number of washes.

For all radioligands, slides were thawed for 45 min before being preincubated twice for 10 min in buffer. Slides were then incubated for 60 min in the appropriate incubation buffer (Table 2.3). Incubation

Table 2.3 | Summary of radioligands used for autoradiography.

Radioligand	Providers	Used in Study	Molar activity (Ci/mmol)	Incubation buffer	Wash buffer	Duration and number of washes	Exposure time
[³ H]PIB	Novandi	Study I	78	PBS (1X), pH7.4 10% Ethanol 1% BSA	PBS (1X), pH7.4 10% Ethanol 4°C	3 × 5 min	3 days
[³ H]UCB-J	Pharmaron Ltd	Study III Study IV Study V	28	50mM Tris-HCl, pH 7.4 5 mM MgCl ₂ , 2 mM EGTA 0.5% BSA	50mM Tris-HCl, pH 7.4 4°C	2 × 10 min	2 days
[³ H]UCB-J	UCB pharma	Study IV	14	50mM Tris-HCl, pH 7.4 5 mM MgCl ₂ , 2 mM EGTA 0.5% BSA	50mM Tris-HCl, pH 7.4 4°C	3 × 5 min	7 days
[³ H]MDL100907	ViTrax	Study IV	56	50 mM Tris-HCl, pH 7.4 0.01% Ascorbic acid 4 nM CaCl ₂ 0.1% BSA	50 mM Tris-HCl, pH 7.4 0.01% Ascorbic acid 4 nM CaCl ₂ (ice-cold)	2 × 10 min	7 days
[³ H]Cimbi-36	Karolinska Institute	Study IV	53	50 mM Tris-HCl, pH 7.4 0.01% Ascorbic acid 4 nM CaCl ₂ 0.1% BSA	50 mM Tris-HCl, pH 7.4 0.01% Ascorbic acid 4 nM CaCl ₂ (ice-cold)	2 × 10 min	7 days

was terminated with several washes with the respective wash buffer (Table 2.3) and a final rinse with deionized water (dH₂O). The slides were air-dried and fixed overnight in a paraformaldehyde vapor chamber (4 °C). The next day, excessive moisture was removed in an exicator, and the slides were then placed in an autoradiography cassette with radioactive tritium standards (ART0123). Sections and standards were exposed to tritium-sensitive IPs. An Amersham TyphoonTM IP or Fujifilm BAS 1000 scanner read the IP after exposure time.

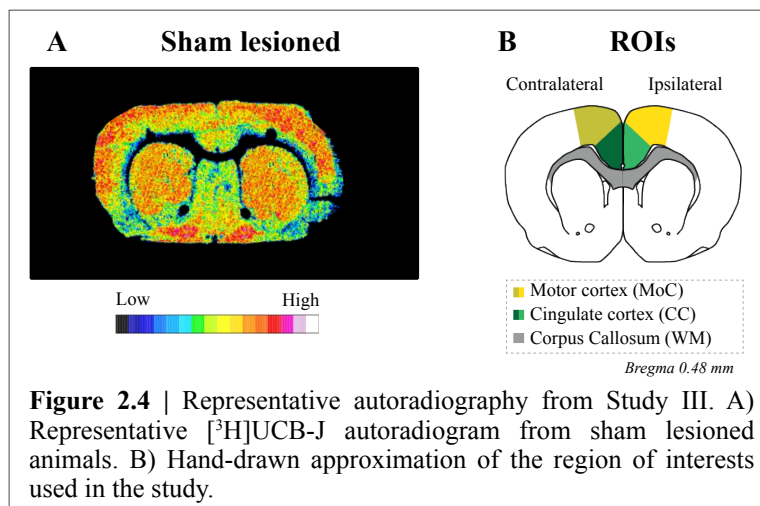
ImageJ was used for calibration, quantification, and data interpretation (Schneider et al., 2012). In hand-drawn ROIs (explained later), the mean pixel density (grayscale) was converted to nCi/mg Tissue Equivalent (TE) using a four-parameter general curve fit (David Rodbard, NIH). The units nCi/mg TE was converted to fmol/mg TE using the decay-corrected specific activity of the radioligand. TB, NSB, and SB were determined (Equation 1.10). For [³H]UCB-J, the white matter can be used as a pseudo-reference region due to almost no amount of specific binding (Raval et al., 2021b). This is more extensively validated for pigs and humans in Study IV and V.

The specific differences in the studies are listed below:

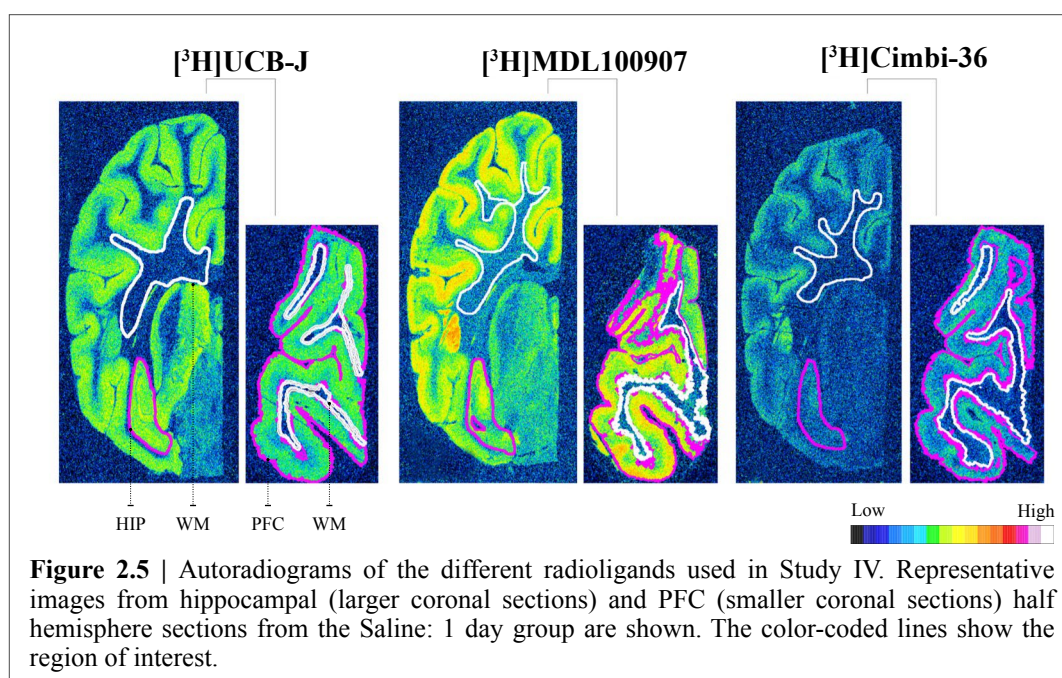
Study I: Only saturation assays were performed in this study. An increasing concentration of [³H]PIB was used for TB, while NSB was determined using thioflavin S (100 μM) and corresponds to [³H]PIB concentration. AD-homogenate-injected pig brain sections (n = 1) and AD post-mortem human brain sections (n = 2 × 2) were incubated with 0 to 5 nM of [³H]PIB. α-PFF injected pig brain sections (n = 1) were incubated with 0 to 40 nM of [³H]PIB. No specific binding was seen in DLB-homogenate-injected pigs or human brain sections; therefore, saturation experiments could not be performed (Raval et al., 2022b). TB was determined in pathology-rich regions or at the injection site using TB slides (see Figure 3.3), while NSB was determined using NSB slides. *In vitro*, BP was calculated with Equation 1.7.

Study III: To compare [³H]UCB-J autoradiography and [11C]UCB-J PET, autoradiography on the

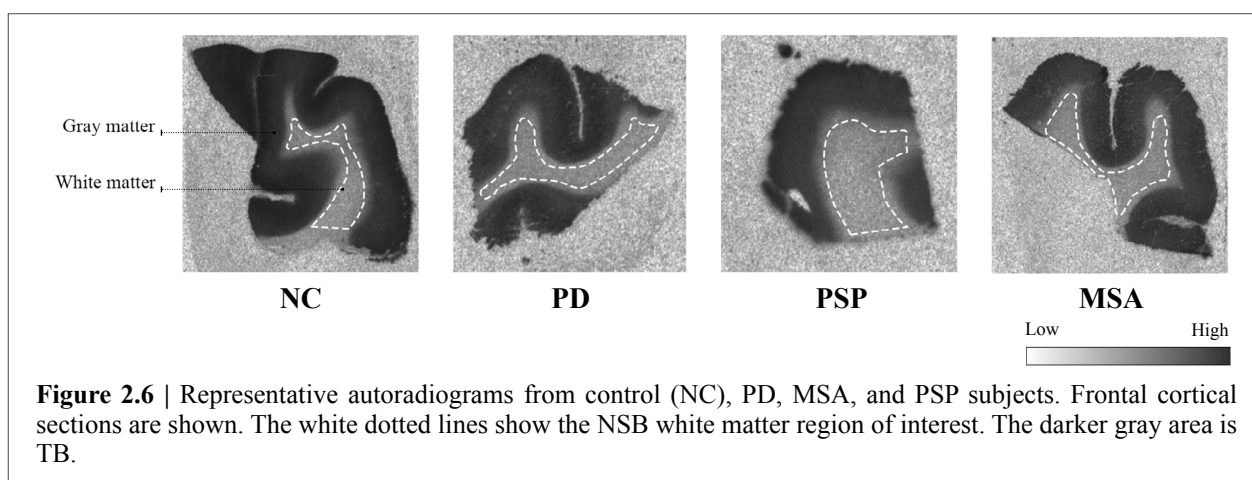
sections was performed with 6 nM [³H]UCB-J. Grey matter from the cingulate and motor cortex was used to determine TB, while the corpus callosum as a white matter region was used for NSB (Figure 2.4).



Study IV: First, a saturation assay with [³H]UCB-J, [³H]MDL100907, and [³H]Cimbi-36 were performed to determine the B_{max} and K_D for the radioligands as well as confirm the use of the white matter as a reference region (Raval et al., 2021b). The assay buffer concentration of the respective radioligands was decided using 4–5× K_D values to accurately determine B_{max} values in the section. Concentration of 60 nM for [³H]UCB-J, 3 nM for [³H]MDL100907 and 1 nM for [³H]Cimbi-36 was used. TB was determined in the hippocampal and cortical grey matter, while NSB was determined in the white matter on the same slides (Figure 2.5).



Study V: Like with Study IV, first, a saturation assay with [^3H]UCB-J was performed in the frontal cortex of control subjects ($n = 3$). [^3H]UCB-J concentration range was 0 to 30 nM for TB and respective [^3H]UCB-J concentration with 10 mM of levetiracetam (Keppra, UCB Pharma) for NSB. Next, the white matter (centrum semiovale) binding was evaluated in all groups. This assay required both TB and NSB slide (20 nM [^3H]UCB-J + 10 mM levetiracetam). Finally, cortical tissue comparisons of the different groups were performed at 20 nM [^3H]UCB-J, where only TB slides were required. For the saturation assay and white matter binding, TB was determined in the gray matter of TB slides, while NSB was determined in the NSB slides. For group comparison, TB was determined in the gray matter of TB slides, while NSB was determined in the white matter of TB slides (Figure 2.6).



GraphPad Prism (v. 9.2.0) was used to analyze the data. B_{\max} and K_D were determined by non-linear regression analysis (Function: One site - total and non-specific binding) for all saturation assays. Statistical analysis for the comparative assays is explained in Section 2.8.

2.7 Statistical Analysis

All data are presented as mean values \pm standard deviation, including error bars in the different figures unless otherwise specified. All software and statistical analyses used in this thesis are listed below:

Study I: Graph-Pad Prism (v. 9.2.0) was used for statistical analysis and data visualization. The non-parametric Kruskal-Wallis one-way analysis of variance (ANOVA) with Dunn's multiple comparison test was used to compare the injected regions to the reference regions.

Study II: Graph-Pad Prism (v. 9.2.0) was used for data visualization. No statistical analyses were performed in this study.

Study III: Jamovi was used for statistical analysis of the data. Data visualization was performed using Graph-Pad Prism (v. 9.0.1). The difference between the ipsilateral and contralateral side for each tracer ([^{18}F]FDG and [^{11}C]UCB-J) in the dopamine and sham lesioned groups was measured using a paired t-test without multiple comparisons correction. Cohen's d_z values (a standardized measure of within-subject differences) (Lakens, 2013) between the ipsilateral and contralateral regions were determined to allow direct comparison of the magnitude of change with [^{18}F]FDG normalized SUVs

and [11C]UCB-J V_T . Pearson r values were calculated between the [3 H]UCB-J SB in fmol/mg TE and respective [11C]UCB-J V_T values from each region in the ipsilateral and contralateral hemisphere, yielding eight different correlation values. These values were averaged for ipsilateral and contralateral separately and provided two Pearson r values.

Study IV: The data were analyzed using R (v. 4.0.3), while Graph-Pad Prism (v. 9.0.0) was used for data visualization. The comparison between group means was done using a permutation test (with 1000 permutations) on log-transformed values and adjusted for multiple comparisons using the Holm method.

Study V: Graph-Pad Prism (v. 9.2.0) was used for statistical analysis and data visualization. Kruskal-Wallis non-parametric ANOVA was used while not correcting for multiple comparisons (number of comparisons = 3) between the NC and PD, PSP, or MSA binding values in the different regions.

Statistic Disclaimer: Due to the small sample size and the number of comparisons made in Study III and V, they are exploratory, meaning strong confirmatory findings have been avoided. As a result, all p -values reported should be viewed as an assessment of indirect evidence against the null hypothesis, which is no difference between groups or hemispheres. Here “significant” or “not significant” within the Neyman-Pearson Null-hypothesis-significance-testing framework has been avoided.

2.8 Data Availability Statement

Study I: All derived data and MATLAB or R scripts are available at a public GitHub repository (https://github.com/nakulrraval/Protien_inj_pig_model_PIB).

Study II: All derived data and R scripts are available at a GitHub repository (https://github.com/nakulrraval/Protien_inj_pig_model_MODAG001). All other requests are directed to this article’s corresponding or first author.

Study III: All raw data, kinetic modeling analysis, and scripts are available at a GitHub repository (https://github.com/nakulrraval/OHDA_rat_UCBJ_FDG).

Study IV and V: The data presented in this study are available on request from the corresponding author. The data are not publicly available due to other ongoing investigations.

2.9 Ethical Statements

Pig experiments: All pig procedures were performed following the European Commission’s Directive 2010/63/EU and complied with the Animal Research: Reporting of *In Vivo* Experiments (ARRIVE) guidelines. Studies I and II were approved by the Danish Council of Animal Ethics under journal no. 2017-15-0201-01375. Study IV was also approved by the Danish Council of Animal Ethics under journal no. 2016-15-0201-01149. Experiments were also approved by the Department of Experimental Medicine, University of Copenhagen. Pigs used in the study are Danish slaughter pigs (Yorkshire×Duroc×Landrace) obtained from a local farm and were given a week to acclimate before the experiment. Individual pens with 12-hour light/dark cycles, free access to water, and weight-adjusted food twice daily were used to house the animals. In Study III, animals were trained up to a

week in the stables to allow human handling.

Rat experiments: All rat experiments conformed to the European Commission's Directive 2010/63/EU with approval from the Danish Council of Animal Ethics (Journal No. 2017-15-0201-01375 and 2017-15-0201-01283) and the Department of Experimental Medicine, University of Copenhagen.

Postmortem human tissue experiments: For Study I and II, the brain regions were obtained from the Neuropathology Core of the Emory Center for Neurodegenerative Disease. For Study V, brain regions were obtained from brains donated to the Bispebjerg Brain Bank (Copenhagen University Hospital, Denmark). A movement disorder specialist followed and clinically diagnosed all patients. All donated brains were neuropathologically examined to confirm the diagnosis. All donors provided informed written consent, and clinical data were obtained retrospectively from the patient's medical reports. The project was approved by the ethical committee of the Capitol Region of Denmark, journal no: H-20062005.

2.10 Funding Acknowledgments

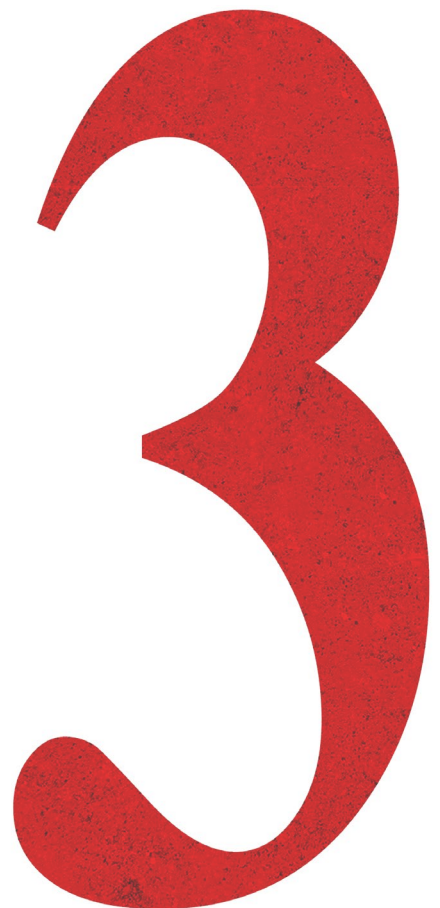


This project has received funding from the European Union's Horizon 2020 research and innovation program under the Marie Skłodowska-Curie grant agreement No. 813528. This project also received funding from Parkinsonforeningen, Denmark (R16-A247) and NeuroPharm (Centre for Experimental Medicine Neuropharmacology). This research project received human brain tissue from the Neuropathology Core of the Emory Center for Neurodegenerative Disease.

Results & Discussion

*“Nothing in life is to be feared, it is only to be understood.
Now is the time to understand more, so that we may fear less.”*

Marie Skłodowska Curie

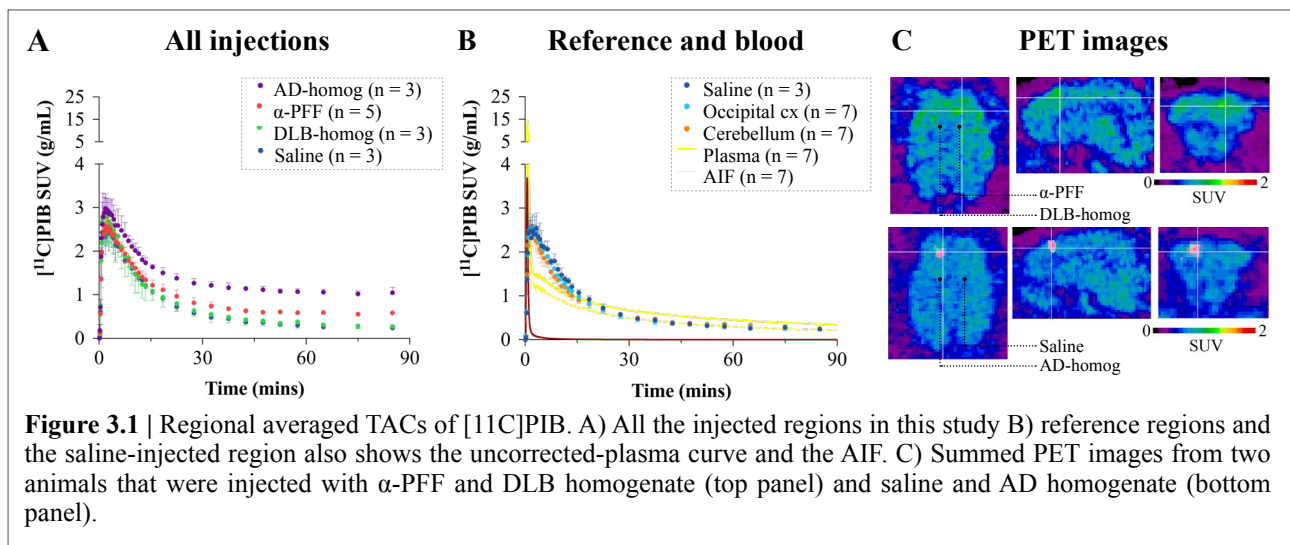


3. Results and Discussion:

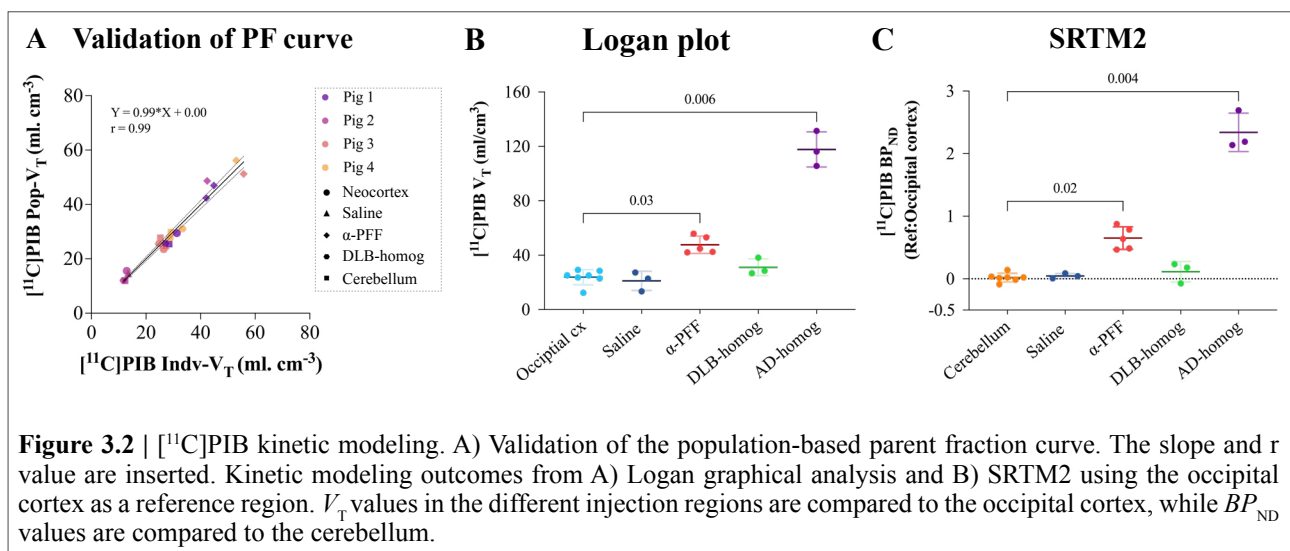
3.1 Study I: Validation of Intracerebral Protein Injection Pig Model

3.1.1 [¹¹C]PIB TACs and Kinetic Modeling Parameters

In the intracerebral protein injection pig model, increased retention of [¹¹C]PIB was found in the regions injected with AD homogenate and α -PFF (Figure 3.1). Compared to the cerebellum and occipital cortex, DLB-homogenate and saline-injected regions showed virtually no retention.



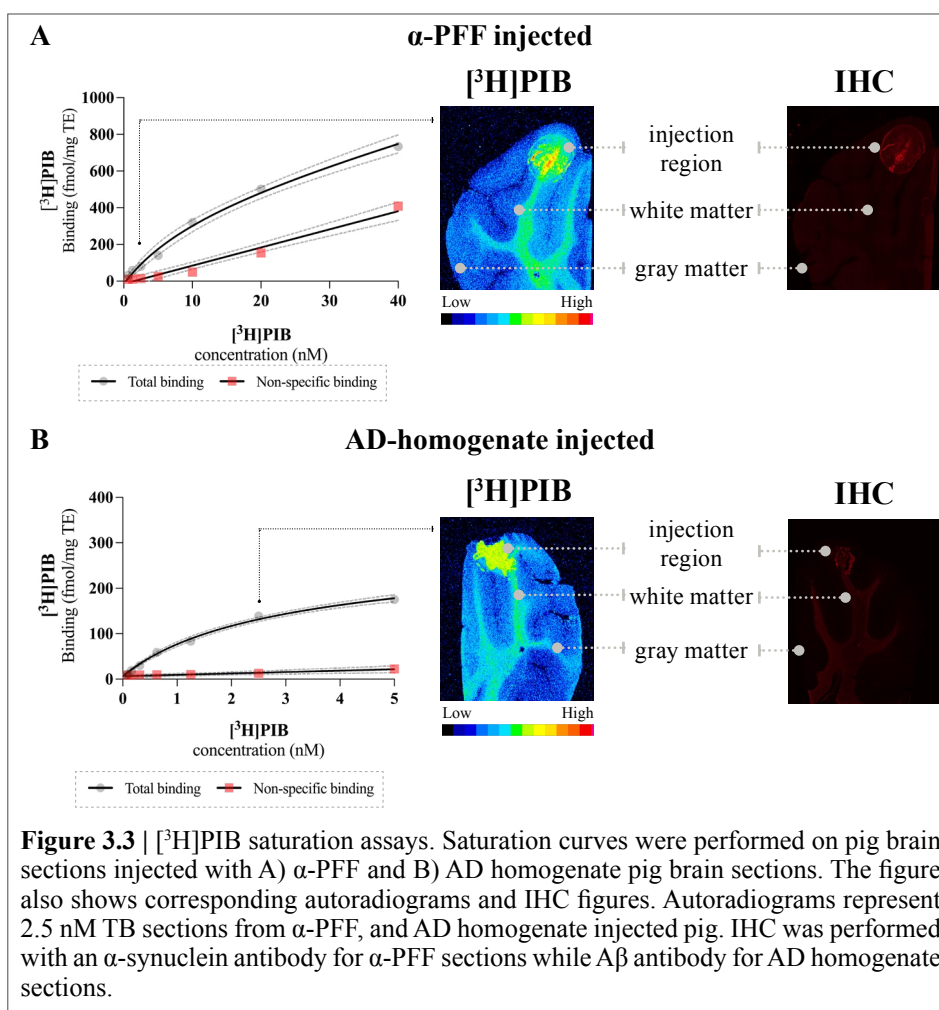
Due to [¹¹C]PIB's affinity to amyloid plaques and other β -sheet structures like tau and α -synuclein, high uptake in AD homogenate and α -PFF injected region was expected (Klunk et al., 2004; Ye et al., 2008; Hellström-Lindahl et al., 2014). But, since [¹¹C]PIB has no affinity for Lewy bodies (Fodero-Tavoletti et al., 2007), the negative control, DLB-homogenate, also met expectations. The uptake in saline-injected regions was not different from that in the occipital cortex, indicating that the injection



itself does not tamper with the integrity of the BBB. Although, this was also shown with the help of gadolinium-enhanced MRI (Raval et al., 2022b).

Invasive and reference tissue kinetic modeling outcomes matched the TAC visual interpretations. Using the Logan graphical analysis, AD-homogenate injected regions showed 4-fold higher V_T values than the occipital cortex, and the α -PFF regions had 2-fold higher V_T values. BP_{ND} values from SRTM2 using the occipital cortex showed an average of 2.3 for AD-homogenate regions and 0.65 for α -PFF regions. Both BP_{ND} and V_T values in saline and DLB homogenate injected regions were close to comparative reference regions (Figure 3.2).

Invasive kinetic modeling with [^{11}C]PIB was challenging, mainly due to 1) R-HPLC analysis difficulties and 2) blood kinetics. The parent fraction curve from the last three HPLC scans could not be estimated because of a technical problem. Instead, from the first four scans, a population-based parent fraction curve was created and used for the last three scans. [^{11}C]PIB's metabolism was fast as less than 10% of the parent remained in plasma at the first manual sample (2.5 mins). As a result of the parent compound's extremely rapid metabolism, both the 1TCM and the 2TCM produced subpar outcomes. Instead, we used Logan graphical analysis with less fitting parameters. To further ease quantification, reference tissue modeling with SRTM2 was also performed (Yaqub et al., 2008; Tolboom et al., 2009).



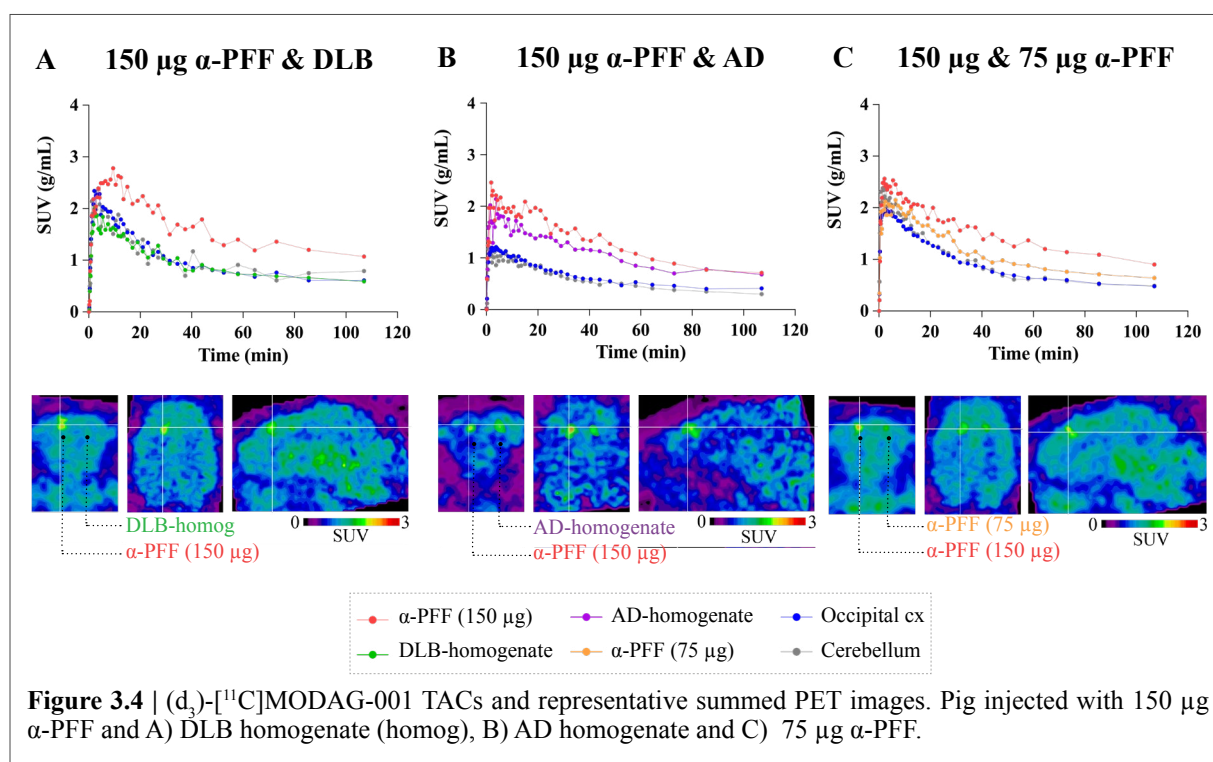
3.1.2 Autoradiographic Characterization of Injection Sites

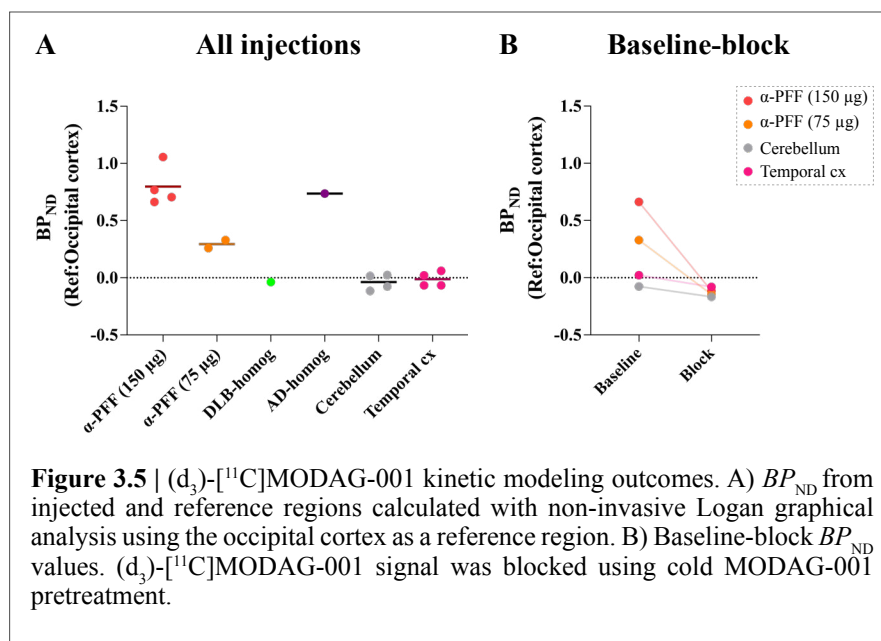
Using our minimally invasive modified-stereotactic approach, the successful injection was confirmed with autoradiography and IHC (Figure 3.3). Using autoradiography and saturation assays, postmortem pigs with injected pathology and diseased human brains were compared to assess the appropriateness of our pig model to human pathology. In the α -PFF region of pig brain sections (n=1), a B_{\max} of 477.2 fmol/mg TE and K_D to be 12.07 nM was seen. This was almost comparable to the *in vitro* results seen in past literature (Ye et al., 2008). Similar K_D but higher B_{\max} in postmortem AD human brain sections (366.7 fmol/mg TE, n=3) was found compared to AD-homogenate injected pig brain section (233.4 fmol/mg TE, n=1). AD-homogenate injected sections had 2.4-times higher BP than α -PFF injected sections, showing satisfactory *in vitro* to *in vivo* comparison. To “humanize” the pig model, postmortem human brain homogenates from patients with relevant neurodegenerative diseases were used. This provides a more realistic model of human pathology compared to synthetic fibril injections. Nevertheless, synthetic fibril assays have proven highly useful in screening novel radioligands and cannot be discarded (Korat et al., 2021).

3.2 Study II: Evaluation of (d₃)-[¹¹C]MODAG-001

3.2.1 (d₃)-[¹¹C]MODAG-001 TACs and Kinetic Modeling Parameters

Using the intracerebral protein injection pig model from Study I, (d₃)-[¹¹C]MODAG-001 was evaluated. Injection of (d₃)-[¹¹C]MODAG-001 shows a high brain uptake (2.5 SUV) and a quick wash-out. Compared to the occipital cortex and cerebellum, regions injected with 150 μ g (n = 4), 75 μ g (n = 2) α -PFF and AD homogenate (n = 1) had higher radioactivity retention. DLB homogenate region (n = 1) TAC, on the other hand, essentially showed no retention (Figure 3.4).





Non-invasive Logan graphical analysis show BP_{ND} values of 0.78 ± 0.1 ($n = 4$) in 150 μg α -PFF, 0.29 ($n = 2$) in 75 μg α -PFF and 0.73 in AD-homogenate injected regions. As expected from visual TAC interpretation, DLB-homogenate injected regions had BP_{ND} values close to zero (Figure 3.5A).

Same day test-retest scans with (d_3) - $[^{11}\text{C}]$ MODAG-001 showed identical TACs and similar BP_{ND} values in target and reference regions. The signal in 150 μg and 75 μg α -PFF was completely blockable with pretreatment of 1 mg/kg of MODAG-001. The temporal cortex and cerebellum both showed a modest decrease in binding (Figure 3.5B).

In Study I, the highest available concentration of α -PFF for intracerebral injection was used due to the proof-of-concept nature of the study. As an added value of the model, different concentrations of α -PFF are used in Study II. With (d_3) - $[^{11}\text{C}]$ MODAG-001, a dose-response of the injected α -PFF was observed, but concentrations below 50-75 μg would be hard to detect since the BP_{ND} values in the 75 μg α -PFF are not substantially high. This attributes to the poor signal-to-noise ratio. On the other hand, there was increased uptake in A β and tau-rich AD homogenates but no significant uptake in DLB homogenates, despite DLB being a pure synuclein pathology. Previously, autoradiography studies have found the highest uptake in human brain sections with AD subjects (Kuebler et al., 2020). (d_3) - $[^{11}\text{C}]$ MODAG-001's lack of affinity for DLB homogenates and its affinity for AD homogenates make us less enthusiastic about its use as a radioligand in human studies. Assuming a similar signal-to-background ratio in humans, the contrast between reference regions and target regions is not adequate for visualization of α -synuclein pathology even though *in vitro* affinity is subnanomolar.

Kuebler et al. use a similar rat model as in this study where α -PFF are intracerebrally injected, and the rats are scanned four days post-injection (Kuebler et al., 2020). A relatively high uptake of (d_3) - $[^{11}\text{C}]$ MODAG-001 can also be seen in the α -PFF injected regions of these rats. The only difference is that the control used in the study was saline, and no other protein aggregated was tested.

3.2.2 (d₃)-[¹¹C]MODAG-001 metabolite and signal-to-noise ratio

The plasma kinetics and metabolism of (d₃)-[¹¹C]MODAG-001 were rapid, with ~10% of the parent radioligand remaining in plasma after 20 min (n = 1 x 2 scans) (Raval et al., 2022a). In the pig euthanized 15 min post tracer injection, 10.8% of (d₃)-[¹¹C]MODAG-001 parent compound remained in the plasma while 56.1% parent compound remained in the brain homogenate from the occipital cortex. The remaining percentage was radio-metabolites (Table 3.1).

Table 3.1 | Percentage of (d₃)-[¹¹C]MODAG-001 parent and radiometabolites. Calculated using radio-HPLC + gamma counting in plasma and brain at approximately 15 min post tracer injection (n = 1).

Sample	Polar metabolites (%)	Polar & non-polar metabolites (%)	Parent tracer (%)
Plasma @ Euthanasia	80.8	8.4	10.8
Brain @ Euthanasia	30.4	13.6	56.1

Comparatively speaking, this was much faster than the mice experiments done by Kuebler et al. (Kuebler et al., 2020). At 15 minutes, the plasma parent fraction in mice was 30%, while the brain parent fraction was 87%. When moving from a smaller species to a larger one, one would expect the metabolic rate to decrease. On the other hand, the deuterated version of [¹¹C]MODAG-001 was used in our study. Deuterium incorporation was meant to improve the pharmacokinetic and metabolic profile of the radioligand (Klenner et al., 2021). However, this was not the case in these experiments. There are two main drawbacks with (d₃)-[¹¹C]MODAG-001 that should be highlighted: 1) Potential radio-metabolites crossing the BBB, 2) Poor signal-to-noise ratio. These may also be interlinked, i.e., poor signal-to-noise ratio due to radio-metabolites in the brain. Still, this theory cannot be extensively concluded due to the limited data regarding the parent fraction in pig brain tissue. Nevertheless, despite its low specificity and low signal-to-background ratio, we believe that (d₃)-[¹¹C]MODAG-001, with its high affinity for α -synuclein, is a promising lead molecule for further radioligand development.

3.3 Study III: Evaluation of [¹¹C]UCB-J in 6-OHDA Rat Model

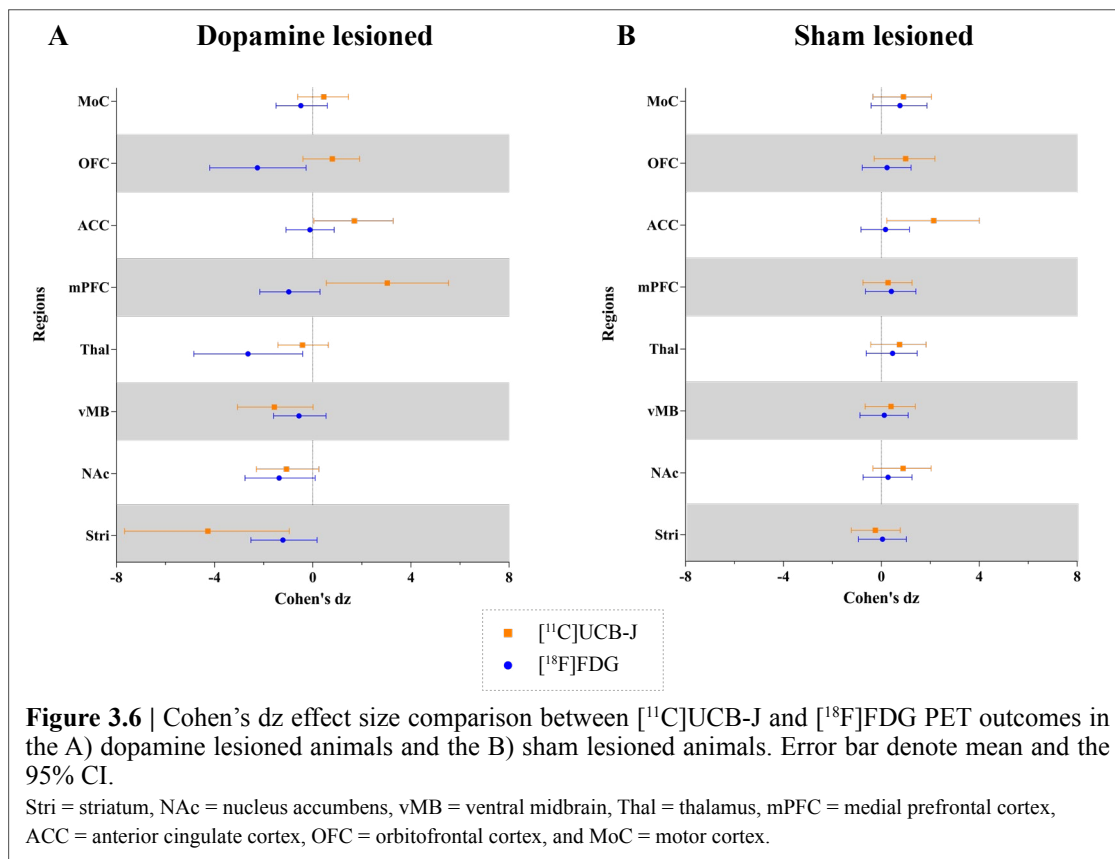
3.3.1 [¹¹C]UCB-J and [¹⁸F]FDG PET Show Divergent Changes

Successful 6-OHDA dopaminergic lesions were confirmed by striatal TH staining. Dopamine lesioned rats show lower [¹¹C]UCB-J V_T values in the ipsilateral striatum and ventral midbrain compared to the contralateral side. In contrast, higher values are seen in the mPFC and anterior cingulate cortex. Sham lesioned animals had higher [¹¹C]UCB-J V_T in the ipsilateral anterior cingulate cortex than the contralateral side. Lower [¹⁸F]FDG uptake was seen in the ipsilateral striatum, thalamus, and orbitofrontal cortex compared to the contralateral side in dopamine lesioned animals (Table 3.2).

Table 3.2 | Summary of group-wise paired t-test performed between the ipsilateral and contralateral hemisphere for each group and tracer. Notable differences are marked as *. Stri= striatum, NAc= nucleus accumbens, vMB= ventral midbrain, Thal= thalamus, mPFC= medial prefrontal cortex, ACC= anterior cingulate cortex, OFC= orbitofrontal cortex, MoC= motor cortex.

Region	$[^{11}\text{C}]\text{UCB-J } V_T$				$[^{18}\text{F}]\text{FDG Normalized SUVs}$			
	Dopamine Lesioned		Sham Lesioned		Dopamine Lesioned		Sham Lesioned	
	% diff	p value	% diff	p value	% diff	p value	% diff	p value
Stri	-8.86 %	0.003*	-0.99 %	0.66	-5.66 %	0.093	0.25 %	0.926
NAc	-5.35 %	0.122	0.56 %	0.173	-7.26 %	0.071	0.93 %	0.62
vMB	-8.72 %	0.052	3.35 %	0.486	-2.89 %	0.343	0.18 %	0.821
Thal	-2.55 %	0.465	1.20 %	0.233	-4.11 %	0.013*	1.09 %	0.425
mPFC	2.59 %	0.009*	1.33 %	0.621	-2.02 %	0.147	1.25 %	0.47
ACC	2.62 %	0.043*	14.08 %	0.023*	-0.23 %	0.832	0.47 %	0.757
OFC	2.88 %	0.209	5.71 %	0.141	-6.32 %	0.020*	0.45 %	0.67
MoC	1.85 %	0.435	5.27 %	0.169	-1.32 %	0.407	3.25 %	0.223

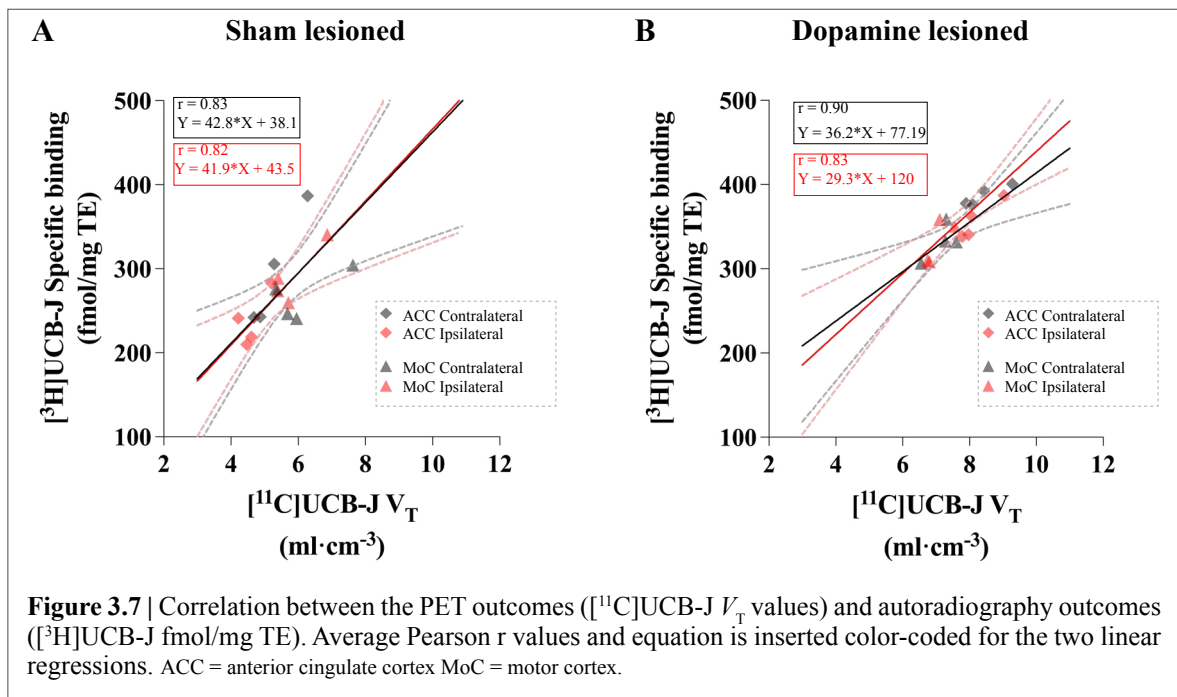
The within-subject effect size between the ipsilateral and contralateral hemispheres is expressed as Cohen's d_z for the dopamine lesioned and sham lesioned animals (Figure 3.6). In dopamine-rich regions of the basal ganglia, both $[^{11}\text{C}]\text{UCB-J}$ and $[^{18}\text{F}]\text{FDG}$ show the expected negative effect. Contrastingly, the cortical regions outcomes of $[^{11}\text{C}]\text{UCB-J}$ and $[^{18}\text{F}]\text{FDG}$ show divergent changes, except for the motor cortex. While $[^{18}\text{F}]\text{FDG}$ demonstrates a negative effect (lower SUV on the lesioned side), $[^{11}\text{C}]\text{UCB-J}$ shows a positive effect (higher V_T on the lesioned side). $[^{18}\text{F}]\text{FDG}$ in the anterior cingulate cortex seems unaffected but positively affected by $[^{11}\text{C}]\text{UCB-J}$. Sham-lesioned animals exhibit no hemispheric changes except for $[^{11}\text{C}]\text{UCB-J}$ in the anterior cingulate cortex.



[^{18}F]FDG PET has been applied as a proxy for neuronal integrity and function for years (Mosconi, 2013). The novel introduction of [^{11}C]UCB-J has provided a more accurate method of measuring synaptic density, which may also be used as a proxy for neuronal integrity. Hence, in this study, we hypothesized that [^{18}F]FDG and [^{11}C]UCB-J would show the exact effects of the 6-OHDA dopaminergic injection. However, the PET outcomes show that it may not represent the same. [^{18}F]FDG metabolism signal is affected by the glial cells around the neurons and hence cannot be accurately used as a proxy for neuronal integrity. On the other hand, [^{11}C]UCB-J only shows presynaptic density, which is also not an accurate proxy for neuronal integrity. We believe that including both tracers will provide a complete view of the neuropathology of neurodegenerative diseases such as PD.

3.3.2 [^{11}C]UCB-J PET vs [^3H]UCB-J Autoradiography

In vitro [^3H]UCB-J autoradiography was performed in all animals' cingulate and motor cortex to further support the PET finding and cortical alterations observed by [^{11}C]UCB-J PET (Figure 3.7). A Pearson r-value of 0.83 was found between [^3H]UCB-J fmol/mg TE and [^{11}C]UCB-J V_T values in sham lesioned rats' contralateral and ipsilateral regions. Correlation analysis in dopamine lesioned rats' contralateral and ipsilateral areas has a Pearson r-value of 0.90 and 0.83. Overall, PET and autoradiography have a strong association.

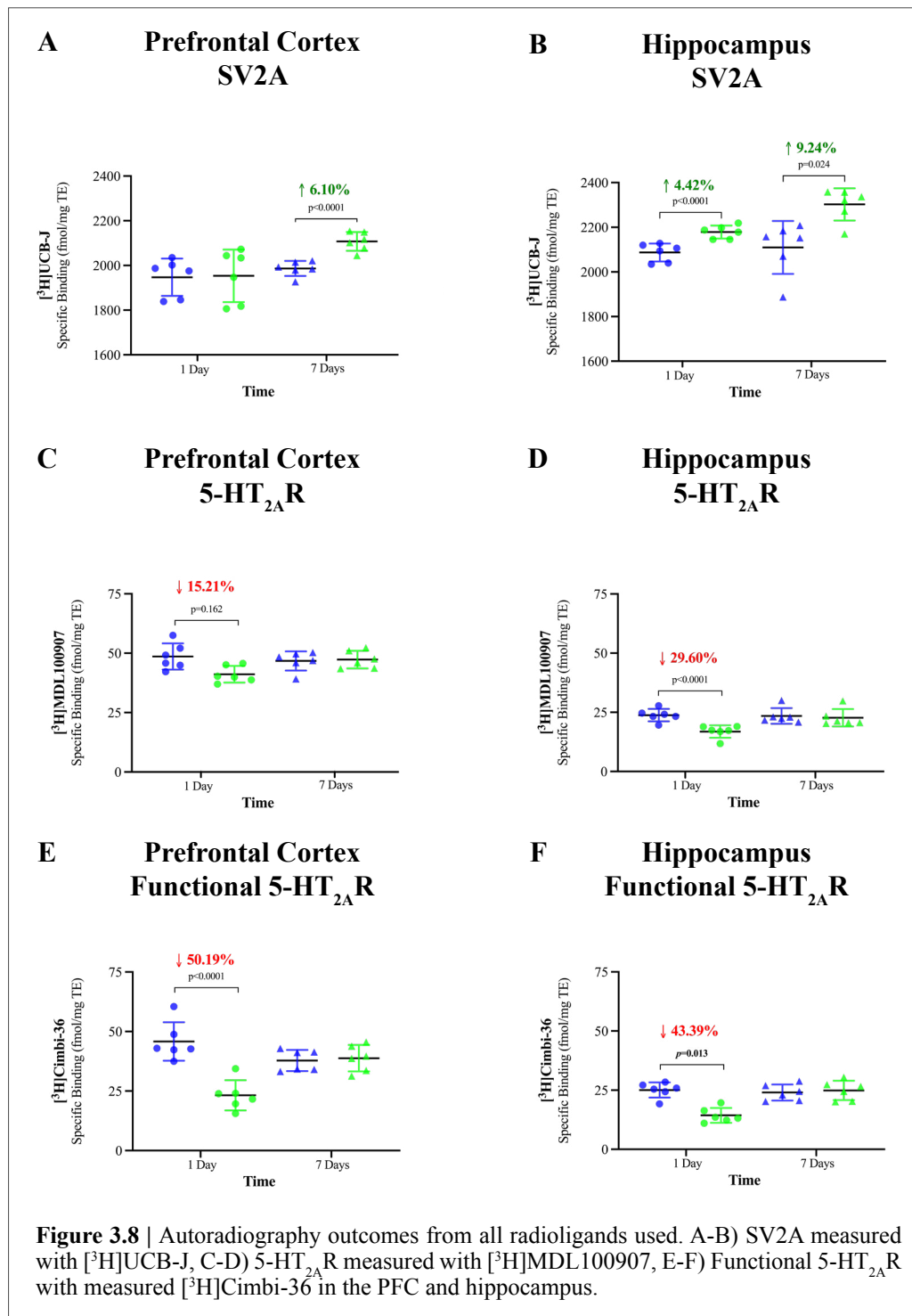


Autoradiography with a specific radioligand is theoretically designed to show the same results as PET. In some instances, this may not be the reality. Since PET is performed at tracer dosages, its results are heavily impacted by the K_D and B_{\max} of the radioligands used. On the other hand, autoradiography is influenced solely by the B_{\max} if performed at high concentrations. Preclinical experiments give us the liberty to perform such comparative experiments. We attempted to verify our PET results using autoradiography, and the data show a high association, making our findings slightly more conclusive.

3.4 Study IV: Effects of a Single Psilocybin Dose in Pigs

3.4.1 Increased SV2A and Decreased 5-HT_{2A}R Post-psilocybin in Pigs

All radioligands were thoroughly characterized and optimized before group comparison in this study. (Raval et al., 2021b). The K_D for each radioligand was determined, and then the assay was performed at a concentration that was ~ 5 -time the K_D for accurate B_{max} comparisons.



One day after treatment, the psilocybin group had significantly higher [³H]UCB-J binding in the hippocampus than the saline-treated group. Seven days later, the psilocybin group had even higher [³H]UCB-J binding in the hippocampus and the PFC than the saline group. At the same time, [³H]MDL100907 binding and [³H]Cimbi-36 binding was significantly lower in the hippocampus and the PFC in the psilocybin group one day after treatment than the saline group. Seven days after the psilocybin interventions, hippocampal and PFC binding of [³H]MDL100907 or [³H]Cimbi-36 was not different from the saline-treated animals. Percent-change and corrected p values are inserted in Figure 3.8.

These results are the first evidence in a large-animal model showing an increase in presynaptic density and a transient change in 5-HT_{2A}R after a single dose of psilocybin. Although, structural change in the dendrites has been shown in cells (Ly et al., 2018) and rodents (Shao et al., 2021). We have established a single dose of psilocybin to normalize 5-HT_{2A}R binding seven days later in healthy individuals (Madsen et al., 2019). The downregulation of 5-HT_{2A}R may also be the reason for the transient tolerance that has been seen in human studies, although not well characterized, and current evidence is only anecdotal. On the other hand, earlier work with LSD and psilocybin has shown cross-tolerance (Isbell et al., 1961). It is intriguing to see if boosting the formation of new synapses necessitates transient down-regulation of 5-HT_{2A}R.

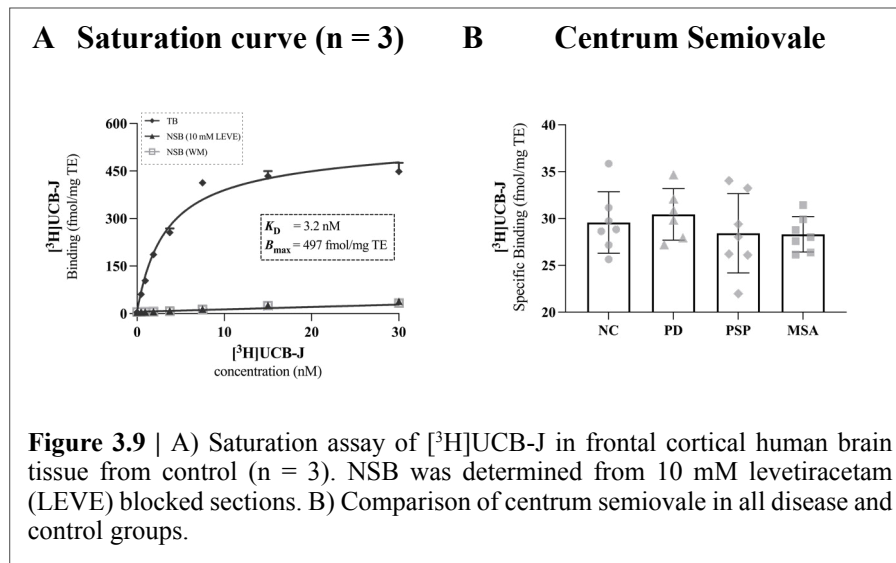
Autoradiography has an additional advantage over other protein-measuring techniques, such as western blot and immunohistochemistry, in that it can measure receptors in the functionally active vs. total receptor pool. Since antagonists bind to the entire receptor pool and agonists bind to functionally active receptors (López-Giménez et al., 2013), both 5-HT_{2A}R pools were measured in these animals. 5-HT_{2A}R density in the PFC was reduced more pronouncedly with [³H]Cimbi-36 than with [³H]MDL100907 after psilocybin treatment (Raval et al., 2021b). Using the two radioligands, we see that antagonists and agonists have different binding preferences.

This study is an application of a novel radioligand. [³H]UCB-J, with its binding to SV2A, was used to test the hypothesis that psychedelic drugs like psilocybin (through 5-HT_{2A}R stimulation) can induce structural neuroplasticity in the brain. To further find the effect of psilocybin on 5-HT_{2A}R, we also used more established radioligands like [³H]MDL100907 or [³H]Cimbi-36.

3.5 Study V: Characterization of [³H]UCB-J in Movement Disorders

3.5.1 Binding Characteristics of [³H]UCB-J in Postmortem Human Brain

The autoradiographic binding characteristics of [³H]UCB-J was measured in frontal cortical tissue in three control subjects (Figure 3.9A). The B_{max} of [³H]UCB-J was 497 fmol/mg TE (95% CI = 466 to 530 fmol/mg TE) and the K_D determined to be 3.2 nM (95% CI = 2.6 to 3.8 nM). NSB was calculated using either the white matter in cortical sections or the levetiracetam-blocked section and showed no difference in binding. [³H]UCB-J binding in the centrum semiovale was also found to be indistinguishable between patients with PD, PSP, MSA, and controls (Figure 3.9B). This allowed us to use white matter as NSB while comparing cortical binding in the different diseases.



Reference regions make *in vivo* evaluation less complicated for practical and kinetic modeling purposes. Most neurodegenerative (and other) patient-control comparative studies have used white matter as a pseudo-reference region (Holland et al., 2020; Matuskey et al., 2020; Mertens et al., 2020). However, this approach is debatable. White matter changes (both at macroscopic and microscopic) in neurodegenerative diseases are to blame (Theilmann et al., 2013; Veselý and Rektor, 2016; Nykjaer et al., 2017). These changes may have an impact on the PET parameters and will produce a bias in the neurodegenerative group compared to healthy controls. Since the binding of [³H]UCB-J in the white matter is identical in all diseases, this suggests that the white matter can be used as a pseudo-reference region. Due to the similarity of PET and autoradiography's core properties, this study uses *in vitro* binding to verify *in vivo* outcomes.

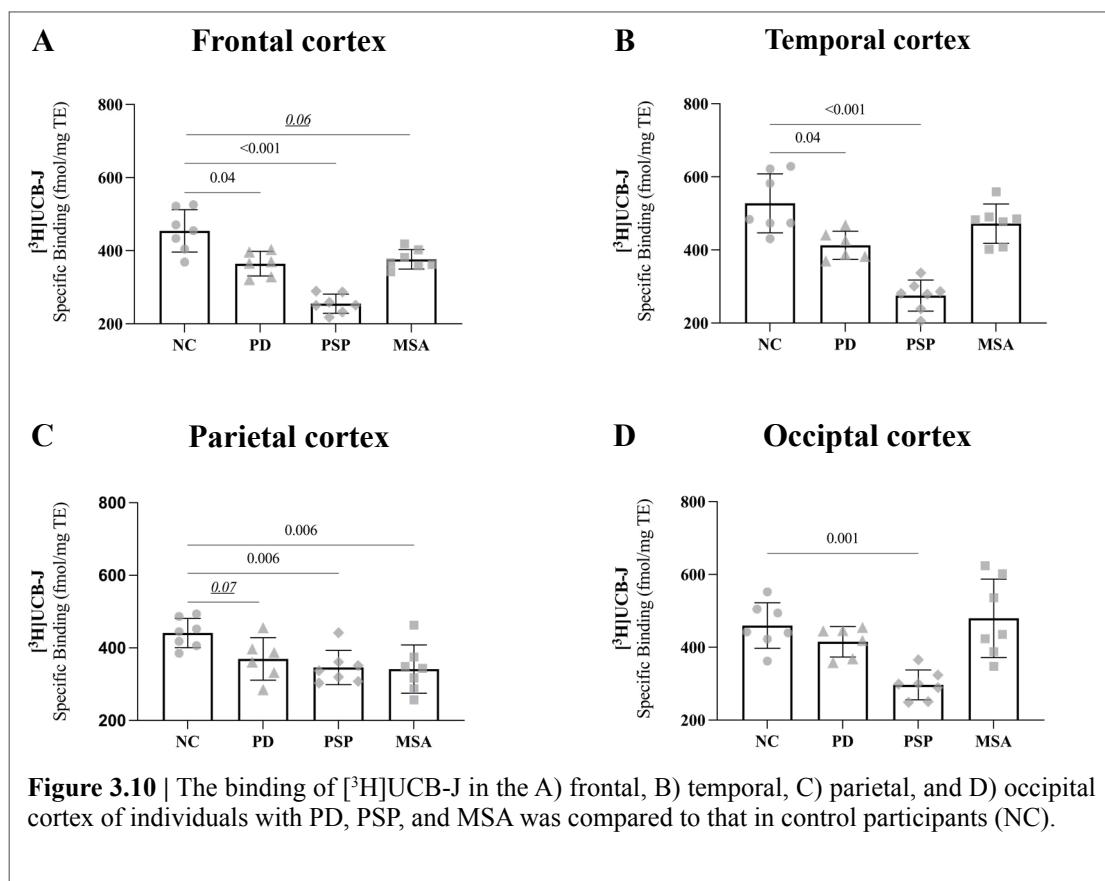
3.5.2 Changes in Neocortical SV2A in PD, PSP, and MSA

Cortical changes in [³H]UCB-J binding were seen in all diseases used in this study. In PD subjects, lower [³H]UCB-J binding was seen in the frontal (-19.7%), temporal (-21.8%) and parietal cortex (-16.1%) compared to controls. PSP patients had an effect in all cortical tissues, and the [³H]UCB-J binding was much lower. Compared to controls, they had lower [³H]UCB-J binding in the frontal (-43.8%), temporal (-47.8%), parietal (35.4%) and occipital cortex (-21.5%). Finally, MSA patients showed lower [³H]UCB-J binding in the frontal (17.1%) and parietal cortex (22.5%) (Figure 3.10).

It is important to emphasize that this is an ongoing project. Postsynaptic density markers such as PSD95 will be evaluated along with presynaptic density measurements. Several attempts at developing a radiotracer for PSD95 are being performed. Although none have been successful as a PET radioligand, some of the radioligands may be helpful for *in vitro* quantification using autoradiography (unpublished). One such radioligand will be potentially characterized and evaluated in these post-mortem human brains. Apart from this, protein aggregates will be quantified. α -synuclein, tau, and A β will be quantified and correlated with presynaptic density loss. Like tau and A β (Coomans et al. 2021; O'Dell et al. 2021), we believe α -synuclein will also strongly correlate to presynaptic loss. While having a mixed pathology with other protein aggregates will have a more substantial effect on

presynaptic density loss. Little information is available in the literature regarding co-pathologies, and this may be a helpful tool to solving the causality of neurodegenerative diseases.

Presynaptic density-corresponding [^3H]UCB-J binding has a lot of potentials to detect changes in gray matter, even if they are small. Presynaptic changes may be linked to changes in the number of neurons in the cortex or the projections from the subcortical regions into the cortex. As a result, it is difficult to pin down the cause of the effects based on the presynaptic alterations alone. Having a measure of the postsynaptic density would be useful, although no marker exists currently. Understanding the pathological changes in the diseased tissue may help answer some of the unanswered questions in neuropathology. This could aid in developing treatment strategies for diseases for which there are currently only a few treatment options.



3.5 Experimental Limitations:

Despite the fact that the thesis's studies were planned and carried out in accordance with our current knowledge and best practice, some limitations should be noted. Several issues and challenges are addressed in the following sections.

Study I: Limitations of the protein injection pig model need to be mentioned; this also applies to Study II. This is a model for radioligand development specifically for the initial screening of novel radioligands and is not intended as a replacement for a realistic model of PD or AD. A thorough *in vitro* evaluation of the proteins is required before beginning *in vivo* experiments, and this should include autoradiography with the radioligand under investigation. Only injection sites in the mPFC are validated, other regions need appropriate validation. Since the intracerebral injections are performed only a few hours before the experiment, it is difficult to ascertain to what extent the proteins enter the cell. Hence the model does not accurately represent the intracellular inclusions seen in α -synucleinopathies (Lashuel et al., 2013; Alafuzoff and Hartikainen, 2017). There is a general assumption that radioligands can easily penetrate brain cells because they must be able to cross the blood-brain barrier, which may not be true sometimes (Sun et al., 2003). As the injection site is a relatively small ROI, the time-activity curves can be prone to noise or a partial volume effect; hence we tried to have the region as big as possible. Bleeding of the dura is a concern that we have encountered during our surgeries. This hematoma could potentially impact the PET signal, although we believe it does not conflict with [^{11}C]PIB or (d_3)-[^{11}C]MODAG-001. Unlike our PET-only scanner setup, we recommend using a hybrid PET/MR or PET/CT setup to keep these hematomas in check.

Study II: The concentration of α -PFF in the model is substantially higher (micromolar range) than that reported in diseased brains, where α -synuclein concentrations are in the nanomolar range. Nonetheless, this setup allowed proof-of-concept scans with (d_3)-[^{11}C]MODAG-001. In any instance, generating a signal from a much lower concentration of α -PFF is nearly impossible due to the poor signal-to-noise ratio of (d_3)-[^{11}C]MODAG-001. The metabolite data collected must be interpreted with caution due to the limited number of animals studied. The brains could not be perfused (unlike mice) since this is a much lengthier process in pigs due to the large blood volume (Musigazi et al., 2018); hence there is some signal “spill-over” from the plasma, which theoretically speaking should be 5%.

Study III: A major limitation of the study is the small group size. This makes it very difficult to make hard conclusions that there is no difference. Hence, the study used an exploratory approach without pre-registered predictions. These preliminary findings should not be seen as conclusive, and we recommend further replications with greater numbers of subjects and a more limited set of analyses. Because the pedunculo-pontine nucleus connects both hemispheres, the contralateral hemisphere may not be an ideal control region (Breit et al., 2008). The results of the [^{18}F]FDG scans should be treated with further caution. A loss in neuronal function may be concealed by increased regional glucose consumption caused by other reasons such as lesion-induced neuroinflammation (Crabbé et al., 2019). We were able to perform four [^{11}C]-radioligand scans with a single radiosynthesis owing to

our clinical HRRT PET scanner and the Rat-hotel's ability to scan up to four animals simultaneously. Although this reduces cost, the resolution for rat PET in the HRRT is lower than that of other other small animal micro-PET systems. As a result, we can only detect subtle differences in small areas due to other factors like partial volume effects.

Study IV: In this study, only two time-points, two brain regions, and highly relevant proteins were chosen to be investigated. It would be intriguing to see if and how long the presynaptic density continues to be increased. It would also be interesting to see the full-time course of 5-HT_{2A}R after a single psilocybin dose. The changes in SV2A and 5-HT_{2A}R were seen in healthy pigs while our hypothesis is mainly oriented towards a disease condition. Hence, it is highly relevant to see much effects in a model of depression (Menneson et al., 2019). An intriguing question revolves around how increased presynaptic density benefits healthy individuals. Lastly, we chose to inject the psilocybin rather than give it orally to the pigs to ensure a precise dosage. This, unfortunately, is not how most patients are dosed. Nevertheless, intravenous dosing has the same effect on 5-HT_{2A}R occupancy as when administered orally, despite the quicker pharmacokinetics (Madsen et al., 2019; Donovan et al., 2020a).

Study V: This study was conducted with a limited sample size, and without complex models for disease comparison, i.e., no covariates are included, but it is adequately powered in light of the substantial effect sizes expected in PSP and PD patients (Holland et al., 2020; Matuskey et al., 2020). Some groups are not balanced; for example, the Parkinson's disease group is made up entirely of male individuals. This is just another reason to avoid using covariates in the analysis.

Conclusions & Future Perspective

*“Please! Don’t all leave. Somebody has to do it, don’t you see?
Somebody has to save the world...”*

Alan Moore
Captain Metropolis
Watchmen



4. Conclusions and Future Perspective

This thesis sheds light on developing, evaluating, and applying novel radioligand in a preclinical research setting. A radioligand's translation to humans requires thorough investigations and strategies to optimize best efforts. Apart from the analyses performed in normal conditions, the application of the radioligand for disease and treatment efficacy is an essential factor. PET imaging is a helpful tool in drug development, disease progression, and understanding neurobiology. It will be challenging to replace this invaluable tool. In general this thesis attempts to better understand the neurobiology behind the experiments to improve radioligand development and ensure accurate translation of radioligands into the clinics.

In **Study I**, our proposal of the novel intracerebral protein injection pig model was demonstrated suitable for radioligand evaluation. The large brain size of the pig makes it an ideal candidate for neurosurgical procedures and PET imaging. The model is a cheap, robust and efficient setup with minimal drawbacks. The availability of a large animal α -synuclein model may play a critical role in developing novel radioligands. Moreover, the modified stereotactic procedure is not just designed for α -synuclein neuroimaging but also for other target proteins or cells that may not naturally occur in normal conditions. Hence it can be utilized as a model for stroke (Bøgh et al., 2021), microglial activation (Espinosa-Oliva et al., 2013), pluripotent stem cells (Alia et al., 2019), and also human cancer xenografts (Selek et al., 2014). Model and setup may also be feasible for efflux studies of the glymphatic system, where an efflux tracer may be injected into this injection site while the animal is in the scanner to measure the efflux of fluids in the brain (Rasmussen et al., 2021).

Study II demonstrated the ability of (d₃)-[¹¹C]MODAG-001 to detect α -PFF *in vivo* using the intracranial protein injection pig model. The radioligand shows good brain uptake, test-retest variability, and a dose-response of different α -PFF concentrations. Although, it comes with a few drawbacks, including poor selectivity for α -synuclein and a low signal-to-noise ratio. MODAG and the Werner Siemens PET group are currently working on (and have presented data at conferences in 2021) the next-generation radioligand, which seems to have better binding properties and kinetics in the rat model of α -PFF depositions. It would be fascinating to see the fate of that radioligand in large animals and human studies (unpublished abstracts: [link](#)). Nevertheless, this is the closest to an α -synuclein detecting radioligand which shows a promising future for α -synuclein neuroimaging. Apart from the lack of appropriate radioligands, the sensitivity of the current scanner may not be adequate to image α -synuclein due to its low brain pathology concentration. This problem may be solved by novel PET scanner development. Yale University is currently working on a novel PET scanner with improved sensitivity. This scanner, called the NeuroeXplorer, apparently has 10-folds higher sensitivity to the HRRT. This dedicated brain PET scanner may help further improve the sensitivity and potentially move a step closer to α -synuclein neuroimaging ([Yale PET website](#)). It is generally assumed that a small molecule would be the right start for an α -synuclein tracer, but antibody PET is an exponentially growing field. Ever since the massive success of A β -antibody-PET by Sehlin, Syvänen, and their group at Uppsala University (Sehlin et al., 2016), the potential

of α -synuclein-antibody-PET is being persuaded in both research and pharmaceutical settings. Their lab very recently showed the potential of α -synuclein-antibody-PET using a deposition mouse model (Roshanbin et al., 2022). Unfortunately, this has only been tested in mice, but the proof of concept is excellent.

Study III was one of the first studies to compare [^{11}C]UCB-J and [^{18}F]FDG PET, first coming from the Yale PET center (Chen et al., 2021). [^{11}C]UCB-J and [^{18}F]FDG PET revealed similar changes in the 6-OHDA model of PD. However, the further region-based analysis suggested a divergent response to the lesion. This is especially relevant in some of the neocortical regions in the CSTC circuit, where higher [^{11}C]UCB-J uptake did not match lower [^{18}F]FDG uptake. In general, the research suggested using both [^{11}C]UCB-J and [^{18}F]FDG scans to understand better diseases like Parkinson's disease, which have CSTC defects that are still difficult to explain (Vriend et al., 2014). Nevertheless, Study V shows a reduction of SV2A in end-stage PD. Hence, we hypothesize this may be relevant in early disease stages. Further in this study, we also validate [^{11}C]UCB-J PET against [^3H]UCB-J autoradiography in the same animals, a task that was not done before.

Study IV is the first large-animal study to investigate the effects of a single psilocybin dose on vital proteins like SV2A and 5-HT_{2A}R. We demonstrate that a single dose of psilocybin increases the presynaptic density marker SV2A with [^3H]UCB-J autoradiography. In the PFC and hippocampus, an increase in SV2A is seen within one day of the intervention, and the increase persists seven days after. Additionally, we find a transient decrease in 5-HT_{2A}R density one day after psilocybin intervention, which is back to normal seven days later. This study has gained significant traction in the last year, and it has led to similar ongoing preclinical as well as clinical studies. The clinical study in healthy and depressed humans using [^{11}C]UCB-J would be one of the first studies to test the neuroplastic hypothesis in humans. Translation of these results will be game-changing for using psychedelics treatment regimes against devastating diseases like major depressive disorder and end-of-life anxiety.

Finally, in the ongoing **Study V**, we find disruption of SV2A in the neocortical postmortem human brain from PD, PSP, and MSA patients. We also demonstrate no difference in white matter binding of [^3H]UCB-J in these disease groups compared to control subjects. We are currently performing semi-quantification of protein aggregates (which include α -synuclein, tau, and A β). We intend to correlate protein aggregates to the SV2A measures. Further, we aim to quantify the postsynaptic density in the near future. We seek to establish a link between presynaptic and postsynaptic density to understand synaptic loss mechanisms instead of only one component of the axon terminal. Some of these brains have also been quantified with stereology. It would be interesting to see the correlation of SV2A and cell populations. This will allow for a complete understanding of the presynaptic disruption while also providing more information on the synaptic histopathology of movement disorders.

With so many clinical PET ligands already on the market, it might be assumed that creating new PET ligands is a straightforward process. This dissertation may serve as a road map for the last stages of radioligand development before in-human evaluation. However, UCB-J and its [^{18}F]-labeled analogs (not discussed in this thesis) is currently being extensively evaluated at multiple PET centers in

humans, yet very little evidence is available about its feasibility as a “gold standard” for presynaptic density.

In general conclusion, Study I and II provides some evidence for improved translational quality when using a more radiochemistry-dedicated PET model. While Study III, IV, and V show the preclinical evaluation of novel radioligands and the characterization of their binding properties. Another method to improve translation from *in vitro* to *in vivo* studies.

As of this day, there are so many different radioligands being developed for different targets within diverse expertise, but not all make it to the clinics. The cost of this *in vitro* and *in vivo* evaluation is tremendous. The development of radioligands will most likely become more expensive in the foreseeable future. To reduce this burden, radioligand development is to be meticulous. Hence the need to develop comprehensive strategies and pipelines. A small and subtle step in that direction is this thesis.

References

- Alafuzoff, I., and Hartikainen, P. (2017). Alpha-synucleinopathies. *Handb. Clin. Neurol.* 145, 339–353. doi:10.1016/B978-0-12-802395-2.00024-9.
- Alberts, B., Bray, D., Hopkin, K., Johnson, A., and Lewis, J. (2013). *Essential Cell Biology*. Garland Science.
- Alexander, G. E. (2004). Biology of Parkinson's disease: pathogenesis and pathophysiology of a multisystem neurodegenerative disorder. *Dialogues Clin. Neurosci.* 6, 259–280. Available at: <https://www.ncbi.nlm.nih.gov/pubmed/22033559>.
- Alia, C., Terrigno, M., Busti, I., Cremisi, F., and Caleo, M. (2019). Pluripotent Stem Cells for Brain Repair: Protocols and Preclinical Applications in Cortical and Hippocampal Pathologies. *Front. Neurosci.* 13, 684. doi:10.3389/fnins.2019.00684.
- Alstrup, A. K. O., and Smith, D. F. (2012). PET neuroimaging in pigs. *Scand J. Lab. Anim. Sci.* 39, 25–45. Available at: <http://sjlas.org/index.php/SJLAS/article/view/246>.
- Amemiya, Y., and Miyahara, J. (1988). Imaging plate illuminates many fields. *Nature* 336, 89–90. doi:10.1038/336089a0.
- Amidfar, M., Kim, Y.-K., Colic, L., Arbabi, M., Mobaraki, G., Hassanzadeh, G., et al. (2017). Increased levels of 5HT2A receptor mRNA expression in peripheral blood mononuclear cells of patients with major depression: correlations with severity and duration of illness. *Nord. J. Psychiatry* 71, 282–288. doi:10.1080/08039488.2016.1276624.
- Bagchi, D. P., Yu, L., Perlmutter, J. S., Xu, J., Mach, R. H., Tu, Z., et al. (2013). Binding of the radioligand SIL23 to α -synuclein fibrils in Parkinson disease brain tissue establishes feasibility and screening approaches for developing a Parkinson disease imaging agent. *PLoS One* 8, e55031. doi:10.1371/journal.pone.0055031.
- Bajjalieh, S. M., Frantz, G. D., Weimann, J. M., McConnell, S. K., and Scheller, R. H. (1994). Differential expression of synaptic vesicle protein 2 (SV2) isoforms. *Journal of Neuroscience* 14, 5223–5235. doi:10.1523/jneurosci.14-09-05223.1994.
- Barthel, H. (2020). First Tau PET Tracer Approved: Toward Accurate *In Vivo* Diagnosis of Alzheimer Disease. *J. Nucl. Med.* 61, 1409–1410. doi:10.2967/jnumed.120.252411.
- Bartholome, O., Van Den Ackerveken, P., Gil, J. S., Bonardeaux, O. de la B., Leprince, P., Franzen, R., et al. (2017). Puzzling out synaptic vesicle 2 family members functions. *Frontiers in Molecular Neuroscience* 10, 148. doi:10.3389/fnmol.2017.00148.
- Beliveau, V., Ganz, M., Feng, L., Ozenne, B., Højgaard, L., Fisher, P. M., et al. (2017). A high-resolution *in vivo* atlas of the human brain's serotonin system. *Journal of Neuroscience* 37, 120–128. doi:10.1523/JNEUROSCI.2830-16.2016.
- Bergström, M., Grahnén, A., and Långström, B. (2003). Positron emission tomography microdosing: a new concept with application in tracer and early clinical drug development. *Eur. J. Clin. Pharmacol.* 59, 357–366. doi:10.1007/s00228-003-0643-x.
- Berry, S. A., Shah, M. C., Khan, N., and Roth, B. L. (1996). Rapid agonist-induced internalization of the 5-hydroxytryptamine(2A) receptor occurs via the endosome pathway *in vitro*. *Mol. Pharmacol.* 50, 306–313.
- Bertoglio, D., Verhaeghe, J., Miranda, A., Kertesz, I., Cybulska, K., Korat, Š., et al. (2020). Validation and noninvasive kinetic modeling of [¹¹C]UCB-J PET imaging in mice. *J. Cereb. Blood Flow Metab.* 40, 1351–1362. doi:10.1177/0271678X19864081.
- Binda, K. H., Lillethorup, T. P., Real, C. C., Bærentzen, S. L., Nielsen, M. N., Orłowski, D., et al. (2021). Exercise protects synaptic density in a rat model of Parkinson's disease. *Exp. Neurol.* 342, 113741. doi:10.1016/j.expneurol.2021.113741.
- Blandini, F., Armentero, M. T., and Martignoni, E. (2008). The 6-hydroxydopamine model: News from the past. *Parkinsonism Relat. Disord.* 14, S124–S129. doi:10.1016/j.parkreldis.2008.04.015.
- Bøgh, N., Olin, R. B., Hansen, E. S., Gordon, J. W., Bech, S. K., Bertelsen, L. B., et al. (2021). Metabolic MRI with hyperpolarized [¹⁻¹³C]pyruvate separates benign oligemia from infarcting penumbra in porcine stroke. *J. Cereb. Blood Flow Metab.* 271678X211018317. doi:10.1177/0271678X211018317.
- Bourdenx, M., Dovero, S., Engeln, M., Bido, S., Bastide, M. F., Dutheil, N., et al. (2015). Lack of additive role of ageing in nigrostriatal neurodegeneration triggered by α -synuclein overexpression. *Acta neuropathologica communication* 3, 46. doi:10.1186/s40478-015-0222-2.
- Breijyeh, Z., and Karaman, R. (2020). Comprehensive Review on Alzheimer's Disease: Causes and Treatment. *Molecules* 25. doi:10.3390/molecules25245789.
- Breit, S., Bouali-Benazzouz, R., Popa, R. C., Gasser, T., Benabid, A. L., and Benazzouz, A. (2007). Effects of 6-hydroxydopamine-induced severe or partial lesion of the nigrostriatal pathway on the neuronal activity of pallido-subthalamic network in the rat. *Exp. Neurol.* 205, 36–47. doi:10.1016/j.expneurol.2006.12.016.
- Breit, S., Martin, A., Lessmann, L., Cerkez, D., Gasser, T., and Schulz, J. B. (2008). Bilateral changes in neuronal activity of the basal ganglia in the unilateral 6-hydroxydopamine rat model. *J. Neurosci. Res.* 86, 1388–1396. doi:10.1002/jnr.21588.
- Brock, S., Mullins, P., Reynolds, N., and Baker, M. (2003). Historical timeline 1853-2003. *Tex. Med.* 99, 12–15.
- Cai, Z., Li, S., Matuskey, D., Nabulsi, N., and Huang, Y. (2019). PET imaging of synaptic density: A new tool for investigation of neuropsychiatric diseases. *Neurosci. Lett.* 691, 44–50. doi:10.1016/j.neulet.2018.07.038.
- Capotosti, F., Vokali, E., Molette, J., Tsika, E., Ravache, M., Juergens, T., et al. (2020). Developing a novel alphasynuclein positron emission tomography (PET) tracer for the diagnosis of synucleinopathies. *Alzheimers. Dement.* 16. doi:10.1002/alz.043249.

- Carhart-Harris, R., Giribaldi, B., Watts, R., Baker-Jones, M., Murphy-Beiner, A., Murphy, R., et al. (2021). Trial of Psilocybin versus Escitalopram for Depression. *N. Engl. J. Med.* 384, 1402–1411. doi:10.1056/NEJMoa2032994.
- Carhart-Harris, R. L., Bolstridge, M., Day, C. M. J., Rucker, J., Watts, R., Erritzoe, D. E., et al. (2018). Psilocybin with psychological support for treatment-resistant depression: six-month follow-up. *Psychopharmacology* 235, 399–408.
- Carhart-Harris, R. L., and Goodwin, G. M. (2017). The Therapeutic Potential of Psychedelic Drugs: Past, Present, and Future. *Neuropsychopharmacology* 42, 2105–2113. doi:10.1038/npp.2017.84.
- Carson, R. E., Breier, A., de Bartolomeis, A., Saunders, R. C., Su, T. P., Schmall, B., et al. (1997). Quantification of amphetamine-induced changes in [¹¹C]raclopride binding with continuous infusion. *J. Cereb. Blood Flow Metab.* 17, 437–447. doi:10.1097/00004647-199704000-00009.
- Carson, R., Naganawa, M., Matuskey, D., Mecca, A., Pittman, B., Toyonaga, T., et al. (2018). Age and sex effects on synaptic density in healthy humans as assessed with SV2A PET. *J. Nucl. Med.* 59, 541–541.
- Catlow, B. J., Song, S., Paredes, D. A., Kirstein, C. L., and Sanchez-Ramos, J. (2013). Effects of psilocybin on hippocampal neurogenesis and extinction of trace fear conditioning. *Exp. Brain Res.* 228, 481–491. doi:10.1007/s00221-013-3579-0.
- Cervenka, S., Hedman, E., Ikoma, Y., Djurfeldt, D. R., Rück, C., Halldin, C., et al. (2012). Changes in dopamine D2-receptor binding are associated to symptom reduction after psychotherapy in social anxiety disorder. *Transl. Psychiatry* 2, e120. doi:10.1038/tp.2012.40.
- Chen, M.-K., Mecca, A. P., Naganawa, M., Gallezot, J.-D., Toyonaga, T., Mondal, J., et al. (2021). Comparison of [¹¹C]UCB-J and [¹⁸F]FDG PET in Alzheimer's disease: A tracer kinetic modeling study. *J. Cereb. Blood Flow Metab.* 0, 1–15. doi:10.1177/0271678X211004312.
- Cherry, S. R., and Gambhir, S. S. (2001). Use of positron emission tomography in animal research. *ILAR J.* 42, 219–232. doi:10.1093/ilar.42.3.219.
- Constantinescu, C., Carroll, V., Gouasmat, A., Tresse, C., Russell, D., Gunn, R., et al. (2019). Evaluation of [¹⁸F]MNI-1126, an ¹⁸F-labeled SV2A PET tracer in healthy, Parkinson disease and Alzheimer's disease subjects. *J. Nucl. Med.* 60, 320–320.
- Conti, M., and Eriksson, L. (2016). Physics of pure and non-pure positron emitters for PET: a review and a discussion. *EJNMMI Phys* 3, 8. doi:10.1186/s40658-016-0144-5.
- Coomans, E. M., Schoonhoven, D. N., Tuncel, H., Verfaillie, S. C. J., Wolters, E. E., Boellaard, R., et al. (2021). *In vivo* tau pathology is associated with synaptic loss and altered synaptic function. *Alzheimers. Res. Ther.* 13, 35. doi:10.1186/s13195-021-00772-0.
- Crabbé, M., Van der Perren, A., Bollaerts, I., Kounelis, S., Baekelandt, V., Bormans, G., et al. (2019). Increased P2X7 Receptor Binding Is Associated With Neuroinflammation in Acute but Not Chronic Rodent Models for Parkinson's Disease. *Front. Neurosci.* 13, 799. doi:10.3389/fnins.2019.00799.
- Crowder, K. M., Gunther, J. M., Jones, T. A., Hale, B. D., Zhang, H. Z., Peterson, M. R., et al. (2002). Abnormal neurotransmission in mice lacking synaptic vesicle protein 2A (SV2A). *Proceedings of the National Academy of Sciences* 96, 15268–15273. doi:10.1073/pnas.96.26.15268.
- Davis, A. K., Barrett, F. S., May, D. G., Cosimano, M. P., Sepeda, N. D., Johnson, M. W., et al. (2020). Effects of Psilocybin-Assisted Therapy on Major Depressive Disorder: A Randomized Clinical Trial. *JAMA Psychiatry.* doi:10.1001/jamapsychiatry.2020.3285.
- de la Fuente Revenga, M., Zhu, B., Guevara, C. A., Naler, L. B., Saunders, J. M., Zhou, Z., et al. (2021). Prolonged epigenomic and synaptic plasticity alterations following single exposure to a psychedelic in mice. *Cell Rep.* 37, 109836. doi:10.1016/j.celrep.2021.109836.
- Delayre, C., Sammaljärvi, J., Billon, S., Muuri, E., Sardini, P., and Siitari-Kauppi, M. (2020). Comparison of phosphor screen autoradiography and micro-pattern gas detector based autoradiography for the porosity of altered rocks. *Sci. Rep.* 10, 9455. doi:10.1038/s41598-020-65791-7.
- Dewey, S. L., Smith, G. S., Logan, J., Brodie, J. D., Fowler, J. S., and Wolf, A. P. (1993). Striatal binding of the PET ligand ¹¹C-raclopride is altered by drugs that modify synaptic dopamine levels. *Synapse* 13, 350–356. doi:10.1002/syn.890130407.
- Donovan, L. L. (2020). Epigenetic and pharmacological investigations of the pig brain: *In vivo* and *in vitro* studies of [¹¹C]Martinostat and psilocybin.
- Donovan, L. L., Johansen, J. V., Ros, N. F., Jaber, E., Linnet, K., Johansen, S. S., et al. (2021). Effects of a single dose of psilocybin on behaviour, brain 5-HT2A receptor occupancy and gene expression in the pig. *Eur. Neuropsychopharmacol.* 42, 1–11. doi:10.1016/j.euroneuro.2020.11.013.
- Donovan, L. L., Magnussen, J. H., Dyssegaard, A., Lehel, S., Hooker, J. M., Knudsen, G. M., et al. (2020b). Imaging HDACs *In vivo*: Cross-Validation of the [¹¹C]Martinostat Radioligand in the Pig Brain. *Mol. Imaging Biol.* 22, 569–577. doi:10.1007/s11307-019-01403-9.
- Duric, V., Banasr, M., Stockmeier, C. A., Simen, A. A., Newton, S. S., Overholser, J. C., et al. (2013). Altered expression of synapse and glutamate related genes in post-mortem hippocampus of depressed subjects. *Int. J. Neuropsychopharmacol.* 16, 69–82. doi:10.1017/S1461145712000016.
- Eberling, J. L., Dave, K. D., and Frasier, M. A. (2013). α -synuclein imaging: a critical need for Parkinson's disease research. *J. Parkinsons. Dis.* 3, 565–567. doi:10.3233/JPD-130247.
- Eckelman, W. (2011). Changes: choosing a target? *Nucl. Med. Biol.* 38, 765–769. doi:10.1016/j.nucmedbio.2010.12.010.

- Endepols, H., Zlatopolskiy, B. D., Zischler, J., Alavinejad, N., Apetz, N., Vus, S., et al. (2022). Imaging of cerebral tryptophan metabolism using 7-[¹⁸F]Trp-PET in a unilateral Parkinsonian rat model. *Neuroimage* 247, 118842. doi:10.1016/j.neuroimage.2021.118842.
- Eslamboli, A., Romero-Ramos, M., Burger, C., Bjorklund, T., Muzyczka, N., Mandel, R. J., et al. (2007). Long-term consequences of human alpha-synuclein overexpression in the primate ventral midbrain. *Brain* 130, 799–815. doi:10.1093/brain/awl382.
- Espinosa-Oliva, A. M., de Pablos, R. M., and Herrera, A. J. (2013). Intracranial injection of LPS in rat as animal model of neuroinflammation. *Methods Mol. Biol.* 1041, 295–305. doi:10.1007/978-1-62703-520-0_26.
- Esteban, S., Lladó, J., Sastre-Coll, A., and García-Sevilla, J. A. (1999). Activation and desensitization by cyclic antidepressant drugs of α_2 -autoreceptors, α_2 -heteroreceptors and 5-HT(1A)-autoreceptors regulating monoamine synthesis in the rat brain *in vivo*. *Naunyn-Schmiedeberg's Arch. Pharmacol.* 360, 135–143. doi:10.1007/s002109900045.
- Ettrup, A., da Cunha-Bang, S., McMahon, B., Lehel, S., Dyssegaard, A., Skibsted, A. W., et al. (2014). Serotonin 2A receptor agonist binding in the human brain with [¹¹C] Cimbi-36. *J. Cereb. Blood Flow Metab.* 34, 1188–1196. doi:10.1038/jcbfm.2014.68.
- Ettrup, A., Holm, S., Hansen, M., Wasim, M., Santini, M. A., Palner, M., et al. (2013). Preclinical safety assessment of the 5-HT_{2A} receptor agonist PET radioligand [¹¹C] cimbi-36. *Mol. Imaging Biol.* 15, 376–383. doi:10.1007/s11307-012-0609-4.
- Farde, L., Nordström, A. L., Wiesel, F. A., Pauli, S., Halldin, C., and Sedvall, G. (1992). Positron emission tomographic analysis of central D1 and D2 dopamine receptor occupancy in patients treated with classical neuroleptics and clozapine. Relation to extrapyramidal side effects. *Arch. Gen. Psychiatry* 49, 538–544. doi:10.1001/archpsyc.1992.01820070032005.
- Finnema, S. J., Nabulsi, N. B., Eid, T., Detyniecki, K., Lin, S. F., Chen, M. K., et al. (2016). Imaging synaptic density in the living human brain. *Sci. Transl. Med.* 8. doi:10.1126/scitranslmed.aaf6667.
- Finnema, S. J., Rossano, S., Naganawa, M., Henry, S., Gao, H., Pracitto, R., et al. (2019). A single-center, open-label positron emission tomography study to evaluate brivaracetam and levetiracetam synaptic vesicle glycoprotein 2A binding in healthy volunteers. *Epilepsia* 60, 958–967. doi:10.1111/epi.14701.
- Fodero-Tavoletti, M. T., Smith, D. P., McLean, C. A., Adlard, P. A., Barnham, K. J., Foster, L. E., et al. (2007). *In vitro* characterization of Pittsburgh compound-B binding to Lewy bodies. *J. Neurosci.* 27, 10365–10371. doi:10.1523/JNEUROSCI.0630-07.2007.
- Fornari, R. V., Wichmann, R., Atsak, P., Atucha, E., Barsegayan, A., Beldjoud, H., et al. (2012). Rodent stereotaxic surgery and animal welfare outcome improvements for behavioral neuroscience. *J. Vis. Exp.*, e3528. doi:10.3791/3528.
- Garber, K. (2012). First FDA-approved beta-amyloid diagnostic hits the market. *Nat. Biotechnol.* 30, 575. doi:10.1038/nbt0712-575.
- Gartz, J. (1996). *Magic mushrooms around the world. A scientific journey across cultures and time.* LIS publs. Los Angeles.
- Gillings, N. (2009). A restricted access material for rapid analysis of [(11)C]-labeled radiopharmaceuticals and their metabolites in plasma. *Nucl. Med. Biol.* 36, 961–965. doi:10.1016/j.nucmedbio.2009.07.004.
- Glud, A. N., Hedegaard, C., Nielsen, M. S., Sørensens, J. C., Bendixen, C., Jensen, P. H., et al. (2011). Direct MRI-guided stereotaxic viral mediated gene transfer of alpha-synuclein in the Göttingen minipig CNS. *Acta Neurobiol. Exp.* 71, 508–518.
- Gomez, F., Lin, Y.-G., Liang, Q., Mintun, M., and Attardo, G. (2016). Quantitative assessment of [¹⁸F]AV-1451 distribution in AD, PSP and PiD Post-Mortem Brain Tissue Sections relative to that of the anti-tau antibody AT8. *J. Nucl. Med.* 57, 348–348.
- González-Maeso, J., Weisstaub, N. V., Zhou, M., Chan, P., Ivic, L., Ang, R., et al. (2007). Hallucinogens Recruit Specific Cortical 5-HT_{2A} Receptor-Mediated Signaling Pathways to Affect Behavior. *Neuron* 53, 439–452. doi:10.1016/j.neuron.2007.01.008.
- Gray, J. A., and Roth, B. L. (2001). Paradoxical trafficking and regulation of 5-HT_{2A} receptors by agonists and antagonists. in *Brain Research Bulletin*, 441–451. doi:10.1016/S0361-9230(01)00623-2.
- Griem-Krey, N., Klein, A. B., Herth, M., and Wellendorph, P. (2019). Autoradiography as a Simple and Powerful Method for Visualization and Characterization of Pharmacological Targets. *J. Vis. Exp.*, 1–11. doi:10.3791/58879.
- Griffiths, R. R., Johnson, M. W., Carducci, M. A., Umbricht, A., Richards, W. A., Richards, B. D., et al. (2016). Psilocybin produces substantial and sustained decreases in depression and anxiety in patients with life-threatening cancer: A randomized double-blind trial. *J. Psychopharmacol.* 30, 1181–1197. doi:10.1177/0269881116675513.
- Hansen, H. D., Lacivita, E., Di Pilato, P., Herth, M. M., Lehel, S., Ettrup, A., et al. (2014). Synthesis, radiolabeling and *in vivo* evaluation of [¹¹C](R)-1-[4-[2-(4-methoxyphenyl)phenyl]piperazin-1-yl]-3-(2-pyrazinyloxy)-2-propanol, a potential PET radioligand for the 5-HT₇receptor. *Eur. J. Med. Chem.* 79, 152–163. doi:10.1016/j.ejmech.2014.03.066.
- Harding, J. D. (2017). Nonhuman Primates and Translational Research: Progress, Opportunities, and Challenges. *ILAR J.* 58, 141–150. doi:10.1093/ilar/ilx033.
- Hartogsohn, I. (2018). The Meaning-Enhancing Properties of Psychedelics and Their Mediator Role in Psychedelic Therapy, Spirituality, and Creativity. *Front. Neurosci.* 12, 129. doi:10.3389/fnins.2018.00129.
- Hellström-Lindahl, E., Westermark, P., Antoni, G., and Estrada, S. (2014). *In vitro* binding of [³H]PIB to human amyloid deposits of different types. *Amyloid* 21, 21–27. doi:10.3109/13506129.2013.860895.

- Heras-Garvin, A., Weckbecker, D., Ryazanov, S., Leonov, A., Griesinger, C., Giese, A., et al. (2019). Anle138b modulates α -synuclein oligomerization and prevents motor decline and neurodegeneration in a mouse model of multiple system atrophy. *Mov. Disord.* 34, 255–263. doi:10.1002/mds.27562.
- Hesselgrave, N., Troppoli, T. A., Wulff, A. B., Cole, A. B., and Thompson, S. M. (2021). Harnessing psilocybin: antidepressant-like behavioral and synaptic actions of psilocybin are independent of 5-HT_{2R} activation in mice. *Proc. Natl. Acad. Sci. U. S. A.* 118. doi:10.1073/pnas.2022489118.
- Heurling, K., Ashton, N. J., Leuzy, A., Zimmer, E. R., Blennow, K., Zetterberg, H., et al. (2019). Synaptic vesicle protein 2A as a potential biomarker in synaptopathies. *Molecular and Cellular Neuroscience* 97, 34–42. doi:10.1016/j.mcn.2019.02.001.
- Heurling, K., Leuzy, A., Jonasson, M., Frick, A., Zimmer, E. R., Nordberg, A., et al. (2017). Quantitative positron emission tomography in brain research. *Brain Res.* 1670, 220–234. doi:10.1016/j.brainres.2017.06.022.
- Hoffe, B., and Holahan, M. R. (2019). The Use of Pigs as a Translational Model for Studying Neurodegenerative Diseases. *Front. Physiol.* 10, 838. doi:10.3389/fphys.2019.00838.
- Hoh, C. K. (2007). Clinical use of FDG PET. *Nucl. Med. Biol.* 34, 737–742. doi:10.1016/j.nucmedbio.2007.07.001.
- Holland, N., Jones, P. S., Savulich, G., Wiggins, J. K., Hong, Y. T., Fryer, T. D., et al. (2020). Synaptic Loss in Primary Tauopathies Revealed by [¹¹C]UCB-J Positron Emission Tomography. *Mov. Disord.* 35, 1834–1842. doi:10.1002/mds.28188.
- Holmes, S. E., Scheinost, D., Finnema, S. J., Naganawa, M., Davis, M. T., DellaGioia, N., et al. (2019). Lower synaptic density is associated with depression severity and network alterations. *Nat. Commun.* 10. doi:10.1038/s41467-019-09562-7.
- Honer, M., Gobbi, L., Martarello, L., and Comley, R. A. (2014). Radioligand development for molecular imaging of the central nervous system with positron emission tomography. *Drug Discov. Today* 19, 1936–1944. doi:10.1016/j.drudis.2014.08.012.
- Hooshyar Yousefi, B., Shi, K., Arzberger, T., Wester, H. J., Schwaiger, M., Yakushev, I., et al. (2019). Translational study of a novel alpha-synuclein PET tracer designed for first-in-human investigating. in *NuclearMedizin 2019* (Georg Thieme Verlag KG), L25. doi:10.1055/s-0039-1683494.
- Howell, L. L., and Murnane, K. S. (2011). Nonhuman primate positron emission tomography neuroimaging in drug abuse research. *J. Pharmacol. Exp. Ther.* 337, 324–334. doi:10.1124/jpet.108.136689.
- Innis, R. B., Cunningham, V. J., Delforge, J., Fujita, M., Gjedde, A., Gunn, R. N., et al. (2007). Consensus nomenclature for *in vivo* imaging of reversibly binding radioligands. *Journal of Cerebral Blood Flow and Metabolism* 27, 1533–1539. doi:10.1038/sj.jcbfm.9600493.
- Isbell, H., Wolbach, A. B., Wikler, A., and Miner, E. J. (1961). Cross tolerance between LSD and psilocybin. *Psychopharmacologia* 2, 147–159. doi:10.1007/BF00407974.
- Iwai, A., Masliah, E., Yoshimoto, M., Ge, N., Flanagan, L., de Silva, H. A., et al. (1995). The precursor protein of non-A beta component of Alzheimer's disease amyloid is a pre-synaptic protein of the central nervous system. *Neuron* 14, 467–475. doi:10.1016/0896-6273(95)90302-x.
- James, S. L., Abate, D., Abate, K. H., Abay, S. M., Abbafati, C., Abbasi, N., et al. (2018). Global, regional, and national incidence, prevalence, and years lived with disability for 354 diseases and injuries for 195 countries and territories, 1990–2017: a systematic analysis for the Global Burden of Disease Study 2017. *Lancet* 392, 1789–1858. doi:10.1016/S0140-6736(18)32279-7.
- Janz, R., Goda, Y., Geppert, M., Missler, M., and Südhof, T. C. (1999). SV2A and SV2B function as redundant Ca²⁺ regulators in neurotransmitter release. *Neuron* 24, 1003–1016. doi:10.1016/s0896-6273(00)81046-6.
- Jørgensen, L. M., Weikop, P., Svarer, C., Feng, L., Keller, S. H., and Knudsen, G. M. (2018). Cerebral serotonin release correlates with [¹¹C]AZ10419369 PET measures of 5-HT_{1B} receptor binding in the pig brain. *J. Cereb. Blood Flow Metab.* 38, 1243–1252. doi:10.1177/0271678X17719390.
- Jørgensen, L. M., Weikop, P., Villadsen, J., Visnapuu, T., Ettrup, A., Hansen, H. D., et al. (2017). Cerebral 5-HT release correlates with [¹¹C]Cimbi36 PET measures of 5-HT_{2A} receptor occupancy in the pig brain. *J. Cereb. Blood Flow Metab.* 37, 425–434. doi:10.1177/0271678X16629483.
- Kaide, S., Watanabe, H., Shimizu, Y., Iikuni, S., Nakamoto, Y., Hasegawa, M., et al. (2020). Identification and Evaluation of Bisquinoline Scaffold as a New Candidate for α -Synuclein-PET Imaging. *ACS Chem. Neurosci.* 11, 4254–4261. doi:10.1021/acscchemneuro.0c00523.
- Kanekal, S., Sahai, A., Jones, R. E., and Brown, D. (1995). Storage-phosphor autoradiography: a rapid and highly sensitive method for spatial imaging and quantitation of radioisotopes. *J. Pharmacol. Toxicol. Methods* 33, 171–178. doi:10.1016/1056-8719(94)00089-m.
- Kang, H. J., Voleti, B., Hajszan, T., Rajkowska, G., Stockmeier, C. A., Licznarski, P., et al. (2012). Decreased expression of synapse-related genes and loss of synapses in major depressive disorder. *Nat. Med.* 18, 1413–1417. doi:10.1038/nm.2886.
- Keller, S. H., L'Estrade, E. N., Dall, B., Palner, M., and Herth, M. (2017a). Quantification accuracy of a new HRRT high throughput rat hotel using transmission-based attenuation correction: A phantom study. in 2016 IEEE Nuclear Science Symposium, Medical Imaging Conference and Room-Temperature Semiconductor Detector Workshop, NSS/MIC/RTSD 2016 doi:10.1109/NSS-MIC.2016.8069467.
- Keller, S. H., Svarer, C., and Sibomana, M. (2013). Attenuation correction for the HRRT PET-scanner using transmission scatter correction and total variation regularization. *IEEE Trans. Med. Imaging* 32, 1611–1621. doi:10.1109/TMI.2013.2261313.

- Keller, S. H., Vigfósdóttir, B., Villadsen, J., Jørgensen, L. M., Hansen, H. D., Sibomana, M., et al. (2017b). Impact of μ -map Processing and Transmission Scan Count Statistics on Quantification of PET Pig Brain Scans and Temporal Variation of Scatter Correction Induced by μ -map Mismatch. in 2017 IEEE Nuclear Science Symposium and Medical Imaging Conference (NSS/MIC) (IEEE), 1–7.
- Kennedy, S. H., Evans, K. R., Krüger, S., Mayberg, H. S., Meyer, J. H., McCann, S., et al. (2001). Changes in regional brain glucose metabolism measured with positron emission tomography after paroxetine treatment of major depression. *Am. J. Psychiatry* 158, 899–905. doi:10.1176/appi.ajp.158.6.899.
- Keyes, J. W., Jr (1995). SUV: standard uptake or silly useless value? *J. Nucl. Med.* 36, 1836–1839.
- Kim, J. S., Lee, J. S., Park, M.-H., Kim, K. M., Oh, S.-H., Cheon, G. J., et al. (2010). Feasibility of template-guided attenuation correction in cat brain PET imaging. *Mol. Imaging Biol.* 12, 250–258. doi:10.1007/s11307-009-0277-1.
- Kirik, D., Annett, L. E., Burger, C., Muzyczka, N., Mandel, R. J., and Björklund, A. (2003). Nigrostriatal alpha-synucleinopathy induced by viral vector-mediated overexpression of human alpha-synuclein: a new primate model of Parkinson's disease. *Proc. Natl. Acad. Sci. U. S. A.* 100, 2884–2889. doi:10.1073/pnas.0536383100.
- Klenner, M. A., Pascali, G., Fraser, B. H., and Darwish, T. A. (2021). Kinetic isotope effects and synthetic strategies for deuterated carbon-11 and fluorine-18 labelled PET radiopharmaceuticals. *Nucl. Med. Biol.* 96-97, 112–147. doi:10.1016/j.nucmedbio.2021.03.011.
- Klunk, W. E., Engler, H., Nordberg, A., Wang, Y., Blomqvist, G., Holt, D. P., et al. (2004). Imaging brain amyloid in Alzheimer's disease with Pittsburgh Compound-B. *Ann. Neurol.* 55, 306–319. doi:10.1002/ana.20009.
- Knudsen, G. M. (2009). Testing for radioligand sensitivity to endogenous neurotransmitter release. *Eur. J. Nucl. Med. Mol. Imaging* 36, 472–474. doi:10.1007/s00259-009-1067-3.
- Koepp, M. J., Gunn, R. N., Lawrence, A. D., Cunningham, V. J., Dagher, A., Jones, T., et al. (1981). Evidence for striatal dopamine release during a video game. *gametophytic gene expression in Lycopodium esculentum*. *Science* 213, 453–455.
- Koprach, J. B., Johnston, T. H., Reyes, G., and Omana, V. (2016). Towards a non-human primate model of alpha-synucleinopathy for development of therapeutics for Parkinson's disease: optimization of AAV1/2 delivery PLoS. Available at: <https://journals.plos.org/plosone/article?id=10.1371/journal.pone.0167235>.
- Korat, Š., Bidesi, N. S. R., Bonanno, F., Di Nanni, A., Hoàng, A. N. N., Herfert, K., et al. (2021). Alpha-Synuclein PET Tracer Development—An Overview about Current Efforts. *Pharmaceuticals* 14, 847. doi:10.3390/ph14090847.
- Kotzbauer, P. T., Giasson, B. I., Kravitz, A. V., Golbe, L. I., Mark, M. H., Trojanowski, J. Q., et al. (2004). Fibrillogenesis of α -synuclein and tau in familial Parkinson's disease caused by the A53T α -synuclein mutation. *Exp. Neurol.* 187, 279–288. doi:10.1016/j.expneurol.2004.01.007.
- Kuebler, L., Buss, S., Leonov, A., Ryazanov, S., Schmidt, F., Maurer, A., et al. (2020). [11C]MODAG-001—towards a PET tracer targeting α -synuclein aggregates. *Eur. J. Nucl. Med. Mol. Imaging.* doi:10.1007/s00259-020-05133-x.
- Kuhar, M. J., and Unnerstall, J. R. (1985). Quantitative receptor mapping by autoradiography: some current technical problems. *Trends Neurosci.* 8, 49–53. doi:10.1016/0166-2236(85)90025-6.
- Lakens, D. (2013). Calculating and reporting effect sizes to facilitate cumulative science: A practical primer for t-tests and ANOVAs. *Front. Psychol.* 4, 863. doi:10.3389/fpsyg.2013.00863.
- Lammertsma, A. A., and Hume, S. P. (1996). Simplified reference tissue model for PET receptor studies. *Neuroimage* 4, 153–158. doi:10.1006/nimg.1996.0066.
- Lashuel, H. A., Overk, C. R., Oueslati, A., and Masliah, E. (2013). The many faces of α -synuclein: from structure and toxicity to therapeutic target. *Nat. Rev. Neurosci.* 14, 38–48. doi:10.1038/nrn3406.
- Lockhart, A., Lamb, J. R., Osredkar, T., Sue, L. I., Joyce, J. N., Ye, L., et al. (2007). PIB is a non-specific imaging marker of amyloid-beta (A β) peptide-related cerebral amyloidosis. *Brain* 130, 2607–2615. doi:10.1093/brain/awm191.
- Logan, J., Fowler, J. S., Volkow, N. D., Wang, G. J., Ding, Y. S., and Alexoff, D. L. (1996). Distribution volume ratios without blood sampling from graphical analysis of PET data. *J. Cereb. Blood Flow Metab.* 16, 834–840. doi:10.1097/00004647-199609000-00008.
- Logan, J., Fowler, J. S., Volkow, N. D., Wolf, A. P., Dewey, S. L., Schlyer, D. J., et al. (1990). Graphical analysis of reversible radioligand binding from time-activity measurements applied to [N-11C-methyl]-(-)-cocaine PET studies in human subjects. *J. Cereb. Blood Flow Metab.* 10, 740–747. doi:10.1038/jcbfm.1990.127.
- López-Giménez, J. F., Vilaró, M. T., Palacios, J. M., and Mengod, G. (2013). Multiple conformations of 5-HT_{2A} and 5-HT_{2C} receptors in rat brain: An autoradiographic study with [¹²⁵I](±)DOI. *Exp. Brain Res.* 230, 395–406. doi:10.1007/s00221-013-3636-8.
- López-Giménez, J. F., Villazón, M., Brea, J., Loza, M. I., Palacios, J. M., Mengod, G., et al. (2001). Multiple conformations of native and recombinant human 5-hydroxytryptamine_{2A} receptors are labeled by agonists and discriminated by antagonists. *Mol. Pharmacol.* 60, 690–699. Available at: <http://molpharm.aspetjournals.org>.
- Luurtsema, G., Pichler, V., Bongarzone, S., Seimille, Y., Elsinga, P., Gee, A., et al. (2021). EANM guideline for harmonisation on molar activity or specific activity of radiopharmaceuticals: impact on safety and imaging quality. *EJNMMI Radiopharm Chem* 6, 34. doi:10.1186/s41181-021-00149-6.

- Ly, C., Greb, A. C., Cameron, L. P., Wong, J. M., Eden, V., Wilson, P. C., et al. (2018). Psychedelics Promote Structural and Functional Neural Plasticity. *Cell Rep.* 23, 3170–3182. doi:10.1016/j.celrep.2018.05.022.
- Lynch, B. A., Lambeng, N., Nocka, K., Kensel-Hammes, P., Bajjalieh, S. M., Matagne, A., et al. (2004). The synaptic vesicle protein SV2A is the binding site for the antiepileptic drug levetiracetam. *Proc. Natl. Acad. Sci. U. S. A.* 101, 9861–9866. doi:10.1073/pnas.0308208101.
- Madsen, K., Hasselbalch, B. J., Frederiksen, K. S., Haahr, M. E., Gade, A., Law, I., et al. (2012). Lack of association between prior depressive episodes and cerebral [¹¹C]PiB binding. *Neurobiol. Aging* 33, 2334–2342. doi:10.1016/j.neurobiolaging.2011.11.021.
- Madsen, M. K., Fisher, P. M., Burmester, D., Dyssegaard, A., Stenbæk, D. S., Kristiansen, S., et al. (2019). Psychedelic effects of psilocybin correlate with serotonin 2A receptor occupancy and plasma psilocin levels. *Neuropsychopharmacology* 44, 1328–1334. doi:10.1038/s41386-019-0324-9.
- Madsen, M. K., Macdonald Fisher, P., Stenbaek, D. S., Kristiansen, S., Burmester, D., Lehel, S., et al. (2020). A single psilocybin dose is associated with long-term increased mindfulness, preceded by a proportional change in neocortical 5-HT_{2A} receptor binding. *Eur. Neuropsychopharmacol.* 9, 1–10. doi:10.1016/j.euroneuro.2020.02.001.
- Maguire, J. J., Kuc, R. E., and Davenport, A. P. (2012). “Radioligand Binding Assays and Their Analysis,” in *Receptor Binding Techniques*, ed. A. P. Davenport (Totowa, NJ: Humana Press), 31–77. doi:10.1007/978-1-61779-909-9_3.
- Mak, E., Holland, N., Jones, P. S., Savulich, G., Low, A., Malpetti, M., et al. (2021). *In vivo* coupling of dendritic complexity with presynaptic density in primary tauopathies. *Neurobiol. Aging* 101, 187–198. doi:10.1016/j.neurobiolaging.2021.01.016.
- Manuel, I., Barrera-Gómez, G., González de San Román, E., Veloso, A., Fernández, J. A., Giral, M. T., et al. (2015). Neurotransmitter receptor localization: from autoradiography to imaging mass spectrometry. *ACS Chem. Neurosci.* 6, 362–373. doi:10.1021/cn500281t.
- Maruyama, M., Shimada, H., Sahara, T., Shinotoh, H., Ji, B., Maeda, J., et al. (2013). Imaging of tau pathology in a tauopathy mouse model and in Alzheimer patients compared to normal controls. *Neuron* 79, 1094–1108. doi:10.1016/j.neuron.2013.07.037.
- Matheson, G. J. (2018). Reliability, Replicability and Reproducibility in PET Imaging.
- Matheson, G. J. (2019). kinfitr: Reproducible PET Pharmacokinetic Modelling in R. *bioRxiv*, 755751. doi:10.1101/755751.
- Mathis, C. A., Lopresti, B. J., Ikonovic, M. D., and Klunk, W. E. (2017). Small-molecule PET Tracers for Imaging Proteinopathies. *Semin. Nucl. Med.* 47, 553–575. doi:10.1053/j.semnuclmed.2017.06.003.
- Matuskey, D., Tinaz, S., Wilcox, K. C., Naganawa, M., Toyonaga, T., Dias, M., et al. (2020). Synaptic Changes in Parkinson Disease Assessed with *in vivo* Imaging. *Ann. Neurol.* 87, 329–338. doi:10.1002/ana.25682.
- Maurer, A., Leonov, A., Ryazanov, S., Herfert, K., Kuebler, L., Buss, S., et al. (2019). ¹¹C radiolabeling of anle253b: A putative PET tracer for Parkinson’s disease that binds to alpha-synuclein fibrils *in vitro* and crosses the blood-brain barrier. *ChemMedChem*. doi:10.1002/cmdc.201900689.
- McCluskey, S. P., Plisson, C., Rabiner, E. A., and Howes, O. (2020). Advances in CNS PET: the state-of-the-art for new imaging targets for pathophysiology and drug development. *Eur. J. Nucl. Med. Mol. Imaging* 47, 451–489. doi:10.1007/s00259-019-04488-0.
- McCulloch, D. E., Grzywacz, M. Z., Madsen, M. K., Jensen, P. S., Ozenne, B., Armand, S., et al. (2021). A Quantitative and Qualitative Report of Psilocybin Induced Mystical-Type Experiences and Their Relation to Lasting Positive Effects. doi:10.31234/osf.io/xqzu2.
- Mecca, A. P., Chen, M. K., O’Dell, R. S., Naganawa, M., Toyonaga, T., Godek, T. A., et al. (2020). *In vivo* measurement of widespread synaptic loss in Alzheimer’s disease with SV2A PET. *Alzheimer’s and Dementia* 16, 974–982. doi:10.1002/alz.12097.
- Mecca, A. P., Chen, M.-K., O’Dell, R. S., Naganawa, M., Toyonaga, T., Godek, T. A., et al. (2022). Association of entorhinal cortical tau deposition and hippocampal synaptic density in older individuals with normal cognition and early Alzheimer’s disease. *Neurobiol. Aging* 111, 44–53. doi:10.1016/j.neurobiolaging.2021.11.004.
- Mendoza-Torreblanca, J. G., Vanoye-Carlo, A., Phillips-Farfán, B. V., Carmona-Aparicio, L., and Gómez-Lira, G. (2013). Synaptic vesicle protein 2A: Basic facts and role in synaptic function. *Eur. J. Neurosci.* 38, 3529–3539. doi:10.1111/ejn.12360.
- Menneson, S., Ménicot, S., Ferret-Bernard, S., Guérin, S., Romé, V., Le Normand, L., et al. (2019). Validation of a Psychosocial Chronic Stress Model in the Pig Using a Multidisciplinary Approach at the Gut-Brain and Behavior Levels. *Front. Behav. Neurosci.* 13, 161. doi:10.3389/fnbeh.2019.00161.
- Mertens, N., Maguire, R. P., Serdons, K., Lacroix, B., Mercier, J., Sciberras, D., et al. (2020). Validation of parametric methods for [¹¹C]UCB-J PET imaging using subcortical white matter as reference tissue. *Mol. Imaging Biol.* 22, 444–452. doi:10.1007/s11307-019-01387-6.
- Metaxas, A., Thygesen, C., Briting, S. R. R., Landau, A. M., Darvesh, S., and Finsen, B. (2019). Increased Inflammation and Unchanged Density of Synaptic Vesicle Glycoprotein 2A (SV2A) in the Postmortem Frontal Cortex of Alzheimer’s Disease Patients. *Front. Cell. Neurosci.* 13, 538. doi:10.3389/fncel.2019.00538.
- Meyer, P. T., Frings, L., Rücker, G., and Hellwig, S. (2017). ¹⁸F-FDG PET in Parkinsonism: Differential diagnosis and evaluation of cognitive impairment. *J. Nucl. Med.* 58, 1888–1898. doi:10.2967/jnumed.116.186403.

- Michaelis, L., Menten, M. L., Johnson, K. A., and Goody, R. S. (2011). The original Michaelis constant: translation of the 1913 Michaelis-Menten paper. *Biochemistry* 50, 8264–8269. doi:10.1021/bi201284u.
- Mintun, M. A., Raichle, M. E., Kilbourn, M. R., Wooten, G. F., and Welch, M. J. (1984). A quantitative model for the *in vivo* assessment of drug binding sites with positron emission tomography. *Ann. Neurol.* 15, 217–227. doi:10.1002/ana.410150302.
- Mosconi, L. (2013). Glucose metabolism in normal aging and Alzheimer's disease: Methodological and physiological considerations for PET studies. *Clinical and Translational Imaging* 1, 217–233. doi:10.1007/s40336-013-0026-y.
- Moses, W. W. (2011). Fundamental Limits of Spatial Resolution in PET. *Nucl. Instrum. Methods Phys. Res. A* 648 Supplement 1, S236–S240. doi:10.1016/j.nima.2010.11.092.
- Musigazi, G. U., De Vleeschauwer, S., Sciote, R., Verbeken, E., and Depreitere, B. (2018). Brain perfusion fixation in male pigs using a safer closed system. *Lab. Anim.* 52, 413–417. doi:10.1177/0023677217752747.
- Nabulsi, N. B., Mercier, J., Holden, D., Carré, S., Najafzadeh, S., Vandergeten, M.-C., et al. (2016). Synthesis and Preclinical Evaluation of ¹¹C-UCB-J as a PET Tracer for Imaging the Synaptic Vesicle Glycoprotein 2A in the Brain. *J. Nucl. Med.* 57, 777–784. doi:10.2967/jnumed.115.168179.
- Nicastro, N., Holland, N., Savulich, G., Carter, S. F., Mak, E., Hong, Y. T., et al. (2020). ¹¹C-UCB-J synaptic PET and multimodal imaging in dementia with Lewy bodies. *European Journal of Hybrid Imaging* 4. doi:10.1186/s41824-020-00093-9.
- Nicolas, J.-M., Hannestad, J., Holden, D., Kervyn, S., Nabulsi, N., Tytgat, D., et al. (2016). Brivaracetam, a selective high-affinity synaptic vesicle protein 2A (SV2A) ligand with preclinical evidence of high brain permeability and fast onset of action. *Epilepsia* 57, 201–209. doi:10.1111/epi.13267.
- Ni, R., and Nitsch, R. M. (2021). Recent Developments in Positron Emission Tomography Tracers for Proteinopathies Imaging in Dementia. *Front. Aging Neurosci.* 13, 751897. doi:10.3389/fnagi.2021.751897.
- Nykjaer, C. H., Brudek, T., Salvesen, L., and Pakkenberg, B. (2017). Changes in the cell population in brain white matter in multiple system atrophy. *Mov. Disord.* 32, 1074–1082. doi:10.1002/mds.26979.
- O'Dell, R. S., Mecca, A. P., Chen, M. K., Naganawa, M., Toyonaga, T., Lu, Y., et al. (2021). Association of A β deposition and regional synaptic density in early Alzheimer's disease: a PET imaging study with [¹¹C]UCB-J. *Alzheimers. Res. Ther.* 13. doi:10.1186/s13195-020-00742-y.
- Ogden, R. T., and Tarpey, T. (2006). Estimation in regression models with externally estimated parameters. *Biostatistics* 7, 115–129. doi:10.1093/biostatistics/kxi044.
- Olson, D. E. (2022). Biochemical Mechanisms Underlying Psychedelic-Induced Neuroplasticity. *Biochemistry*. doi:10.1021/acs.biochem.1c00812.
- Ono, M., Takahashi, M., Shimozaawa, A., Fujinaga, M., Mori, W., Nagai, Y., et al. (2021). *In vivo* visualization of propagating α -synuclein pathologies in mouse and marmoset models by a bimodal imaging probe, C05-05. *bioRxiv*, 2020.10.23.349860. doi:10.1101/2020.10.23.349860.
- Osmond, H. (1957). A Review of the Clinical Effects of Psychotomimetic Agents. *Ann. N. Y. Acad. Sci.* 66, 418–434. doi:10.1111/j.1749-6632.1957.tb40738.x.
- Palner, M., Kjaerby, C., Knudsen, G. M., and Cumming, P. (2011). Effects of unilateral 6-OHDA lesions on [³H]-N-propylnorapomorphine binding in striatum *ex vivo* and vulnerability to amphetamine-evoked dopamine release in rat. *Neurochem. Int.* 58, 243–247. doi:10.1016/j.neuint.2010.12.007.
- Parker, C. A., Gunn, R. N., Rabiner, E. A., Slifstein, M., Comley, R., Salinas, C., et al. (2012). Radiosynthesis and characterization of ¹¹C-GSK215083 as a PET radioligand for the 5-HT₆ receptor. *J. Nucl. Med.* 53, 295–303. doi:10.2967/jnumed.111.093419.
- Peelaerts, W., Bousset, L., Van der Perren, A., Moskalyuk, A., Pulizzi, R., Giugliano, M., et al. (2015). α -Synuclein strains cause distinct synucleinopathies after local and systemic administration. *Nature* 522, 340–344. doi:10.1038/nature14547.
- Phelps, M. E., Hoffman, E. J., Mullani, N. A., and Ter-Pogossian, M. M. (1975). Application of annihilation coincidence detection to transaxial reconstruction tomography. *J. Nucl. Med.* 16, 210–224. Available at: <https://www.ncbi.nlm.nih.gov/pubmed/1113170>.
- Pike, C. J., Burdick, D., Walencewicz, A. J., Glabe, C. G., and Cotman, C. W. (1993). Neurodegeneration induced by beta-amyloid peptides *in vitro*: the role of peptide assembly state. *J. Neurosci.* 13, 1676–1687.
- Plavén-Sigra, P. (2018). Positron Emission Tomography: Development, Evaluation and Application of Quantification Methods.
- Polak, J., and Wharton, J. (1993). Receptor autoradiography: principles and practice. Oxford University Press.
- Rasmussen, M. K., Mestre, H., and Nedergaard, M. (2021). Fluid Transport in the Brain. *Physiol. Rev.* doi:10.1152/physrev.00031.2020.
- Raval, N. R., Gudmundsen, F., Juhl, M., Andersen, I. V., Speth, N., Videbæk, A., et al. (2021a). Synaptic Density and Neuronal Metabolic Function Measured by Positron Emission Tomography in the Unilateral 6-OHDA Rat Model of Parkinson's Disease. *Front. Synaptic Neurosci.* 13, 715811. doi:10.3389/fnsyn.2021.715811.
- Raval, N. R., Johansen, A., Donovan, L. L., Ros, N. F., Ozenne, B., Hansen, H. D., et al. (2021b). A Single Dose of Psilocybin Increases Synaptic Density and Decreases 5-HT_{2A} Receptor Density in the Pig Brain. *Int. J. Mol. Sci.* 22, 835. doi:10.3390/ijms22020835.
- Raval, N. R., Madsen, C. A., Shalgunov, V., Nasser, A., Battisti, U. M., Beaman, E. E., et al. (2022a). Evaluation of the α -synuclein PET radiotracer (d3)-[¹¹C]MODAG-001 in pigs. *bioRxiv*, 2022.02.05.479231. doi:10.1101/2022.02.05.479231.

- Raval, N. R., Nasser, A., Madsen, C. A., Beschorner, N., Beaman, E. E., Juhl, M., et al. (2022b). An *in vivo* pig model for testing novel PET radioligands targeting cerebral protein aggregates. *bioRxiv*, 2021.12.31.473908. doi:10.1101/2021.12.31.473908.
- Recasens, A., Dehay, B., Bové, J., Carballo-Carbajal, I., Doveiro, S., Pérez-Villalba, A., et al. (2014). Lewy body extracts from Parkinson disease brains trigger α -synuclein pathology and neurodegeneration in mice and monkeys. *Ann. Neurol.* 75, 351–362. doi:10.1002/ana.24066.
- Rigney, G., Ayubcha, C., Werner, T. J., and Alavi, A. (2021). An Update on the State of Tau Radiotracer Development: a Brief Review. *Mol. Imaging Biol.* 23, 797–808. doi:10.1007/s11307-021-01612-1.
- Robinson, J. L., Molina-Porcel, L., Corrada, M. M., Raible, K., Lee, E. B., Lee, V. M.-Y., et al. (2014). Perforant path synaptic loss correlates with cognitive impairment and Alzheimer's disease in the oldest-old. *Brain* 137, 2578–2587. doi:10.1093/brain/awu190.
- Roshanbin, S., Xiong, M., Hultqvist, G., Söderberg, L., Zachrisson, O., Meier, S., et al. (2022). *In vivo* imaging of alpha-synuclein with antibody-based PET. *Neuropharmacology*, 108985. doi:10.1016/j.neuropharm.2022.108985.
- Ross, S., Bossis, A., Guss, J., Agin-Liebes, G., Malone, T., Cohen, B., et al. (2016). Rapid and sustained symptom reduction following psilocybin treatment for anxiety and depression in patients with life-threatening cancer: A randomized controlled trial. *J. Psychopharmacol.* 30, 1165–1180. doi:10.1177/0269881116675512.
- Sabri, O., Seibyl, J., Rowe, C., and Barthel, H. (2015). Beta-amyloid imaging with florbetaben. *Clin Transl Imaging* 3, 13–26. doi:10.1007/s40336-015-0102-6.
- Saikali, S., Meurice, P., Sauleau, P., Eliat, P.-A., Bellaud, P., Randuineau, G., et al. (2010). A three-dimensional digital segmented and deformable brain atlas of the domestic pig. *J. Neurosci. Methods* 192, 102–109. doi:10.1016/j.jneumeth.2010.07.041.
- Salinas, C. A., Searle, G. E., and Gunn, R. N. (2015). The simplified reference tissue model: model assumption violations and their impact on binding potential. *J. Cereb. Blood Flow Metab.* 35, 304–311. doi:10.1038/jcbfm.2014.202.
- Schiffer, W. K., Mirrione, M. M., Biegón, A., Alexoff, D. L., Patel, V., and Dewey, S. L. (2006). Serial microPET measures of the metabolic reaction to a microdialysis probe implant. *J. Neurosci. Methods* 155, 272–284. doi:10.1016/j.jneumeth.2006.01.027.
- Schneider, C. A., Rasband, W. S., and Eliceiri, K. W. (2012). NIH Image to ImageJ: 25 years of Image Analysis HHS Public Access.
- Sehlin, D., Fang, X. T., Cato, L., Antoni, G., Lannfelt, L., and Syvänen, S. (2016). Antibody-based PET imaging of amyloid beta in mouse models of Alzheimer's disease. *Nat. Commun.* 7, 10759. doi:10.1038/ncomms10759.
- Sejnowski, T. J., Churchland, P. S., and Movshon, J. A. (2014). Putting big data to good use in neuroscience. *Nat. Neurosci.* 17, 1440–1441. doi:10.1038/nn.3839.
- Selek, L., Seigneuret, E., Nugue, G., Wion, D., Nissou, M. F., Salon, C., et al. (2014). Imaging and histological characterization of a human brain xenograft in pig: the first induced glioma model in a large animal. *J. Neurosci. Methods* 221, 159–165. doi:10.1016/j.jneumeth.2013.10.002.
- Shalgunov, V., van Waarde, A., Booij, J., Michel, M. C., Dierckx, R. A. J. O., and Elsinga, P. H. (2019). Hunting for the high-affinity state of G-protein-coupled receptors with agonist tracers: Theoretical and practical considerations for positron emission tomography imaging. *Med. Res. Rev.* 39, 1014–1052. doi:10.1002/med.21552.
- Shao, L.-X., Liao, C., Gregg, I., Davoudian, P. A., Savalia, N. K., Delagarza, K., et al. (2021). Psilocybin induces rapid and persistent growth of dendritic spines in frontal cortex *in vivo*. *Neuron* 109, 2535–2544.e4. doi:10.1016/j.neuron.2021.06.008.
- Sharma, V., Luker, G. D., and Piwnica-Worms, D. (2002). Molecular imaging of gene expression and protein function *in vivo* with PET and SPECT. *J. Magn. Reson. Imaging* 16, 336–351. doi:10.1002/jmri.10182.
- Shelton, R. C., Sanders-Bush, E., Manier, D. H., and Lewis, D. A. (2009). Elevated 5-HT 2A receptors in postmortem prefrontal cortex in major depression is associated with reduced activity of protein kinase A. *Neuroscience* 158, 1406–1415. doi:10.1016/j.neuroscience.2008.11.036.
- Shi, J., Anderson, D., Lynch, B. A., Castaigne, J.-G., Foerch, P., and Lebon, F. (2011). Combining modelling and mutagenesis studies of synaptic vesicle protein 2A to identify a series of residues involved in racetam binding. *Biochem. Soc. Trans.* 39, 1341–1347. doi:10.1042/BST0391341.
- Shimozawa, A., Ono, M., Takahara, D., Tarutani, A., Imura, S., Masuda-Suzukake, M., et al. (2017). Propagation of pathological α -synuclein in marmoset brain. *Acta Neuropathol Commun* 5, 12. doi:10.1186/s40478-017-0413-0.
- Song, J., Hanniford, D., Doucette, C., Graham, E., Poole, M. F., Ting, A., et al. (2005). Development of homogenous high-affinity agonist binding assays for 5-HT₂ receptor subtypes. *Assay Drug Dev. Technol.* 3, 649–659. doi:10.1089/adt.2005.3.649.
- Spies, M., Knudsen, G. M., Lanzenberger, R., and Kasper, S. (2015). The serotonin transporter in psychiatric disorders: insights from PET imaging. *Lancet Psychiatry* 2, 743–755. doi:10.1016/S2215-0366(15)00232-1.
- Srinivasan, B. (2021). A guide to the Michaelis-Menten equation: steady state and beyond. *FEBS J.* doi:10.1111/febs.16124.
- Stenbæk, D. S., Dam, V. H., Fisher, P. M., Hansen, N., Hjordt, L. V., and Frokjaer, V. G. (2017). No evidence for a role of the serotonin 4 receptor in five-factor personality traits: A positron emission tomography brain study. *PLoS One* 12, e0184403. doi:10.1371/journal.pone.0184403.
- Strohäker, T., Jung, B. C., Liou, S.-H., Fernandez, C. O., Riedel, D., Becker, S., et al. (2019). Structural heterogeneity of α -synuclein fibrils amplified from patient brain extracts. *Nat. Commun.* 10, 5535. doi:10.1038/s41467-019-13564-w.

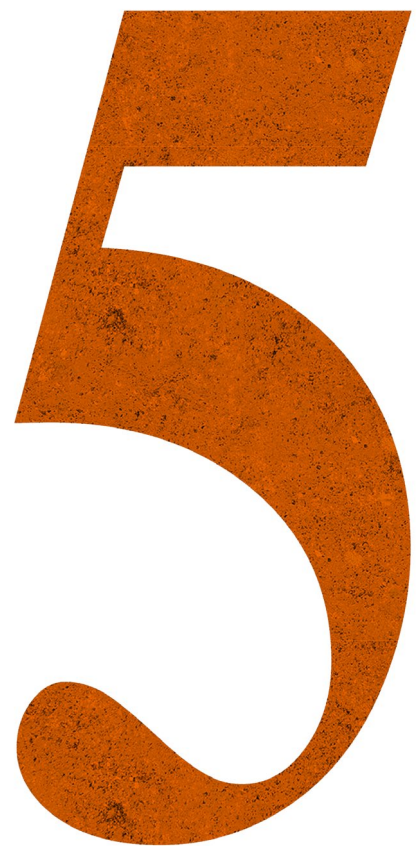
- Südhof, T. C. (1999). Composition of Synaptic Vesicles. Lippincott-Raven Available at: <https://www.ncbi.nlm.nih.gov/books/NBK28154/> [Accessed February 4, 2022].
- Sun, W., Ginovart, N., Ko, F., Seeman, P., and Kapur, S. (2003). *In vitro* evidence for dopamine-mediated internalization of D2-receptors after amphetamine: differential findings with [³H]raclopride versus [³H]spiperone. *Mol. Pharmacol.* 63, 456–462. doi:10.1124/mol.63.2.456.
- Sureau, F. C., Reader, A. J., Comtat, C., Leroy, C., Ribeiro, M. J., Buvat, I., et al. (2008). Impact of image-space resolution modeling for studies with the high-resolution research tomograph. *J. Nucl. Med.* 49, 1000–1008. doi:10.2967/jnumed.107.045351.
- Takano, A., Varrone, A., Gulyás, B., Salvadori, P., Gee, A., Windhorst, A., et al. (2016). Guidelines to PET measurements of the target occupancy in the brain for drug development. *Eur. J. Nucl. Med. Mol. Imaging* 43, 2255–2262. doi:10.1007/s00259-016-3476-4.
- Tanzey, S. S., Thompson, S., Scott, P. J., and Brooks, A. F. (2018). Gallium-68: methodology and novel radiotracers for positron emission tomography (2012–2017). *Pharm Pat Anal* 7, 193–227. doi:10.4155/ppa-2018-0016.
- Thakur, P., Breger, L. S., Lundblad, M., Wan, O. W., Mattsson, B., Luk, K. C., et al. (2017). Modeling Parkinson's disease pathology by combination of fibril seeds and α -synuclein overexpression in the rat brain. *Proceedings of the National Academy of Sciences* 114, E8284–E8293. doi:10.1073/PNAS.1710442114.
- Theilmann, R. J., Reed, J. D., Song, D. D., Huang, M. X., Lee, R. R., Litvan, I., et al. (2013). White-matter changes correlate with cognitive functioning in Parkinson's disease. *Front. Neurol.* 4, 37. doi:10.3389/fneur.2013.00037.
- Thompson, S., Kealey, S., Sephton, S. M., and Aigbirhio, F. I. (2020). Radiochemistry with Carbon-11. *Handbook of Radiopharmaceuticals*, 143–249. doi:10.1002/9781119500575.ch7.
- Thomsen, M. B., Ferreira, S. A., Schacht, A. C., Jacobsen, J., Simonsen, M., Betzer, C., et al. (2021a). PET imaging reveals early and progressive dopaminergic deficits after intra-striatal injection of preformed alpha-synuclein fibrils in rats. *Neurobiol. Dis.* 149. doi:10.1016/j.nbd.2020.105229.
- Thomsen, M. B., Jacobsen, J., Lillethorup, T. P., Schacht, A. C., Simonsen, M., Romero-Ramos, M., et al. (2021b). *In vivo* imaging of synaptic SV2A protein density in healthy and striatal-lesioned rats with [¹¹C]UCB-J PET. *J. Cereb. Blood Flow Metab.* 41, 819–830. doi:10.1177/0271678X20931140.
- Tjerkaski, J., Cervenka, S., Farde, L., and Matheson, G. J. (2020). Kinfitr - an open-source tool for reproducible PET modelling: validation and evaluation of test-retest reliability. *EJNMMI Res.* 10, 77. doi:10.1186/s13550-020-00664-8.
- Tolboom, N., Yaqub, M., Boellaard, R., Luurtsema, G., Windhorst, A. D., Scheltens, P., et al. (2009). Test-retest variability of quantitative [¹¹C]PIB studies in Alzheimer's disease. *Eur. J. Nucl. Med. Mol. Imaging* 36, 1629–1638. doi:10.1007/s00259-009-1129-6.
- Turku PET Centre, University of Turku Turku PET centre: PET data analysis and modelling. Available at: <http://www.turkupetcentre.net/petanalysis/> [Accessed February 2, 2022].
- Uzuegbunam, B., Li, J., Paslawski, W., Weber, W., Svenningson, P., Ågren, H., et al. (2022). Towards Novel [¹⁸F] Fluorine-labeled Radiotracers for the Imaging of α -Synuclein Fibrils. *Front. Aging Neurosci.* 14. doi:10.3389/fnagi.2022.830704.
- Vanhaute, H., Ceccarini, J., Michiels, L., Koole, M., Sunaert, S., Lemmens, R., et al. (2020). *In vivo* synaptic density loss is related to tau deposition in amnesic mild cognitive impairment. *Neurology* 95, e545–e553. doi:10.1212/WNL.0000000000009818.
- Verdurand, M., Levigoureux, E., Zeinyeh, W., Berthier, L., Mendjel-Herda, M., Cadarossanesaib, F., et al. (2018). *In Silico, in vitro, and in vivo* Evaluation of New Candidates for α -Synuclein PET Imaging. *Mol. Pharm.* 15, 3153–3166. doi:10.1021/acs.molpharmaceut.8b00229.
- Vernaleken, I., Buchholz, H.-G., Kumakura, Y., Siessmeier, T., Stoeter, P., Bartenstein, P., et al. (2007). “Prefrontal” cognitive performance of healthy subjects positively correlates with cerebral FDOPA influx: an exploratory [¹⁸F]-fluoro-L-DOPA-PET investigation. *Hum. Brain Mapp.* 28, 931–939. doi:10.1002/hbm.20325.
- Vesely, B., and Rektor, I. (2016). The contribution of white matter lesions (WML) to Parkinson's disease cognitive impairment symptoms: A critical review of the literature. *Parkinsonism Relat. Disord.* 22 Suppl 1, S166–170. doi:10.1016/j.parkreldis.2015.09.019.
- Villadsen, J., Hansen, H. D., Jørgensen, L. M., Keller, S. H., Andersen, F. L., Petersen, I. N., et al. (2017). Automatic delineation of brain regions on MRI and PET images from the pig. *J. Neurosci. Methods* 294, 51–58. doi:10.1016/j.jneumeth.2017.11.008.
- Visanji, N. P., Brotchie, J. M., Kalia, L. V., Koprach, J. B., Tandon, A., Watts, J. C., et al. (2016). α -Synuclein-Based Animal Models of Parkinson's Disease: Challenges and Opportunities in a New Era. *Trends Neurosci.* 39, 750–762. doi:10.1016/j.tins.2016.09.003.
- Vodička, P., Smetana, K., Dvořánková, B., Emerick, T., Xu, Y. Z., Ourednik, J., et al. (2005). The miniature pig as an animal model in biomedical research. *Ann. N. Y. Acad. Sci.* 1049, 161–171. doi:10.1196/annals.1334.015.
- Vollenweider, F. X., and Smallridge, J. W. (2022). Classic Psychedelic Drugs: Update on Biological Mechanisms. *Pharmacopsychiatry.* doi:10.1055/a-1721-2914.
- Vriend, C., Pattij, T., Van Der Werf, Y. D., Voorn, P., Booij, J., Rutten, S., et al. (2014). Depression and impulse control disorders in Parkinson's disease: Two sides of the same coin? *Neuroscience and Biobehavioral Reviews* 38, 60–71. doi:10.1016/j.neubiorev.2013.11.001.
- Wager, T. T., Hou, X., Verhoest, P. R., and Villalobos, A. (2016). Central Nervous System Multiparameter Optimization Desirability: Application in Drug Discovery. *ACS Chem. Neurosci.* 7, 767–775. doi:10.1021/acschemneuro.6b00029.

- Wagner, J., Ryazanov, S., Leonov, A., Levin, J., Shi, S., Schmidt, F., et al. (2013). Anle138b: a novel oligomer modulator for disease-modifying therapy of neurodegenerative diseases such as prion and Parkinson's disease. *Acta Neuropathol.* 125, 795–813. doi:10.1007/s00401-013-1114-9.
- Winterdahl, M., Audrain, H., Landau, A. M., Smith, D. F., Bonaventure, P., Shoblock, J. R., et al. (2014). PET brain imaging of neuropeptide Y2 receptors using N-11C-methyl-JNJ-31020028 in pigs. *J. Nucl. Med.* 55, 635–639. doi:10.2967/jnumed.113.125351.
- Wu, Y., and Carson, R. E. (2002). Noise reduction in the simplified reference tissue model for neuroreceptor functional imaging. *J. Cereb. Blood Flow Metab.* 22, 1440–1452. doi:10.1097/01.WCB.0000033967.83623.34.
- Xia, C.-F., Arteaga, J., Chen, G., Gangadharmath, U., Gomez, L. F., Kasi, D., et al. (2013). [(18)F]T807, a novel tau positron emission tomography imaging agent for Alzheimer's disease. *Alzheimers. Dement.* 9, 666–676. doi:10.1016/j.jalz.2012.11.008.
- Xiong, M., Roshanbin, S., Rokka, J., Schlein, E., Ingelsson, M., Sehlin, D., et al. (2021). *In vivo* imaging of synaptic density with [11C]UCB-J PET in two mouse models of neurodegenerative disease. *Neuroimage* 239, 118302. doi:10.1016/j.neuroimage.2021.118302.
- Yaden, D. B., and Griffiths, R. R. (2021). The Subjective Effects of Psychedelics Are Necessary for Their Enduring Therapeutic Effects. *ACS Pharmacol Transl Sci* 4, 568–572. doi:10.1021/acspsci.0c00194.
- Yang, W., Wang, G., Wang, C.-E., Guo, X., Yin, P., Gao, J., et al. (2015). Mutant Alpha-Synuclein Causes Age-Dependent Neuropathology in Monkey Brain. *Journal of Neuroscience* 35, 8345–8358. doi:10.1523/JNEUROSCI.0772-15.2015.
- Yaqub, M., Tolboom, N., Boellaard, R., van Berckel, B. N. M., van Tilburg, E. W., Luurtsema, G., et al. (2008). Simplified parametric methods for [11C]PIB studies. *Neuroimage* 42, 76–86. doi:10.1016/j.neuroimage.2008.04.251.
- Ye, L., Velasco, A., Fraser, G., Beach, T. G., Sue, L., Osredkar, T., et al. (2008). *In vitro* high affinity alpha-synuclein binding sites for the amyloid imaging agent PIB are not matched by binding to Lewy bodies in postmortem human brain. *J. Neurochem.* 105, 1428–1437. doi:10.1111/j.1471-4159.2008.05245.x.
- Yuan, H., Sarre, S., Ebinger, G., and Michotte, Y. (2005). Histological, behavioural and neurochemical evaluation of medial forebrain bundle and striatal 6-OHDA lesions as rat models of Parkinson's disease. *J. Neurosci. Methods* 144, 35–45. doi:10.1016/j.jneumeth.2004.10.004.
- Zhang, L., and Villalobos, A. (2017). Strategies to facilitate the discovery of novel CNS PET ligands. *EJNMMI Radiopharm Chem* 1, 13. doi:10.1186/s41181-016-0016-2.
- Zhang, Y., Hong, H., and Cai, W. (2011). PET tracers based on Zirconium-89. *Curr. Radiopharm.* 4, 131–139. doi:10.2174/1874471011104020131.
- Ziebell, M., Andersen, B. B., Thomsen, G., Pinborg, L. H., Karlsborg, M., Hasselbalch, S. G., et al. (2012). Predictive value of dopamine transporter SPECT imaging with [123I]PE2I in patients with subtle parkinsonian symptoms. *Eur. J. Nucl. Med. Mol. Imaging* 39, 242–250. doi:10.1007/s00259-011-1976-9.
- Zimmer, L., and Luxen, A. (2012). PET radiotracers for molecular imaging in the brain: past, present and future. *Neuroimage* 61, 363–370. doi:10.1016/j.neuroimage.2011.12.037.

Appendix

“Don’t sweat the first draft. No one will ever see it. No one cares. And neither should you.”

Neil Gaiman



Aim I

To establish a pig model with intracerebral protein injections that will help assess novel radioligands.

Study

I

Objection I

To validate the intracerebral protein injection pig model using [¹¹C]PIB.

An *in vivo* pig model for testing novel PET radioligands targeting cerebral protein aggregates

1 Nakul Ravi Raval ^{1,2}, Arafat Nasser ¹, Clara Aabye Madsen ^{1,2}, Natalie Beschorner ³, Emily
2 Eufaula Beaman ¹, Morten Juhl ⁴, Szabolcs Lehel ⁵, Mikael Palner ^{1,6,7}, Claus Svarer ¹, Pontus
3 Plavén-Sigraý ¹, Louise Møller Jørgensen ^{1,2,8}, Gitte Moos Knudsen ^{*1,2}

4 ¹ Neurobiology Research Unit, Copenhagen University Hospital (Rigshospitalet), Copenhagen,
5 Denmark

6 ² Faculty of Health and Medical Sciences, University of Copenhagen, Copenhagen, Denmark

7 ³ Center for Translational Neuromedicine, University of Copenhagen, Copenhagen, Denmark

8 ⁴ Cardiology Stem Cell Centre, Copenhagen University Hospital (Rigshospitalet), Copenhagen,
9 Denmark

10 ⁵ Department of Clinical Physiology, Nuclear Medicine & PET, Copenhagen University Hospital
11 (Rigshospitalet), Copenhagen, Denmark

12 ⁶ Department of Clinical Research, Clinical Physiology and Nuclear Medicine, University of
13 Southern Denmark, Odense, Denmark

14 ⁷ Department of Nuclear Medicine, Odense University Hospital, Odense, Denmark

15 ⁸ Copenhagen Spine Research Unit, Copenhagen University Hospital (Rigshospitalet), Glostrup,
16 Denmark

17

18 *** Correspondence:**

19 Gitte Moos Knudsen

20 Neurobiology Research Unit

21 Section 8057, Rigshospitalet

22 Blegdamsvej 9

23 DK-2100 Copenhagen Ø

24 Denmark

25 Email: gmk@nru.dk

26 **Keywords:** Positron emission tomography, [¹¹C]PIB, protein injection model, alpha-synuclein,
27 amyloid-beta, brain imaging, autoradiography, large animal PET

28

29 **Abstract**

30 Positron emission tomography (PET) has become an essential clinical tool for diagnosing
31 neurodegenerative diseases with abnormal accumulation of proteins like amyloid- β or tau. Despite
32 many attempts, it has not been possible to develop an appropriate radioligand for imaging aggregated
33 α -synuclein in the brain for diagnosing, e.g., Parkinson's Disease. Access to a large animal model
34 with α -synuclein pathology would critically enable a more translationally appropriate evaluation of
35 novel radioligands.

36 We here establish a pig model with cerebral injections of α -synuclein preformed fibrils or brain
37 homogenate from postmortem human brain tissue from individuals with Alzheimer's disease (AD) or
38 dementia with Lewy body (DLB) into the pig's brain, using minimally invasive surgery and validated
39 against saline injections. In the absence of a suitable α -synuclein radioligand, we validated the model
40 with the unselective amyloid- β tracer [^{11}C]PIB, which has a high affinity for β -sheet structures in
41 aggregates. Gadolinium-enhanced MRI confirmed that the blood-brain barrier was intact. A few
42 hours post-injection, pigs were PET scanned with [^{11}C]PIB. Quantification was done with Logan
43 invasive graphical analysis and simplified reference tissue model 2 using the occipital cortex as a
44 reference region. After the scan, we retrieved the brains to confirm successful injection using
45 autoradiography and immunohistochemistry.

46 We found four times higher [^{11}C]PIB uptake in AD-homogenate-injected regions and two times
47 higher uptake in regions injected with α -synuclein-preformed-fibrils compared to saline. The
48 [^{11}C]PIB uptake was the same in non-injected (occipital cortex, cerebellum) and injected (DLB-
49 homogenate, saline) regions. With its large brain and ability to undergo repeated PET scans as well
50 as neurosurgical procedures, the pig provides a robust, cost-effective, and good translational model
51 for assessment of novel radioligands including, but not limited to, proteinopathies.

52 **1. Introduction**

53 Several neurodegenerative diseases share the pathology of misfolded proteins (Lázaro et al., 2019),
54 and positron emission tomography (PET) neuroimaging has become the primary imaging modality to
55 precisely diagnose and quantify such proteinopathies in patients. As of now, many suitable PET
56 radioligands are in use for neuroimaging of amyloid- β and tau (Mathis et al., 2017); these aggregated
57 proteins are seen in diseases such as Alzheimer's disease (AD), frontotemporal dementia, and
58 progressive supranuclear palsy. By contrast, attempts to develop a suitable radioligand for
59 neuroimaging of α -synuclein aggregates or inclusions, the hallmark of Parkinson's disease (PD),
60 multiple system atrophy, and dementia with Lewy bodies (DLB) have largely failed. A PET
61 radioligand targeting α -synuclein would critically assist in an earlier and more precise diagnosis,
62 which would be helpful for both the patient and clinician, and it could facilitate the development of
63 efficacious treatments.

64 In preclinical studies, some radioligands have shown promise for detection of α -synuclein aggregates
65 (Hooshyar Yousefi et al., 2019; Capotosti et al., 2020; Kaide et al., 2020; Kuebler et al., 2020), as
66 described in an extensive review on small molecules PET imaging of α -synuclein (Korat et al., 2021).
67 Nevertheless, because of lack of specificity or affinity to α -synuclein, no tracers have succeeded in
68 translating to humans. α -synuclein radioligands may also require higher selectivity and affinity due to
69 the lower aggregated protein pathology seen in α -synucleinopathies compared to the extensive
70 pathology seen in amyloid- β - and tauopathies (Braak and Braak, 2000; Lashuel et al., 2013).

71 Moreover, α -synuclein inclusions are mostly intracellularly located which may make them less
72 accessible to radioligands compared to extracellular amyloid- β aggregates.

73 A particular challenge has been an unmet need for an appropriate α -synuclein larger animal model.
74 Novel PET radioligands are often initially tested in rodents due to lower costs and availability of
75 disease models, then translated to higher species, including humans. Radioligands with low rodent
76 brain uptake risk to be discarded, although it is known that rodents have higher efflux transporter
77 activity than larger animals (Shalgunov et al., 2020). That said, access to an appropriate large animal
78 proteinopathy model would substantially advance the preclinical evaluation of novel radioligands for
79 neuroimaging, e.g., α -synuclein, and reduce the risk of failure due to poor translation from in vitro to
80 humans. The pig has become an attractive alternative to nonhuman primates, which are associated
81 with high costs, feasibility, repeatability, and not the least, the use is associated with ethical concerns
82 (Harding, 2017). Our porcine model can be the first step in screening of novel radioligands and is not
83 intended as a replacement of a realistic model of PD or MSA. We here propose the use of domestic
84 pigs with intracerebral protein injections as a suitable translational model for testing new
85 radioligands. We and others have previously made widespread use of the pig for this purpose (Parker
86 et al., 2012; Ettrup et al., 2013; Hansen et al., 2014; Winterdahl et al., 2014; Donovan et al., 2020)
87 because the pig has high predictive value for a successful translation to humans. In our pig model
88 here, we make intracerebral injections of either α -synuclein preformed fibrils, postmortem AD
89 human brain homogenate (containing amyloid- β and tau pathology), postmortem DLB human brain
90 homogenate with pure α -synuclein pathology, and control these injections with saline. Due to the
91 absence of an appropriate α -synuclein radioligand, we validate our model using [^{11}C]PIB, a non-
92 specific radioligand for amyloid- β (Klunk et al., 2004), which also has affinity to α -synuclein
93 preformed fibrils but not to Lewy bodies (Ye et al., 2008). To confirm the integrity of the blood-brain
94 barrier, we conducted gadolinium-enhanced MRI scans and to confirm brain pathology, we
95 characterized the injected brain regions with immunohistochemistry and autoradiography.

96 **2. Methods**

97 **2.1 Animals**

98 Seven female domestic pigs (crossbreed of Landrace \times Yorkshire \times Duroc) weighing on average
99 27 ± 1 kg (ranging from 25-31 kg) and approximately 10-11 weeks old were used in the present study
100 (Table 1). Animals were sourced from a local farm and prior to any experiments. They were
101 acclimatized for 7-9 days in an enriched environment. All animal procedures were performed
102 following the European Commission's Directive 2010/63/EU, approved by the Danish Council of
103 Animal Ethics (Journal no. 2017-15-0201-01375), and complied with the ARRIVE guidelines. The
104 overall design of the study is shown in Figure 1.

105 **2.2 Preparation and surgical procedure**

106 Pigs were injected in the medial prefrontal cortex (mPFC) with 25 μL of α -synuclein preformed
107 fibrils (6.4 mg/mL), AD human brain homogenate (10% homogenate in saline), DLB human brain
108 homogenate (10% homogenate in saline), or saline (Table 1). The details and characteristics of the
109 preformed fibrils and human brains are provided in the supplementary information (Supplementary
110 Table 1). The substrates were injected in both hemispheres, as detailed for each pig in Table 1, and in
111 accordance with our procedure for targeting mPFC (Jørgensen et al., 2017, 2018).

112 A detailed description of preparation, anesthesia and transport has previously been described by us
113 (Jørgensen et al., 2021). Briefly, anesthesia was induced by intramuscular (IM) injection of Zoletil

114 mixture and maintained with 10-15 mg/kg/h intravenous (IV) propofol infusion. Analgesia was
115 achieved with 5 µg/kg/h fentanyl IV infusion. Endotracheal intubation allowed for ventilation with
116 34% oxygen in normal air at 10-12 mL/kg. The left and right femoral arteries were catheterized with
117 Seldinger Arterial Catheter (Arrow International, Inc., Reading, PA, USA). The left and right
118 superficial mammary veins and ear veins were also catheterized. A urinary catheter was placed to
119 avoid discomfort and stress throughout the surgery and scanning schedule. The animals were
120 monitored for heart rate, blood pressure, peripheral oxygen saturation (SpO₂), end-tidal CO₂
121 (EtCO₂), blood glucose, and temperature throughout the scan, except while undergoing MRI scans.

122 Intracerebral injections were performed using a modified stereotactic approach: An in-house
123 instrument for modified stereotactic procedures containing a head-rest plate, a flexible arm attached
124 with a micro-manipulator (World Precision Instruments, Sarasota, FL, USA), and a micro-syringe
125 infusion pump system (World Precision Instruments, Sarasota, FL, USA) (Supplementary Figure 1).
126 The flexible arm allowed the micro-manipulator to be positioned and fixed relative to the target entry
127 point with a trajectory perpendicular to the skull, as illustrated in Supplementary Figure 1. For the
128 first two experiments (Fig 1 and 2), we used a prototype of the device with slightly less arm
129 flexibility and a different micro-manipulator brand and syringe-type, although the capacity, needle
130 size, length, and tip shape were the same. However, the prototype did provide injections comparable
131 to the remaining ones, as validated with immunohistochemistry.

132 After installation of local anesthesia, midline incision, and skull exposure, two burr holes were
133 placed bilaterally, 25 mm anterior and 8 mm lateral to bregma, followed by hemostasis and dura
134 puncture. We have previously validated this target point: 8, 25, 14 mm in the X, Y, Z coordinate
135 relative to bregma, to center on grey matter in the mPFC (Jørgensen et al., 2017, 2018). The syringe
136 and the needle were then positioned and fixed in a trajectory perpendicular to the skull and with the
137 needle tip adjusted to the skull entry point. The syringes (250 µL SGE Gas-tight Teflon Luer Lock
138 Syringes (World Precision Instruments, Sarasota, FL, USA) [different syringes for the different
139 injectates]) were attached with SilFlex tubing (World Precision Instruments, Sarasota, FL, USA),
140 NanoFil Injection Holder (World Precision Instruments, Sarasota, FL, USA) and 28 G Hamilton Kel-
141 F hub blunt tip needle (Hamilton Central Europe, Giarmata, Romania). The SilFlex tubing and
142 NanoFil Injection Holder were removed during homogenate injection because of the viscous content.

143 Using the micromanipulator, the needle was slowly advanced to the mPFC target point
144 (perpendicular to the skull). The injection was performed over two steps with 10 µL, and 15 µL
145 injected 1 mm apart (centered at the mPFC target point). The infusion was delivered at 450 nL/min
146 using the micro-syringe infusion pump followed by a 7-minute pause before a slow withdrawal of the
147 needle to avoid backflow. After the procedure, both burr holes were packed with an absorbable
148 hemostatic gelatin sponge (Curaspon[®], CuraMedical BV, Assendelft, Netherlands), and the incision
149 was sutured shut. The animals were then transported to the scanner facilities and connected to the
150 respirator.

151 **2.3 PET scanning protocol and radiochemistry**

152 All pigs were PET-scanned with a Siemens high-resolution research tomograph (HRRT) scanner
153 (CPS Innovations/Siemens, Malvern, PA, USA). [¹¹C]PIB was prepared at the Copenhagen
154 University Hospital, Rigshospitalet, as per routine clinical preparation. The complete method of
155 preparation is explained in the supplementary information (Supplementary Figure 2). Data
156 acquisition lasted 90 min after bolus injection (over ~20 s) of [¹¹C]PIB through one of the superficial

157 mammary veins (IV). The injected dose was 448 ± 41 MBq, while injected mass was 4.82 ± 4.3 μ g
158 (mean \pm SD).

159 **2.4 Blood sampling and HPLC analyses**

160 Manual arterial blood samples were drawn at 2.5, 5, 10, 20, 30, 40, 50, 70, and 90 min after injection,
161 while an ABSS autosampler (Allogg Technology, Strängnäs, Sweden) continuously measured arterial
162 whole blood radioactivity during the first 20 min. The manual blood samples were measured for total
163 radioactivity in whole blood and plasma using an automated gamma counter (Cobra 5003; Packard
164 Instruments, Downers Grove, CT, USA) cross-calibrated against the HRRT. Radiolabeled parent and
165 metabolite fractions were determined in plasma using an automatic column-switching radio-high
166 performance liquid chromatography (HPLC) as previously described (Gillings, 2009), equipped with
167 an extraction column Shim-pack MAYI-ODS (50 μ m, 30 x 4.6 mm; Shimadzu Corporation, Kyoto,
168 Japan) eluting with 50 mM HNa_2PO_4 pH 7.0 and 2% isopropanol (v/v) at a flow rate of 3 mL/min,
169 and an Onyx Monolithic C18 analytical column (50 x 4.6 mm, Phenomenex, Torrance, CA, USA)
170 eluting with 26% acetonitrile and 74% 100 mM HNa_2PO_4 pH 7.0 (v/v) at a flow rate of 3 mL/min.
171 Before analysis by radio-HPLC, the plasma samples were filtered through a syringe filter (Whatman
172 GD/X 13 mm, PVDF membrane, 0.45 μ m pore size; Frisette ApS, Knebel, Denmark). Plasma was
173 diluted 1:1 with the extraction buffer, and up to 4 mL of plasma sample was used. The eluent from
174 the HPLC system was passed through the radiochemical detector (Posi-RAM Model 4; LabLogic,
175 Sheffield, UK) for online detection of radioactive parent and metabolites. Eluents from the HPLC
176 were collected with a fraction collector (Foxy Jr FC144; Teledyne, Thousand Oaks, CA, USA), and
177 fractions were counted offline in a gamma well counter (2480 Wizard2 Automatic Gamma Counter,
178 PerkinElmer, Turku, Finland). The parent fraction was determined as the percentage of the
179 radioactivity of the parent to the total radioactivity collected. Examples of radio-HPLC
180 chromatograms from a pig are shown in Supplementary Figure 3.
181 The parent fraction curve from the last three HPLC scans could not be estimated because of a technic
182 al problem with the HPLC. For the final three scans, we used a population-
183 based parent fraction curve derived from the first four scans (Table 1, Supplementary Figure 6).

184

185 **2.5 Gadolinium-contrast MRI scanning protocol**

186 The integrity of the BBB post-intracerebral injection was assessed by determining the %-difference
187 ΔT_1 -map of the pre-gadolinium and the post-gadolinium scans. The MRI data were acquired on a 3T
188 Prisma scanner (Siemens, Erlangen, Germany) using a human 64-channel head coil (active coil
189 elements were HC3-7 and NC1). Three pigs were scanned in the MRI scanner as previously
190 described by us (Jørgensen et al., 2021). The pigs underwent two T1-map scans: pre-and post-
191 gadolinium contrast injection. The protocol for T1-weighted 3D magnetization-prepared rapid
192 gradient-echo (MP-RAGE) MRI was: frequency direction = anterior to posterior; dimension= 144 x
193 256 x 256; slice thickness = 0.9 mm; repetition time = 2000 ms; echo time = 2.58 ms; inversion time
194 = 972 ms; flip angle = 8°; base resolution = 256 x 256, and acquisition time = 192 s. After the pre-
195 gadolinium T1-map scan, pigs received gadolinium IV (0.1 mmol/kg, Gadovist® [gadobutrol], Bayer
196 A/S, Copenhagen, Denmark) through a superficial mammary vein and were rescanned 5 mins later
197 with another T1-map scan. Data were processed using a custom code in MATLAB 9.5.0 (R2018b)
198 (The MathWorks Inc., Natick, MA, USA). DICOM files were converted to NIfTI-1 using dcm2niix
199 (Li et al., 2016). The post-gadolinium T1-map was co-registered and resliced to the pre-gadolinium
200 T1-map using SPM12. A %-difference map (ΔT_1 -map) was created from the resliced post-

201 gadolinium and pre-gadolinium T1-maps (Equation 1). Three regions in the ΔT_1 -map were
 202 measured: left injection site, right injection site, and occipital cortex

$$203 \quad \Delta T_1 \text{ map} = \left(\frac{\text{Post_gadolinium } T_1 \text{ map} - \text{Pre_gadolinium } T_1 \text{ map}}{\text{Pre_gadolinium } T_1 \text{ map}} \right) \times 100 \text{ (Equation 1)}$$

204 2.6 [³H]PIB autoradiography

205 At the end of the scanning, the animals were euthanized by IV injection of 20 mL
 206 pentobarbital/lidocaine. After euthanasia, the brains were removed, snap-frozen with powdered dry-
 207 ice, and stored at -80°C until further use. 20 μm coronal cryosections were sectioned on a cryostat
 208 (Thermo Scientific/Epredia™ CryoStar™ NX70 Cryostat, Shandon Diagnostics Limited, Runcorn,
 209 UK) and mounted on Superfrost Plus™ adhesion microscope slides (Thermo Fisher Scientific,
 210 Waltham, MA, USA). Sections were stored at -80°C for the remaining period of the study.

211 We performed [³H]PIB (Novandi Chemistry AB, Södertälje, Sweden, Molar activity: 78 Ci/mmol)
 212 autoradiography to calculate the total available binding sites (B_{max}) and equilibrium dissociation
 213 constant (K_D) in the injected pig brain, and compared this to the B_{max} and K_D of human brain regions
 214 that were used to create the homogenates. We performed saturation assays using increasing
 215 concentrations of [³H]PIB for total binding and [³H]PIB + thioflavin S (100 μM) for non-specific
 216 binding on AD-homogenate-injected pig brain slices (n=1, 0 to 5 nM of [³H]PIB), α -synuclein-
 217 preformed-fibril-injected pig brain slices (n=1, 0 to 40 nM of [³H]PIB), and AD post-mortem human
 218 brain slices (n = 2 x 2 regions, 0 to 5 nM of [³H]PIB). Since there was no specific binding in DLB-
 219 homogenate-injected pig slices or DLB human brain slices, we could not perform saturation assays
 220 on these sections. Human brain slices were prepared in the same fashion as pig brain slices, including
 221 section thickness and storage. Detailed procedure for autoradiography is available in the
 222 supplementary information.

223 The data were analyzed using GraphPad Prism (v. 9.2.0; GraphPad Software, San Diego, CA, USA).
 224 Non-linear regression analysis (Function: One site - total and non-specific binding) was used to
 225 calculate B_{max} and K_D values for all three assays. The fitting method used was the least squared
 226 regression with no weighting. In vitro binding potential (BP) was calculated with Equation 2.

227

$$228 \quad BP = \frac{B_{\text{max}}}{K_D} \quad \text{(Equation 2)}$$

229 2.7 PET data reconstruction and preprocessing

230 PET list-mode emission files were reconstructed using the OP-3D-OSEM algorithm, including
 231 modeling the point-spread function, with 16 subsets, ten iterations, and standard corrections (Sureau
 232 et al., 2008). During reconstruction, attenuation correction was performed using the MAP-TR μ -map
 233 (Keller et al., 2013). Emission data were binned into time frames of increasing lengths: 6 \times 10 s, 6 \times
 234 20 s, 4 \times 30 s, 9 \times 60 s, 2 \times 180 s, 8 \times 300 s, 3 \times 600 s. Each time frame consisted of 207 planes of
 235 256 \times 256 voxels of 1.22 \times 1.22 \times 1.22 mm in size.

236 Brain parcellation was done with our previously published automatic PET-MR pig brain atlas method
 237 (Villadsen et al., 2017). The neocortex, occipital cortex, and cerebellum non-vermis (henceforth
 238 denoted as the cerebellum) were extracted from the Saikali atlas (Saikali et al., 2010) for the present
 239 study. Two additional regions for the injection site were hand-drawn on the atlas from an

240 approximate injection site that was initially characterized around the site of needle penetration as
241 visualized by the MRI scans and postmortem extracted brain. This was also further confirmed and
242 optimized by positive immunohistochemistry slices from the region (Supplementary Figures 4 and
243 5). Regions approximately $0.32\text{-}0.35\text{ cm}^3$ (~ 250 voxels) in size were placed symmetrically in the left
244 and right hemispheres. This region is slightly larger than the injection site itself, but this gives leeway
245 for any potential mechanical error during the stereotactic operation. Wherever possible (not possible
246 in, e.g., saline-injected regions), the automatic region was visually inspected with late-scan frames
247 averaged.

248 Regional radioactivity concentration (kBq/mL) was normalized to injected dose (MBq) and corrected
249 for the animal weight (kg) to provide standardized uptake values (SUV, g/mL) used to make average
250 plots as in Figure 2. PMOD 3.7 (PMOD Technologies, Zürich, Switzerland) was used to visualize
251 and create the representative PET and MR images.

252 **2.8 Kinetic modeling**

253 Kinetic modeling was performed using *kinfitr* (v. 0.6.0) (Matheson, 2019; Tjerkaski et al., 2020) in R
254 (v. 4.0.2; "Taking Off Again," R core team, Vienna, Austria). The Logan Graphical Analysis was
255 applied to estimate the total volume of distribution (V_T) values (Logan et al., 1990), using a
256 metabolite corrected input function derived from radioactivity measurements of arterial blood
257 samples. Reference tissue modeling was performed with the simplified reference tissue model 2
258 (SRTM2), with an average k_2' , to calculate non-displaceable binding potential (BP_{ND}) using the
259 occipital cortex as the reference region (Yaqub et al., 2008). For more details on the kinetic
260 modeling, see supplementary information.

261 **2.9 Statistical analyses**

262 Graph-Pad Prism (v. 9.2.0; GraphPad Software, San Diego, CA, USA) was used for data
263 visualization and statistical analysis. All data are presented as mean values \pm standard deviation. The
264 difference in PET outcomes (Logan V_T and SRTM2 BP_{ND}) between the injected regions and
265 reference tissues was calculated using the non-parametric Kruskal–Wallis one-way analysis of
266 variance (ANOVA). For assessment of change in gadolinium-contrast MR, we used the Friedman
267 non-parametric ANOVA test with paired testing. Post-hoc ANOVA tests were corrected for multiple
268 comparisons by Dunn's multiple comparison test (Dunn, 1964).

269 **3 Results**

270 **3.1 [^{11}C]PIB time-activity curves**

271 After [^{11}C]PIB injection, we observed high brain uptake and rapid tracer wash-out. The blood and
272 brain kinetics of [^{11}C]PIB were very fast, with less than 10% of the parent radioligand remaining in
273 plasma after 2.5 mins (Figure 2 and Supplementary Figure 6). We found higher radioactivity
274 retention in the AD-homogenate- and α -synuclein-preformed-fibrils injected region (Figure 2A).
275 Compared to the cerebellum and the occipital cortex, almost no retention was seen in DLB-
276 homogenate and saline-injected regions (Figure 2A and B).

277 **3.2 Kinetic modeling of [^{11}C]PIB**

278 [^{11}C]PIB binding parameters from Logan graphical analysis and SRTM2 are summarized in Table 2.
279 We found 4-fold higher V_T values in the AD-homogenate injected region compared to the occipital

280 cortex ($p = 0.006$) and 2-fold higher V_T values in the α -synuclein-preformed fibrils region ($p = 0.034$)
281 (Figure 3A). We found no difference between the saline- and DLB-injected regions.

282 Compared to the cerebellum, the average BP_{ND} of 2.34 was higher ($p = 0.004$) in the AD-homogenate
283 injected region, and the average BP_{ND} of 0.65 was also higher ($p=0.016$) in the α -synuclein-
284 preformed-fibrils injected region. There was no difference in BP_{ND} in the saline- or DLB-homogenate
285 injected regions compared to the cerebellum (Figure 3B).

286 3.3 Characterization of the injection site

287 Using our minimally invasive method, we successfully injected all animals in the same symmetrical
288 brain region. Prefrontal cortical immunostaining (α -synuclein and amyloid- β) and thioflavin S
289 staining at the injection site confirmed the presence of α -synuclein preformed fibrils, AD
290 homogenates, and DLB homogenates, respectively (Supplementary information). To evaluate the
291 appropriateness of our pig model, we compared B_{max} and K_D in both the pig and human brains. This
292 was done for the α -synuclein-preformed fibrils and AD-homogenate injected pig brain regions as
293 well as for the AD postmortem human brain slices using [3H]PIB autoradiography saturation assays
294 (Figure 4 and Table 3). We determined B_{max} to be 477.2 fmol/mg TE and K_D of 12.07 nM in the α -
295 synuclein-preformed fibrils region in pig brain slices ($n=1$). We found a higher B_{max} on the AD
296 postmortem human brain slices (366.7 fmol/mg TE, $n=3$) compared to AD-homogenate-injected pig
297 brain slices (233.4 fmol/mg TE, $n=1$). However, the K_D is similar at 2.46 nM in AD-homogenate-
298 injected pig brain slices versus 2.54 nM in AD postmortem human brain slices. We also found 2.4
299 times higher binding potential in AD-homogenate-injected pig brain slices compared to α -synuclein-
300 preformed fibrils-injected pig brain slices.

301 3.4 Blood-brain barrier integrity

302 We found no statistically significant difference in the T_1 -maps before and after gadolinium injection.
303 Still, in cases, with local hemorrhage near the site of needle penetration (Figure 5A, red ROI), some
304 regions had higher gadolinium uptake than the occipital cortex. Also, the amplitude of the [^{11}C]PIB
305 time-activity curves (Figure 2B and Figure 3) did not suggest that the injected regions had higher
306 uptake compared to non-injured brain tissue. Finally, the uptake in saline-injected regions did not
307 differ from that of the occipital cortex, supporting that the injection itself does not hamper the
308 integrity of the BBB.

309 4 Discussion

310 We here describe a large animal model for testing radioligands against specific targets, such as
311 abnormally configured protein structures, and the study is built on amyloid- β and its radiotracer
312 [^{11}C]PIB (Lockhart et al., 2007; Hellström-Lindahl et al., 2014). Such a large animal model is
313 valuable in addition to rodent studies because of the pig's larger and gyrated brain. We show that
314 when the pig brain is injected with synthetic proteins or brain homogenates, the blood-brain barrier
315 remains intact, the injected region's protein levels are comparable to the characteristics in the human
316 brain, and the *in vivo* binding characteristics allow for realistic quantification.

317 We validated our acute model by injecting α -synuclein preformed fibrils, AD human brain
318 homogenate, or DLB human brain homogenate in pigs' mPFC and visualized these regions *in vivo*
319 using [^{11}C]PIB PET. [^{11}C]PIB uptake in the injection site was used as a proof of concept for this
320 model. We found high regional [^{11}C]PIB uptake in the AD homogenate and moderate uptake in α -
321 synuclein preformed fibril injected regions. We also confirmed the absence of specific uptake or

322 binding of the radioligand in DLB homogenate injected or saline injected regions. Collectively, these
323 results suggest that the model provides a tool for preclinical characterization of novel radioligands,
324 including collecting information about the pharmacokinetics and affinities of the brain pathology.

325 [¹¹C]PIB is a well-characterized radioligand for amyloid- β plaques (Price et al., 2005; Peretti et al.,
326 2019), routinely used to quantify amyloid- β plaques and for differential diagnosis and staging in
327 neurodegenerative diseases. Although [¹¹C]PIB has the highest affinity to amyloid plaques, it also
328 displays affinity towards other β -sheet structures like tau and α -synuclein. We chose to use [¹¹C]PIB
329 as proof of concept since it shows affinity to α -synuclein preformed fibrils (Fodero-Tavoletti et al.,
330 2007; Ye et al., 2008) and AD brain homogenates (Klunk et al., 2004; Lockhart et al., 2007). By
331 contrast, and as a negative control, [¹¹C]PIB has no affinity to Lewy bodies commonly seen in PD or
332 DLB histology (Fodero-Tavoletti et al., 2007; Ye et al., 2008), which we also confirmed both in vivo
333 and in vitro.

334 To the best of our knowledge, this is the first time [¹¹C]PIB has been tested in pigs with full arterial
335 blood sampling and kinetic modeling. Our laboratory and Aarhus University (Alstrup et al., 2018)
336 have previously performed [¹¹C]PIB scans in pigs (unpublished), where the data was quantified using
337 reference tissue modeling. Invasive kinetic modeling with [¹¹C]PIB was challenging since the 1-
338 tissue compartment model yielded a poor fit, while the 2-tissue compartment model failed, most
339 likely because of the very fast metabolism of the parent compound. Instead, we used the graphical
340 method, i.e., Logan Graphical analysis. We also used the SRTM2 with the occipital cortex as a
341 reference region (Yaqub et al., 2008; Tolboom et al., 2009). In humans, SRTM2 modeling of
342 [¹¹C]PIB is commonly used with the cerebellum as the reference region, but when that was attempted
343 in the pig brain, we got negative BP_{ND} values in DLB injected, saline injected and occipital cortex.
344 Hence, we used the occipital cortex instead as a reference region.

345 Postmortem human brain homogenates from patients with relevant neurodegenerative disorders were
346 introduced to “humanize” the pig model. We evaluated that the B_{max} in the injected pig brain was
347 realistically representing what is seen in the individuals with AD who served as the donors of tissue
348 homogenate. The observation that we found slightly lower B_{max} values in pig brain slices representing
349 the AD homogenate injected regions compared to human brain slices from AD patients confirms the
350 suitability of our pig model. We also performed a [³H]PIB saturation assay on the α -synuclein
351 preformed fibril injected pig brain slices. Compared to the AD homogenate slices, the α -synuclein
352 preformed fibril injected pig brain slices had a 2.4-times lower BP , as we also found in the in vivo
353 PET studies. It can be argued that injection of human brain homogenates provides a more realistic
354 model of the human AD brain compared to synthetic protein injections with, e.g., preformed fibrils
355 but in any instance, the synthesized protein must be thoroughly evaluated in vitro before using the
356 model. In the current study, we used the highest available concentration of all the injectates for proof
357 of concept. As an added value of the model in future studies, the concentration of the injectates can
358 be varied to confirm the expected dose-dependent effect of radioligand binding.

359 Whereas the strategy of intracerebrally injecting α -synuclein (and amyloid- β) and scanning animals
360 immediately after previously has been used in rodents (Verdurand et al., 2018; Kuebler et al., 2020),
361 this is the first study to involve larger animals. A few other large animal models of α -synuclein
362 pathology have been published: the viral-vector model in minipigs (Lillethorup et al., 2018) and
363 nonhuman primates (Kirik et al., 2002; Yang et al., 2015; Koprach et al., 2016), and α -synuclein
364 protein or homogenate inoculation models also in nonhuman primates (Recasens et al., 2014;
365 Shimozawa et al., 2017). The disadvantages of these models are that they are challenging to create,
366 expensive to maintain and it often takes months to develop pathology. National regulations on ethical

367 considerations can also restrict access to experimental studies in nonhuman primates. By contrast,
368 our model combines surgery and scanning on the same day, using non-survival pigs and a systematic
369 scanning technique for in vivo radioligand characterization (Ettrup et al., 2013; Andersen et al., 2015;
370 Jørgensen et al., 2018). Studies in pigs are cheaper than other large animals as the use of pigs is
371 considered less ethically challenging.

372 Conventional strategies for intracerebral injection involve an MR-guided stereotactic approach (Glud
373 et al., 2011). This requires MR-guided calculation of the stereotactic coordinates prior to surgery for
374 the injection, which is a tedious and time-consuming procedure. In the present study, we employed a
375 minimally invasive approach with a modified stereotactic instrument and a previously validated
376 target point in the grey matter of mPFC (Jørgensen et al., 2017, 2018), which made the procedure
377 much faster; the process including injection of the experimental substrates in mPFC was completed
378 within 3-4 hours. The concern whether the blood-brain barrier would retain its integrity right after the
379 intracerebral injection was addressed by the finding that the gadolinium-enhanced post-injection MR
380 assured no blood-brain barrier leakage, except in the cases where the needle had induced minor
381 traumatic hemorrhage – this was clearly outside the region with pathology. This observation was
382 further supported by the saline-injected region having a radioligand uptake similar to the reference
383 regions (Table 2).

384 Some limitations with the model presented should be mentioned. Although this model can be used
385 for survival studies, we have only validated bilateral injection sites in the medial prefrontal cortex. A
386 thorough in vitro evaluation of the proteins is necessary before commencing in vivo experiments,
387 preferably including autoradiography with the radioligand to be evaluated. The latter includes
388 identification of K_D and B_{max} to establish the in vitro binding potential, which should reflect the PET
389 signal. It is difficult to ascertain to which extent the injected proteins are localized only
390 extracellularly; in human pathology, Lewy bodies and tau is mainly intracellularly localized. Given
391 that radioligands must be able to penetrate the blood-brain barrier, it is generally assumed, however,
392 that they also easily penetrate the brain cells. Further, the injection site constitutes a relatively small
393 volume of interest which inherently is prone to noisy time-activity curves or to partial volume effect.
394 Further, bleeding from dura or the cerebral tissue resulting from the injection could potentially
395 impact the PET signal. We saw confined hematomas in 1 out of 5 injections, but this was clearly
396 recognized and when taken into account, it did not prevent a proper analysis. For future use of the
397 model, we recommend using hybrid PET/CT or PET/MR so that eventual hemorrhage can be
398 accounted.

399 5 Conclusions

400 We here provide a novel large model for assessment of novel radioligands targeting the brain and
401 show its suitability for testing radioligands for brain regional proteinopathies. The large pig brain
402 makes it suitable for neurosurgical procedures and the pigs can undergo multiple PET scans and
403 frequent blood sampling. The described pig model represents a robust and efficient set-up with few
404 limitations. The availability of a large animal α -synuclein model is instrumental for testing novel
405 radioligands, not only for α -synuclein neuroimaging but also for other target proteins where the target
406 is not naturally occurring in the brain, or where the presence can be artificially enhanced locally in
407 the brain.

408

409 6 Acknowledgments



410

411 This project has received funding from the European Union's Horizon 2020 research and innovation
 412 program under the Marie Skłodowska-Curie grant agreement No. 813528. This project also received
 413 funding from Parkinson foreningen, Denmark (R16-A247). Pontus Plavén Sigray was supported by
 414 the Lundbeck Foundation (R303-2018-3263). Natalie Beschorner was supported by the Lundbeck
 415 Foundation (R322-2019-2744). We would like to express our sincere gratitude to Patrick MacDonald
 416 Fisher for his technical assistance in MRI scanning protocols and data processing. We want to thank
 417 Lundbeck A/S, Valby, Denmark, for providing the α -synuclein preformed fibrils. This research
 418 project received human brain tissue from the Neuropathology Core of the Emory Center for
 419 Neurodegenerative Disease; we are grateful for their support. We would sincerely like to thank the
 420 staff and veterinarians at EMED, Panum, København University.

421 7 Author Contributions

422 NRR, LMJ, GMK: conceptualization and design. NRR, LMJ: surgical setup. NRR, AN, CAM, NB,
 423 EEB, SL: experimental studies. NRR, AN, CS, SL, PPS, MJ: analysis and software. NRR, GMK:
 424 resources. NR, PPS, LMJ, GMK: data curation. NRR: preparation of manuscript draft including
 425 figures. NRR, AN, CAM, NB, EEB, MJ, SL, MPP, CS, PPS, LMJ, GMK: manuscript review and
 426 editing. MP, CS, PPS, LMJ, GMK: supervision. NRR, MP, GMK: funding acquisition. All authors
 427 have read and agreed to the published version of the manuscript.

428 8 Conflict of Interest

429 Lundbeck A/S, Denmark provided the α -synuclein preformed fibrils as part of the European Union's
 430 Horizon 2020 research and innovation program under the Marie Skłodowska-Curie grant agreement
 431 No. 813528. However, they had no other financial interests in the project. GMK received honoraria
 432 as a speaker and consultant for Sage Pharmaceuticals/Biogen and Sanos A/S. All other authors
 433 declare no conflict of interest.

434 9 Data availability statement

435 All data, including MATLAB and R scripts, is available at a GitHub repository
 436 (https://github.com/nakulrraval/Protien_inj_pig_model_PIB). All other requests are directed to this
 437 article's corresponding or first author.

438 10 References:

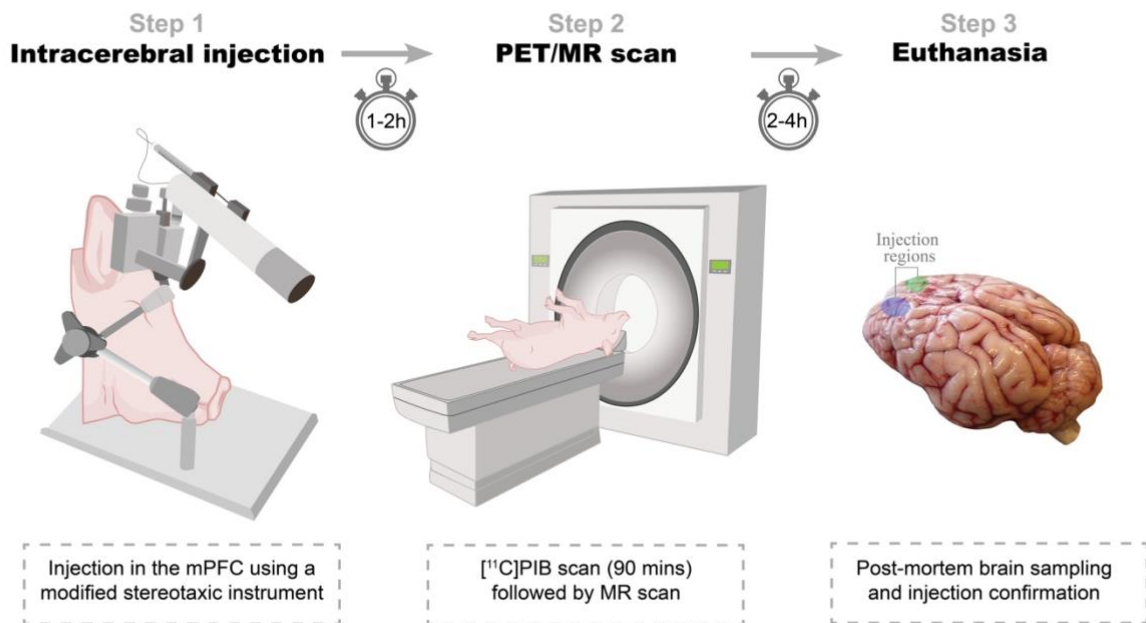
- 439 Alstrup, A. K. O., Munk, O. L., and Landau, A. M. (2018). PET radioligand injection for pig
 440 neuroimaging. *of Laboratory Animal ...* 44. Available at:
 441 <http://sjlas.org/index.php/SJLAS/article/view/509>.
- 442 Braak, H., and Braak, E. (2000). Pathoanatomy of Parkinson's disease. *J. Neurol.* 247 Suppl 2, II3–
 443 10. doi:10.1007/PL00007758.
- 444 Capotosti, F., Vokali, E., Molette, J., Tsika, E., Ravache, M., Juergens, T., et al. (2020). Developing a
 445 novel alpha-synuclein positron emission tomography (PET) tracer for the diagnosis of
 446 synucleinopathies. *Alzheimers. Dement.* 16. doi:10.1002/alz.043249.

- 447 Donovan, L. L., Magnussen, J. H., Dyssegaard, A., Lehel, S., Hooker, J. M., Knudsen, G. M., et al.
448 (2020). Imaging HDACs In Vivo: Cross-Validation of the [11 C]Martinostat Radioligand in the
449 Pig Brain. *Mol. Imaging Biol.* 22, 569–577. doi:10.1007/s11307-019-01403-9.
- 450 Dunn, O. J. (1964). Multiple Comparisons Using Rank Sums. *Technometrics* 6, 241–252.
451 doi:10.1080/00401706.1964.10490181.
- 452 Ettrup, A., Holm, S., Hansen, M., Wasim, M., Santini, M. A., Palner, M., et al. (2013). Preclinical
453 safety assessment of the 5-HT_{2A} receptor agonist PET radioligand [11C]cimbi-36. *Mol.*
454 *Imaging Biol.* 15, 376–383. doi:10.1007/s11307-012-0609-4.
- 455 Fodero-Tavoletti, M. T., Smith, D. P., McLean, C. A., Adlard, P. A., Barnham, K. J., Foster, L. E., et
456 al. (2007). In vitro characterization of Pittsburgh compound-B binding to Lewy bodies. *J.*
457 *Neurosci.* 27, 10365–10371. doi:10.1523/JNEUROSCI.0630-07.2007.
- 458 Gillings, N. (2009). A restricted access material for rapid analysis of [(11)C]-labeled
459 radiopharmaceuticals and their metabolites in plasma. *Nucl. Med. Biol.* 36, 961–965.
460 doi:10.1016/j.nucmedbio.2009.07.004.
- 461 Glud, A. N., Hedegaard, C., Nielsen, M. S., Sørensen, J. C., Bendixen, C., Jensen, P. H., et al.
462 (2011). Direct MRI-guided stereotaxic viral mediated gene transfer of alpha-synuclein in the
463 Göttingen minipig CNS. *Acta Neurobiol. Exp.* 71, 508–518. Available at:
464 <https://www.ncbi.nlm.nih.gov/pubmed/22237496>.
- 465 Hansen, H. D., Herth, M. M., Ettrup, A., Andersen, V. L., Lehel, S., Dyssegaard, A., et al. (2014).
466 Radiosynthesis and in vivo evaluation of novel radioligands for pet imaging of cerebral 5-HT
467 receptors. *J. Nucl. Med.* 55, 640–646. doi:10.2967/jnumed.113.128983.
- 468 Harding, J. D. (2017). Nonhuman Primates and Translational Research: Progress, Opportunities, and
469 Challenges. *ILAR J.* 58, 141–150. doi:10.1093/ilar/ilx033.
- 470 Hellström-Lindahl, E., Westermark, P., Antoni, G., and Estrada, S. (2014). In vitro binding of
471 [³H]PIB to human amyloid deposits of different types. *Amyloid* 21, 21–27.
472 doi:10.3109/13506129.2013.860895.
- 473 Hooshyar Yousefi, B., Shi, K., Arzberger, T., Wester, H. J., Schwaiger, M., Yakushev, I., et al.
474 (2019). Translational study of a novel alpha-synuclein PET tracer designed for first-in-human
475 investigating. in *NuklearMedizin 2019* (Georg Thieme Verlag KG), L25. doi:10.1055/s-0039-
476 1683494.
- 477 Jørgensen, L. M., Baandrup, A. O., Mandeville, J., Glud, A. N., Sørensen, J. C. H., Weikop, P., et al.
478 (2021). An fMRI-compatible system for targeted electrical stimulation. *Research Square*.
479 doi:10.21203/rs.3.rs-313183/v1.
- 480 Jørgensen, L. M., Weikop, P., Svarer, C., Feng, L., Keller, S. H., and Knudsen, G. M. (2018).
481 Cerebral serotonin release correlates with [11C]AZ10419369 PET measures of 5-HT_{1B} receptor
482 binding in the pig brain. *J. Cereb. Blood Flow Metab.* 38, 1243–1252.
483 doi:10.1177/0271678X17719390.
- 484 Jørgensen, L. M., Weikop, P., Villadsen, J., Visnapuu, T., Ettrup, A., Hansen, H. D., et al. (2017).
485 Cerebral 5-HT release correlates with [11C]Cimbi36 PET measures of 5-HT_{2A} receptor

- 486 occupancy in the pig brain. *J. Cereb. Blood Flow Metab.* 37, 425–434.
487 doi:10.1177/0271678X16629483.
- 488 Kaide, S., Watanabe, H., Shimizu, Y., Iikuni, S., Nakamoto, Y., Hasegawa, M., et al. (2020).
489 Identification and Evaluation of Bisquinoline Scaffold as a New Candidate for α -Synuclein-PET
490 imaging. *ACS Chem. Neurosci.* 11, 4254–4261. doi:10.1021/acchemneuro.0c00523.
- 491 Keller, S. H., Svarer, C., and Sibomana, M. (2013). Attenuation correction for the HRRT PET-
492 scanner using transmission scatter correction and total variation regularization. *IEEE Trans.*
493 *Med. Imaging* 32, 1611–1621. doi:10.1109/TMI.2013.2261313.
- 494 Kirik, D., Rosenblad, C., Burger, C., Lundberg, C., Johansen, T. E., Muzyczka, N., et al. (2002).
495 Parkinson-Like Neurodegeneration Induced by Targeted Overexpression of α -Synuclein in the
496 Nigrostriatal System. *Journal of Neuroscience* 22, 2780–2791. doi:10.1523/JNEUROSCI.22-07-
497 02780.2002.
- 498 Klunk, W. E., Engler, H., Nordberg, A., Wang, Y., Blomqvist, G., Holt, D. P., et al. (2004). Imaging
499 brain amyloid in Alzheimer's disease with Pittsburgh Compound-B. *Ann. Neurol.* 55, 306–319.
500 doi:10.1002/ana.20009.
- 501 Koprach, J. B., Johnston, T. H., Reyes, G., and Omana, V. (2016). Towards a nonhuman primate
502 model of alpha-synucleinopathy for development of therapeutics for Parkinson's disease:
503 optimization of AAV1/2 delivery *PLoS*. Available at:
504 <https://journals.plos.org/plosone/article?id=10.1371/journal.pone.0167235>.
- 505 Korat, Š., Bidesi, N. S. R., Bonanno, F., Di Nanni, A., Hoàng, A. N. N., Herfert, K., et al. (2021).
506 Alpha-Synuclein PET Tracer Development—An Overview about Current Efforts.
507 *Pharmaceuticals* 14, 847. doi:10.3390/ph14090847.
- 508 Kuebler, L., Buss, S., Leonov, A., Ryazanov, S., Schmidt, F., Maurer, A., et al. (2020).
509 [11C]MODAG-001—towards a PET tracer targeting α -synuclein aggregates. *Eur. J. Nucl. Med.*
510 *Mol. Imaging*. doi:10.1007/s00259-020-05133-x.
- 511 Lashuel, H. A., Overk, C. R., Oueslati, A., and Masliah, E. (2013). The many faces of α -synuclein:
512 from structure and toxicity to therapeutic target. *Nat. Rev. Neurosci.* 14, 38–48.
513 doi:10.1038/nrn3406.
- 514 Lázaro, D. F., Bellucci, A., Brundin, P., and Outeiro, T. F. (2019). Editorial: Protein Misfolding and
515 Spreading Pathology in Neurodegenerative Diseases. *Front. Mol. Neurosci.* 12, 312.
516 doi:10.3389/fnmol.2019.00312.
- 517 Lillethorup, T. P., Glud, A. N., Landeck, N., Alstrup, A. K. O., Jakobsen, S., Vang, K., et al. (2018).
518 In vivo quantification of glial activation in minipigs overexpressing human α -synuclein. *Synapse*
519 72, e22060. doi:10.1002/syn.22060.
- 520 Li, X., Morgan, P. S., Ashburner, J., Smith, J., and Rorden, C. (2016). The first step for
521 neuroimaging data analysis: DICOM to NIfTI conversion. *J. Neurosci. Methods* 264, 47–56.
522 doi:10.1016/j.jneumeth.2016.03.001.
- 523 Lockhart, A., Lamb, J. R., Osredkar, T., Sue, L. I., Joyce, J. N., Ye, L., et al. (2007). PIB is a non-
524 specific imaging marker of amyloid-beta (A β) peptide-related cerebral amyloidosis. *Brain*

- 525 130, 2607–2615. doi:10.1093/brain/awm191.
- 526 Logan, J., Fowler, J. S., Volkow, N. D., Wolf, A. P., Dewey, S. L., Schlyer, D. J., et al. (1990).
527 Graphical analysis of reversible radioligand binding from time-activity measurements applied to
528 [N-11C-methyl]-(-)-cocaine PET studies in human subjects. *J. Cereb. Blood Flow Metab.* 10,
529 740–747. doi:10.1038/jcbfm.1990.127.
- 530 Makky, A., Bousset, L., Polesel-Maris, J., and Melki, R. (2016). Nanomechanical properties of
531 distinct fibrillar polymorphs of the protein α -synuclein. *Sci. Rep.* 6, 37970.
532 doi:10.1038/srep37970.
- 533 Matheson, G. J. (2019). kinfitr: Reproducible PET Pharmacokinetic Modelling in R. *bioRxiv*,
534 755751. doi:10.1101/755751.
- 535 Mathis, C. A., Lopresti, B. J., Ikonovic, M. D., and Klunk, W. E. (2017). Small-molecule PET
536 Tracers for Imaging Proteinopathies. *Semin. Nucl. Med.* 47, 553–575.
537 doi:10.1053/j.semnuclmed.2017.06.003.
- 538 Parker, C. A., Gunn, R. N., Rabiner, E. A., Slifstein, M., Comley, R., Salinas, C., et al. (2012).
539 Radiosynthesis and characterization of 11C-GSK215083 as a PET radioligand for the 5-HT6
540 receptor. *J. Nucl. Med.* 53, 295–303. doi:10.2967/jnumed.111.093419.
- 541 Peretti, D. E., Reesink, F. E., Doorduyn, J., de Jong, B. M., De Deyn, P. P., Dierckx, R. A. J. O., et al.
542 (2019). Optimization of the k2' Parameter Estimation for the Pharmacokinetic Modeling of
543 Dynamic PIB PET Scans Using SRTM2. *Frontiers in Physics* 7, 212.
544 doi:10.3389/fphy.2019.00212.
- 545 Price, J. C., Klunk, W. E., Lopresti, B. J., Lu, X., Hoge, J. A., Ziolkowski, S. K., et al. (2005). Kinetic
546 modeling of amyloid binding in humans using PET imaging and Pittsburgh Compound-B. *J.*
547 *Cereb. Blood Flow Metab.* 25, 1528–1547. doi:10.1038/sj.jcbfm.9600146.
- 548 Recasens, A., Dehay, B., Bové, J., Carballo-Carbajal, I., Dovero, S., Pérez-Villalba, A., et al. (2014).
549 Lewy body extracts from Parkinson disease brains trigger α -synuclein pathology and
550 neurodegeneration in mice and monkeys. *Ann. Neurol.* 75, 351–362. doi:10.1002/ana.24066.
- 551 Saikali, S., Meurice, P., Sauleau, P., Eliat, P.-A., Bellaud, P., Randuineau, G., et al. (2010). A three-
552 dimensional digital segmented and deformable brain atlas of the domestic pig. *J. Neurosci.*
553 *Methods* 192, 102–109. doi:10.1016/j.jneumeth.2010.07.041.
- 554 Schneider, C. A., Rasband, W. S., and Eliceiri, K. W. (2012). NIH Image to ImageJ: 25 years of
555 Image Analysis HHS Public Access.
- 556 Shalgunov, V., Xiong, M., L'Estrade, E. T., Raval, N. R., Andersen, I. V., Edgar, F. G., et al. (2020).
557 Blocking of efflux transporters in rats improves translational validation of brain radioligands.
558 *EJNMMI Res.* 10, 124. doi:10.1186/s13550-020-00718-x.
- 559 Shimozawa, A., Ono, M., Takahara, D., Tarutani, A., Imura, S., Masuda-Suzukake, M., et al. (2017).
560 Propagation of pathological α -synuclein in marmoset brain. *Acta Neuropathol Commun* 5, 12.
561 doi:10.1186/s40478-017-0413-0.
- 562 Sureau, F. C., Reader, A. J., Comtat, C., Leroy, C., Ribeiro, M. J., Buvat, I., et al. (2008). Impact of

- 563 image-space resolution modeling for studies with the high-resolution research tomograph. *J.*
564 *Nucl. Med.* 49, 1000–1008. doi:10.2967/jnumed.107.045351.
- 565 Tjerkaski, J., Cervenka, S., Farde, L., and Matheson, G. J. (2020). Kinfitr - an open-source tool for
566 reproducible PET modelling: validation and evaluation of test-retest reliability. *EJNMMI Res.*
567 10, 77. doi:10.1186/s13550-020-00664-8.
- 568 Tolboom, N., Yaqub, M., Boellaard, R., Luurtsema, G., Windhorst, A. D., Scheltens, P., et al. (2009).
569 Test-retest variability of quantitative [11C]PIB studies in Alzheimer's disease. *Eur. J. Nucl. Med.*
570 *Mol. Imaging* 36, 1629–1638. doi:10.1007/s00259-009-1129-6.
- 571 Verdurand, M., Levigoureux, E., Zeinyeh, W., Berthier, L., Mendjel-Herda, M., Cadarossanesaib, F.,
572 et al. (2018). In Silico, in Vitro, and in Vivo Evaluation of New Candidates for α -Synuclein PET
573 Imaging. *Mol. Pharm.* 15, 3153–3166. doi:10.1021/acs.molpharmaceut.8b00229.
- 574 Villadsen, J., Hansen, H. D., Jørgensen, L. M., Keller, S. H., Andersen, F. L., Petersen, I. N., et al.
575 (2017). Automatic delineation of brain regions on MRI and PET images from the pig. *J.*
576 *Neurosci. Methods* 294, 51–58. doi:10.1016/j.jneumeth.2017.11.008.
- 577 Winterdahl, M., Audrain, H., Landau, A. M., Smith, D. F., Bonaventure, P., Shoblock, J. R., et al.
578 (2014). PET brain imaging of neuropeptide Y2 receptors using N-11C-methyl-JNJ-31020028 in
579 pigs. *J. Nucl. Med.* 55, 635–639. doi:10.2967/jnumed.113.125351.
- 580 Yang, W., Wang, G., Wang, C.-E., Guo, X., Yin, P., Gao, J., et al. (2015). Mutant Alpha-Synuclein
581 Causes Age-Dependent Neuropathology in Monkey Brain. *Journal of Neuroscience* 35, 8345–
582 8358. doi:10.1523/JNEUROSCI.0772-15.2015.
- 583 Yaqub, M., Tolboom, N., Boellaard, R., van Berckel, B. N. M., van Tilburg, E. W., Luurtsema, G., et
584 al. (2008). Simplified parametric methods for [11C]PIB studies. *Neuroimage* 42, 76–86.
585 doi:10.1016/j.neuroimage.2008.04.251.
- 586 Ye, L., Velasco, A., Fraser, G., Beach, T. G., Sue, L., Osredkar, T., et al. (2008). In vitro high affinity
587 alpha-synuclein binding sites for the amyloid imaging agent PIB are not matched by binding to
588 Lewy bodies in postmortem human brain. *J. Neurochem.* 105, 1428–1437. doi:10.1111/j.1471-
589 4159.2008.05245.x.
- 590 Lammertsma, A. A., and Hume, S. P. (1996). Simplified reference tissue model for PET receptor
591 studies. *Neuroimage* 4, 153–158. doi:10.1006/nimg.1996.0066.

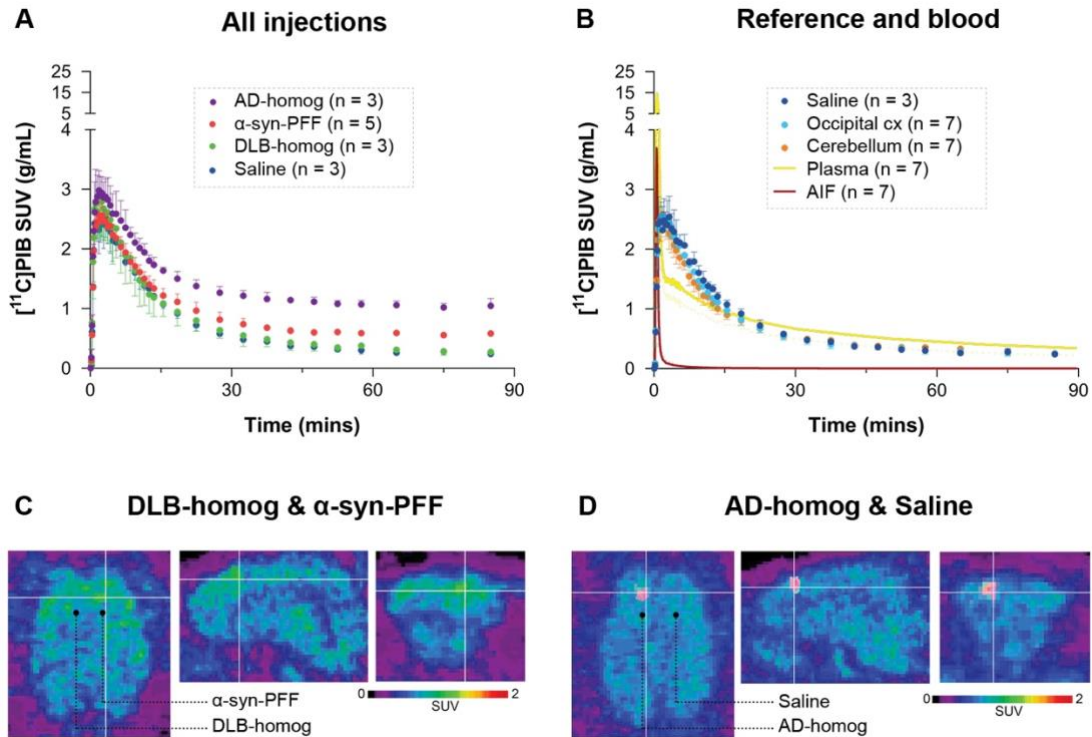


592

593 **Figure 1.** Study design. *Step 1:* Intracerebral injections. A-synuclein preformed fibrils, Alzheimer’s
 594 disease human brain homogenate, dementia with Lewy bodies human brain homogenate, or saline is
 595 injected in either hemisphere. *Step 2:* PET/MR scan. Animals are PET scanned with [¹¹C]PIB. Some
 596 animals are also MRI scanned in a 3T scanner. *Step 3:* Euthanasia. After the final scan, animals are
 597 euthanized, their brains removed, and injection sites’ pathology confirmed.

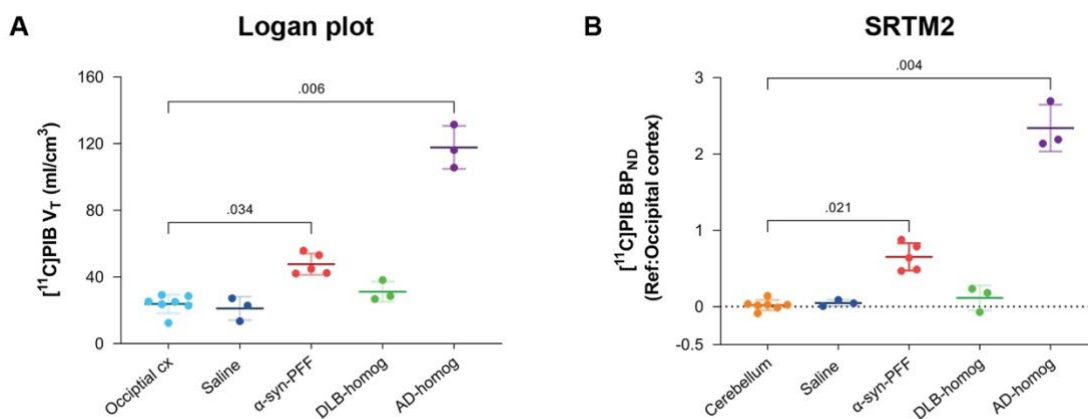
598

599



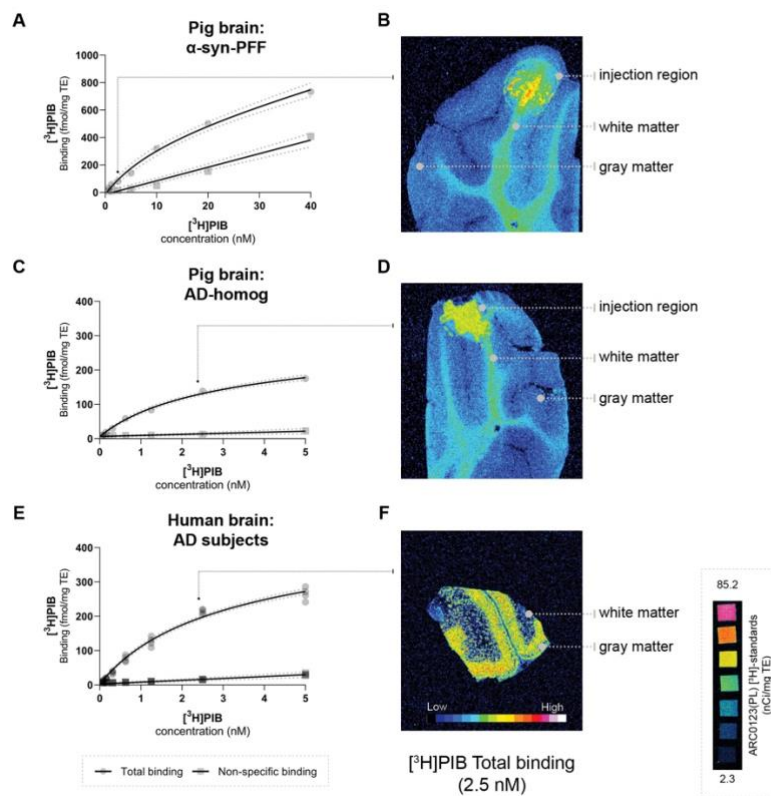
600

601 **Figure 2.** Regional time-activity curves of [¹¹C]PIB in A) the different injection regions and B) the
 602 reference regions and saline-injected region with the uncorrected plasma curve and arterial input
 603 function. Representative summed PET across the entire duration of the scan (0-90 mins) images
 604 showing injection regions including C) SUV scaled brain images including the brain areas injected
 605 with α -synuclein preformed fibrils or DLB homogenate and D) AD homogenate or saline.



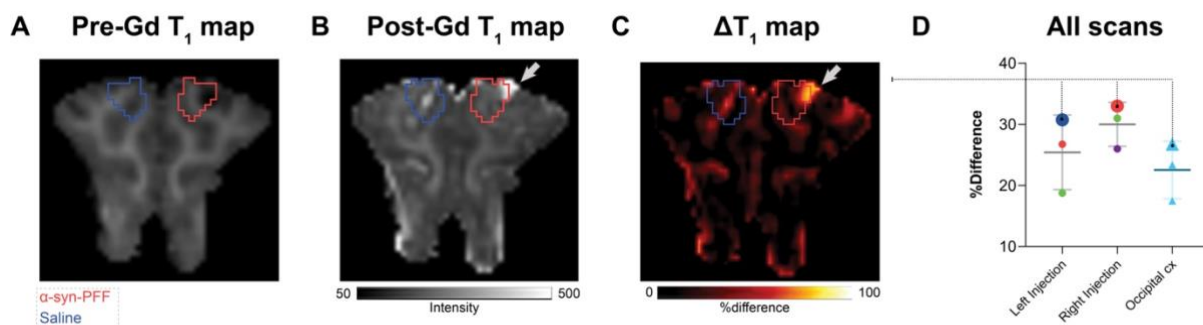
606

607 **Figure 3.** Kinetic modeling of [¹¹C]PIB. A) Kinetic modeling with arterial input (Logan). Direct
 608 comparison of V_T values in the different injection regions to the occipital cortex. B) Kinetic modeling
 609 with occipital cortex as a reference region (SRTM2). BP_{ND} values are compared to the cerebellum.



610

611 **Figure 4.** Saturation assays (A, C, E) and: corresponding representative autoradiograms (B, D, F
 612 [total binding at 2.5 nM]) of [³H]PIB in the pig brain: A: α -syn-PFF injected, D: AD-homogenate
 613 injected, and F) Human AD brain. Scale (ARC0123(PL)) inserted.



614

615 **Figure 5.** Representative pre- (A) and post- (B) gadolinium-enhanced MRI of the injected region. (C)
 616 ΔT_1 maps are shown as %difference, i.e. % (post-Gd - pre-Gd) / pre-Gd. (D) The right and left
 617 injection regions (Right Injection vs. Left Injection) were compared to the occipital cortex. Data
 618 points were color-coded for the different injections with larger symbols from the animals shown in
 619 A-C: red circles = α -synuclein preformed fibrils injected region, dark blue circle = saline injected
 620 region, green circles = DLB homogenate injected region, purple circle = AD homogenate injected
 621 region, and light blue triangles = occipital cortex.

622

623 **Table 1.** Overview of animals. Bodyweight, injection substance, injected dose/mass of [¹¹C]PIB, and
 624 availability of parent fraction curve, and gadolinium contrast MR scan.

625

Pig no.	Weight (kg)	Injection in the left injection site	Injection in the right injection site	Injected dose [¹¹ C]PIB (MBq)	Injected mass [¹¹ C]PIB (µg)	Individual parent fraction curve	Gd-MRI scan
1	28	α-syn-PFF	α-syn-PFF	500	1.72	✓	-
2	27	α-syn-PFF	Saline	492	1.85	✓	-
3	25	Saline	α-syn-PFF	378	2.43	✓	✓
4	28	α-syn-PFF	DLB-homogenate	440	7.94	✓	✓
5	31	DLB-homogenate	AD-homogenate	447	13.49	-	✓
6	28	DLB-homogenate	AD-homogenate	461	3.97	-	-
7	27	Saline	AD-homogenate	424	2.34	-	-

α-syn-PFF = α-synuclein preformed fibrils (160µg/25µL)
 Saline = physiological saline (25µL)
 DLB-homogenate = Dementia with Lewy bodies human brain homogenate (10%, 25µL) [Braak stage II, n = 2 x2 regions, Aβ and tau -ve]
 AD-homogenate = Alzheimer's disease human brain homogenate (10%, 25µL) [Braak stage IV, n = 2 x2 regions, α-syn -ve]
 Gd-MRI scan = Gadolinium-enhanced MRI

626

627 **Table 2.** Summary of kinetic modeling outcomes of [¹¹C]PIB. All values denote the mean ± standard
 628 deviation. PFF=preformed fibrils. NA= not applicable.

629

Regions	Kinetic Modelling Outcome	
	V _T (ml/cm ³)	BP _{ND}
α-syn-PFF	47.7 ± 6.3	0.65 ± 0.18
AD-homogenate	118.1 ± 12.9	2.34 ± 0.31
DLB-homogenate	31.1 ± 6.1	0.11 ± 0.16
Saline	21.2 ± 6.1	0.05 ± 0.03
Occipital cortex	23.8 ± 5.5	NA (reference)
Cerebellum	25.8 ± 6.8	0.01 ± 0.03

630 **Table 3.** Summary of B_{\max} and K_D . Values (95% confidence interval) from [^3H]PIB saturation assays
 631 performed on injected pigs and human frozen brain sections. n= number of unique individuals. BP=
 632 binding potential.

633

Sections	n	B_{\max} (fmol/mg TE)	K_D (nM)	BP
Pig brain α -syn-PFF injected	1	477.2 (353.2 to 682.6)	12.07 (5.70 to 25.94)	39.53
Pig brain AD-homogenate injected	1	233.4 (202.3 to 273.8)	2.46 (1.83 to 3.35)	94.87
Human brain AD patients	2 (2 regions)	366.7 (332.8 to 407.0)	2.54 (2.09 to 3.12)	144.37

634

635

636

Supplementary Material

1 α -synuclein preformed fibrils and post-mortem human brain pathological details

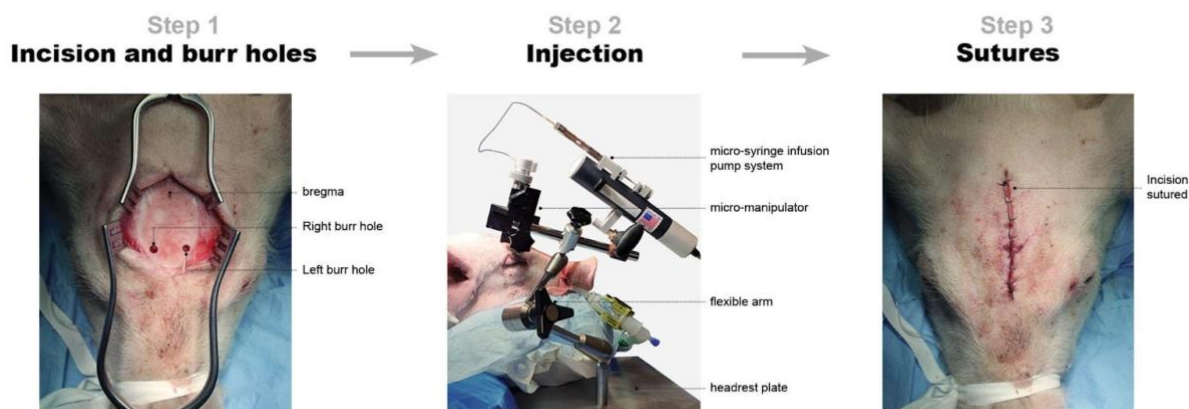
α -synuclein preformed fibrils were produced at Lundbeck A/S, Denmark, using their optimized protocols following previously published literature (Makky et al., 2016). Preformed fibrils were sonicated after fibrillization, aliquoted, and stored at -80°C until further use.

The post-mortem human brain homogenates used are a mixture of two regions (frontal and temporal) for each of two different subjects with each disease (i.e., AD and DLB). Samples, predominantly from the gray matter, were weighed from all regions and subjects; approximately 100 mg was used. All samples (both diseases separately) were added to an Eppendorf tube followed by an adequate amount of saline to make a 10% solution (w/v) and homogenized using an automatic tissue homogenizer (IKA® T10basic ULTRA-TURRAX® Disperser, IKA®-Werke GmbH & Co. KG, Staufen, Germany) for approximately 3 min to make a homogenous solution, aliquoted and stored at -80°C until further use.

Supplementary Table 1. Neuropathological characteristics of the post-mortem human brains used in the study. Details include primary neuropathological diagnosis: Alzheimer's disease (AD) or Dementia with Lewy bodies-Neocortical (LBD), frequency of Lewy bodies: frequent (F) or sparse to moderate (S-P), Braak staging, ABC, CERAD (The Consortium to Establish a Registry for Alzheimer's Disease), Thal staging, Post-mortem interval (PMI), age at onset, age at death, ApoE (Apolipoprotein E) genotype and sex of the brain available for this study.

Primary Diagnosis	Frontal Lewy Bodies	Parietal Lewy Bodies	Braak Stage	ABC	CERAD	Thal	PMI (h)	Age at onset (y)	Age at Death (y)	ApoE gene	Sex
AD1	0	0	VI	3	3	5	11	53	70	E3/E4	m
AD2	0	0	VI	3	3	5	14.5	60	68	E3/E3	m
LBD1	F	S-M	II	0	0	0	15.5	47	68	E3/E3	m
LBD2	F	S-M	II	0	0	0	19.5	61	69	E3/E3	m

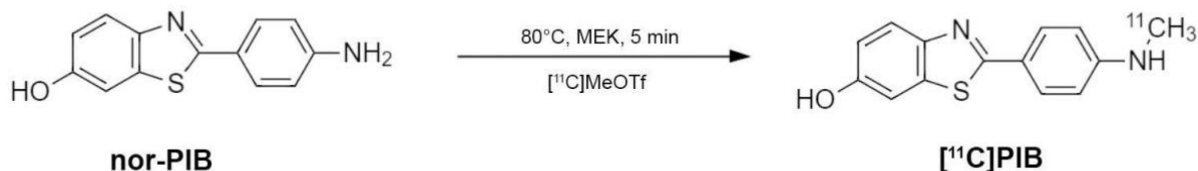
2 Images and diagrams of the surgical procedure



Supplementary Figure 1. Surgical procedure. *Step 1*: Incision and burr holes. Sagittal midline incision followed by the location of bregma. Burr holes are placed in precise relation to the bregma as per protocol. *Step 2*: Injection of substrates. The image shows an injection procedure and the details of the modified stereotactic frame. *Step 3*: Sutures. Sutures are placed, and the animal is ready for transport to the scanners.

3 [¹¹C]PIB radiochemistry

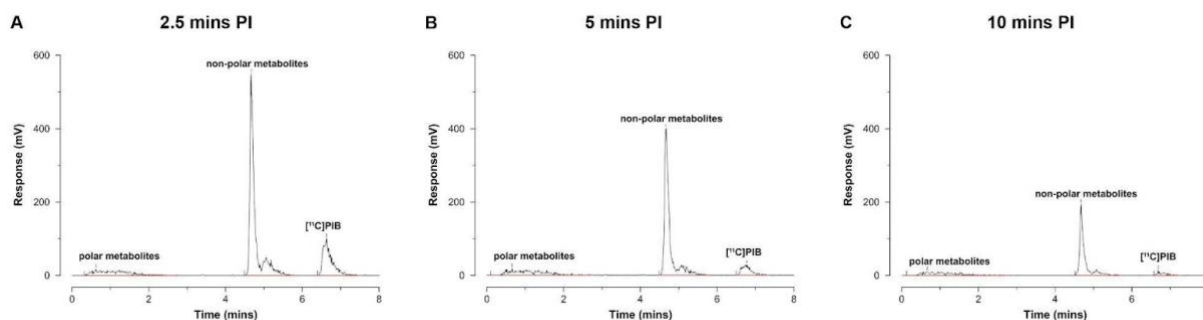
[¹¹C]PIB was prepared by reacting [¹¹C]methyl triflate with 1.0 mg nor-PIB precursor dissolved in 300 mL methylethylketone (MEK) for 3 min at 80°C (Supplementary Figure 2). The reaction mixture was diluted with 4.5 mL 0.1% phosphoric acid and subsequently injected onto an Onyx Monolithic C18 semi-preparative HPLC column (10 x 100 mm, Phenomenex, Torrance, CA, USA). Eluent: 10 mM ascorbic acid in 0.1% phosphoric acid / ethanol 96% (70:30); flow rate 6.0 mL/min; wavelength $\lambda=250$ nm. The fraction containing the product was collected within 1 min (6.0 mL) and passed through a sterile filter into a 20 mL sterile vial containing 9.0 mL 0.1 M phosphate buffer (pH=7), giving a final solution for injection containing $\leq 10\%$ (v/v) ethanol.



Supplementary Figure 2. Synthesis of [¹¹C]PIB.

4 Addition analysis with blood and plasma

To exclude the possibility that the fast metabolism of [^{11}C]PIB was due to the instability of the compound in plasma or blood, we verified the stability of [^{11}C]PIB. The samples were spiked with [^{11}C]PIB and incubated at room temperature for up to 75 min. Samples were processed and analyzed by radio-HPLC as described above in the main manuscript. We found that at room temperature, [^{11}C]PIB was completely stable in plasma and whole blood for up to 75 min of incubation.



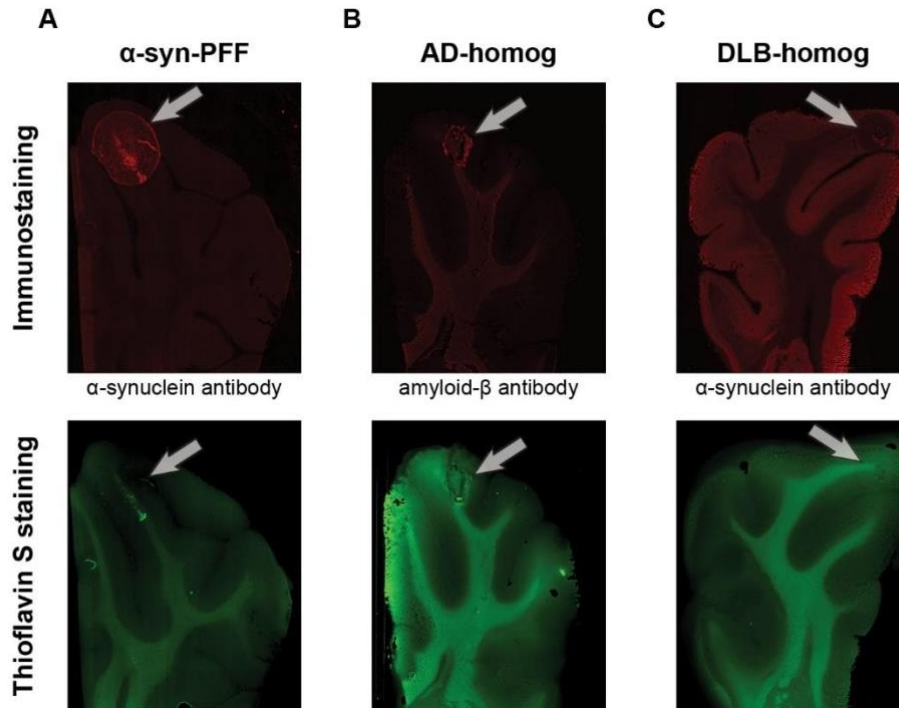
Supplementary Figure 3. HPLC chromatograms. A-C) Representative radio-chromatograms 2.5 min (A), 5 min (B), and 10 min post-injection of [^{11}C]PIB (n=1).

5 Fluorescence immunostaining

Fluorescence immunostaining was performed on sections containing the injection site to validate the injection site and confirm injection of injectate. The sections were processed for standard immunohistochemistry (IHC) with α -synuclein (GTX21904-Mouse [4B12], GeneTex, Hsinchu City, Taiwan) and amyloid- β (ab252816-Rat [2E9], Abcam, Cambridge, UK) primary antibodies detected with goat anti-mouse or goat anti-rat IgG H&L (Alexa Fluor[®] 647) (ab150115/ab150167, Abcam, Cambridge, UK) secondary antibodies. The frozen sections were first fixed in 4% formaldehyde for 20 min. After a 10 min wash in phosphate-buffered saline (PBS), antigen retrieval was performed in a microwave oven in 25 mM sodium citrate buffer pH 7.5 for α -synuclein containing section or Tris/EDTA buffer pH 9.0 for amyloid- β containing section. Buffer temperature was raised to boiling for 5 secs, sections left in the microwave for 10 min, then 20 min under the hood. After, they were washed with PBS-TritonX100 0.4% and then incubated for 60 min with PBS + 0.4% TritonX100 and 5% bovine serum albumin (BSA). Buffer was poured off, sectioned for incubated overnight in primary antibody (α -synuclein: 0.2 ng/ml) (amyloid- β : 0.5 $\mu\text{g}/\text{ml}$) in PBS + 0.1% Tween20 at 4 $^{\circ}\text{C}$. The next day, sectioned were washed thrice in PBS and then incubated in secondary antibody (diluted 1:200) in PBS + 0.1% Tween20 for 1 hour at room temperature. Finally, the sections were washed thrice in PBS followed by one wash in deionized H₂O (dH₂O). After the standard IHC, the sections were washed in increasing ethanol concentration (1 min in 70% ethanol and 1 min in 85%) and then incubated in 0.25% thioflavin S solution in 85% ethanol (filtered) for 15 mins. Incubation was followed by a wash in decreasing ethanol concentration and finally a wash with dH₂O. After the staining protocol, the sections were overnight mounted in EverBrite[™] Hardset Mounting Medium (Biotium, Inc., Fremont, CA, USA). Sections were imaged using an EC Plan-Neofluoar 5x/0.16

Supplementary Material: Protein injection pig model

objective on an Axio Observer 7 fitted with a motorized stage and Axiocam 506mono CCD camera (Carl Zeiss, Birkørød, Denmark) to create stitched images covering large regions of interest. ThS was imaged using a filter set comprising a 470/40 nm bandpass for excitation, 495 nm beamsplitter, and 525/50 nm bandpass emission (Filter Set 38 HE, Carl Zeiss, Birkørød, Denmark). For Alexa Fluor® 647, an excitation of 640/30 nm, beamsplitter of 660, and emission of 690/50 filter set was used (Filter Set 50, Carl Zeiss, Birkørød, Denmark).



Supplementary Figure 4. Successful injections were ensured by immunostaining (top row) and thioflavin S staining (bottom row). Representative examples of A) α -synuclein-preformed-fibrils injected hemisphere, B) AD-homogenate injected hemisphere, and C) DLB-homogenate injected hemisphere.

6 $[^3\text{H}]\text{PIB}$ saturation assay

Sections were thawed to room temperature for 45 min before pre-washing twice for 10 min in assay buffer (PBS, 1% BSA, 10% ethanol, and pH 7.4). Sections were incubated in assay buffer containing varying concentrations of $[^3\text{H}]\text{PIB}$ (0 to 5 nM for AD-homogenate-injected pig brain and AD human brain slices) (0 to 40 nM for α -synuclein-preformed-fibril-injected pig brain slices) for total binding (TB) and the same varying concentrations of $[^3\text{H}]\text{PIB}$ with 100 μM of thioflavin S for non-specific binding (NSB). The sections were incubated for 60 min. Incubation was terminated by three 5-min washes with 4°C wash buffer (PBS, 10% ethanol, and pH 7.4) followed by a rapid rinse in 4°C dH₂O.

After washing, the slides were rapidly air-dried and fixated overnight in a paraformaldehyde vapor chamber in cold storage (4°C). The next day, the samples were moved to an exicator for 60 min to remove any excess moisture and then placed in a cassette for autoradiography with tritium sensitive image plates (BAS-IP TR2040 E, Science Imaging Scandinavia AB, Nacka, Sweden) along with radioactive tritium standards (ART0123, American Radiolabeled Chemical, Inc., St. Louis, MO, USA). The image plates were exposed for three days. After the exposure, the image plates were read using an Amersham™ Typhoon™ IP (Cytiva, Uppsala, Sweden) at 10 μm resolution. Calibration, quantification, and data evaluation were done using ImageJ software (NIH Image, Bethesda, MD, USA) (Schneider et al., 2012). The regions of interest were hand-drawn. The four-parameter general curve fit (David Rodbard, NIH) of decay corrected tritium standards was used to convert mean pixel density (grayscale) to nCi/mg Tissue Equivalent (TE). TB was determined in the pathology-rich regions or at the injection site from TB slides, while NSB was determined in pathology-rich regions or at the injection site from NSB slides. Finally, the decay-corrected specific activity of [³H]PIB was used to convert nCi/mg TE to fmol/mg TE which was used to calculate the B_{\max} and K_D and the binding potential (BP) as the ratio between the two parameters.

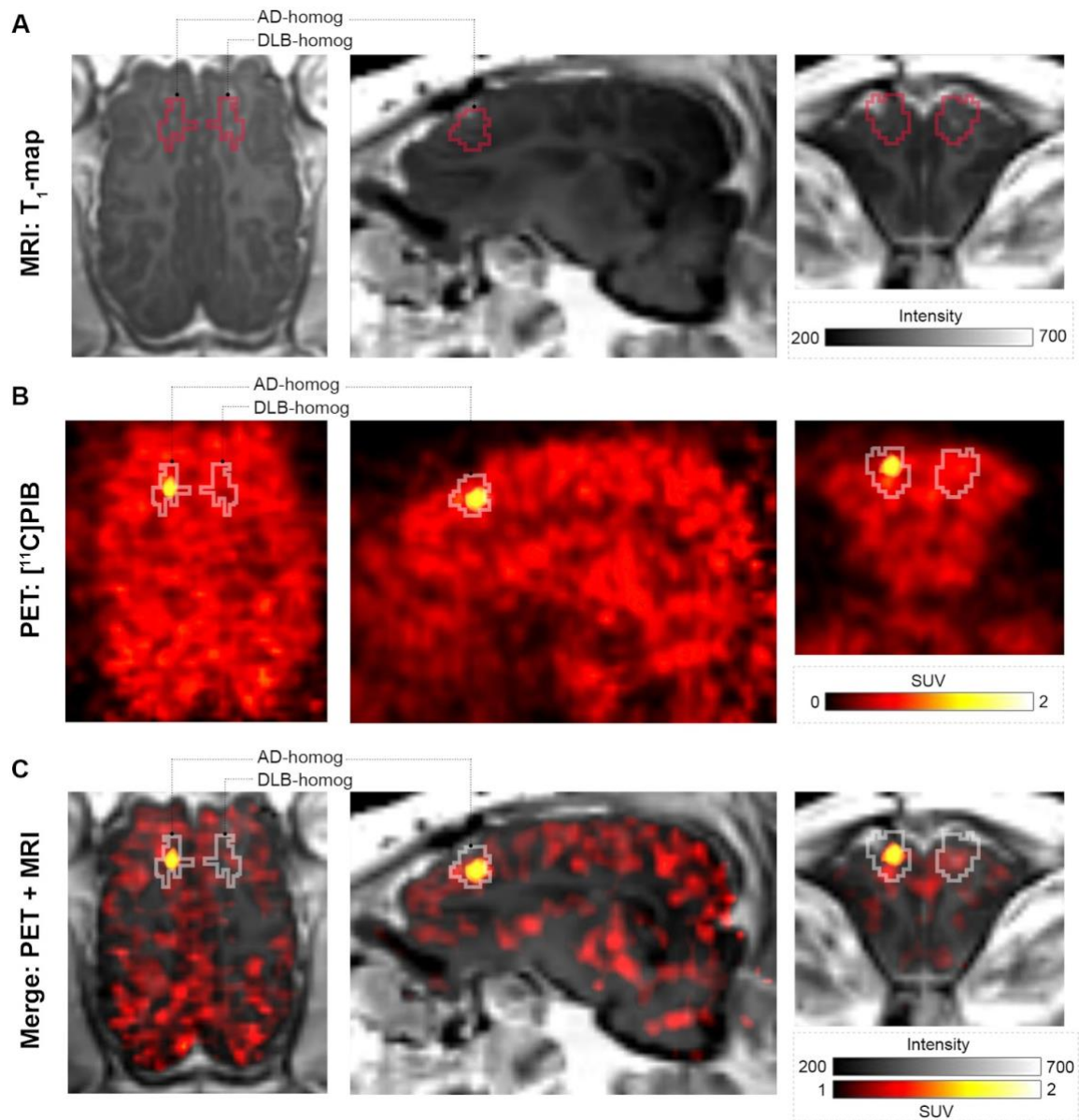
7 Kinetic Modelling and Population-based parent fraction

Supplementary Figure 5 shows the volume of interest for the injection regions that are added to the existing atlas and further used in the study. All animals' regional time-activity curves and blood data, including whole blood activity, plasma activity, and parent fraction throughout the scan, were loaded to *kinfitr*. The parent fraction curve was fit to a model. We tested multiple models for the parent fraction curve and found the inverted gamma function (inverse gamma model) to have the best fit using the Bayesian information criterion (data not shown). The blood volume (V_B) was set to 0.05 (5%). Blood delay (arterial input function delay compared to brain time-activity curve) and weights were calculated and set according to standard protocol. The optimal threshold time (t^*) was computed using the inbuilt function of *kinfitr* called "Logan_tstar." We found a t^* of 10 (last 10 data points from the Logan plot) ideal since it had the least maximum percentage of variance and stable V_T values.

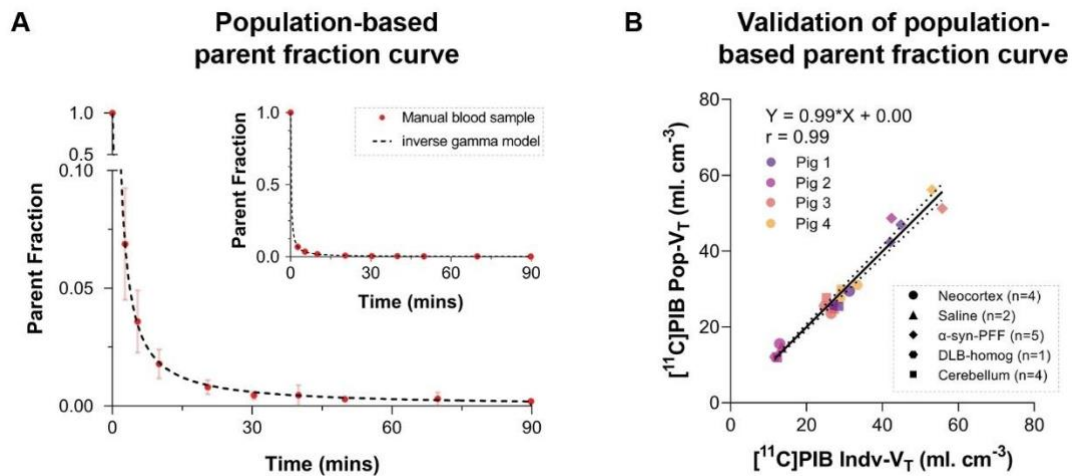
Due to a technical failure with the HPLC equipment, the parent fraction curve from the last three scans could not be estimated. Instead, we created a population-based parent fraction curve from the first four scans and used it for the last three scans (Table 1, Supplementary Figure 6). This was created by averaging the available parent fraction curves at their respective time-point. The population-based curve was validated by plotting Logan V_T values from the individual parent fraction curve against V_T values from the population-based parent fraction curve in the first four animals. We found a highly significant correlation between these two V_T values (Pearson $r = 0.99$, $p < 0.0001$) (Supplementary Figure 6).

For reference tissue modeling using the SRTM2, the k'_2 was first estimated by fitting the time-activity curves from all animals to their occipital cortex using SRTM (Lammertsma and Hume, 1996). The k'_2 parameter was extracted from all the high binding regions (only AD-homogenate and α -synuclein-preformed-fibril injected regions) and averaged, providing a k'_2 of 0.03. After fixing k'_2 to 0.03, we fit the time-activity curves from all the animals to their occipital cortex using the SRTM2 to extract the non-displaceable binding potential (BP_{ND}) values.

Supplementary Material: Protein injection pig model



Supplementary Figure 5. Injection region volume of interests on representative A) T₁-map MRI, B) [¹¹C]PIB summed PET image, and C) merged PET + MR image in a pig injected with AD-homogenates and DLB-homogenates. PET image is created over the entire scan duration (0-90 mins) using the "Triangle" interpolation function of PMOD for better visualization of the injection region. The SUV scaling is changed for the merged image to reduce the background.



Supplementary Figure 6. Population-based parent fraction curve and its validation. A) Population-based parent fraction curves from $n=4$ animals fit an inverse gamma model. B) Validation of the population-based parent fraction curve. Logan V_T values calculated from the population-based parent fraction curve plotted against Logan plot V_T values calculated from individual parent fraction curves from the same animals. Equation from the linear regression and Pearson's r value is inserted.

8 Reference

Lammertsma, A. A., and Hume, S. P. (1996). Simplified reference tissue model for PET receptor studies. *Neuroimage* 4, 153–158. doi:10.1006/nimg.1996.0066.

Makky, A., Bousset, L., Polesel-Maris, J., and Melki, R. (2016). Nanomechanical properties of distinct fibrillar polymorphs of the protein α -synuclein. *Sci. Rep.* 6, 37970. doi:10.1038/srep37970.

Schneider, C. A., Rasband, W. S., and Eliceiri, K. W. (2012). NIH Image to ImageJ: 25 years of Image Analysis HHS Public Access.



DECLARATION OF CO-AUTHORSHIP

The declaration is for PhD students and must be completed for each conjointly authored article. Please note that if a manuscript or published paper has ten or less co-authors, all co-authors must sign the declaration of co-authorship. If it has more than ten co-authors, declarations of co-authorship from the corresponding author(s), the senior author and the principal supervisor (if relevant) are a minimum requirement.

1. Declaration by	
Name of PhD student	Nakul Ravi Raval
E-mail	nakul.raval@nru.dk
Name of principal supervisor	Prof. Dr. Gitte Moos Knudsen
Title of the PhD thesis	Translational Positron Emission Tomography: Animal Models and In vitro Autoradiography for Radioligand Development

2. The declaration applies to the following article	
Title of article	An in vivo pig model for testing novel PET radioligands targeting cerebral protein aggregates
Article status	
Published <input type="checkbox"/>	Accepted for publication <input checked="" type="checkbox"/>
Date:	Date: 31/01/22
Manuscript submitted <input type="checkbox"/>	Manuscript not submitted <input type="checkbox"/>
Date:	
If the article is published or accepted for publication, please state the name of journal, year, volume, page and DOI (if you have the information).	Front. Neurosci. - Brain Imaging Methods

3. The PhD student's contribution to the article <i>(please use the scale A-F as benchmark)</i> Benchmark scale of the PhD-student's contribution to the article	A, B, C, D, E, F
A. Has essentially done all the work (> 90 %) B. Has done most of the work (60-90 %) C. Has contributed considerably (30-60 %) D. Has contributed (10-30 %) E. No or little contribution (<10 %) F. Not relevant	
1. Formulation/identification of the scientific problem	B
2. Development of the key methods	C

3. The PhD student's contribution to the article (please use the scale A-F as benchmark)	
Benchmark scale of the PhD-student's contribution to the article	A, B, C, D, E, F
A. Has essentially done all the work (> 90 %) B. Has done most of the work (60-90 %) C. Has contributed considerably (30-60 %) D. Has contributed (10-30 %) E. No or little contribution (<10 %) F. Not relevant	
3. Planning of the experiments and methodology design and development	C
4. Conducting the experimental work/clinical studies/data collection/obtaining access to data	B
5. Conducting the analysis of data	B
6. Interpretation of the results	A
7. Writing of the first draft of the manuscript	A
8. Finalisation of the manuscript and submission	A
Provide a short description of the PhD student's specific contribution to the article. ⁱ	
NRR helped design the study outline. With the help and guidance of LMJ, NRR designed a modified stereotactic frame, performed the pig surgeries and PET scans. NRR also performed the in vitro analysis as well as processing the data, conducting data analysis, interpretation of results. NRR wrote the first draft and submitted the manuscript.	

4. Material from another thesis / dissertationⁱⁱ	
Does the article contain work which has also formed part of another thesis, e.g. master's thesis, PhD thesis or doctoral dissertation (the PhD student's or another person's)?	Yes: <input type="checkbox"/> No: <input checked="" type="checkbox"/>
If yes, please state name of the author and title of thesis / dissertation.	
If the article is part of another author's academic degree, please describe the PhD student's and the author's contributions to the article so that the individual contributions are clearly distinguishable from one another.	

5. Signatures of the co-authorsⁱⁱⁱ				
	Date	Name	Title	Signature
1.	03/01/22	Gitte Moos Knudsen	Professor	

5. Signatures of the co-authors ⁱⁱⁱ				
2.	03/01/22	Louise Møller Jørgensen	MD, PhD	

6. Signature of the principal supervisor
I solemnly declare that the information provided in this declaration is accurate to the best of my knowledge. Date: 03/02/2022 Principal supervisor: 

7. Signature of the PhD student
I solemnly declare that the information provided in this declaration is accurate to the best of my knowledge. Date: 01/01/2022 PhD student: 

Please learn more about responsible conduct of research on the [Faculty of Health and Medical Sciences' website](#).

ⁱ This can be supplemented with an additional letter if needed.

ⁱⁱ Please see Ministerial Order on the PhD Programme at the Universities and Certain Higher Artistic Educational Institutions (PhD Order) § 12 (4):

"Any articles included in the thesis may be written in cooperation with others, provided that each of the co-authors submits a written declaration stating the PhD student's or the author's contribution to the work."

ⁱⁱⁱ If more signatures are needed please add an extra sheet.

Aim I

To establish a pig model with intracerebral protein injections that will help assess novel radioligands.

Study

III

Objection I

To evaluate the novel α -synuclein radioligand, (d₃)-[¹¹C] MODAG-001 in the intracerebral protein injection pig model.

Evaluation of the α -synuclein PET radiotracer (d₃)-[¹¹C]MODAG-001 in pigs

1 Nakul Ravi Raval^{1,2}, Clara Aabye Madsen^{†,1,2}, Vladimir Shalgunov^{†,3,4}, Arafat Nasser¹, Umberto Maria
2 Battisti³, Emily Eufaula Beaman¹, Morten Juhl⁵, Louise Møller Jørgensen^{1,2,6}, Matthias Manfred Herth^{3,4},
3 Hanne Demant Hansen¹, Pontus Plavén-Sigra¹, Gitte Moos Knudsen^{*1,2}

6 ¹Neurobiology Research Unit, Copenhagen University Hospital (Rigshospitalet), Copenhagen, Denmark
7 ²Department of Clinical Medicine, Faculty of Health and Medical Sciences, University of Copenhagen,
8 Copenhagen, Denmark
9 ³Department of Drug Design and Pharmacology, Faculty of Health and Medical Sciences, University of
10 Copenhagen, Copenhagen, Denmark
11 ⁴Department of Clinical Physiology, Nuclear Medicine & PET, Copenhagen University Hospital
12 (Rigshospitalet), Copenhagen, Denmark
13 ⁵Cardiology Stem Cell Centre, Copenhagen University Hospital (Rigshospitalet), Copenhagen, Denmark
14 ⁶Copenhagen Spine Research Unit, Copenhagen University Hospital (Rigshospitalet), Copenhagen,
15 Denmark

16 [†]Contributed equally

17 ^{*}Corresponding author

18 Corresponding author:
19 Gitte Moos Knudsen
20 Neurobiology Research Unit
21 Section 8057, Rigshospitalet
22 Blegdamsvej 9
23 DK-2100 Copenhagen Ø
24 Denmark
25 Email: gmk@nru.dk

26 Abstract

27 **Background:**

28 A positron emission tomography (PET) radiotracer to neuroimage α -synuclein aggregates would be a
29 crucial addition for early diagnosis and treatment development in disorders such as Parkinson's disease,
30 where elevated aggregate levels is a histopathological hallmark. The radiotracer (d₃)-[¹¹C]MODAG-001
31 has recently shown promise for visualization of α -synuclein pre-formed fibrils (α -PFF) in rodents. We

32 here test the radiotracer in a pig model where proteins are intracerebrally injected immediately before
33 scanning. Four pigs were injected in one hemisphere with 150 μg α -PFF, and in the other hemisphere,
34 either 75 μg α -PFF or human brain homogenate from either dementia with Lewy bodies (DLB) or
35 Alzheimer's disease (AD) was injected. All pigs underwent one or two (d_3)-[^{11}C]MODAG-001 PET
36 scans, quantified with the non-invasive Logan graphical analysis using the occipital cortex as a reference
37 region.

38 **Results:**

39 The α -PFF and AD homogenate injected brain regions had high uptake of (d_3)-[^{11}C]MODAG-001
40 compared to the occipital cortex or cerebellum. BP_{ND} values in 150 μg α -PFF injected regions was 0.78,
41 and in the AD homogenate injected regions was 0.73. By contrast, the DLB homogenate injected region
42 did not differ in uptake and clearance compared to the reference regions. The time-activity curves and
43 BP_{ND} values in the 150 μg and 75 μg injected region of α -PFFs show a dose-dependent effect, and the
44 PET signal could be blocked by pretreatment with unlabeled MODAG-001.

45 **Conclusion:**

46 We find that both α -PFF and AD brain homogenates give rise to increased binding of (d_3)-[^{11}C]MODAG-
47 001 when injected into the pig brain. Despite its limited specificity for cerebral α -synuclein pathology,
48 (d_3)-[^{11}C]MODAG-001 shows promise as a lead tracer for future radiotracer development.

49 **Keywords**

50 Alpha-synuclein, PET tracer, Positron emission tomography, intracerebral protein injection, amyloid-beta,
51 brain imaging, larger animal PET, pig model

52 Background

53 Parkinson's disease (PD), dementia with Lewy bodies (DLB), and multiple system atrophy (MSA) are
54 histopathologically characterized by progressive nigrostriatal, limbic and neocortical neurodegeneration
55 and aggregation of the intracellular presynaptic protein α -synuclein [1–3]. These diseases are collectively
56 known as α -synucleinopathies [4]. Patients with PD or DLB have α -synuclein-rich neuronal inclusions
57 called Lewy bodies and Lewy neurites, predominantly in the substantia nigra in PD and throughout the
58 cerebral cortex in DLB [5]. On the other hand, patients with MSA show filamentous aggregates in
59 oligodendrocytes and neurons [6]. However, it is yet unknown to which extent α -synuclein aggregates
60 contribute to neurodegeneration (Wong and Krainc 2017), and further, the clinical diagnosis of a PD or
61 PD+ disorder is difficult, particularly in the early phases [7]. In drug-naive patients with subtle clinical
62 parkinsonian motor symptoms, dopamine transporter neuroimaging has high sensitivity and specificity in
63 distinguishing between patients with and without striatal neurodegeneration [8] but access to a
64 neuroimaging tool to specifically assess α -synuclein aggregates would be a highly valuable addition.

65 Positron emission tomography (PET) has proven valuable for the detection of amyloid- β and tau protein
66 aggregates and is used for differential diagnosis and drug development evaluation for neurodegenerative
67 conditions such as Alzheimer's disease (AD) [9]. PET imaging of α -synuclein would be advantageous
68 for, e.g., early disease detection, differential diagnosis, and monitoring disease progression of
69 synucleinopathies. In addition, the field is moving towards early eradication of α -synuclein aggregates as
70 a promising therapeutic strategy in α -synucleinopathies, an approach that would require in vivo imaging
71 for clinical application. As of today, no clinically validated PET radioligand exists for imaging α -
72 synuclein [10, 11].

73 Several attempts to develop a suitable radioligand for α -synuclein have been made, and some tracers
74 looked promising in rodents [12–16]. One of these is the diphenylpyrazole derivative [^{11}C]MODAG-
75 001/(d₃)-[^{11}C]MODAG-001 [12]. It was developed from the lead structure anle138b, a compound with

76 therapeutic properties in PD and MSA rodent models due to its binding characteristics to α -synuclein
77 aggregates [17, 18]. Anle138b and its derivatives, like [³H]/[¹¹C]MODAG-001, have undergone extensive
78 in vitro and rodent biodistribution experiments [12, 19]. (d₃)-[¹¹C]MODAG-001 showed the most promise
79 as a candidate radioligand for detecting α -synuclein aggregates due to its high affinity, good brain
80 penetration, and ability to detect α -synuclein pre-formed fibril (α -PFF) in a protein deposition rat model
81 [12].

82 In the present study, we test and characterize (d₃)-[¹¹C]MODAG-001 in a large animal model. To evaluate
83 binding characteristics to α -synuclein aggregates, we use a pig model where α -PFF is intracerebrally
84 injected (ICI) immediately before scanning, creating an artificial target brain region [20]. We assess the
85 sensitivity of the radioligand to identify α -synucleinopathy DLB human brain homogenate injected in the
86 pig brain. The binding selectivity to α -synuclein is assessed by comparison to a brain region where
87 amyloid and tau pathology-rich AD human brain homogenate is injected.

88 Methods

89 Radiochemistry

90 Precursor and reference compound for (d₃)-[¹¹C]MODAG-001 were prepared as previously described
91 [12]; see supplementary information for more details. (d₃)-[¹¹C]MODAG-001 was obtained by reductive
92 amination of desmethyl precursor with [¹¹C]CH₂O. The radioactivity yield was 650±297 MBq
93 (mean±SD) (n=9, range 250-1214) after 70 min of synthesis time. The radiochemical purity of the
94 formulated tracer was >95%. Radiochemical conversion from trapped [¹¹C]CH₃I was 45±2 % (n=6).
95 Molar activity at the end of the radioligand synthesis was on average 28.14±5.3 GBq/μmol.

96 Animals

97 We included four female domestic pigs (crossbreed of Landrace, Yorkshire, and Duroc) weighing 27±1
98 kg and aged 10-11 weeks (Table 1). Before any experiments, pigs were sourced from a local farm and
99 acclimatized for 7-10 days in an enriched environment.

100 Preparation and surgical procedure

101 A detailed description of the preparation, anesthesia, surgery, and transport has previously been described
102 [21, 22]. Briefly, anesthesia was induced with an intramuscular (IM) injection of Zoletil mixture and
103 maintained with 10-15 mg/kg/h propofol intravenous (IV) infusion. Analgesia was achieved with 5
104 µg/kg/h fentanyl IV infusion. Endotracheal intubation allowed for ventilation with 34% oxygen in normal
105 air at 10-12 mL/kg. The left and right superficial mammary veins, ear veins, and femoral arteries were
106 catheterized for venous and arterial access. The animals' heart rate, blood pressure, peripheral oxygen
107 saturation (SpO₂), end-tidal CO₂ (EtCO₂), blood glucose, and temperature were monitored throughout the
108 scan. Using a modified stereotactic approach [20], pigs were intracerebrally injected into the medial
109 prefrontal cortex (mPFC) with 25 µL of 3 or 6 mg/mL α-PFF (molecular weight of monomer: 14,460 Da,
110 corresponding to 208 µM or 415 µM) (produced at H. Lundbeck A/S, Copenhagen, Denmark), AD
111 human brain homogenate (10% homogenate in saline [α-synuclein aggregates -ve]) or DLB human brain
112 homogenate (10% homogenate in saline [amyloid-β and tau aggregates -ve]), as outlined for each pig in
113 Table 1. The post-mortem human brain homogenates used in this study are the same as described
114 previously [20], namely a homogenate mixture of two regions (frontal and temporal) from 2 different
115 patients with each disease (i.e., AD and DLB). In a previous study, the injection target point in the mPFC:
116 8, 25, 14 mm in X, Y, Z coordinates relative to bregma was validated [20]. After the surgical procedure,
117 the animals were transported to the scanner facilities.

118

119 **Table 1.** Pig characteristics: Body weight, injectate in the PFC, injected dose/mass of (d₃)-[¹¹C]MODAG-
120 001, and availability of blocking and test-retest scans.

Pig no.	Weight (kg)	Injection in the right PFC	Injection in the left PFC	(d ₃)-[¹¹ C]MODAG-001		MODAG-001 blocking study	Test-retest
				Scan 1: Injected dose (MBq) & mass (µg)	Scan 2: Injected dose (MBq) & mass (µg)		
1	28	DLB homogenate	150µg α-PFF	181 MBq (3.18 µg)	-	-	-
2	25	AD homogenate	150µg α-PFF	334 MBq (7.43 µg)	-	-	-
3	26	75µg α-PFF	150µg α-PFF	359 MBq (6.75 µg)	436 MBq (8 µg)	-	✓
4	29	75µg α-PFF	150µg α-PFF	322 MBq (6.64 µg)	302 MBq (4.58 µg)	✓	-

150µg α-PFF: α-synuclein preformed fibrils (150µg/25µL, 415 µM)
75µg α- PFF: α-synuclein preformed fibrils (75µg/25µL, 208 µM)
DLB homogenate: Dementia with Lewy bodies human brain homogenate (10%, 25µL) [Braak stage II, n=2 x2 regions, Aβ and tau -ve]
AD homogenate: Alzheimer's disease human brain homogenate (10%, 25µL) [Braak stage IV, n=2 x2 regions, α-syn -ve]
MODAG-001 block: 1 mg/kg dissolved in 19% dimethyl sulfoxide in saline

121 PET scanning protocol

122 Pigs were PET-scanned either once or twice (same day) in a Siemens high-resolution research tomograph
123 (HRRT) scanner (CTI /Siemens, Malvern, PA, USA). (d₃)-[¹¹C]MODAG-001 was injected as a rapid
124 bolus (~20 seconds) through one of the superficial mammary veins (IV), and PET data were acquired
125 over 121 min. Molar activity at the time of injection was 19.0±2.1 GBq/µmol (injected dose and mass in
126 Table 1). Pig 3 received a test-retest on the same day. In Pig 4, we perform a self-blocking study with 1
127 mg/kg non-deuterated unlabelled MODAG-001. Unlabelled MODAG-001 (29.1 mg) was dissolved in 40
128 mL of saline with 19% dimethyl sulfoxide to ensure full solubility and injected IV over 15 min starting ~6
129 min before the injection of (d₃)-[¹¹C]MODAG-001.

130 Blood sampling and radio-HPLC analysis

131 Radio-HPLC analysis of plasma samples were performed in Fig 4 for both baseline and block scans.
132 Manual arterial blood samples were drawn at 1.5, 5, 20, 40, and 60 min after injection. Samples were also
133 drawn at 90 and 120 min, but data is not shown due to low and noisy radioactivity counts. Fig 4 also
134 received a third injection of (d₃)-[¹¹C]MODAG-001 (180 MBq, 3.74 μg) to assess radiometabolites
135 crossing the blood-brain barrier for which a blood and brain sample was acquired at 15 min and 22 min
136 post tracer injection. A blood sample was drawn before injection of 20 mL pentobarbital/lidocaine for
137 euthanasia. Immediately after, the skull was exposed, and the occipital bone was sawed open. A small
138 brain sample from the occipital cortex was excised and rinsed in saline to remove excessive blood.
139 Radiolabeled parent and metabolite fractions were determined in plasma and brain tissue using isocratic
140 elution, as previously described [12], but with some modifications (details in Supplementary
141 information).

142 *In vitro* methodologies

143 After the last scanning, the animals were euthanized by IV injection of 20 mL pentobarbital and lidocaine.
144 After euthanasia, the brains were removed, snap-frozen with powdered dry-ice, and stored at -20 °C until
145 further use. Intracerebrally injections were confirmed using fluorescence immunohistochemistry;
146 procedure and results are available in the supplementary data.

147 PET data reconstruction and preprocessing

148 PET scans were reconstructed using ordinary Poisson 3D ordered subsets expectation-maximization,
149 including modeling the point-spread function, using 16 subsets, ten iterations, and standard corrections
150 [23]. Attenuation correction was performed using the MAP-TR μ-map [24]. Emission data were binned
151 into time frames of increasing lengths:
152 6 × 10 s, 6 × 20 s, 4 × 30 s, 9 × 60 s, 8 × 120 s, 4 × 180 s, 2 × 240 s, 1 × 300 s, 1 × 360 s, 1 × 420 s, 1 ×
153 600 s, 1 × 900 s, and 1 × 1680 s. Each frame consisted of 207 planes of 256 × 256 voxels of 1.22 × 1.22 ×
154 1.22 mm in size. Brain parcellation was performed according to our previously published automatic PET-

155 MR pig brain atlas method [25]. The input for the methodology was frame-length weighted, summed PET
156 images of the total scan time (0–120 min). Time-activity curves (TACs) from the neocortex, occipital
157 cortex, temporal cortex, cerebellum (here defined as without vermis), and injection regions were extracted
158 for the present study. The regions of the injection sites were delineated as described in our previous study
159 [20], while all other regions were part of the Saikali atlas [26] modified for PET [25].

160 Pharmacokinetic modeling

161 For image quantification, we used the non-invasive Logan graphical analysis [27] with the occipital
162 cortex and cerebellum as reference regions. In order to estimate the average k_2 over R_1 ratio (k_2'), we
163 applied the simplified reference tissue model (SRTM) [28] to high binding regions (i.e., α -PFF injected
164 regions) and calculated k_2' . For the non-invasive Logan plot, we chose the threshold time, t^* , of 23 min
165 (last 15 frames) since it showed the lowest average maximum percentage of variance. BP_{ND} values
166 estimated using the occipital cortex as a reference region were more stable than those derived using the
167 cerebellum. These are therefore presented in the results section below.

168 All kinetic modeling was performed using the “*kinfitr*” package (v. 0.6.1) (Matheson, 2019; Tjerkaski et
169 al., 2020) in R (v. 4.0.2; “Taking Off Again,” R core team, Vienna, Austria).

170 For the pig that received a test-retest scan, we calculated the % test-rest change using Equation 1. For the
171 pig that received a baseline-block scan, we calculated the % blocking in the α -PFF injected regions using
172 Equation 2.

173

$$174 \text{TrT change (\%)} = \left(\frac{\text{mean}(\text{test2: all region } BP_{ND}) - \text{mean}(\text{test1: all region } BP_{ND})}{\text{mean}(\text{test1 \& test2: all region } BP_{ND})} \right) \times 100 \quad (\text{Eq. 1})$$

$$175 \text{Blocking (\%)} = \left(\frac{BP_{ND}(\text{baseline}) - BP_{ND}(\text{block})}{BP_{ND}(\text{baseline})} \right) \times 100 \quad (\text{Eq. 2})$$

176 Regional radioactivity concentration (kBq/mL) was normalized to injected dose (MBq) and corrected for
177 the animal weight (kg) to provide standardized uptake values (SUV, g/mL) used in graphical plots in
178 Figures 1 and 3. PMOD 3.7 (PMOD Technologies, Zürich, Switzerland) was used to visualize and create
179 all representative PET images (Figure 1 and 3), which are summed images over the entire period of the

180 scan (0-121 min) with the “Triangle” PMOD pixel interpolation function; for more details see
181 “<https://www.pmod.com/files/download/v31/doc/pbas/4145.htm>”. Graph-Pad Prism (v. 9.2.0; GraphPad
182 Software, San Diego, CA, USA) was used for data visualization.

183 Results

184 Brain uptake and kinetics of (d₃)-[¹¹C]MODAG-001

185 We observed high brain uptake (~ 2.5 SUV) and a relatively quick radioligand wash-out after (d₃)-
186 [¹¹C]MODAG-001 injection. The plasma kinetics of (d₃)-[¹¹C]MODAG-001 were relatively fast, with
187 approximately 10% of the parent radioligand remaining in plasma after 20 min (Supplementary Figure 1).
188 Regions with either 150 µg (n = 4) or 75 µg (n = 2) α-PFF and AD homogenate (n = 1) had higher
189 radioactivity retention (Figure 1A-C and Figure 2A) compared to the occipital cortex and cerebellum. By
190 contrast, the DLB homogenate region (n = 1) TAC behaved essentially as background tissue radiotracer
191 retention (Figure 1A). Almost identical TACs were seen in the pig with test-retest scans (Supplementary
192 Figure 2). In a pig euthanized 15 min after tracer injection, 10.8% of (d₃)-[¹¹C]MODAG-001 parent
193 compound remained in the plasma while 56.1 % parent compound remained in brain homogenate from
194 the occipital cortex (Supplementary Table 1). The remaining signal from the plasma and brain came from
195 polar and non-polar radiometabolites (Supplementary Table 1).

196 Blocking experiment using MODAG-001

197 Pretreatment with 1 mg/kg MODAG-001 shortly before the injection of (d₃)-[¹¹C]MODAG-001
198 significantly reduced the radioactive signal in the 150 µg and 75 µg α-PFF regions, which showed
199 substantially faster radioligand kinetics than the regional baseline TACs (Figure 2B); the TACs became
200 comparable to those in the occipital cortex and cerebellum (Figure 3B).

201 Kinetic modeling of (d₃)-[¹¹C]MODAG-001

202 BP_{ND} in different brain regions are shown in Figure 3A. BP_{ND} in the 150 μg α-PFF regions was 0.78 ± 0.1
203 (mean±SD, n = 4) while in the 75 μg regions, BP_{ND} α-PFF injected regions was 0.29 (n = 2), showing a
204 dose-dependent effect of (d₃)-[¹¹C]MODAG-001 binding to the α-PFF. BP_{ND} in the AD homogenate
205 region was 0.73, in the same order as the 150 μg α-PFF. The DLB homogenate region, cerebellum, and
206 temporal cortex had BP_{ND} values close to zero (Figure 3A). The (d₃)-[¹¹C]MODAG-001 test-retest scan
207 on the same day showed a -6.2% change in BP_{ND} (Supplementary figure 2). Pretreatment with MODAG-
208 001 resulted in a reduction in regional binding levels such that they became comparable to the reference
209 regions. In the pig that underwent a baseline-block study, we observed >100% occupancy in the α-PFF
210 injected regions. A modest reduction in binding was also observed in the temporal cortex and cerebellum
211 (Figure 3B).

212 Discussion

213 PET neuroimaging of aggregated protein has proved critical for diagnosing and monitoring disease
214 progression and treatment evaluation in neurodegenerative diseases with amyloid-β and tau pathology
215 [29, 30]. The ability to detect and quantify α-synuclein aggregates in the living human brain would be a
216 milestone achievement for the research of PD and other α-synucleinopathies [10, 31]. Due to its high
217 affinity to α-synuclein and favorable binding in rodent models, [¹¹C]MODAG-001 and its analogs are
218 currently some of the most promising radioligands for α-synuclein neuroimaging [12, 19].

219 To the best of our knowledge, this is the first time (d₃)-[¹¹C]MODAG-001 has been tested in a higher
220 species and shown promising translational results. We evaluated (d₃)-[¹¹C]MODAG-001 in a pig model of
221 intracerebral injection of α-PFF and postmortem human AD and DLB brain homogenates. We see high
222 brain uptake and quick-wash out of the radioligand in the brain. The pharmacokinetics in healthy mice
223 and the α-PFF rat model were comparable to that in pigs [12]. We saw a relatively high uptake of the

224 radioligand in the α -PFF regions at micromolar concentrations, with a dose-dependent response with 150
225 μg (415 μM) and 75 μg (208 μM) injections (Figure 1-3).

226 Kuebler et al. tested both [^{11}C]MODAG-001 and the deuterium incorporated (d_3)-[^{11}C]MODAG-001 [12];
227 deuterium incorporation was meant to improve the pharmacokinetic and metabolic profile of the
228 radioligand [32]. Notably, we observed faster metabolism in the pigs than what was observed in the mice,
229 which are much smaller mammals [33]. The results showed that $\sim 10\%$ parent fraction remained 15 min
230 post-injection in the pigs, compared to $\sim 30\%$ parent fraction in mice. Radio-HPLC on brain homogenate
231 (non-perfused) from a pig euthanized at 15 min showed $\sim 50\%$ parent fraction; in contrast, mice showed
232 on average $\sim 90\%$ parent fraction after 15 min (Supplementary Figure 1, Supplementary Table 1).

233 We performed the non-invasive kinetic modeling with the occipital cortex as a reference region since we
234 previously have shown in our pig model that the occipital cortex has similar tissue properties as saline-
235 injected target regions and that these are not affected by the intracerebral injection [22].

236 Due to the lack of other high-affinity molecules, an unlabelled MODAG-001 block scan was our best
237 option to examine the signal specificity. Pretreatment of 1 mg/kg of MODAG-001 leads to complete
238 blocking of the specific (d_3)-[^{11}C]MODAG-001 binding in the α -PFF injected region. We observe a very
239 high blocking percentage with values above 100% (using BP_{ND} values from reference modeling),
240 although these estimates are based on only one pig and likely prone to noise.

241 We also see high uptake in the amyloid- β and tau-rich AD homogenates but no significant uptake in the
242 DLB homogenate region (Figure 1 and 3); this is remarkable since DLB is considered to have a pure α -
243 synuclein pathology. Ideally, a radioligand should have high α -synuclein selectivity for it to distinguish α -
244 synuclein aggregates from amyloid- β and tau aggregates [10, 34]. Several things make us less enthusiastic
245 about the prospect of (d_3)-[^{11}C]MODAG-001 as a radioligand in human studies: (d_3)-[^{11}C]MODAG-001
246 did not display high binding in the DLB homogenate region; this could be due to low concentrations of
247 aggregated α -synuclein, as is most often seen in human pathology, especially at early disease stages. This

248 null-finding could also be due to the hypothesized difference in pathological morphology in pure α -
249 synuclein DLB subjects [35]. (d₃)-[¹¹C]MODAG-001 was also not very selective for α -synuclein and had
250 significant binding to the AD homogenate region. This observation is also on par with previous
251 autoradiography studies where the highest uptake was noted in human brain sections with AD [12].
252 Improving the signal-to-background ratio and selectivity will be critical for the further development of the
253 tracer, and this work is currently ongoing [12].

254 The intracerebral protein injection model used in the current study also comes with a set of limitations.
255 Since the intracerebral injections are done a few hours prior to scanning, it is unlikely that protein
256 aggregates enter into the brain cells, which does not mimic the intracellular inclusions seen in α -
257 synucleinopathies well [3, 5]. The concentration of the α -PFF in the model is much higher than that of
258 diseased brains, where α -synuclein is found to be at nanomolar concentration [12, 36]. This particular
259 setup allowed us to show proof of concept for α -synuclein aggregate detecting radioligands. The signal-
260 to-background ratio of (d₃)-[¹¹C]MODAG-001 makes it challenging to detect pathologically relevant α -
261 synuclein, i.e., at nanomolar concentrations.

262 In spite of the poor specificity and relatively modest signal-to-background ratio, we believe that (d₃)-
263 [¹¹C]MODAG-001 with its high affinity for α -synuclein is a suitable lead molecule for further radioligand
264 development and evaluation.

265 Conclusions

266 We demonstrate in vivo detection of α -PFF in pigs using (d₃)-[¹¹C]MODAG-001, which has previously
267 only been shown using a similar α -PFF injection rat model. The radioligand shows excellent brain
268 kinetics and test-retest variability. Although (d₃)-[¹¹C]MODAG-001 displays low specificity towards α -
269 synuclein and a potential passage of radiometabolites through the blood-brain barrier, it shows promise as
270 a lead tracer for further radiotracer development.

271 List of abbreviations

- 272 α -PFF: α -synuclein preformed fibrils
273 AD: Alzheimer's disease
274 BP_{ND}: binding potential non-displaceable
275 DLB: dementia with Lewy bodies
276 HRRT: high-resolution research tomograph
277 IV: intra-venous
278 IM: intra-muscular
279 mPFC: medial prefrontal cortex
280 MSA: multiple system atrophy
281 PD: Parkinson's disease
282 PET: positron emission tomography
283 R-HPLC: radio-high performance liquid chromatography
284 SRTM: simplified reference tissue model
285 SUV: standardized uptake values
286 TAC: time-activity curve

287 Declarations

288 Ethics approval

- 289 All animal procedures were performed in accordance with the European Commission's Directive
290 2010/63/EU, as well as the ARRIVE guidelines, and were approved by the Danish Council of Animal
291 Ethics (Journal no. 2017-15-0201-01375).

292 Consent for publication

293 Not applicable

294 Availability of data and material

295 All data, including R scripts, is available at a GitHub repository

296 (https://github.com/nakulrraval/Protien_inj_pig_model_MODAG001). All other requests are directed to
297 this article's corresponding or first author.

298 Competing interests

299 Lundbeck A/S, Denmark provided the α -synuclein preformed fibrils as part of the European Union's
300 Horizon 2020 research and innovation program under the Marie Skłodowska-Curie grant agreement No.
301 813528. However, they had no other financial interests in the project. GMK received honoraria as a
302 speaker and consultant for Sage Pharmaceuticals/Biogen and Sanos A/S. All other authors declare no
303 conflict of interest.

304 Funding



306 This project has received funding from the European Union's Horizon 2020 research and innovation
307 program under the Marie Skłodowska-Curie grant agreement No. 813528. This project also received
308 funding from Parkinsonforeningen, Denmark (R16-A247). Pontus Plavén Sigray was supported by the
309 Lundbeck Foundation (R303-2018-3263). Vladimir Shalgunov was supported by the Lundbeck
310 Foundation (R303-2018-3567), the Novo Nordisk Foundation (grant agreement no. NNF18SA0034956),

311 and BRIDGE – Translational Excellence Program at the Faculty of Health and Medical Sciences,
312 University of Copenhagen.

313 Authors' contribution

314 NRR, MMH, HDH, PPS, GMK: conceptualization and design. NRR, CAM, EEB, LMJ, HDH: surgical
315 setup and PET scanning. VS, AN, UMB: compound synthesis, radiochemistry, and HPLC analysis. NRR,
316 VS, AN, UMB, MJ, PPS: analysis and software. NRR, MMH, HDH, GMK: resources. NR, HDH, PPS,
317 GMK: data curation. LMJ, MMH, HDH, PPS, GMK: supervision. NRR: preparation of manuscript draft
318 including figures. NRR, CAM, VS, AN, UMB, EEB, MJ, LMJ, MMH, HDH, PPS, GMK: manuscript
319 review and editing. NRR, MMH, GMK: funding acquisition. All authors have read and agreed to the
320 current version of the manuscript.

321 Acknowledgments

322 We want to thank Lundbeck A/S, Valby, Denmark, for providing the α -synuclein preformed fibrils. This
323 research project received human brain tissue from the Neuropathology Core of the Emory Center for
324 Neurodegenerative Disease; we are grateful for their support. We would sincerely like to thank the staff
325 and veterinarians at EMED, Panum, København University, and the PET and cyclotron unit at
326 Rigshospitalet. Further, we would like to thank Ran Sing Saw, Marko Rosenholm, and Natalie
327 Beschorner for their help during PET scans. We also extend our thanks to Ran Sing Saw for scientific
328 discussions.

329 References:

330 1. Braak H, Braak E (2000) Pathoanatomy of Parkinson's disease. *J Neurol* 247 Suppl 2:II3–10

- 331 2. Vekrellis K, Xilouri M, Emmanouilidou E, Rideout HJ, Stefanis L (2011) Pathological roles of α -
332 synuclein in neurological disorders. *Lancet Neurol* 10:1015–1025
- 333 3. Lashuel HA, Overk CR, Oueslati A, Masliah E (2013) The many faces of α -synuclein: from
334 structure and toxicity to therapeutic target. *Nat Rev Neurosci* 14:38–48
- 335 4. Alafuzoff I, Hartikainen P (2017) Alpha-synucleinopathies. *Handb Clin Neurol* 145:339–353
- 336 5. Goedert M, Jakes R, Spillantini MG (2017) The Synucleinopathies: Twenty Years On. *J Parkinsons*
337 *Dis* 7:S51–S69
- 338 6. Valera E, Masliah E (2018) The neuropathology of multiple system atrophy and its therapeutic
339 implications. *Auton Neurosci* 211:1–6
- 340 7. Tolosa E, Wenning G, Poewe W (2006) The diagnosis of Parkinson’s disease. *Lancet Neurol* 5:75–
341 86
- 342 8. Ziebell M, Andersen BB, Thomsen G, Pinborg LH, Karlsborg M, Hasselbalch SG, Knudsen GM
343 (2012) Predictive value of dopamine transporter SPECT imaging with [¹²³I]PE2I in patients with
344 subtle parkinsonian symptoms. *Eur J Nucl Med Mol Imaging* 39:242–250
- 345 9. Tiepolt S, Patt M, Aghakhanyan G, Meyer PM, Hesse S, Barthel H, Sabri O (2019) Current
346 radiotracers to image neurodegenerative diseases. *EJNMMI Radiopharm Chem* 4:17
- 347 10. Korat Š, Bidesi NSR, Bonanno F, et al (2021) Alpha-Synuclein PET Tracer Development—An
348 Overview about Current Efforts. *Pharmaceuticals* 14:847
- 349 11. Bidesi NSR, Vang Andersen I, Windhorst AD, Shalgunov V, Herth MM (2021) The role of
350 neuroimaging in Parkinson’s disease. *J Neurochem* 159:660–689
- 351 12. Kuebler L, Buss S, Leonov A, et al (2020) [¹¹C]MODAG-001—towards a PET tracer targeting α -

- 352 synuclein aggregates. *Eur J Nucl Med Mol Imaging*. <https://doi.org/10.1007/s00259-020-05133-x>
- 353 13. Capotosti F, Vokali E, Molette J, et al (2020) Developing a novel alpha-synuclein positron emission
354 tomography (PET) tracer for the diagnosis of synucleinopathies. *Alzheimers Dement*.
355 <https://doi.org/10.1002/alz.043249>
- 356 14. Hooshyar Yousefi B, Shi K, Arzberger T, Wester HJ, Schwaiger M, Yakushev I, Weber W (2019)
357 Translational study of a novel alpha-synuclein PET tracer designed for first-in-human investigating.
358 In: *NuklearMedizin 2019*. Georg Thieme Verlag KG, p L25
- 359 15. Kaide S, Watanabe H, Shimizu Y, Iikuni S, Nakamoto Y, Hasegawa M, Itoh K, Ono M (2020)
360 Identification and Evaluation of Bisquinoline Scaffold as a New Candidate for α -Synuclein-PET
361 Imaging. *ACS Chem Neurosci* 11:4254–4261
- 362 16. Verdurand M, Levigoureux E, Zeinyeh W, et al (2018) In Silico, in Vitro, and in Vivo Evaluation of
363 New Candidates for α -Synuclein PET Imaging. *Mol Pharm* 15:3153–3166
- 364 17. Wagner J, Ryazanov S, Leonov A, et al (2013) Anle138b: a novel oligomer modulator for disease-
365 modifying therapy of neurodegenerative diseases such as prion and Parkinson's disease. *Acta*
366 *Neuropathol* 125:795–813
- 367 18. Heras-Garvin A, Weckbecker D, Ryazanov S, Leonov A, Griesinger C, Giese A, Wenning GK,
368 Stefanova N (2019) Anle138b modulates α -synuclein oligomerization and prevents motor decline
369 and neurodegeneration in a mouse model of multiple system atrophy. *Mov Disord* 34:255–263
- 370 19. Maurer A, Leonov A, Ryazanov S, et al (2019) ¹¹C radiolabeling of anle253b: A putative PET
371 tracer for Parkinson's disease that binds to alpha-synuclein fibrils in vitro and crosses the blood-
372 brain barrier. *ChemMedChem*. <https://doi.org/10.1002/cmdc.201900689>
- 373 20. Raval NR, Nasser A, Madsen CA, et al (2022) An in vivo pig model for testing novel PET

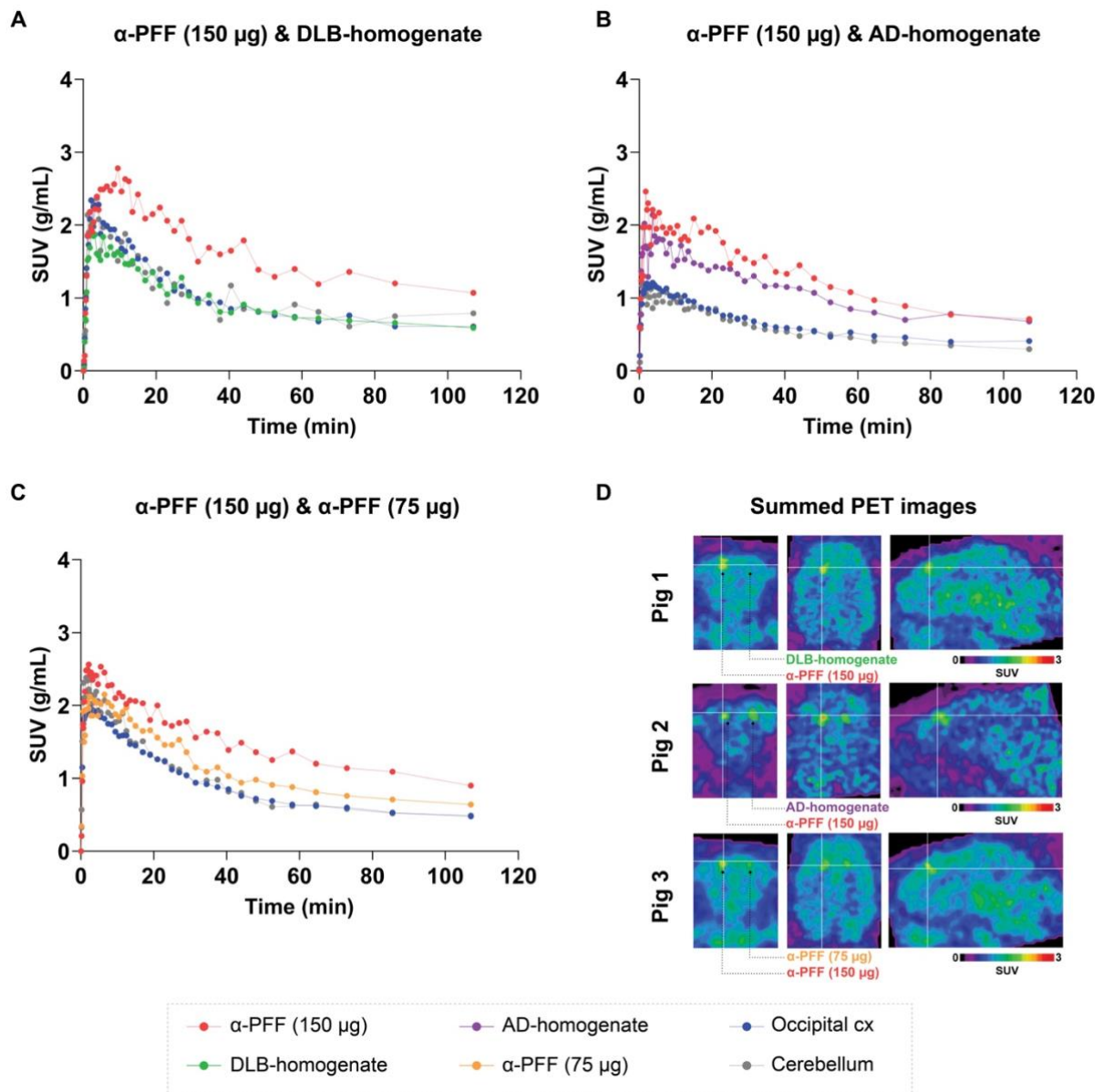
- 374 radioligands targeting cerebral protein aggregates. bioRxiv 2021.12.31.473908
- 375 21. Jørgensen LM, Baandrup AO, Mandeville J, Glud AN, Sørensen JCH, Weikop P, Jespersen B,
376 Hansen AE, Thomsen C, Knudsen GM (2021) An FMRI-compatible system for targeted electrical
377 stimulation. Research Square. <https://doi.org/10.21203/rs.3.rs-313183/v1>
- 378 22. Raval NR, Nasser A, Madsen CA, et al (2022) An in vivo pig model for testing novel PET
379 radioligands targeting cerebral protein aggregates. bioRxiv 2021.12.31.473908
- 380 23. Sureau FC, Reader AJ, Comtat C, Leroy C, Ribeiro MJ, Buvat I, Trébossen R (2008) Impact of
381 image-space resolution modeling for studies with the high-resolution research tomograph. *J Nucl*
382 *Med* 49:1000–1008
- 383 24. Keller SH, Svarer C, Sibomana M (2013) Attenuation correction for the HRRT PET-scanner using
384 transmission scatter correction and total variation regularization. *IEEE Trans Med Imaging* 32:1611–
385 1621
- 386 25. Villadsen J, Hansen HD, Jørgensen LM, Keller SH, Andersen FL, Petersen IN, Knudsen GM, Svarer
387 C (2017) Automatic delineation of brain regions on MRI and PET images from the pig. *J Neurosci*
388 *Methods* 294:51–58
- 389 26. Saikali S, Meurice P, Sauleau P, Eliat P-A, Bellaud P, Randuineau G, Vérin M, Malbert C-H (2010)
390 A three-dimensional digital segmented and deformable brain atlas of the domestic pig. *J Neurosci*
391 *Methods* 192:102–109
- 392 27. Logan J, Fowler JS, Volkow ND, Wang GJ, Ding YS, Alexoff DL (1996) Distribution volume ratios
393 without blood sampling from graphical analysis of PET data. *J Cereb Blood Flow Metab* 16:834–840
- 394 28. Lammertsma AA, Hume SP (1996) Simplified reference tissue model for PET receptor studies.
395 *Neuroimage* 4:153–158

- 396 29. Barthel H, Sabri O (2017) Clinical Use and Utility of Amyloid Imaging. *J Nucl Med* 58:1711–1717
- 397 30. Shah M, Catafau AM (2014) Molecular Imaging Insights into Neurodegeneration: Focus on Tau
398 PET Radiotracers. *J Nucl Med* 55:871–874
- 399 31. Eberling JL, Dave KD, Frasier MA (2013) α -synuclein imaging: a critical need for Parkinson's
400 disease research. *J Parkinsons Dis* 3:565–567
- 401 32. Klenner MA, Pascali G, Fraser BH, Darwish TA (2021) Kinetic isotope effects and synthetic
402 strategies for deuterated carbon-11 and fluorine-18 labelled PET radiopharmaceuticals. *Nucl Med*
403 *Biol* 96-97:112–147
- 404 33. Tang H, Mayersohn M (2018) Porcine prediction of pharmacokinetic parameters in people: A pig in
405 a poke? *Drug Metab Dispos* 46:1712–1724
- 406 34. Alpha-Synuclein Imaging Prize. <https://www.michaeljfox.org/news/alpha-synuclein-imaging-prize>.
407 Accessed 24 Dec 2021
- 408 35. Peng C, Gathagan RJ, Lee VM-Y (2018) Distinct α -Synuclein strains and implications for
409 heterogeneity among α -Synucleinopathies. *Neurobiol Dis* 109:209–218
- 410 36. Morgan SA, Lavenir I, Fan J, Masuda-Suzukake M, Passarella D, DeTure MA, Dickson DW, Ghetti
411 B, Goedert M (2020) α -Synuclein filaments from transgenic mouse and human synucleinopathy-
412 containing brains are major seed-competent species. *J Biol Chem* 295:6652–6664

413

414

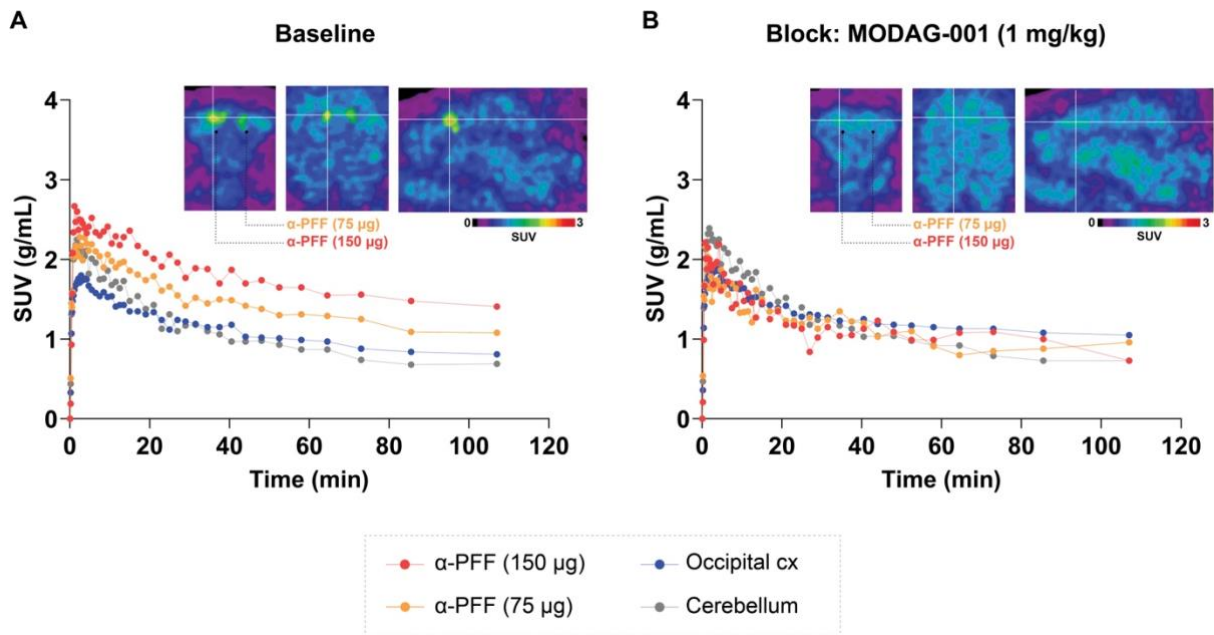
415



416

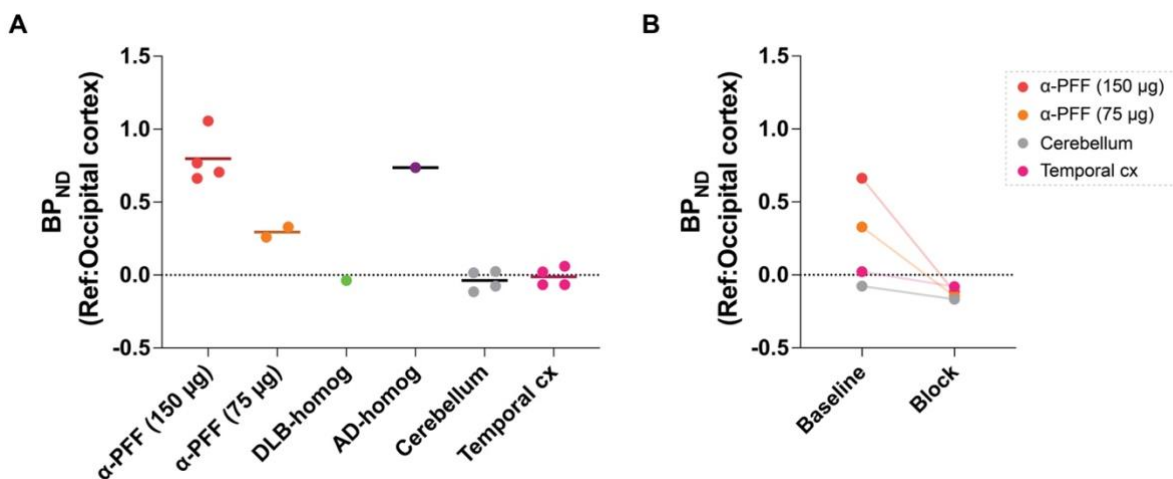
417 **Figure 1.** Regional TACs of (d₃)-[¹¹C]MODAG-001 in pigs injected with 150 μ g α -PFF and A) DLB
418 homogenate, B) AD homogenate and C) 75 μ g α -PFF. TACs for the two reference regions, ie, the
419 occipital cortex and cerebellum, are also shown. D) SUV-scaled PET images from representative TACs.

20



420

421 **Figure 2.** (d₃)-[¹¹C]MODAG-001 baseline and block. TACs and SUV scaled PET images A) (d₃-
422 [¹¹C]MODAG-001 baseline and B) (d₃)-[¹¹C]MODAG-001+ MODAG-001 (1 mg/kg) block scan from a
423 pig with 150 µg and 75 µg α-PFF.



424

425 **Figure 3.** Kinetic modeling outcomes of (d₃)-[¹¹C]MODAG-001. A) BP_{ND} as determined with the non-
426 invasive Logan graphical analysis using the occipital cortex as a reference region, in the injected brain
427 regions, temporal cortex, and cerebellum. Retest and block are not included. B) BP_{ND} at baseline after
428 (d₃)-[¹¹C]MODAG-001 blocking.

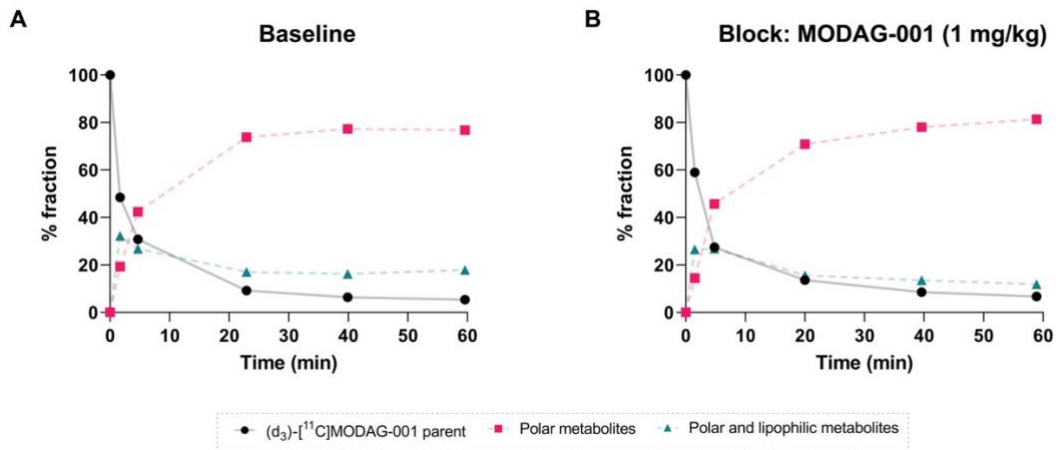
429

Supplementary information

1

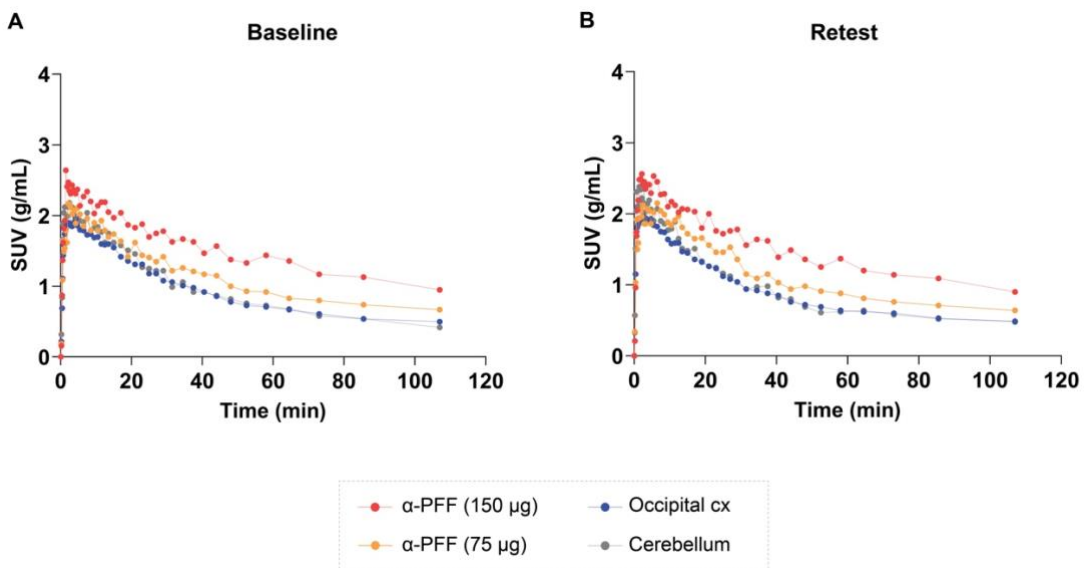
Supplementary Figures

2



3

4 **Supplementary Figure 1. (d₃)-[¹¹C]MODAG-001 parent and metabolites.** Time course of the
5 percentage of (d₃)-[¹¹C]MODAG-001 parent and metabolites in pig arterial plasma (n = 1 x 2 scans). The
6 bold black line shows the course of the parent fraction over 60 min while the dashed pink and green line
7 shows the course of the radiometabolite seen in the pigs.



8

9 **Supplementary Figure 2. Test-retest TACs** from a pig injected with 150 µg and 75 µg α -synuclein-
10 preformed-fibrils (α -PFF) that received two (d₃)-[¹¹C]MODAG-001 as a test (A) and retest/rescan (B).

11 Supplementary Data

12 Synthesis of reagents

13 All reagents and solvents were dried prior to use according to standard methods. Commercial reagents
14 were used without further purification. Analytical TLC was performed using silica gel 60 F254 (Merck)
15 with detection by UV absorption and/or by charring following immersion in a 7% ethanolic solution of
16 sulfuric acid or KMnO₄-solution (1.5 g of KMnO₄, 10 g K₂CO₃, and 1.25 mL 10% NaOH in 200 mL
17 water). Purification of compounds was carried out by column chromatography on silica gel (40-60 µm, 60
18 Å) or employing a CombiFlash NextGen 300+ (Teledyne ISCO). ¹H and ¹³C NMR spectra were recorded
19 on Bruker (400 and 600 MHz instruments), using Chloroform-d, Methanol-d₄ or DMSO-d₆ as deuterated
20 solvent and with the residual solvent as the internal reference. For all NMR experiments the deuterated
21 solvent signal was used as the internal lock. Chemical shifts are reported in δ parts per million (ppm).
22 Coupling constants (J values) are given in Hertz (Hz). Multiplicities of ¹H NMR signals are reported as
23 follows: s, singlet; d, doublet; dd, doublet of doublets; ddd, doublet of doublets of doublets; dt, doublet of
24 triplets; t, triplet; q, quartet; m, multiplet; br, broad signal. NMR spectra of all compounds are reprocessed
25 in MestReNova software (version 12.0.22023) from original FID's files. Mass spectra analysis was
26 performed using MS-Acquity-A: Waters Acquity UPLC
27 with QDa-detector.

28 4-[3-(4-Dimethylaminophenyl)-1*H*-pyrazol-5-yl]-2-bromopyridine (MODAG-001)

29 To a solution of 1-[4-(dimethylamino)phenyl]ethanone (490 mg, 3.00 mmol) and methyl 2-
30 bromopyridine-4-carboxylate (843 mg, 3.9 mmol) in DMSO (7.5 mL) and THF (1.9 mL) sodium hydride

31 (60 % in oil, 3.9 mmol, 156 mg) was added, and the reaction mixture was stirred at 20 °C for 15 hours.
32 The reaction mixture was poured into 50 mL of an ice water and 1 M phosphate buffer, pH 7 (10 mL),
33 stirred for one hour, the resulting precipitate was filtered off, washed with water (2 × 10 mL), methanol (10
34 mL), hexane (10 mL), and dried on the air to obtain a crude intermediate 1-(2-bromopyridin-4-yl)-3-[4-
35 (dimethylamino)phenyl]propane-1,3-dione as an orange solid. To a suspension of this crude intermediate
36 in THF (20 mL) hydrazine hydrate (292 µL, 300 mg, 6 mmol) was added. The reaction mixture was
37 stirred at 70 °C for five hours, cooled and concentrated *in vacuo*. The residue was suspended in methanol
38 (10 mL), filtered off, washed with cold methanol (2 × 5 mL), recrystallized from *n*-butanol (10 mL) and
39 *N,N*-dimethylformamide (0.2 mL), and dried to afford 0.47 g (46%) of (4-[3-(4-dimethylaminophenyl)-
40 1*H*-pyrazol-5-yl]-2-bromopyridine as a light pink solid. ¹H NMR (600 MHz, DMSO) δ 13.45 (d, J = 2.0
41 Hz, 1H), 8.40 (d, J = 5.1 Hz, 1H), 8.02 (d, J = 1.4 Hz, 1H), 7.86 (dd, J = 5.1, 1.4 Hz, 1H), 7.62 (d, J = 8.8
42 Hz, 2H), 7.25 (d, J = 2.0 Hz, 1H), 6.81 (d, J = 8.9 Hz, 2H), 2.96 (s, 6H); ¹³C NMR (101 MHz, DMSO) δ
43 151.27, 150.76, 147.87, 145.32, 144.78, 142.70, 126.60, 123.52, 119.55, 116.92, 112.71, 99.80, 40.37.

44 *Tert*-butyl (4-acetylphenyl)carbamate

45 A mixture of 4-aminoacetophenone (2.00 g, 14.79 mmol) and di-*tert*-butyl dicarbonate (3.52 g, 16.13
46 mmol) in THF (40 mL) was refluxed for 5 h. After dilution with diethyl ether (45 mL), the mixture was
47 washed sequentially with saturated aqueous citric acid solution (20 mL), 1N NaHCO₃ (30 mL), and brine
48 (30 mL). The organic layer was dried over anhydrous MgSO₄ and evaporated to give white crystals. The
49 compound was recrystallized from EtOAc to give 3.2 g (92%) of the desired product. R_f = 0.27 (80/20 *n*-
50 heptane/EtOAc); ¹H NMR (400 MHz, CDCl₃) δ 7.90 (d, J = 8.5 Hz, 2H), 7.45 (d, J = 8.5 Hz, 2H), 6.80 (s,
51 1H), 2.55 (s, 3H), 1.52 (s, 9H); ¹³C NMR (101 MHz, CDCl₃) δ 196.90, 152.18, 142.95, 131.85, 129.84,
52 117.42, 81.28, 28.27, 26.35.

53 *Tert*-butyl (4-acetylphenyl)(methyl-d₃)carbamate

54 A mixture of *tert*-butyl *N*-(4-acetylphenyl)carbamate (2.1 g, 8.92 mmol) in anhydrous THF (50 mL)
55 under nitrogen was cooled to 0 °C, and sodium hydride (0.43 g, 10.71 mmol, 60 wt % dispersion in
56 mineral oil) was added portion-wise over the course of 10 min. After 20 min, CD₃I (1.39 mL, 22.31
57 mmol) was added, and the white suspension was warmed to room temperature and stirred until it formed
58 an amber solution. After completion, the reaction was quenched with water (50 mL) and extracted with
59 CH₂Cl₂ (3 x 20 mL). Purification by flash chromatography (90/10 *n*-heptane/EtOAc) afforded 1.71 g
60 (76%) of the desired product as a colorless oil. R_f = 0.38 (80/20 *n*-heptane/EtOAc); ¹H NMR (400 MHz,
61 CDCl₃) δ 7.94 (d, J = 8.5 Hz, 2H), 7.38 (d, J = 8.6 Hz, 2H), 2.60 (s, 3H), 1.50 (s, 9H); ¹³C NMR (101
62 MHz, CDCl₃) δ 197.08, 154.11, 148.05, 133.43, 128.84, 124.29, 81.13, 36.31 (m), 28.29, 26.50.

63 1-(4-((Methyl-d₃)amino)phenyl)ethan-1-one

64 To a solution of the *tert*-butyl (4-acetylphenyl)(methyl-d₃)carbamate (2.05 g, 8.12 mmol) in CH₂Cl₂ (20
65 mL) was added TFA (6.24 mL, 81.24 mmol). The solution was stirred at rt for 12 hours. The reaction was
66 quenched with a saturated solution of NaHCO₃ (20 mL) and the organic phase separated. Evaporation
67 under reduced pressure afforded 1.22 g (99%) of the desired product as a magenta solid. R_f = 0.25 (70/30
68 *n*-heptane/EtOAc); ¹H NMR (400 MHz, CDCl₃) δ 7.82 (d, J = 8.8 Hz, 2H), 6.55 (d, J = 8.8 Hz, 2H), 4.10
69 (s, 1H), 2.49 (s, 3H); ¹³C NMR (101 MHz, CDCl₃) δ 196.45, 153.15, 130.78, 126.56, 111.09, 29.36 (m)
70 25.99.

71 1-(4-(Methyl(methyl-d₃)amino)phenyl)ethan-1-one

72 To a mixture of 1-(4-((methyl-d₃)amino)phenyl)ethan-1-one (1.00 g, 6.57 mmol) and K₂CO₃ (2.27 g,
73 16.42 mmol) in acetone (50 mL) was added CH₃I (1.63 mL, 26.28 mmol) was added, and the white
74 suspension was stirred for 12 hours at room temperature. After completion, the reaction was quenched
75 with water (60 mL) and extracted with CH₂Cl₂ (3 x 40 mL). Purification by flash chromatography (80/20
76 *n*-heptane/EtOAc) afforded 1.05 g (96%) of the desired product as a white solid. R_f = 0.35 (70/30 *n*-

77 heptane/EtOAc); ¹H NMR (400 MHz, CDCl₃) δ 7.88 (d, J = 9.0 Hz, 2H), 6.71 (d, J = 9.0 Hz, 2H), 3.06 (s,
78 3H), 2.51 (s, 3H); ¹³C NMR (151 MHz, CDCl₃) δ 196.40, 153.08, 130.54, 126.05, 111.13, 40.27, 39.57
79 (m), 26.02.

80 4-(5-(2-Bromopyridin-4-yl)-1H-pyrazol-3-yl)-N-methyl-N-(methyl-d₃)aniline (d₃-MODAG-001
81 reference)

82 To a solution of 1-(4-(Methyl(methyl-d₃)amino)phenyl)ethan-1-one (0.63 g, 3.79 mmol) and methyl 2-
83 bromopyridine-4-carboxylate (1.06 g, 4.92 mmol) in DMSO (15 mL) and THF (4 mL) sodium hydride
84 (0.19 g, 7.58 mmol, 60 wt % dispersion in mineral oil) was added, and the reaction mixture was stirred at
85 20 °C for 15 hours. The reaction mixture was poured into 50 mL of an ice water and 1 M phosphate
86 buffer, pH 7 (10 mL). The resulting precipitate was filtered off, washed with water (2 x 10 mL), methanol
87 (10 mL), hexane (10 mL), and dried on to obtain the crude dione intermediate as an orange solid. To a
88 suspension of this crude intermediate in THF (20 mL) hydrazine hydrate (0.37 mL, 7.58 mmol) was
89 added. The reaction mixture was stirred at 70 °C for five hours, cooled and concentrated under reduced
90 pressure. The residue was suspended in methanol (10 mL), filtered off, washed with cold methanol and
91 recrystallized from n-butanol (10 mL) and N,N-dimethylformamide (0.2 mL) to give 0.56 g (43%) of the
92 desired product. ¹H NMR (600 MHz, DMSO) δ 13.46 (s, 1H), 8.40 (d, J = 5.1 Hz, 1H), 8.03 (s, 1H), 7.86
93 (d, J = 5.2 Hz, 1H), 7.63 (d, J = 8.3 Hz, 2H), 7.25 (s, 1H), 6.79 (d, J = 8.3 Hz, 2H), 2.94 (s, 3H).

94 Tert-butyl (4-(3-(2-bromopyridin-4-yl)-3-oxopropanoyl)phenyl)(methyl-d₃)carbamate

95 To a solution of tert-butyl N-(4-acetylphenyl)-N-(²H₃)methylcarbamate (1.7 g, 6.73 mmol) and methyl 2-
96 bromopyridine-4-carboxylate (1.89 g, 8.75 mmol) in DMSO (15 mL) and THF (4 mL) sodium hydride
97 (0.35 g, 8.75 mmol, 60 wt % dispersion in mineral oil) was added, and the reaction mixture was stirred at
98 20 °C for 15 hours. The reaction mixture was poured into 50 mL of an ice water and 1 M phosphate
99 buffer, pH 7 (10 mL). Extraction with CH₂Cl₂ (3 x 40 mL) afforded 3.1 g of crude. Purification by flash
100 chromatography (90/10 n-heptane/EtOAc) afforded 1.05 g (36%) of the desired product as a yellow oil.

101 R_f = 0.17 (80/20 n-heptane/EtOAc); ¹H NMR (400 MHz, CDCl₃) δ 8.53 (dd, J = 5.1, 0.7 Hz, 1H), 8.02 –
102 7.92 (m, 3H), 7.73 (dd, J = 5.1, 1.5 Hz, 1H), 7.44 (d, J = 8.9 Hz, 2H), 6.80 (s, 1H), 1.50 (s, 9H); ¹³C NMR
103 (101 MHz, CDCl₃) δ 187.86, 179.09, 154.02, 150.94, 148.47, 145.14, 143.16, 130.87, 128.05, 125.13,
104 124.41, 119.49, 94.07, 81.37, 35.76 (m), 28.31.

105 Tert-butyl (4-(5-(2-bromopyridin-4-yl)-1H-pyrazol-3-yl)phenyl)(methyl-d₃)carbamate

106 To a suspension of tert-butyl (4-(3-(2-bromopyridin-4-yl)-3-oxopropanoyl)phenyl)(methyl-d₃)carbamate
107 (0.70 g, 1.60 mmol) in THF (20 mL) hydrazine hydrate (0.16 mL, 3.20 mmol) was added. The reaction
108 mixture was stirred at 60 °C for five hours, cooled and concentrated under reduced pressure. The
109 compound was purified by flash chromatography (98/2 CH₂Cl₂/MeOH) to yield 0.68 g (98%) of the
110 desired compound as a white foam. R_f = 0.35 (95/5 CH₂Cl₂/MeOH); ¹H NMR (400 MHz, CDCl₃) δ 10.88
111 (s, 1H), 8.40 (d, J = 5.2 Hz, 1H), 7.92 (s, 1H), 7.67 (dd, J = 5.2, 1.5 Hz, 1H), 7.55 (d, J = 8.5 Hz, 2H),
112 7.35 (d, J = 8.5 Hz, 2H), 6.87 (s, 1H), 1.50 (s, 9H); ¹³C NMR (101 MHz, CDCl₃) δ 154.64, 150.50,
113 144.41, 142.93, 125.83, 125.73, 124.15, 119.11, 100.97, 80.97, 53.42, 36.23 (m), 28.37.

114 4-(5-(2-Bromopyridin-4-yl)-1H-pyrazol-3-yl)-N-(methyl-d₃)aniline (desmethyl precursor for
115 reductive amination)

116 To a solution of tert-butyl (4-(5-(2-bromopyridin-4-yl)-1H-pyrazol-3-yl)phenyl)(methyl-d₃)carbamate
117 (0.60 g, 1.39 mmol) in CH₂Cl₂ (5 mL) was added TFA (1.06 mL, 13.90 mmol). The reaction was stirred
118 for 2 hours and concentrated under reduced pressure. Purification by flash chromatography (98/2
119 CH₂Cl₂/MeOH) afforded 0.42 (91%) g of the desired compound as a beige solid. R_f = 0.30 (95/5
120 CH₂Cl₂/MeOH); ¹H NMR (400 MHz, DMSO) δ 13.29 (s, 1H), 8.31 (d, J = 5.2 Hz, 1H), 7.92 (s, 1H), 7.76
121 (d, J = 5.2 Hz, 1H), 7.45 (d, J = 8.2 Hz, 2H), 7.11 (s, 1H), 6.53 (d, J = 8.4 Hz, 2H), 5.84 (s, 1H).

122 Radiochemistry

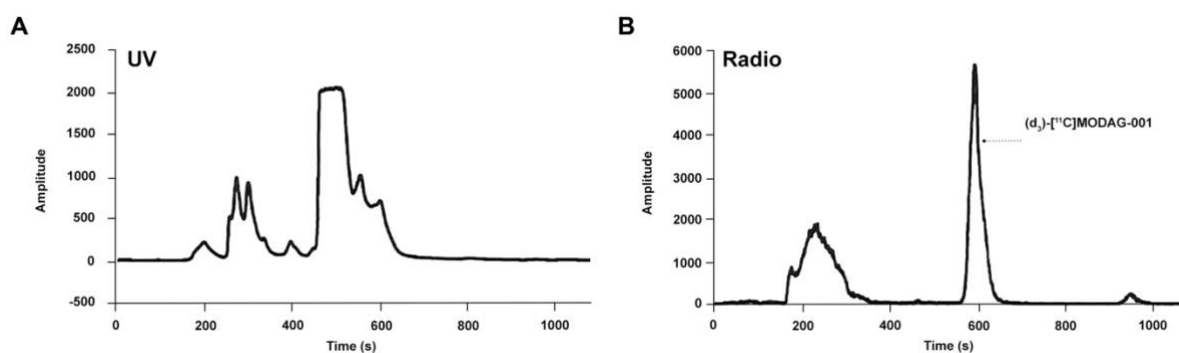
123 General information

124 Radiochemistry was performed at the Department of Clinical Physiology, Nuclear Medicine & PET,
125 Rigshospitalet, Denmark. [¹¹C]CH₄ was produced via the ¹⁴N(p,α)¹¹C reaction in a gaseous target of N₂
126 (+10% H₂) with a 16 MeV proton beam in a Scanditronix MC32 cyclotron (Scandtronix Magnet AB,
127 Vislanda, Sweden) and converted into [¹¹C]CH₃I via gas-phase iodination as described in Larsen et. al.
128 [1]. The time at which [¹¹C]CH₄ was delivered to the synthesis module is defined as the start-of-synthesis,
129 while the end-of-synthesis is defined as the time at which the activity of the formulated (d₃)-
130 [¹¹C]MODAG-001 was measured. Automated synthesis was performed on a Scansys Laboratorieteknik
131 (Scansys Laboratorieteknik ApS, Værløse, Denmark) synthesis module housed in a hot cell. Analytical
132 HPLC was performed on a Dionex system connected to a P680A pump, a UVD 170U UV/Vis detector,
133 and a Scansys radiodetector. The system was controlled by Chromeleon software. Semi-preparative
134 HPLC was performed on the built-in HPLC system in the synthesis module.

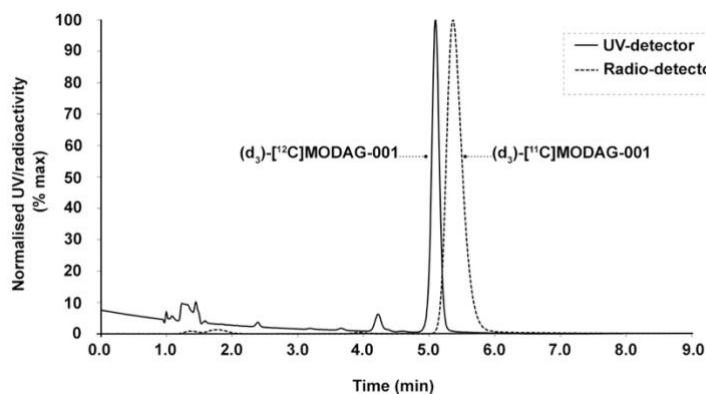
135 Synthesis of (d₃)-[¹¹C]MODAG-001

136 (d₃)-[¹¹C]MODAG-001 was prepared as described in [2] with minor modifications. Namely, [¹¹C]CH₃I
137 was bubbled in a helium stream through a solution of trimethylamine N-oxide (5 mg) and 4-(5-(2-
138 bromopyridin-4-yl)-1H-pyrazol-3-yl)-N-(methyl-d₃)aniline (1 mg) in diethyl formamide (350 μL) at -20
139 °C. The mixture was heated to 60 °C for 5 min and subsequently cooled to 40 °C. Sodium
140 cyanoborohydride (7-8 mg) in a mixture of diethyl formamide (60 μL) and sodium citrate buffer (100
141 mM pH 4.6, 0.55 mL) was added and heated to 100 °C for 5 min. After labeling, the reaction was diluted
142 with water (2.7 mL) and purified with semipreparative HPLC (Supplementary Figure 3) on a Luna C18
143 column (5 μm, 100 Å, 250 mm x 10 mm, Phenomenex, Germany) with 33 % MeCN and 0.1% TFA in
144 water at a flow rate of 4 mL/min. The HPLC fraction containing the product was diluted with 70 mL of

145 water and loaded onto a Sep Pak C18 Plus Light cartridge (Waters, USA). The product was eluted with
146 0.7 mL of ethanol and diluted with 10 mL of phosphate buffer (100 mM, pH 7.2).
147
148 Radiochemical conversion (RCC) of (d₃)-[¹¹C]MODAG-001 was determined by analyzing an aliquot
149 labeling of the reaction mixture by analytical radio-HPLC. The identity of (d₃)-[¹¹C]MODAG-001 was
150 confirmed by co-elution with an unlabelled ¹²C-reference compound on radio-HPLC. The molar activity
151 (Am) was determined by integrating the area of the UV absorbance peak corresponding to the
152 radiolabeled product on the analytical HPLC chromatogram (average of 2 runs). This area was converted
153 into mass concentration by comparison with a calibration curve for a known range of concentrations of
154 (d₃)-MODAG-001 reference.



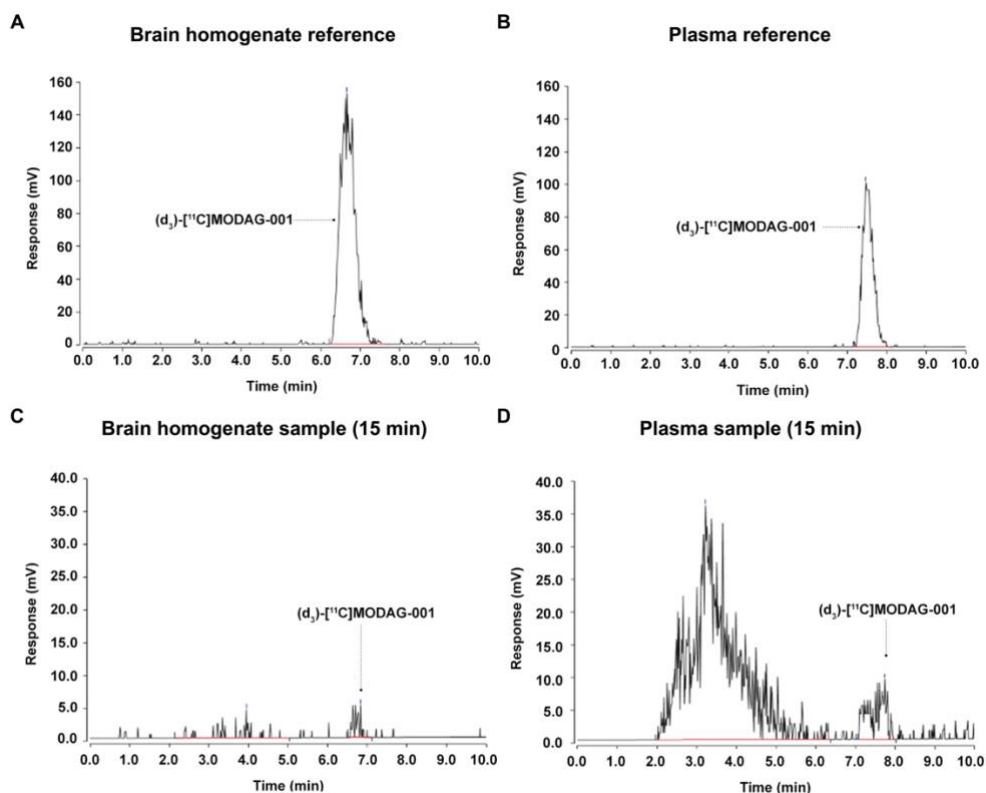
155
156 **Supplementary Figure 3. Semipreparative HPLC.** Representative UV and radio trace for (d₃-
157 [¹¹C]MODAG-001.



159 **Supplementary Figure 4. Analytical HPLC.** Representative UV and radio trace for (d₃)-[¹¹C]MODAG-
160 001 spiked with unlabelled (d₃)-[¹²C]MODAG-001. HPLC conditions: Luna 5µm PFP(2) 150x4.6 mm
161 eluted with ACN/water/TFA (30/70/0.1 v/v) at 1.5 mL/min.

162 Radio-HPLC of blood and brain samples:

163 The HPLC system was equipped with a Luna C18(2) column (5 µm, 250 x 4.6 mm; Phenomenex,
164 Torrance, CA, USA) eluting with 65% of 0.1% (v/v) trifluoroacetic acid in water and 35 % acetonitrile at
165 a flow rate of 1.5 mL/min. Blood was centrifuged for 5 min at 3234 x g, 4°C. Brain tissue was weighed,
166 homogenized in 4 volumes of PBS, and centrifuged for 5 min at 3234 x g and 4°C. Plasma and brain
167 homogenate was precipitated with ice-cold acetonitrile (1:1) and centrifuged for 5 min at 6000 x g, 4°C.
168 The supernatant of both samples was subsequently filtered through a syringe filter (Whatman GD/X 13
169 mm, PVDF membrane, 0.45 mm pore size; Frisette ApS, Knebel, Denmark) before injection of 3 mL
170 into the HPLC. The eluent from the HPLC system was passed through the radiochemical detector (Posi-
171 RAM Model 4; LabLogic, Sheffield, UK) for online detection of radioactive metabolites and parent
172 tracer. Eluents from the HPLC were collected with a fraction collector (Foxy Jr FC144; Teledyne,
173 Thousand Oaks, CA, USA), and fractions were counted offline in a gamma well counter (2480 Wizard2
174 Automatic Gamma Counter, PerkinElmer, Finland). The parent fraction was determined as the percentage
175 of the radioactivity of the parent to the total radioactivity collected.



176

177 **Supplementary Figure 5. HPLC chromatograms.** Representative reference radio-chromatograms from
178 (d₃)-[¹¹C]MODAG-001 spiked brain homogenate (A) and plasma (B). Radio-chromatograms from brain
179 homogenate (C) and plasma (D) samples 15 min post tracer injection at euthanasia (n=1).

180 **Supplementary Table 1: Percentage of (d₃)-[¹¹C]MODAG-001 parent and radiometabolites.**

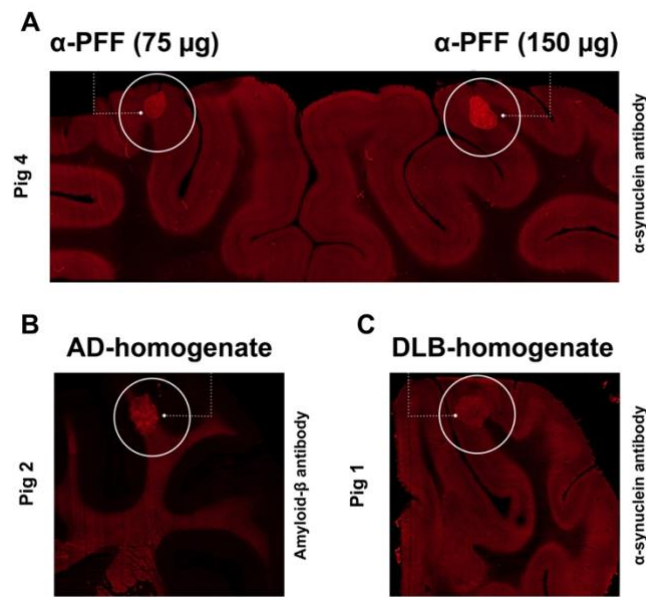
181 Percentage of parent and radiometabolite calculated with radio-HPLC + gamma counting in plasma and
182 brain at approximately 15 min post tracer injection (n = 1).

Sample	Polar Metabolites (%)	Polar & Lipophilic Metabolites (%)	Parent tracer (%)
Plasma @Euthanasia (15 min)	80.8	8.4	10.8
Brain @Euthanasia (22 min)	30.4	13.6	56.1

183

184 Fluorescence immunostaining

185 Fluorescence immunostaining was performed on sections containing the injection site to validate the
186 injection site and confirm injection of injectate. The sections were processed for standard
187 immunohistochemistry (IHC) with α -synuclein (GTX21904-Mouse [4B12], GeneTex, Hsinchu City,
188 Taiwan) and amyloid- β (ab252816-Rat [2E9], Abcam, Cambridge, UK) primary antibodies detected with
189 goat anti-mouse or goat anti-rat IgG H&L (Alexa Fluor® 647) (ab150115/ab150167, Abcam, Cambridge,
190 UK) secondary antibodies. α -synuclein containing sections were α -PFF, and dementia with Lewy bodies
191 (DLB) homogenate injected pig brain sections while amyloid- β containing sections were Alzheimer's
192 disease (AD) homogenate injected regions. The frozen sections were first fixed in 4% formaldehyde for
193 20 min. After a 10 min wash in phosphate-buffered saline (PBS), antigen retrieval was performed in a
194 microwave oven in 25 mM sodium citrate buffer pH 7.5 for α -synuclein containing section or Tris/EDTA
195 buffer pH 9.0 for amyloid- β containing section. Buffer temperature was raised to boiling for 5 secs,
196 sections left in the microwave for 10 min, then 20 min under the hood. After, they were washed with
197 PBS-TritonX100 0.4% and then incubated for 60 min with PBS + 0.4% TritonX100 and 5% bovine
198 serum albumin (BSA). Buffer was poured off, sectioned for incubated overnight in primary antibody (α -
199 synuclein: 0.2 ng/ml) (amyloid- β : 0.5 μ g/ml) in PBS + 0.1% Tween20 at 4 °C. The next day, sectioned
200 were washed thrice in PBS and then incubated in secondary antibody (diluted 1:200) in PBS + 0.1%
201 Tween20 for 1 hour at room temperature. Finally, the sections were washed thrice in PBS followed by
202 one wash in deionized H₂O (dH₂O). After the staining protocol, the sections were mounted in EverBrite™
203 Hardset Mounting Medium (Biotium, Inc., Fremont, CA, USA). Sections were imaged using an EC Plan-
204 Neofluoar 5x/0.16 objective on an Axio Observer 7 fitted with a motorized stage and Axiocam 506mono
205 CCD camera (Carl Zeiss, Birkerød, Denmark) to create stitched images covering large regions of interest.
206 For Alexa Fluor® 647, an excitation of 640/30 nm, beamsplitter of 660, and emission of 690/50 filter set
207 was used (Filter Set 50, Carl Zeiss, Birkerød, Denmark).



208

209 **Supplementary Figure 6. Fluorescence immunostaining.** Successful injections were ensured by
210 immunostaining injection site containing sections. Representative examples of pig injected with A) α-PFF
211 (right side = 150 μg, left side = 75 μg) B) AD-homogenate, and C) DLB-homogenate.

212 Reference:

- 213 1. Larsen P, Ulin J, Dahlstrøm K, Jensen M (1997) Synthesis of [¹¹C]iodomethane by iodination of
214 [¹¹C]methane. *Appl Radiat Isot* 48:153–157
- 215 2. Kuebler L, Buss S, Leonov A, et al (2020) [¹¹C]MODAG-001—towards a PET tracer targeting α-
216 synuclein aggregates. *Eur J Nucl Med Mol Imaging*. <https://doi.org/10.1007/s00259-020-05133-x>

DECLARATION OF CO-AUTHORSHIP

The declaration is for PhD students and must be completed for each conjointly authored article. Please note that if a manuscript or published paper has ten or less co-authors, all co-authors must sign the declaration of co-authorship. If it has more than ten co-authors, declarations of co-authorship from the corresponding author(s), the senior author and the principal supervisor (if relevant) are a minimum requirement.

1. Declaration by	
Name of PhD student	Nakul Ravi Raval
E-mail	nakul.raval@nru.dk
Name of principal supervisor	Prof. Dr. Gitte Moos Knudsen
Title of the PhD thesis	Translational Positron Emission Tomography: Animal Models and In vitro Autoradiography for Radioligand Development

2. The declaration applies to the following article	
Title of article	Evaluation of the α -synuclein PET radiotracer (d ₃)-[¹¹ C]MODAG-001 in pigs
Article status	
Published <input type="checkbox"/>	Accepted for publication <input type="checkbox"/>
Date:	Date:
Manuscript submitted <input checked="" type="checkbox"/>	Manuscript not submitted <input type="checkbox"/>
Date: 17/01/22	
If the article is published or accepted for publication, please state the name of journal, year, volume, page and DOI (if you have the information).	

3. The PhD student's contribution to the article <i>(please use the scale A-F as benchmark)</i> Benchmark scale of the PhD-student's contribution to the article	A, B, C, D, E, F
A. Has essentially done all the work (> 90 %) B. Has done most of the work (60-90 %) C. Has contributed considerably (30-60 %) D. Has contributed (10-30 %) E. No or little contribution (<10 %) F. Not relevant	
1. Formulation/identification of the scientific problem	B
2. Development of the key methods	B

3. The PhD student's contribution to the article (please use the scale A-F as benchmark) Benchmark scale of the PhD-student's contribution to the article		A, B, C, D, E, F
A. Has essentially done all the work (> 90 %) B. Has done most of the work (60-90 %) C. Has contributed considerably (30-60 %) D. Has contributed (10-30 %) E. No or little contribution (<10 %) F. Not relevant		
3. Planning of the experiments and methodology design and development		A
4. Conducting the experimental work/clinical studies/data collection/obtaining access to data		C
5. Conducting the analysis of data		A
6. Interpretation of the results		A
7. Writing of the first draft of the manuscript		A
8. Finalisation of the manuscript and submission		B
Provide a short description of the PhD student's specific contribution to the article. ⁱ		
NRR under the supervision of GMK designed the study. NRR further performed the surgery, PET scans, analysis and in vitro experiments required for the article. NRR wrote the first draft and submitting the manuscript.		

4. Material from another thesis / dissertationⁱⁱ	
Does the article contain work which has also formed part of another thesis, e.g. master's thesis, PhD thesis or doctoral dissertation (the PhD student's or another person's)?	Yes: <input type="checkbox"/> No: <input checked="" type="checkbox"/>
If yes, please state name of the author and title of thesis / dissertation.	
If the article is part of another author's academic degree, please describe the PhD student's and the author's contributions to the article so that the individual contributions are clearly distinguishable from one another.	

5. Signatures of the co-authorsⁱⁱⁱ				
	Date	Name	Title	Signature
1.	03/02/22	Gitte Moos Knudsen	Professor	

5. Signatures of the co-authors ⁱⁱⁱ				
2.	19/01/22	Pontus Plavén-Sigray	PhD	
3.	19/01/22	Hanne Demant Hansen	PhD	

6. Signature of the principal supervisor	
I solemnly declare that the information provided in this declaration is accurate to the best of my knowledge.	
Date: 03/02/2022	
Principal supervisor:	

7. Signature of the PhD student	
I solemnly declare that the information provided in this declaration is accurate to the best of my knowledge.	
Date: 17/01/22	
PhD student:	

Please learn more about responsible conduct of research on the [Faculty of Health and Medical Sciences' website](#).

ⁱ This can be supplemented with an additional letter if needed.

ⁱⁱ Please see Ministerial Order on the PhD Programme at the Universities and Certain Higher Artistic Educational Institutions (PhD Order) § 12 (4):

"Any articles included in the thesis may be written in cooperation with others, provided that each of the co-authors submits a written declaration stating the PhD student's or the author's contribution to the work."

ⁱⁱⁱ If more signatures are needed please add an extra sheet.

Aim II

To optimize, evaluate, and apply [¹¹C]UCB-J PET and [³H]UCB-J autoradiography for SV2A quantification as a marker for synaptic density in a preclinical setting.

Study

III

Objection I

To compare synaptic density and neuronal metabolic function in the unilateral 6-OHDA dopamine lesioned rat model of Parkinson's disease.



Synaptic Density and Neuronal Metabolic Function Measured by Positron Emission Tomography in the Unilateral 6-OHDA Rat Model of Parkinson's Disease

Nakul Ravi Raval^{1,2†}, Frederik Gudmundsen^{1†}, Morten Juhl³, Ida Vang Andersen^{1,4}, Nikolaj Speth¹, Annesofie Videbæk¹, Ida Nymann Petersen⁵, Jens D. Mikkelsen^{1,6}, Patrick MacDonald Fisher¹, Matthias Manfred Herth^{4,5}, Pontus Plavén-Sigray¹, Gitte Moos Knudsen^{1,2} and Mikael Palner^{1,7,8*}

¹ Neurobiology Research Unit, Copenhagen University Hospital, Rigshospitalet, Copenhagen, Denmark, ² Faculty of Health and Medical Sciences, University of Copenhagen, Copenhagen, Denmark, ³ Cardiology Stem Cell Centre, Copenhagen University Hospital, Rigshospitalet, Copenhagen, Denmark, ⁴ Department of Drug Design and Pharmacology, Faculty of Health and Medical Sciences, University of Copenhagen, Copenhagen, Denmark, ⁵ Department of Clinical Physiology, Nuclear Medicine & PET, Copenhagen University Hospital, Rigshospitalet, Copenhagen, Denmark, ⁶ Department of Neuroscience, University of Copenhagen, Copenhagen, Denmark, ⁷ Clinical Physiology and Nuclear Medicine, Department of Clinical Research, University of Southern Denmark, Odense, Denmark, ⁸ Department of Nuclear Medicine, Odense University Hospital, Odense, Denmark

OPEN ACCESS

Edited by:

Anne M. Landau,
Aarhus University, Denmark

Reviewed by:

Doris Doudet,
University of British Columbia,
Canada
Caroline Cristiano Real,
Aarhus University, Denmark

*Correspondence:

Mikael Palner
mikael.palner@nru.dk

[†] These authors have contributed
equally to this work and share first
authorship

Received: 27 May 2021

Accepted: 06 October 2021

Published: 18 November 2021

Citation:

Raval NR, Gudmundsen F, Juhl M, Andersen IV, Speth N, Videbæk A, Petersen IN, Mikkelsen JD, Fisher PM, Herth MM, Plavén-Sigray P, Knudsen GM and Palner M (2021) Synaptic Density and Neuronal Metabolic Function Measured by Positron Emission Tomography in the Unilateral 6-OHDA Rat Model of Parkinson's Disease. *Front. Synaptic Neurosci.* 13:715811. doi: 10.3389/fnsyn.2021.715811

Parkinson's disease (PD) is caused by progressive neurodegeneration and characterised by motor dysfunction. Neurodegeneration of dopaminergic neurons also causes aberrations within the cortico-striato-thalamo-cortical (CSTC) circuit, which has been hypothesised to lead to non-motor symptoms such as depression. Individuals with PD have both lower synaptic density and changes in neuronal metabolic function in the basal ganglia, as measured using [¹¹C]UCB-J and [¹⁸F]FDG positron emission tomography (PET), respectively. However, the two radioligands have not been directly compared in the same PD subject or in neurodegeneration animal models. Here, we investigate [¹¹C]UCB-J binding and [¹⁸F]FDG uptake in the CSTC circuit following a unilateral dopaminergic lesion in rats and compare it to sham lesioned rats. Rats received either a unilateral injection of 6-hydroxydopamine (6-OHDA) or saline in the medial forebrain bundle and rostral substantia nigra ($n = 4/\text{group}$). After 3 weeks, all rats underwent two PET scans using [¹⁸F]FDG, followed by [¹¹C]UCB-J on a separate day. [¹⁸F]FDG uptake and [¹¹C]UCB-J binding were both lower in the ipsilateral striatal regions compared to the contralateral regions. Using [¹¹C]UCB-J, we could detect an 8.7% decrease in the ipsilateral ventral midbrain, compared to a 2.9% decrease in ventral midbrain using [¹⁸F]FDG. Differential changes between hemispheres for [¹¹C]UCB-J and [¹⁸F]FDG outcomes were also evident in the CSTC circuit's cortical regions, especially in the orbitofrontal cortex and medial prefrontal cortex where higher synaptic density yet lower neuronal metabolic function was observed, following lesioning. In conclusion, [¹¹C]UCB-J and [¹⁸F]FDG PET can detect divergent changes

following a dopaminergic lesion in rats, especially in cortical regions that are not directly affected by the neurotoxin. These results suggest that combined [¹¹C]UCB-J and [¹⁸F]FDG scans could yield a better picture of the heterogeneous cerebral changes in neurodegenerative disorders.

Keywords: Parkinson's disease (PD), dopamine neurodegeneration, 6-OHDA = 6-hydroxydopamine, CSTC = cortico-striato-thalamo-cortical, FDG – PET, SV2A, SV2 proteins, UCB-J

INTRODUCTION

Several techniques have been developed to identify disease-related neuronal patterns to aid early detection and differential diagnoses of Parkinson's disease (PD). Examples of such methods are positron emission tomography (PET) imaging to measure glucose metabolism (Loane and Politis, 2011), dopamine synthesis, transporters, or receptors (Kerstens and Varrone, 2020). In PD, one affected neuronal circuit is the cortico-striato-thalamo-cortical (CSTC) circuit (Vriend et al., 2014). The CSTC circuit connects the cortex with the basal ganglia to control and coordinate goal-directed behaviour. This circuit can be further divided into three loops: the motor, limbic, and associative circuits (Groenewegen and Trimble, 2007; Vriend et al., 2014). The dopamine system innervates the striatal regions of the CSTC circuits and is critical in modulating their output. A model of 6-hydroxydopamine (6-OHDA) induced dopaminergic lesion leads to modulation within the CSTC, which will further help understand this circuit (Schwartz and Huston, 1996).

[¹¹C]UCB-J is a PET radioligand showing high affinity to synaptic vesicle glycoprotein 2A (SV2A) (Nabulsi et al., 2016). SV2A is ubiquitously expressed throughout the brain (Bajjalieh et al., 1994; Südhof, 2004) and is a suitable proxy for synaptic density (Finnema et al., 2016). Accordingly, [¹¹C]UCB-J PET may serve as a biomarker in neurodegenerative disorders, where the loss of synapses is thought to play a vital role in the pathophysiology (Holland et al., 2020; Matuskey et al., 2020; Mecca et al., 2020; Nicastro et al., 2020; Wilson et al., 2020; O'Dell et al., 2021). [¹⁸F]fluorodeoxyglucose (FDG) is a glucose analog used to measure neuronal glucose consumption and metabolic function. [¹⁸F]FDG PET has also been used as a surrogate marker for neuronal integrity and function (Mosconi, 2013). Only very recently, [¹⁸F]FDG and [¹¹C]UCB-J were tested in the same Alzheimer patients (Chen et al., 2021), where [¹¹C]UCB-J proved valuable as a clinical tracer and marker for disease progression, which may be helpful in drug development. This combination of radioligands has not been tested in human PD subjects or animal models of neurodegeneration.

Here, we present a multimodal PET study using dynamic [¹¹C]UCB-J and static [¹⁸F]FDG scans in the rat model of 6-OHDA severe unilateral-dopaminergic lesioning induced by combined unilateral 6-OHDA injection in the medial forebrain bundle and rostral substantia nigra (Yuan et al., 2005; Blandini et al., 2008). We have previously shown that 6-OHDA lesioning lowers postsynaptic dopamine receptor density and presynaptic capacity to release amphetamine (Palmer et al., 2011). Thus, we hypothesise that the loss of dopaminergic neurons will cause a decrease in [¹¹C]UCB-J binding and [¹⁸F]FDG uptake,

especially in the ipsilateral basal ganglia (substantia nigra, ventral tegmental area, whole striatum, dorsolateral striatum, dorsomedial striatum, and nucleus accumbens). Furthermore, we compare the effect sizes of [¹⁸F]FDG uptake and [¹¹C]UCB-J binding to detect changes after a unilateral dopaminergic lesioning of the rat brain. As a control to assess differential changes, we used both the contralateral hemisphere and compared the 6-OHDA model to a group of sham-lesioned rats. Several studies have successfully detected changes in regional [¹⁸F]FDG uptake after a 6-OHDA lesion in both rats (Casteels et al., 2008; Jang et al., 2012; Silva et al., 2013; Kordys et al., 2017) and mice (Im et al., 2016). One recent study has also performed [¹¹C]UCB-J PET in the 6-OHDA lesion model, although with some methodological differences (Thomsen et al., 2021b).

The results of our study indicate that dopaminergic lesions lead to a loss of presynaptic density in the striatal regions, as measured by [¹¹C]UCB-J, which is similar to changes in neuronal metabolic function, as measured by [¹⁸F]FDG. Interestingly, the dopaminergic lesion caused divergent changes between the two radioligands in cortical regions of the CSTC circuit.

MATERIALS AND METHODS

Animals

Sixteen female Long-Evans WT rats (216 ± 25 g, 10–11 weeks old when scanned) (Janvier) were used in this study. Eight animals used in the model study and eight animals used in the baseline study (**Supplementary Data 1.1**). The animals were held under standard laboratory conditions with 12-h light/12-h dark cycles and *ad libitum* access to food and water. All animal experiments conformed to the European Commission's Directive 2010/63/EU with approval from the Danish Council of Animal Ethics (Journal No. 2017-15-0201-01375 and 2017-15-0201-01283) and the Department of Experimental Medicine, University of Copenhagen.

Stereotactic Surgery and 6-OHDA Lesion

The animals were acclimatised in the surgery room for at least 1 h. Analgesia was provided with carprofen (Rimadyl, Zoetis, NJ, United States) 5 mg/kg, subcutaneous (SC), 45 min before the surgery and 24 and 48 h postoperative. Before commencing the surgery, animals received desmethylimipramine (25 mg/kg, intraperitoneal (IP) mixed in physiological saline). Desmethylimipramine protects the noradrenergic neurons from the neurotoxic effects (Esteban et al., 1999). Anaesthesia was induced with 3% isoflurane in oxygen and maintained through surgery with 1.2–1.8% isoflurane in oxygen. The rats were fixed

on a stereotaxic apparatus (Kopf Instruments, Tujunga, CA, United States) with the incisor bar set 3.3 mm below the level of the ear bars. An incision was made on the scalp, and two bur-holes were drilled on one side of the skull using a dental micromotor and round bur (0.5 mm). A 2 $\mu\text{g}/\mu\text{L}$ solution of 6-OHDA (2,5-Dihydroxytyramine hydrobromide, Sigma-Aldrich, Søborg, Denmark) in physiological saline containing 0.02% ascorbic acid or physiological saline (containing 0.02% ascorbic acid) was drawn into a 10 μL syringe with a 33 g needle (World Precision Instruments, Sarasota, FL, United States). Three μL were infused into the medial forebrain bundle (coordinates: AP = 4.8 mm, ML = 1.7 mm, DV = 8 mm) and 3 μL infused rostral to substantia nigra (coordinates: AP = 3.6 mm, ML = 2 mm, DV = 8.3 mm) relative to the bregma to ensure unilateral dopaminergic degeneration. The infusion was delivered at 151 nL/minutes driven by an infusion pump (World Precision Instruments, Sarasota, FL, United States), followed by a 7 min pause prior to a slow withdrawal of the syringe needle. The incision was sutured back. After recovery from anaesthesia, rats were returned to the recovery cage and housed alone for 48 h and then housed in pairs for recovery of 21 days to allow the development of the lesions.

Study Design and Confirmation of Lesion

Four rats were injected unilaterally with 6-OHDA, while another four were injected with physiological saline and divided into two groups, i.e., dopamine lesioned and sham lesioned; **Figure 1** shows the study's overall design. After the recovery period, the rats were subjected to two PET scans $[^{18}\text{F}]\text{FDG}$ at day 21 and $[^{11}\text{C}]\text{UCB-J}$ at approximately day 23. One month (26–33 days) after the injection, the rats were euthanised by decapitation, and the brains rapidly removed and frozen on dry ice.

To validate the extent of the lesion, tyrosine hydroxylase (TH) immunostaining was performed on 20 μm coronal cryosections containing the striatum. Frozen brains were sectioned on a cryostat (Leica CM1800, Leica Biosystems, Buffalo Grove, IL, United States) and mounted on Superfrost PlusTM adhesion microscope slides (Thermo Fischer Scientific, MS, United States). Sections were stored at -80°C for the remaining period of the study. The sections were dried and processed for standard TH immunohistochemistry. Briefly, the frozen sections were first fixed in cold (4°C) 4% formaldehyde for 15 min. The sections were then prewashed in 0.05 M phosphate-buffered saline (PBS, pH 7.4) with 1% bovine serum albumin and then incubated overnight in a purified antiserum against TH generated in rabbits (Sigma-Aldrich, Søborg, Denmark; cat#AB152) diluted 1:500 in PBS + 0.1% Triton-X overnight at 4°C . The immunoreactivity was detected using the avidin-biotin detection method (biotinylated donkey-anti rabbit IgG (Sigma-Aldrich, Søborg, Denmark, #SAB3700966); avidin-biotin-peroxidase complex (Thermo Fischer Scientific, MS, United States #32020) and reacted for peroxidase activity in 0.1% diaminobenzidine mixed with 0.003% H_2O_2 in PBS for 15 min. Finally, the sections were washed in distilled water and embedded in Pertex.

The stained slides were imaged on a Zeiss Axio Observer 7 using an EC Plan-Neofluor 5 \times /0.16 objective by stitching

multiple fields of view to cover the entire section. The resulting colour image was analysed in ImageJ 1.53G (NIH Image, Bethesda, MD, United States) by a workflow involving masking potential artefacts by automatic threshold (Moment) and conversion to 16-bit grayscale. From these, crude regions of interest encompassing the striatum were identified for quantification. Automated thresholds were used to measure the intensities in mean grey values (Minimum) and stained areas in pixel values (Moment). The intensities and areas of the ipsilateral striatum were normalised to the contralateral striatum and are presented as percentages.

$[^{18}\text{F}]\text{FDG}$ and $[^{11}\text{C}]\text{UCB-J}$ Positron Emission Tomography Scans

All scans were performed on the Siemens HRRT (High-Resolution Research Tomography), and all rats were examined using both $[^{11}\text{C}]\text{UCB-J}$ and $[^{18}\text{F}]\text{FDG}$. The rats were transported to the scanner at least 2 h before the scan. Anaesthesia was induced using 3% isoflurane in oxygen. All rats were placed in a 2×2 custom made rat holder (illustration in **Figure 1**), enabling simultaneous scanning of four rats (Keller et al., 2017; Shalgunov et al., 2020; Casado-Sainz et al., 2021). While in the custom-made rat holder, the rats were kept under anaesthesia with a constant flow of isoflurane ($\sim 2\%$ isoflurane in oxygen). They were placed in the HRRT scanner for the time of the scan. The rats were kept warm using an infrared lamp and monitored for respiration throughout the entire scan. A rotating point source ^{137}Cs transmission scan (Keller et al., 2013) was carried out before or after each emission scan.

$[^{18}\text{F}]\text{FDG}$ was acquired from the in-house clinical production of the department of clinical physiology, nuclear medicine and PET, Rigshospitalet, Denmark. Rats were fasted overnight before the scan. The animals were briefly anaesthetised, and $[^{18}\text{F}]\text{FDG}$ was administered intraperitoneal with an average injected dose of 25.05 ± 3.1 MBq. The rats were placed back in their home cage to wake up from the anaesthesia to achieve $[^{18}\text{F}]\text{FDG}$ uptake while awake. Forty-five minutes after the $[^{18}\text{F}]\text{FDG}$ injection, the rats were anaesthetised, placed in the holder, and a PET emission scan was acquired for 45 min.

$[^{11}\text{C}]\text{UCB-J}$ was produced in-house using a modified protocol (see **Supplementary Data 1.4**) adapted from Nabulsi et al. (2016). The tail veins were cannulated (BD Neoflon 25G, Stockholm, Sweden) before the scan. At the start of the scan, intravenous (IV) injections were given over 7–10 s through the tail vein catheter, with an average dose of 20.8 ± 2.1 MBq (injected mass = 0.04 ± 0.01 μg). Heparinised saline (500–600 μL) was flushed through the catheter after tracer injection. The acquisition time for $[^{11}\text{C}]\text{UCB-J}$ was 60 min.

Positron Emission Tomography Image Reconstruction

All list-mode data was dynamically reconstructed using ordinary Poisson 3D ordered subset expectation maximisation with point spread function modelling, resulting in PET image frames consisting of 207 planes of 256×256 voxels ($1.22 \times 1.22 \times 1.22$ mm). The reconstruction of the attenuation

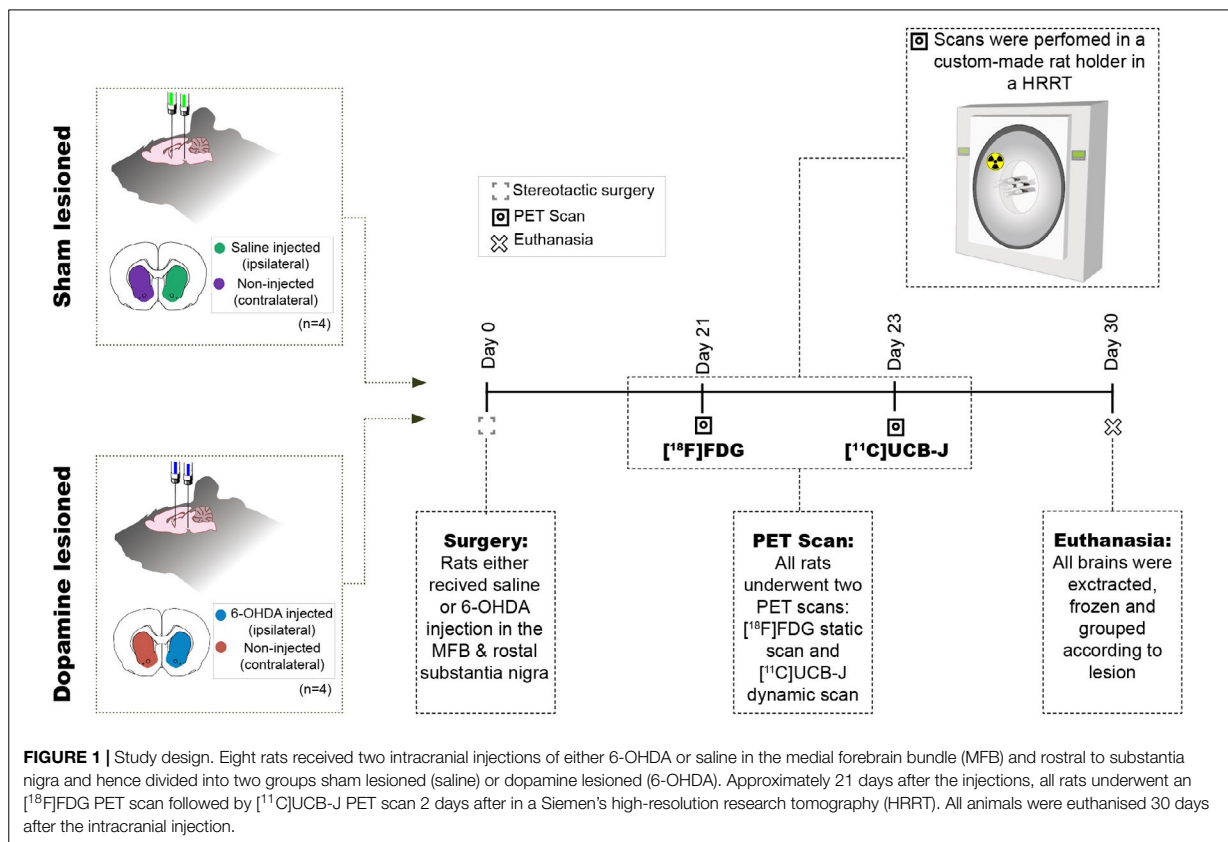


FIGURE 1 | Study design. Eight rats received two intracranial injections of either 6-OHDA or saline in the medial forebrain bundle (MFB) and rostral substantia nigra and hence divided into two groups sham lesioned (saline) or dopamine lesioned (6-OHDA). Approximately 21 days after the injections, all rats underwent an $[^{18}\text{F}]\text{FDG}$ PET scan followed by $[^{11}\text{C}]\text{UCB-J}$ PET scan 2 days after in a Siemens high-resolution research tomography (HRRT). All animals were euthanised 30 days after the intracranial injection.

map from the transmission scan was performed using the maximum *a posteriori* algorithm for transmission data. All $[^{11}\text{C}]\text{UCB-J}$ scans were transformed into 33 dynamic frames (6×10 , 6×20 , 6×60 , 8×120 , and 7×300 s), while $[^{18}\text{F}]\text{FDG}$ scans were transformed into 5-min frames and then averaged into a single frame.

Quantification of Positron Emission Tomography Data

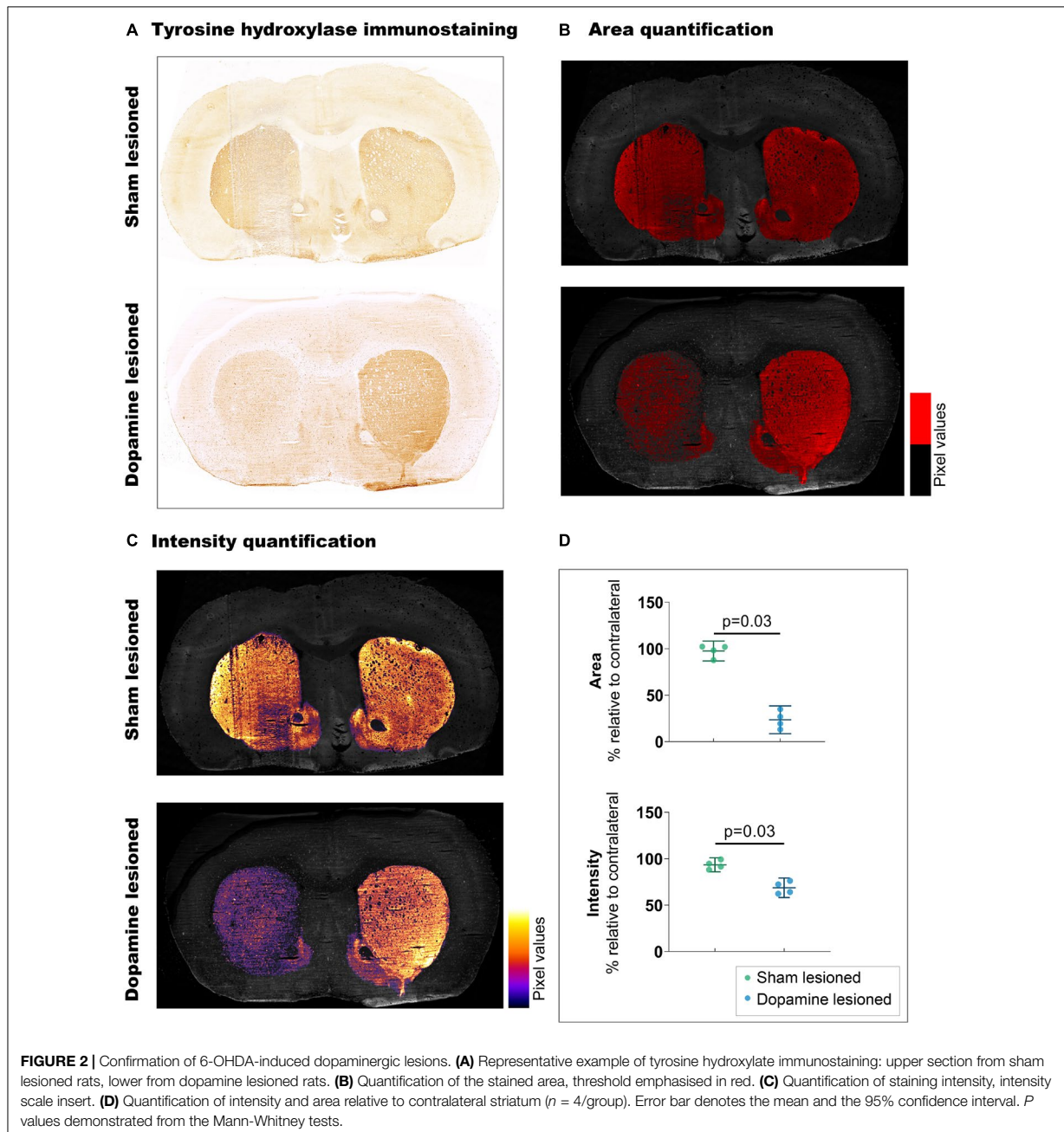
Pre-processing of all PET scans were done with PMOD 3.7 (PMOD Technologies, Zurich, Switzerland). Kinetic modelling were done with PMOD 3.0 (PMOD Technologies, Zurich, Switzerland). All rats were scanned in full-body, and brains were manually cropped out. For $[^{18}\text{F}]\text{FDG}$ scans, static images were manually co-registered to a standard $[^{18}\text{F}]\text{FDG}$ PET template. For $[^{11}\text{C}]\text{UCB-J}$ scans, a summed image of the last 13 frames were manually co-registered to an average T1-weighted magnetic resonance brain image in standard space. MR template used was a summed image from various rats, not part of this study, generously provided by Kristian Nygaard Mortensen. Volumes of interest (VOIs)-atlas of selected regions from the CSTC circuit from Schiffer's atlas (Schiffer et al., 2006) were applied to the PET image in standard space. The regions (depicted in Figure 3 and Supplementary Figure 5) included in this

study were: anterior cingulate cortex, medial prefrontal cortex, motor cortex, nucleus accumbens, orbitofrontal cortex, striatum, thalamus, and ventral midbrain (a region covering both the ventral tegmental area and substantia nigra). The dorsomedial striatum and dorsolateral striatum were manually delineated and used in the study (Shalgunov et al., 2020; Casado-Sainz et al., 2021). All images and co-registration were visually checked for accuracy following spatial transformation.

For $[^{18}\text{F}]\text{FDG}$, the unit of measurement (Bq/mL) for each cropped image was transformed into standardised uptake values (SUV) by adjusting for body weight and injected dose. A whole-brain normalisation factor (WB_{NF}) was calculated for each rat using (Eq. 1). The SUV values from all the VOIs were normalised using WB_{NF} .

$$WB_{NF} = \frac{\text{Average of whole-brain } [^{18}\text{F}]\text{FDG SUV for all rats}}{\text{Whole-brain } [^{18}\text{F}]\text{FDG SUV for rat X}} \quad (1)$$

For $[^{11}\text{C}]\text{UCB-J}$, time-activity curves (TACs) for all VOIs were extracted from the PET images. Estimates for the total blood activity was acquired using a non-invasive image-derived input function (IDIF) that was used for estimating a surrogate of V_T . V_T was determined in each VOI, using the one-tissue compartment model (1TCM), which has previously been



validated for [¹¹C]UCB-J in mice (Bertoglio et al., 2020; Xiong et al., 2021). The IDIF was extracted from each PET image by delineating the whole blood activity in the lumen of the heart's left ventricle. This delineation was achieved by using the "region growing" function in PMOD in the early time frame by dropping a "seed" at the point of highest activity in the heart and producing a VOI which is about the size of the rat's left ventricle (5–6 voxels). In order to fit the 1TCM to the TACs, the blood volume fraction

(V_B) was fixed at 5%. In addition to V_T , the micro-parameters K_1 and k_2 were also extracted from the kinetic modelling. These micro-parameters were checked for the difference due to the surgical procedure or any other reason. 1TC model fit to a representative region, ipsilateral and contralateral striatum, are shown in **Supplementary Figure 6**. All micro parameters (K_1 and k_2) for all regions are recorded in **Supplementary Table 3**. In addition to kinetic modelling, TACs were converted into

SUVs. Ipsilateral and contralateral striatum and ventral midbrain (sham and dopamine lesioned) TACs were averaged for visual representation. This was performed using GraphPad Prism 9 (GraphPad Software, San Diego, CA, United States).

Statistics

Due to the limited sample size and the number of comparisons undertaken, the study is exploratory in nature, meaning that caution should be taken around drawing strong confirmatory conclusions from the data. As such, all *p*-values reported should be considered as a continuous assessment of indirect evidence against the null hypothesis of no difference between groups or hemispheres, and binary conclusions of “significant” or “not significant” within the Neyman-Pearson Null-hypothesis-significance-testing framework should be avoided.

The data were analysed using Jamovi [Version 1.6, The jamovi project (2021) (Computer Software). Retrieved from <https://www.jamovi.org>] and RStudio (v.1.3.1073) (R version 4.0.3; “Bunny-Wunnies Freak Out,” R core team, Vienna, Austria). Graph-Pad Prism (v. 9.0.1; GraphPad Software, San Diego, CA, United States) was used for data visualisation. All data are presented as mean values ± standard deviation unless otherwise specified. The TH immunostaining comparison of the dopamine and sham lesion (ipsilateral side corrected to the contralateral side) was performed with an independent samples *t*-test (Mann-Whitney test).

To allow direct comparison of [¹⁸F]FDG normalised SUVs and [¹¹C]UCB-J *V_T*, Cohen’s *d_z* values (a standardised measure of within-subject differences) between the ipsilateral regions and contralateral regions were calculated (Lakens, 2013). Cohen’s *d_z* (standardised measure of between-group differences) values were used to compare the effect size measured by the two tracers. This shows the efficacy of detecting differences with the two radioligands.

To further explore and compare the different regions, the difference between the ipsilateral and contralateral side for each tracer ([¹⁸F]FDG and [¹¹C]UCB-J) in the dopamine and sham lesioned groups was calculated in Jamovi using paired *t*-test without correction for multiple comparisons.

We performed tests on [¹⁸F]FDG normalised SUVs and [¹¹C]UCB-J *V_T* between the two lesioned groups in regions outside the basal ganglia: thalamus, medial prefrontal cortex, anterior cingulate cortex, orbitofrontal cortex and motor cortex. These tests were performed using an independent samples *t*-test (Mann-Whitney test).

RESULTS

Confirmation of Lesion

Striatal TH immunostaining confirmed unilateral dopaminergic lesions in the striatum (Figure 2). We observed a 73.9% decrease (*p* = 0.03) in the stained area from the sham lesioned animals (97.50% ± 6.77) to the dopamine lesioned animals (23.54% ± 9.41). These observations were accompanied by a 24.68% reduction in staining intensity (*p* = 0.03) between sham lesioned (93.39% ± 4.73) and dopamine lesioned animals (68.72% ± 6.62).

Representative [¹¹C]UCB-J and [¹⁸F]FDG Positron Emission Tomography Images

Representative [¹¹C]UCB-J and [¹⁸F]FDG PET images from a rat in the dopamine and sham lesioned group are shown in Figure 3. A template structural T1 MR image is used for illustrative purpose only. Regional VOIs are shown on summed PET images in Supplementary Figure 5. For [¹¹C]UCB-J, a difference was visually noticed between the ipsilateral and contralateral side of the 6-OHDA injection, especially in the striatal regions and ventral midbrain (red arrows in Figure 3). Hemispheric differences were not evident in the sham lesioned animal. For [¹⁸F]FDG, changes were also evident between the ipsilateral and contralateral hemisphere in the cortex, striatal regions, and ventral midbrain in the dopamine lesioned animal (red arrows in Figure 3), while no apparent differences were seen in the sham lesioned animal.

Decreased [¹¹C]UCB-J *V_T* in Dopamine Lesioned Hemisphere

Visually, a lower average [¹¹C]UCB-J uptake can be seen through averaged TACs in the ipsilateral striatum and ventral midbrain compared to the contralateral hemisphere in dopamine lesioned animals (Figures 4A,B). No changes were noticed in the sham lesioned animals (Figures 4C,D). [¹¹C]UCB-J *V_T* values were lower in the ipsilateral side of the striatum, dorsolateral striatum and ventral midbrain but higher in the medial prefrontal cortex and anterior cingulate cortex compared to the contralateral side (Figure 4E and Table 1). In the sham lesioned animals, higher [¹¹C]UCB-J *V_T* values were also seen in the ipsilateral anterior cingulate cortex compared to the contralateral side. No other differences were observed in [¹¹C]UCB-J *V_T* (Figure 4F and Table 1) between the ipsilateral and contralateral sides in the sham lesioned rats.

Decreased [¹⁸F]FDG Uptake in Dopamine Lesioned Hemisphere

There was a lower uptake of [¹⁸F]FDG in all striatal regions (only statistically significant in dorsolateral striatum), thalamus and orbitofrontal cortex in the ipsilateral side of dopamine lesioned rats, compared to the contralateral side (Figure 5 and Table 1). No substantial differences were found between the ipsilateral and contralateral sides within the sham lesioned animals.

[¹¹C]UCB-J and [¹⁸F]FDG Show Divergent Effect Sizes in Dopamine and Sham Lesioned Animals

Both [¹¹C]UCB-J and [¹⁸F]FDG show an expected negative effect of the dopaminergic lesion in all dopamine rich regions, including the ventral midbrain, striatum, dorsomedial striatum, dorsolateral striatum and nucleus accumbens (Figure 6). Results are reported as Cohen’s *d_z* values, showing the within-subject effect size between the ipsilateral and contralateral hemispheres. The ventral midbrain and striatum show a larger effect with [¹¹C]UCB-J than [¹⁸F]FDG, although with confidence intervals overlapping the mean of the other radioligand. The dorsomedial striatum, dorsolateral striatum and nucleus accumbens also have

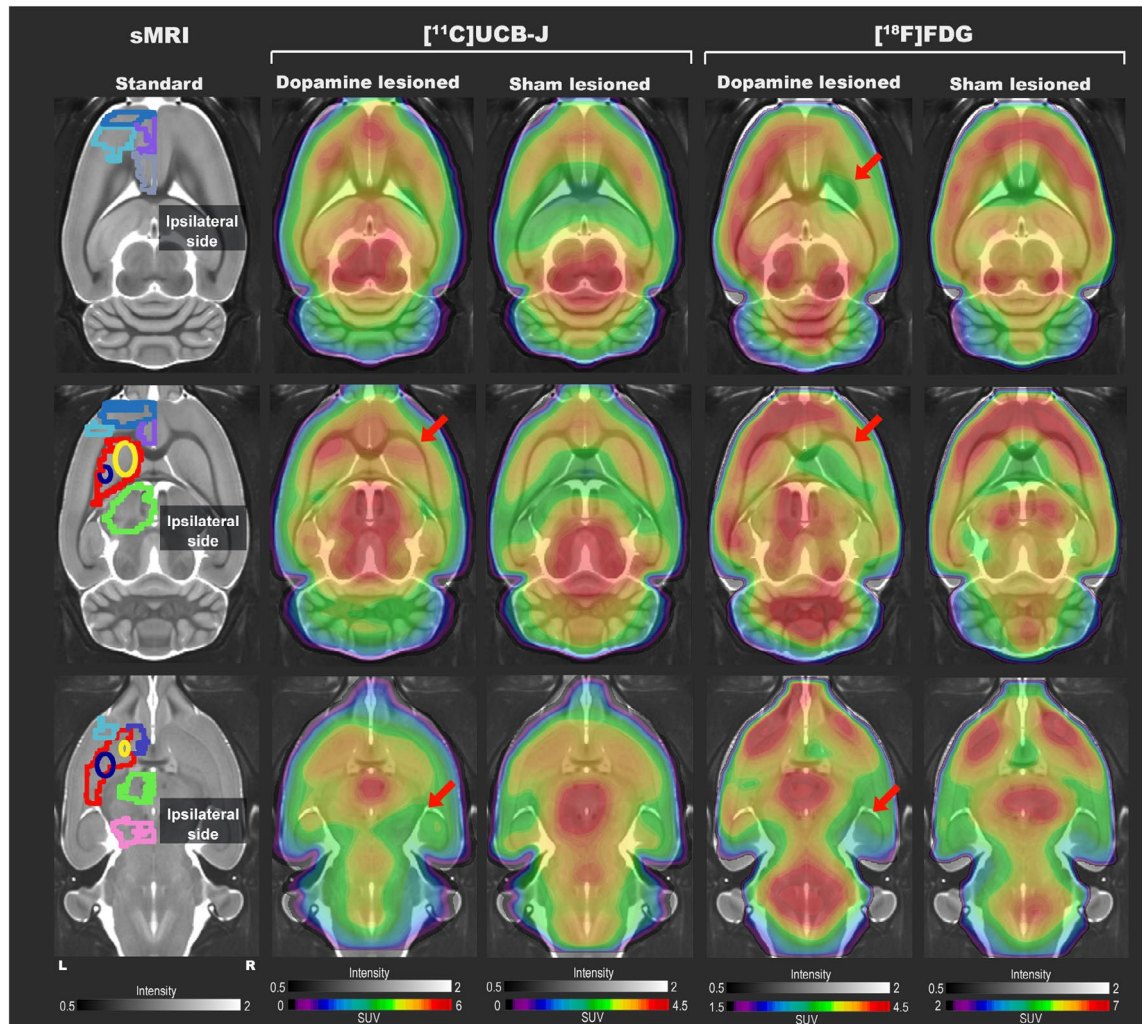


FIGURE 3 | Representative $[^{11}\text{C}]\text{UCB-J}$ and $[^{18}\text{F}]\text{FDG}$ PET SUV horizontal brain slices from a dopamine and a sham lesioned rat. Standard structural MRI (for illustrative purposes) slices show the selected volumes of interest in one hemisphere; mPFC (medium blue), OFC (purple), motor cortex (light blue), ACC (grey), striatum (red), dorsomedial striatum (yellow), dorsolateral striatum (navy blue), thalamus (green), NAc (dark blue), and ventral midbrain (pink). For $[^{11}\text{C}]\text{UCB-J}$, the SUV image represents the sum of 15–60 min; for $[^{18}\text{F}]\text{FDG}$, it is the sum of all 45 min. The red arrow shows decreased tracer uptake in dopamine lesioned animals.

overlapping confidence intervals and shows a similar effect with $[^{11}\text{C}]\text{UCB-J}$ or $[^{18}\text{F}]\text{FDG}$.

Besides dopamine rich regions, there is a seemingly larger reduction with $[^{18}\text{F}]\text{FDG}$ compared to $[^{11}\text{C}]\text{UCB-J}$ in the thalamus; however, the $[^{18}\text{F}]\text{FDG}$ confidence interval still includes the mean of $[^{11}\text{C}]\text{UCB-J}$. Divergent changes can be seen in cortical regions when comparing $[^{11}\text{C}]\text{UCB-J}$ and $[^{18}\text{F}]\text{FDG}$ except for the motor cortex, which shows no effect of the dopamine lesion. In particular, the medial prefrontal cortex and orbitofrontal cortex shows a negative effect with $[^{18}\text{F}]\text{FDG}$ (higher SUV on the lesioned side), while it shows a positive effect with $[^{11}\text{C}]\text{UCB-J}$ (lower V_T on the lesioned side). The anterior cingulate cortex

shows no effect with $[^{18}\text{F}]\text{FDG}$ but a positive effect with $[^{11}\text{C}]\text{UCB-J}$. Sham lesioned animals do not show differences between hemispheres, except for $[^{11}\text{C}]\text{UCB-J}$ in the anterior cingulate cortex.

Changes in Cortical Regions Between $[^{11}\text{C}]\text{UCB-J}$ Binding and $[^{18}\text{F}]\text{FDG}$ Uptake

A *post hoc* analysis of changes in the cortical regions and thalamus between the lesion and sham group (Figure 7) showed an increase in $[^{11}\text{C}]\text{UCB-J}$ V_T values in the anterior cingulate cortex (37.36%, $p = 0.03$) whereas there is no difference in $[^{18}\text{F}]\text{FDG}$ uptake (2.6%, $p = 0.68$). On the contrary, a lower $[^{18}\text{F}]\text{FDG}$ uptake

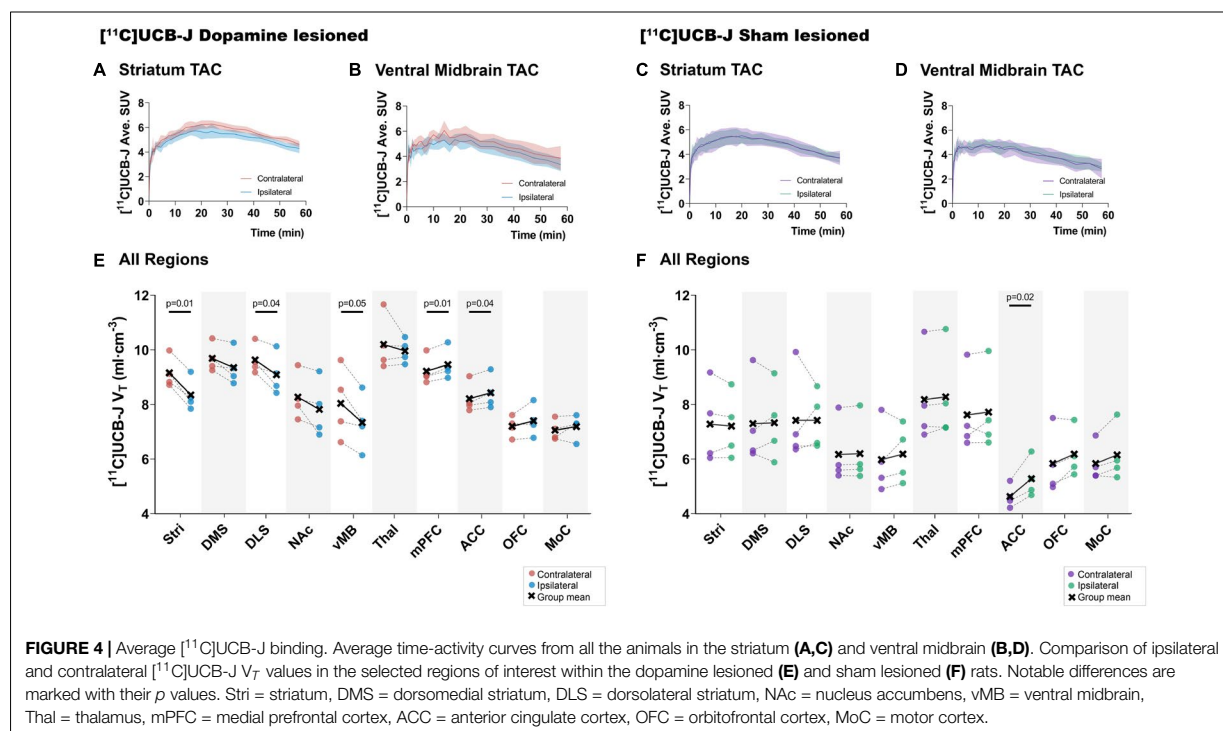


TABLE 1 | Group-wise summary of the paired t-test between the ipsilateral and contralateral regions for each tracer and group.

Region	[¹¹ C]UCB-J V _T				[¹⁸ F]FDG Normalized SUVs			
	Dopamine lesioned		Sham lesioned		Dopamine lesioned		Sham lesioned	
	% diff	p value	% diff	p value	% diff	p value	% diff	p value
Stri	-8.86%	0.003*	-0.99%	0.66	-5.66%	0.093	0.25%	0.926
DMS	-3.48%	0.085	0.39%	0.919	-7.42%	0.077	-1.84%	0.553
DLS	-5.58%	0.046*	0.02%	0.998	-6.30%	0.022*	-0.45%	0.893
NAc	-5.35%	0.122	0.56%	0.173	-7.26%	0.071	0.93%	0.62
vMB	-8.72%	0.052	3.35%	0.486	-2.89%	0.343	0.18%	0.821
Thal	-2.55%	0.465	1.20%	0.233	-4.11%	0.013*	1.09%	0.425
mPFC	2.59%	0.009*	1.33%	0.621	-2.02%	0.147	1.25%	0.47
ACC	2.62%	0.043*	14.08%	0.023*	-0.23%	0.832	0.47%	0.757
OFC	2.88%	0.209	5.71%	0.141	-6.32%	0.020*	0.45%	0.67
MoC	1.85%	0.435	5.27%	0.169	-1.32%	0.407	3.25%	0.223

To aid overview, notable differences are marked as *. Stri = striatum, DMS = dorsomedial striatum, DLS = dorsolateral striatum, NAc = nucleus accumbens, vMB = ventral midbrain, Thal = thalamus, mPFC = medial prefrontal cortex, ACC = anterior cingulate cortex, OFC = orbitofrontal cortex, MoC = motor cortex.

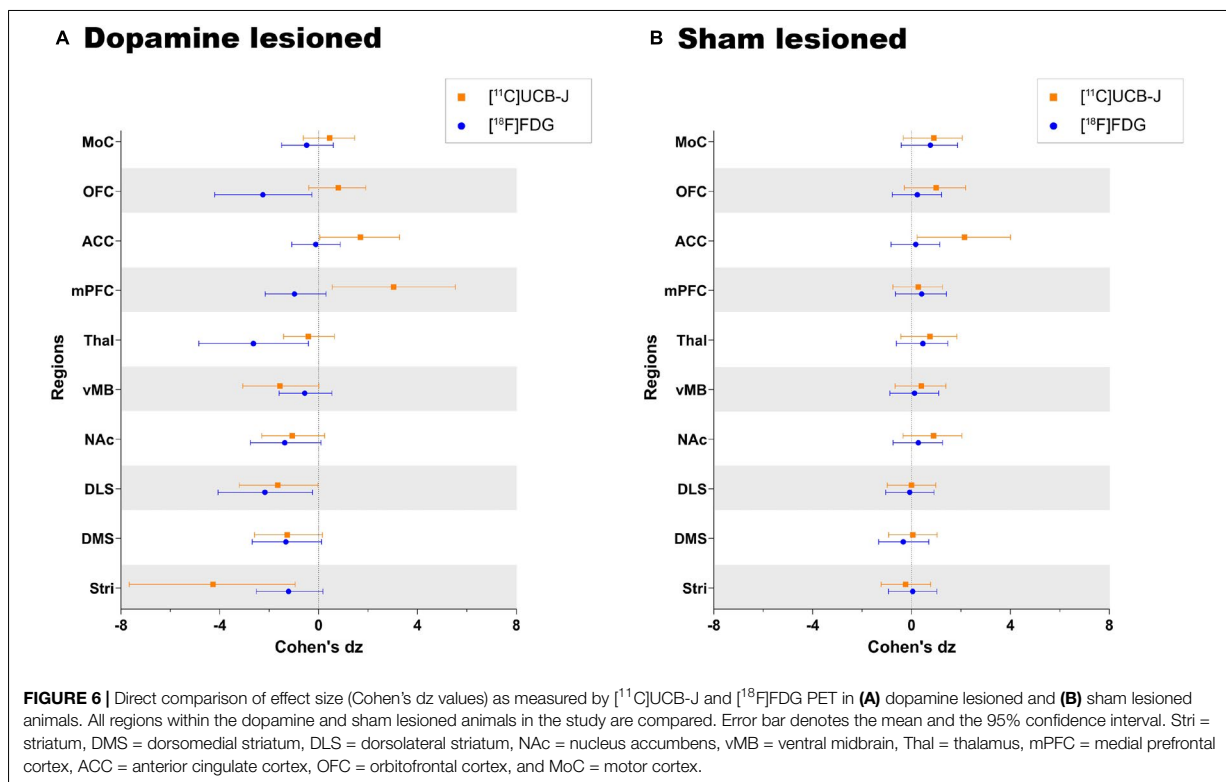
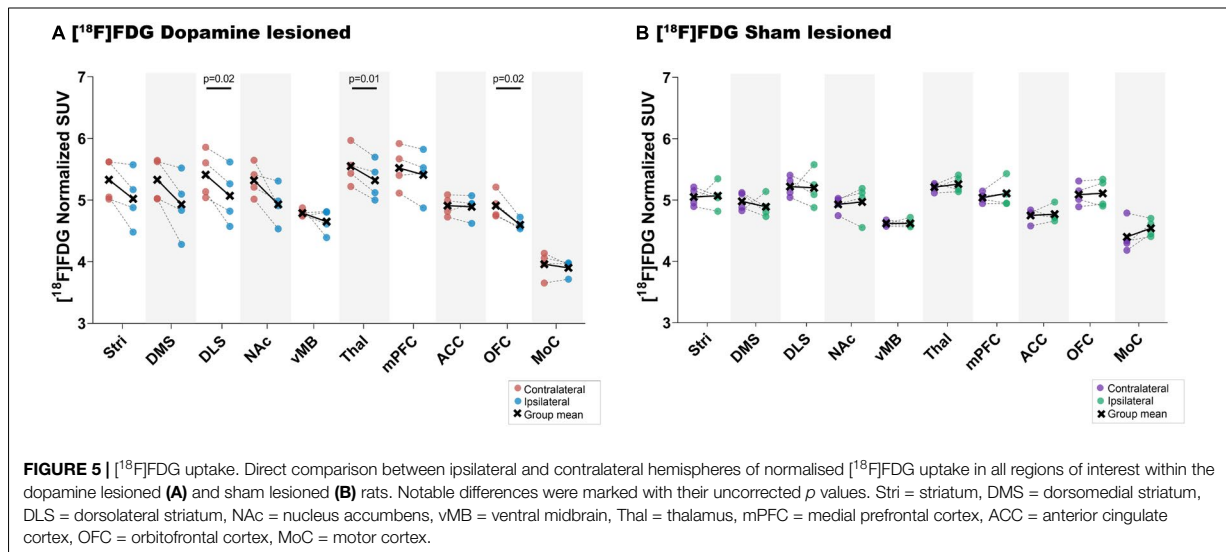
is observed in the motor cortex (-16.42%, p = 0.03) and the orbitofrontal cortex (-11.08%, p = 0.03), which is not the case for [¹¹C]UCB-J V_T (16.8%, p = 0.34 and 19.8%, p = 0.20).

DISCUSSION

This study explored regional differences in [¹¹C]UCB-J binding and [¹⁸F]FDG uptake using a unilateral 6-OHDA dopaminergic lesion in rats, a commonly used animal model for PD. We

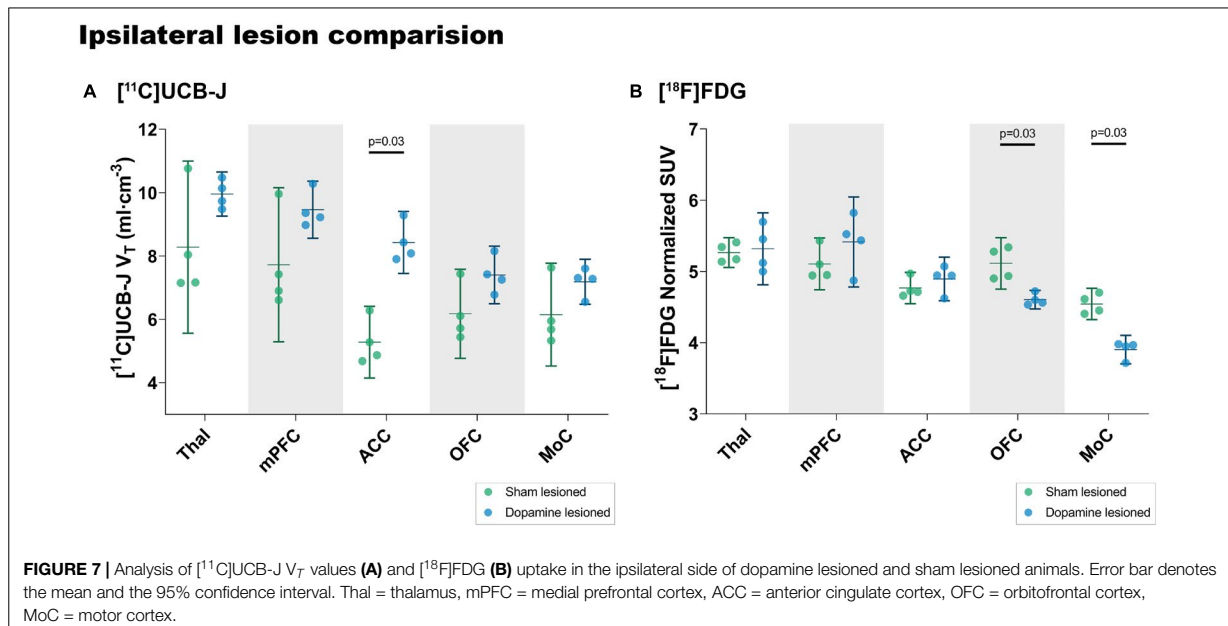
observed differences in SV2A density and neuronal metabolic function between ipsilateral and contralateral hemispheres, especially the basal ganglia, which are well known to be innervated by dopaminergic terminals. This suggests a decline in dopaminergic neurons and synapses due to the 6-OHDA lesion, consistent with TH immunostaining (Figure 2).

We derived effect sizes between the ipsilateral and contralateral regions to directly compare [¹¹C]UCB-J and [¹⁸F]FDG. The regions within the basal ganglia show similar effects with the two radioligands, lower SV2A density and



metabolic function, in the ipsilateral region compared to the contralateral region. Especially lower SV2A density in the striatum, dorsolateral striatum, and ventral midbrain compared to the contralateral regions. We see a strong correlation between *in vitro* autoradiography ([³H]UCB-J fmol/mg tissue equivalent) and PET quantification ([¹¹C]UCB-J *V_T*) in the sham and

dopamine lesioned animal (**Supplementary Data 1.2**). This further confirms the validity of the [¹¹C]UCB-J PET data. A lower ipsilateral metabolic function is also observed in the regions of basal ganglia, which is consistent with previous 6-OHDA lesion studies showing an ipsilateral decrease in [¹⁸F]FDG uptake in the striatal regions compared to the



contralateral regions (Casteels et al., 2008; Jang et al., 2012; Kordys et al., 2017). No such changes are evident in baseline animals (**Supplementary Data 1.1**). Our observations are in line with the common understanding of the CSTC circuitry, in which the striatal response is in part sculptured by the dopaminergic input from substantia nigra (Vriend et al., 2014). Hence, diminished activity in dopamine neurons projecting to the striatum due to the 6-OHDA lesion would lead to a decline in striatal activity, as is evident from the changes in $[^{18}\text{F}]\text{FDG}$ uptake.

A difference of moderate magnitude between the ipsilateral and contralateral thalamus was noted for $[^{18}\text{F}]\text{FDG}$ but not for $[^{11}\text{C}]\text{UCB-J}$. Although dopamine denervation of the rodent thalamus is scant (Papadopoulos and Parnavelas, 1990), we still observe decreased metabolic function. This may be due to the overall decreased function of the lesioned thalamus.

The cortical regions also show divergent group differences with $[^{11}\text{C}]\text{UCB-J}$ and $[^{18}\text{F}]\text{FDG}$. In the orbitofrontal cortex and medial prefrontal cortex, $[^{18}\text{F}]\text{FDG}$ uptake is lower in the ipsilateral regions compared to contralateral regions. By contrast, $[^{11}\text{C}]\text{UCB-J}$ shows higher SV2A density in the ipsilateral regions compared to the contralateral regions. To our knowledge, it is the first time that a lower orbitofrontal cortex metabolic function is demonstrated in this rat model; a decrease has previously only been reported in the prefrontal cortex (Casteels et al., 2008), while other studies show unaltered metabolism (Kurachi et al., 1995). The decrease in orbitofrontal and medial prefrontal cortical metabolic function may be due to the disrupted dopaminergic innervation from the substantia nigra to the orbitofrontal cortex (Murphy and Deutch, 2018).

$[^{11}\text{C}]\text{UCB-J}$ binding is higher in the anterior cingulate cortex in most of the tests that we perform, except baseline animals

(**Supplementary Data 1.1**). While showing no effect in metabolic function, the anterior cingulate cortex's SV2A density was higher ipsilaterally, both in the sham and dopamine lesioned animals. Likewise, the anterior cingulate cortex had higher SV2A density in the dopamine lesioned animals than sham lesioned animals, both in ipsilateral (**Figure 7**) and contralateral hemispheres (**Supplementary Figure 4**). These changes are also evident *in vitro* using $[^3\text{H}]\text{UCB-J}$ autoradiography (**Supplementary Data 1.2**) in the sham and dopamine lesioned animals (**Supplementary Figure 3; Supplementary Table 2**). Such changes in the cingulate cortex have not been previously shown in this model. We speculate that the cause is the surgery itself, as the anterior cingulate cortex is part of the pain matrix (Bliss et al., 2016), but further testing is necessary to understand this observation. In addition, a reduced mechanical nociceptive threshold has been extensively reported in the 6-OHDA model, which maybe is directly related to changes in synaptic density in the anterior cingulate cortex (Buhidma et al., 2020).

We observed a lower metabolic function in the ipsilateral motor cortex and the orbitofrontal cortex between the 6-OHDA-injected and saline-injected cortices. The difference in the motor cortex is also seen in patients with PD, but reduced metabolic function in the orbitofrontal cortex are not commonly seen in PD subjects (Meyer et al., 2017). Such cortical reduction was not detected with $[^{11}\text{C}]\text{UCB-J}$, implying the relative robustness in detecting circuit changes with $[^{18}\text{F}]\text{FDG}$.

Disease-specific changes in SV2A density, i.e., synaptic loss, has now been demonstrated in rodent models of neurodegeneration with intracranial injections of neurotoxic agents or with protein inoculation models of PD (Thomsen et al., 2021a,b). Such synaptic loss is also demonstrated in other Alzheimer's disease and PD mice models (Toyonaga et al., 2019;

Xiong et al., 2021). Our study supports the recent study's findings with lower SV2A density within the basal ganglia as reported with PET as well as autoradiography in the 6-OHDA rat model (Binda et al., 2021; Thomsen et al., 2021b), although there are methodological differences, such as employing different kinetic models and site of injection.

[¹¹C]UCB-J has now been used in monkeys (Nabulsi et al., 2016), pigs (Thomsen et al., 2020), mice (Bertoglio et al., 2020), rats (Thomsen et al., 2021b), and humans (Finnema et al., 2016) and show favourable brain penetration, fast uptake and acceptable washout kinetics. In rats and mice, various kinetic modelling was performed using an arterial blood sampling scheme or image-derived input function (IDIF) from the heart (Bertoglio et al., 2020; Glorie et al., 2020; Thomsen et al., 2021b). The 1TCM and 2TCM both work favourably with [¹¹C]UCB-J using the heart as an IDIF (Bertoglio et al., 2020; Glorie et al., 2020). The use of IDIF and whole-brain normalisation allows longitudinal studies in rodents since blood sampling often is laborious and error-prone. Although most of these studies use mice, we assume it translates well to rats.

The small sample size is a limitation of our study, making it particularly hard to conclude that there are no differences (type 2 error). For that reason, we took an exploratory approach without pre-registered predictions and without corrections for multiple testing. As such, the results should be seen as preliminary, and we caution against confirmatory conclusions from the results and encourage future replications using larger samples and a more limited selection of analyses. Further, the contralateral hemisphere may not be an ideal control region because of the inter-hemisphere anatomical connection of the basal ganglia through the pedunculopontine nucleus (Breit et al., 2008). [¹⁸F]FDG results must be evaluated with caution. Other factors, such as neuroinflammation due to the injection or lesion, could evoke increased regional glucose consumption, thus concealing a decreased neuronal function (Blandini et al., 2008). Crabbé et al. have shown an increase in P2X7 receptor (key mediator in neuroinflammation), as well as translocator protein (TSPO) in 6-OHDA, lesioned animals compared to sham lesioned animals using autoradiography (Crabbé et al., 2019). These changes were significant at 21 days; hence uptake of [¹⁸F]FDG in the ventral midbrain may be due to neuroinflammation, which is hard to differentiate using [¹⁸F]FDG. Our setup in a clinical high-resolution PET scanner allows for simultaneous scanning of up to four rats, which further allowed us to perform four [¹¹C]scans with a single radiosynthesis. Although this saves resources and enables a more direct comparison between rats, the resolution of the HRRT is lower than other available single-subject small animal micro-PET systems. Hence, our ability to identify potentially apparent biological differences in small regions is limited due to, e.g., partial volume effects.

Regardless, we found a pattern in the regional cortical synaptic density and neuronal metabolic function, which could be clinically relevant, especially changes within the anterior cingulate cortex and orbitofrontal cortex. We see a clear advantage of including both tracers to get a clearer picture of the neuropathology of neurodegenerative diseases like PD.

CONCLUSION

[¹¹C]UCB-J and [¹⁸F]FDG PET revealed similar changes in the basal ganglia following 6-OHDA dopaminergic lesion in rats. A region-based analysis suggested a divergent response to lesions, especially in the cortical regions, orbitofrontal cortex and medial prefrontal cortex, where higher synaptic density yet lower neuronal metabolic function was observed. Taken together, the results suggest that combined [¹¹C]UCB-J and [¹⁸F]FDG scans may yield a better understanding of aberrant CSTC circuit function and a better diagnostic outcome in patients with neurodegenerative disorders.

DATA AVAILABILITY STATEMENT

The datasets presented in this study can be found in online repositories. The names of the repository/repositories and accession number(s) can be found below: <https://github.com/nakulrraval/6-OHDA-rat-PET-paper>.

ETHICS STATEMENT

The animal study was reviewed and approved by the Danish Council of Animal Ethics (Journal Nos. 2017-15-0201-01375 and 2017-15-0201-01283) and the Department of Experimental Medicine, University of Copenhagen.

AUTHOR CONTRIBUTIONS

NR, FG, PP-S, and MP: conceptualisation, methodology, and software. NR, FG, and PP-S: validation. NR, FG, and MJ: formal analysis. NR, FG, IA, NS, and AV: investigation. NR, MJ, and MP: resources. NR and MP: data curation. NR: writing—original draft preparation and visualisation. NR, FG, MJ, IP, PP-S, GK, and MP: writing—review and editing. JM, PF, MH, PP-S, GK, and MP: supervision. NR, GK, and MP: funding acquisition. All authors have read and agreed to the published version of the manuscript.

FUNDING



This project has received funding from the European Union's Horizon 2020 Research and Innovation Programme under the Marie Skłodowska-Curie grant agreement no 813528. This project also received funding from Parkinson foreningen, Denmark (R16-A247). MP received funding from the Lundbeck Foundation (R192-2015-1591 and R194-2015-1589), Augustinus Foundation (18-3746 and 17-1982), Independent Research Fund Denmark (5053-00036B), and Savværksejer Jeppe Juhls og Hustrus Ovita Juhls Mindelegat and Købmand i Odense Johann og Hanne Weimann født Seedorffs Legat.

ACKNOWLEDGMENTS

The authors would like to thank and show sincere gratitude to the veterinarians and staff at the Department of Experimental Medicine, the University of Copenhagen, for their continued assistance with animal experiments. The authors would also like to thank the Department of Clinical Physiology, Nuclear Medicine and PET for their continuous support in imaging. Structural reference rat MR image is generously provided

by Kristian Nygaard Mortensen, Center for Translational Neuromedicine, University of Copenhagen.

SUPPLEMENTARY MATERIAL

The Supplementary Material for this article can be found online at: <https://www.frontiersin.org/articles/10.3389/fnsyn.2021.715811/full#supplementary-material>

REFERENCES

- Bajjalieh, S. M., Frantz, G. D., Weimann, J. M., McConnell, S. K., and Scheller, R. H. (1994). Differential expression of synaptic vesicle protein 2 (SV2) isoforms. *J. Neurosci.* 14, 5223–5235. doi: 10.1523/jneurosci.14-09-05223.1994
- Bertoglio, D., Verhaeghe, J., Miranda, A., Kertesz, I., Cybulska, K., Korat, Š, et al. (2020). Validation and noninvasive kinetic modeling of [¹¹C]UCB-J PET imaging in mice. *J. Cereb. Blood Flow Metab.* 40, 1351–1362. doi: 10.1177/0271678X19864081
- Binda, K. H., Lillethorup, T. P., Real, C. C., Bærentzen, S. L., Nielsen, M. N., Orłowski, D., et al. (2021). Exercise protects synaptic density in a rat model of Parkinson's disease. *Exp. Neurol.* 342:113741. doi: 10.1016/j.expneurol.2021.113741
- Blandini, F., Armentero, M. T., and Martignoni, E. (2008). The 6-hydroxydopamine model: news from the past. *Parkinsonism Relat. Disord.* 14, S124–S129. doi: 10.1016/j.parkreldis.2008.04.015
- Bliss, T. V. P., Collingridge, G. L., Kaang, B. K., and Zhuo, M. (2016). Synaptic plasticity in the anterior cingulate cortex in acute and chronic pain. *Nat. Rev. Neurosci.* 17, 485–496. doi: 10.1038/nrn.2016.68
- Breit, S., Martin, A., Lessmann, L., Cerkez, D., Gasser, T., and Schulz, J. B. (2008). Bilateral changes in neuronal activity of the basal ganglia in the unilateral 6-hydroxydopamine rat model. *J. Neurosci. Res.* 86, 1388–1396. doi: 10.1002/jnr.21588
- Buhidma, Y., Rukavina, K., Chaudhuri, K. R., and Duty, S. (2020). Potential of animal models for advancing the understanding and treatment of pain in Parkinson's disease. *NPJ Parkinsons Dis.* 6, 1–7. doi: 10.1038/s41531-019-0104-6
- Casado-Sainz, A., Gudmundsen, F., Baerentzen, S. L., Lange, D., Ringsted, A., Martinez-Tajada, I., et al. (2021). Nigro-striatal dopamine activation lowers behavioral and neuronal phenotypes associated with obsessive-compulsive disorder. *bioRxiv* [Preprint] bioRxiv 2021.02.11.430770, doi: 10.1101/2021.02.11.430770
- Casteels, C., Lauwers, E., Bormans, G., Baekelandt, V., and Van Laere, K. (2008). Metabolic-dopaminergic mapping of the 6-hydroxydopamine rat model for Parkinson's disease. *Eur. J. Nucl. Med. Mol. Imaging* 35, 124–134. doi: 10.1007/s00259-007-0558-3
- Chen, M.-K., Mecca, A. P., Naganawa, M., Gallezot, J.-D., Toyonaga, T., Mondal, J., et al. (2021). Comparison of [¹¹C]UCB-J and [¹⁸F] FDG PET in Alzheimer's disease: a tracer kinetic modeling study. *J. Cereb. Blood Flow Metab.* 41, 2395–2409. doi: 10.1177/0271678X211004312
- Crabbé, M., Van Der Perren, A., Bollaerts, I., Kounelis, S., Baekelandt, V., Bormans, G., et al. (2019). Increased P2X7 receptor binding is associated with neuroinflammation in acute but not chronic rodent models for Parkinson's disease. *Front. Neurosci.* 13:799. doi: 10.3389/fnins.2019.00799
- Esteban, S., Lladó, J., Sastre-Coll, A., and García-Sevilla, J. A. (1999). Activation and desensitization by cyclic antidepressant drugs of α 2- autoreceptors, α 2- heteroreceptors and 5-HT(1A)-autoreceptors regulating monoamine synthesis in the rat brain in vivo. *Naunyn Schmiedeberg's Arch. Pharmacol.* 360, 135–143. doi: 10.1007/s002109900045
- Finnema, S. J., Nabulsi, N. B., Eid, T., Detyniecki, K., Lin, S. F., Chen, M. K., et al. (2016). Imaging synaptic density in the living human brain. *Sci. Transl. Med.* 8:348ra96. doi: 10.1126/scitranslmed.aaf6667
- Glorie, D., Verhaeghe, J., Miranda, A., De Lombaerde, S., Stroobants, S., and Staelens, S. (2020). Sapap3 deletion causes dynamic synaptic density abnormalities: a longitudinal [¹¹C]UCB-J PET study in a model of obsessive-compulsive disorder-like behaviour. *EJNMMI Res.* 10:140. doi: 10.1186/s13550-020-00721-2
- Groenewegen, H. J., and Trimble, M. (2007). The ventral striatum as an interface between the limbic and motor systems. *CNS Spectr.* 12, 887–892. doi: 10.1017/S1092852900015650
- Holland, N., Jones, P. S., Savulich, G., Wiggins, J. K., Hong, Y. T., Fryer, T. D., et al. (2020). Synaptic loss in primary tauopathies revealed by [¹¹C]UCB-J positron emission tomography. *Mov. Disord.* 35, 1834–1842. doi: 10.1002/mds.28188
- Im, H. J., Hahn, J., Kang, H., Choi, H., Lee, H., Hwang, D. W., et al. (2016). Disrupted brain metabolic connectivity in a 6-OHDA-induced mouse model of Parkinson's disease examined using persistent homology-based analysis. *Sci. Rep.* 6:33875. doi: 10.1038/srep33875
- Jang, D. P., Min, H. K., Lee, S. Y., Kim, I. Y., Park, H. W., Im, Y. H., et al. (2012). Functional neuroimaging of the 6-OHDA lesion rat model of Parkinson's disease. *Neurosci. Lett.* 513, 187–192. doi: 10.1016/j.neulet.2012.02.034
- Keller, S. H., L'Estrade, E. N., Dall, B., Palmer, M., and Herth, M. (2017). "Quantification accuracy of a new HRRT high throughput rat hotel using transmission-based attenuation correction: a phantom study," in *Proceedings of the 2016 IEEE Nuclear Science Symposium, Medical Imaging Conference and Room-Temperature Semiconductor Detector Workshop, NSS/MIC/RTSD 2016*, (Strasbourg: IEEE), 1–3. doi: 10.1109/NSSMIC.2016.8069467
- Keller, S. H., Svarer, C., and Sibomana, M. (2013). Attenuation correction for the HRRT PET-scanner using transmission scatter correction and total variation regularization. *IEEE Trans. Med. Imaging* 32, 1611–1621. doi: 10.1109/TMI.2013.2261313
- Kerstens, V. S., and Varrone, A. (2020). Dopamine transporter imaging in neurodegenerative movement disorders: PET vs. SPECT. *Clin. Transl. Imaging* 8, 349–356. doi: 10.1007/s40336-020-00386-w
- Kordys, E., Apetz, N., Schneider, K., Duncan, E., Büschbell, B., Rohleder, C., et al. (2017). Motor impairment and compensation in a hemiparkinsonian rat model: correlation between dopamine depletion severity, cerebral metabolism and gait patterns. *EJNMMI Res.* 7:68. doi: 10.1186/s13550-017-0317-9
- Kurachi, M., Yasui, S. I., Kurachi, T., Shibata, R., Murata, M., Hagino, H., et al. (1995). Hypofrontality does not occur with 6-hydroxydopamine lesions of the medial prefrontal cortex in rat brain. *Eur. Neuropsychopharmacol.* 5, 63–68. doi: 10.1016/0924-977X(94)00136-Y
- Lakens, D. (2013). Calculating and reporting effect sizes to facilitate cumulative science: a practical primer for t-tests and ANOVAs. *Front. Psychol.* 4:863. doi: 10.3389/fpsyg.2013.00863
- Loane, C., and Politis, M. (2011). Positron emission tomography neuroimaging in Parkinson's disease. *Am. J. Transl. Res.* 3, 323–341.
- Matuskey, D., Tinaz, S., Wilcox, K. C., Naganawa, M., Toyonaga, T., Dias, M., et al. (2020). Synaptic changes in Parkinson disease assessed with in vivo imaging. *Ann. Neurol.* 87, 329–338. doi: 10.1002/ana.25682
- Mecca, A. P., Chen, M. K., O'Dell, R. S., Naganawa, M., Toyonaga, T., Godek, T. A., et al. (2020). In vivo measurement of widespread synaptic loss in Alzheimer's disease with SV2A PET. *Alzheimers Dement.* 16, 974–982. doi: 10.1002/alz.12097
- Meyer, P. T., Frings, L., Rücker, G., and Hellwig, S. (2017). 18F-FDG PET in Parkinsonism: differential diagnosis and evaluation of cognitive impairment. *J. Nucl. Med.* 58, 1888–1898. doi: 10.2967/jnumed.116.186403
- Mosconi, L. (2013). Glucose metabolism in normal aging and Alzheimer's disease: methodological and physiological considerations for PET studies. *Clin. Transl. Imaging* 1, 217–233. doi: 10.1007/s40336-013-0026-y

- Murphy, M. J. M., and Deutch, A. Y. (2018). Organization of afferents to the orbitofrontal cortex in the rat. *J. Comp. Neurol.* 526, 1498–1526. doi: 10.1002/cne.24424
- Nabulsi, N. B., Mercier, J., Holden, D., Carr, S., Najafzadeh, S., Vandergeten, M. C., et al. (2016). Synthesis and preclinical evaluation of ¹¹C-UCB-J as a PET tracer for imaging the synaptic vesicle glycoprotein 2A in the brain. *J. Nucl. Med.* 57, 777–784. doi: 10.2967/jnumed.115.168179
- Nicastro, N., Holland, N., Savulich, G., Carter, S. F., Mak, E., Hong, Y. T., et al. (2020). ¹¹C-UCB-J synaptic PET and multimodal imaging in dementia with Lewy bodies. *Eur. J. Hybrid Imaging* 4:25. doi: 10.1186/s41824-020-0093-9
- O'Dell, R. S., Mecca, A. P., Chen, M. K., Naganawa, M., Toyonaga, T., Lu, Y., et al. (2021). Association of Aβ deposition and regional synaptic density in early Alzheimer's disease: a PET imaging study with [¹¹C]UCB-J. *Alzheimers Res. Ther.* 13:11. doi: 10.1186/s13195-020-00742-y
- Palner, M., Kjaerby, C., Knudsen, G. M., and Cumming, P. (2011). Effects of unilateral 6-OHDA lesions on [³H]-N-propylnorapomorphine binding in striatum ex vivo and vulnerability to amphetamine-evoked dopamine release in rat. *Neurochem. Int.* 58, 243–247. doi: 10.1016/j.neuint.2010.12.007
- Papadopoulos, G. C., and Parnavelas, J. G. (1990). Distribution and synaptic organization of dopaminergic axons in the lateral geniculate nucleus of the rat. *J. Comp. Neurol.* 294, 356–361. doi: 10.1002/cne.902940305
- Schiffer, W. K., Mirrione, M. M., Biegón, A., Alexoff, D. L., Patel, V., and Dewey, S. L. (2006). Serial microPET measures of the metabolic reaction to a microdialysis probe implant. *J. Neurosci. Methods* 155, 272–284. doi: 10.1016/j.jneumeth.2006.01.027
- Schwartz, R. K. W., and Huston, J. P. (1996). The unilateral 6-hydroxydopamine lesion model in behavioral brain research. Analysis of functional deficits, recovery and treatments. *Prog. Neurobiol.* 50, 275–331. doi: 10.1016/S0301-0082(96)00040-8
- Shalgunov, V., Xiong, M., L'Estrade, E. T., Raval, N. R., Andersen, I. V., Edgar, F. G., et al. (2020). Blocking of efflux transporters in rats improves translational validation of brain radioligands. *EJNMMI Res.* 10:124. doi: 10.1186/s13550-020-00718-x
- Silva, M. D., Glaus, C., Hesterman, J. Y., Hoppin, J., Puppa, G. H., Kazules, T., et al. (2013). Regional, kinetic [¹⁸F]FDG PET imaging of a unilateral Parkinsonian animal model. *Am. J. Nucl. Med. Mol. Imaging* 3, 129–141.
- Südhof, T. C. (2004). The synaptic vesicle cycle. *Annu. Rev. Neurosci.* 27, 509–547. doi: 10.1146/annurev.neuro.26.041002.131412
- Thomsen, M. B., Jacobsen, J., Lillethorup, T. P., Schacht, A. C., Simonsen, M., Romero-Ramos, M., et al. (2021b). In vivo imaging of synaptic SV2A protein density in healthy and striatal-lesioned rats with [¹¹C]UCB-J PET. *J. Cereb. Blood Flow Metab.* 41, 819–830. doi: 10.1177/0271678X20931140
- Thomsen, M. B., Ferreira, S. A., Schacht, A. C., Jacobsen, J., Simonsen, M., Betzer, C., et al. (2021a). PET imaging reveals early and progressive dopaminergic deficits after intra-striatal injection of preformed alpha-synuclein fibrils in rats. *Neurobiol. Dis.* 149:105229. doi: 10.1016/j.nbd.2020.105229
- Thomsen, M. B., Schacht, A. C., Alstrup, A. K. O., Jacobsen, J., Lillethorup, T. P., Bærentzen, S. L., et al. (2020). Preclinical PET studies of [¹¹C]UCB-J binding in minipig brain. *Mol. Imaging Biol.* 22, 1290–1300. doi: 10.1007/s11307-020-01506-8
- Toyonaga, T., Smith, L. M., Finnema, S. J., Gallezot, J. D., Naganawa, M., Bini, J., et al. (2019). In vivo synaptic density imaging with ¹¹C-UCB-J detects treatment effects of saracatinib in a mouse model of Alzheimer disease. *J. Nucl. Med.* 60, 1780–1786. doi: 10.2967/jnumed.118.223867
- Vriend, C., Pattij, T., Van Der Werf, Y. D., Voorn, P., Booij, J., Rutten, S., et al. (2014). Depression and impulse control disorders in Parkinson's disease: two sides of the same coin? *Neurosci. Biobehav. Rev.* 38, 60–71. doi: 10.1016/j.neubiorev.2013.11.001
- Wilson, H., Pagano, G., de Natale, E. R., Mansur, A., Caminiti, S. P., Polychronis, S., et al. (2020). Mitochondrial complex 1, sigma 1, and synaptic vesicle 2A in early drug-naïve Parkinson's disease. *Mov. Disord.* 35, 1416–1427. doi: 10.1002/mds.28064
- Xiong, M., Roshanbin, S., Rokka, J., Schlein, E., Ingelsson, M., Sehlin, D., et al. (2021). In vivo imaging of synaptic density with [¹¹C]UCB-J PET in two mouse models of neurodegenerative disease. *Neuroimage* 239:118302. doi: 10.1016/j.neuroimage.2021.118302
- Yuan, H., Sarre, S., Ebinger, G., and Michotte, Y. (2005). Histological, behavioural and neurochemical evaluation of medial forebrain bundle and striatal 6-OHDA lesions as rat models of Parkinson's disease. *J. Neurosci. Methods* 144, 35–45. doi: 10.1016/j.jneumeth.2004.10.004

Conflict of Interest: MP: Compass Pathways Plc (research collaboration), GK: H. Lundbeck A/S (research collaboration), Compass Pathways Plc (research collaboration), Elysis (research collaboration), Novo Nordisk, Novozymes, Chr. Hansen (stockholder), Sage Therapeutics and Sanos (Advisor). GK is currently the president of the European College of Neuropsychopharmacology.

The remaining authors declare that the research was conducted in the absence of any commercial or financial relationships that could be construed as a potential conflict of interest.

Publisher's Note: All claims expressed in this article are solely those of the authors and do not necessarily represent those of their affiliated organizations, or those of the publisher, the editors and the reviewers. Any product that may be evaluated in this article, or claim that may be made by its manufacturer, is not guaranteed or endorsed by the publisher.

Copyright © 2021 Raval, Gudmundsen, Juhl, Andersen, Speth, Videbæk, Petersen, Mikkelsen, Fisher, Herth, Plavén-Sigray, Knudsen and Palner. This is an open-access article distributed under the terms of the Creative Commons Attribution License (CC BY). The use, distribution or reproduction in other forums is permitted, provided the original author(s) and the copyright owner(s) are credited and that the original publication in this journal is cited, in accordance with accepted academic practice. No use, distribution or reproduction is permitted which does not comply with these terms.

Supplementary Material

1 Supplementary Data

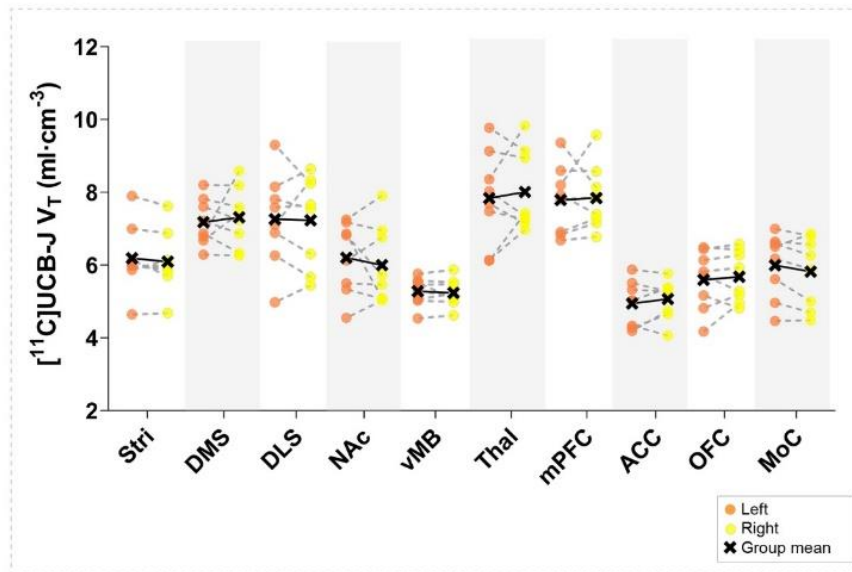
1.1 Baseline [¹¹C]UCB-J

1.1.1 Methods and Materials:

To validate any potential hemisphere asymmetry, we acquired baseline [¹¹C]UCB-J PET in a different group of eight female Long-Evans WT rats (193 ± 6 g, 9-10 weeks old when scanned) (Janvier). The animals were held under standard laboratory conditions with 12-hour light/12-hour dark cycles and ad libitum access to food and water. All animal experiments conformed to the European Commission's Directive 2010/63/EU with approval from the Danish Council of Animal Ethics (Journal no. 2017-15-0201-01283) and the Department of Experimental Medicine, University of Copenhagen.

Scans were performed in the same fashion as previously described in the main manuscript. Briefly, after transport to the Siemens HRRT scanner, anaesthesia was induced using 3% isoflurane in oxygen. All rats were placed in a 2 x 2 custom made rat holder. Four rats were scanned at a time. While in the custom-made rat holder, the rats were kept under anaesthesia with a constant flow of isoflurane (~2% isoflurane in oxygen). At the start of the scan, intravenous (IV) injections were given over 7-10 secs through the tail vein catheter, with an average dose of 17.2 ± 2.5 MBq (injected mass = 0.06 ± 0.07 μ g). Heparinised saline (500-600 μ L) was flushed through the catheter after tracer injection. The acquisition time for [¹¹C]UCB-J was 60 minutes.

PET image reconstruction and pre-processing were also performed in the same fashion as previously described. The data were analysed using Jamovi (Version 1.6, The jamovi project (2021) [Computer Software]. The difference between the left and right hemispheres for [¹¹C]UCB-J in the baseline animals was calculated in Jamovi using paired t-test without correction for multiple comparisons. Cohen's dz values between the regions in the right and left hemispheres were also calculated. GraphPad Prism (v. 9.2.0; GraphPad Software, San Diego, CA, USA) was used for data visualisation.

[¹¹C]UCB-J Baseline Left vs Right hemisphere (n=8)

Supplementary Figure 1. Baseline [¹¹C]UCB-J. Comparison of the [¹¹C]UCB-J V_T between the left and right hemisphere in baseline animals (n=8). Stri= striatum, DMS= dorsomedial striatum, DLS= dorsolateral striatum, NAc= nucleus accumbens, vMB= ventral midbrain, Thal= thalamus, mPFC= medial prefrontal cortex, ACC= anterior cingulate cortex, OFC= orbitofrontal cortex, MoC= motor cortex.

Supplementary Table 1. Summary of the paired t-test between the regions in the left and right hemisphere for [¹¹C]UCB-J in the baseline animals (n=8). Cohen's dz values and its 95% confidence interval has also been added. Stri= striatum, DMS= dorsomedial striatum, DLS= dorsolateral striatum, NAc= nucleus accumbens, vMB= ventral midbrain, Thal= thalamus, mPFC= medial prefrontal cortex, ACC= anterior cingulate cortex, OFC= orbitofrontal cortex, MoC= motor cortex.

<u>[¹¹C]UCB-J V_T in left vs right hemisphere</u>					
Baseline animals					
Region	% diff	p value	Cohen's dz	Cohen's dz 95% CI	
				Upper	Lower
Stri	1.50%	0.254	-0.4394	-1.154	0.303
DMS	-1.82%	0.649	0.168	-0.536	0.861
DLS	0.41%	0.913	-0.04	-0.732	0.655
NAc	3.26%	0.528	-0.235	-0.93	0.476
vMB	0.82%	0.553	-0.2203	-0.915	0.489
Thal	-2.16%	0.61	0.1889	-0.517	0.882
mPFC	-0.69%	0.844	0.072	-0.624	0.763
ACC	-2.45%	0.317	0.3808	-0.352	1.089
OFC	-1.52%	0.552	0.2208	-0.489	0.915
MoC	2.91%	0.126	-0.615	-1.359	0.164

1.1.2 Results:

No differences were observed in [^{11}C]UCB-J V_T (Supplementary Figure 1 and Supplementary Table 1) between the regions in the left and right hemispheres at baseline.

1.2 Cortical autoradiography with [^3H]UCB-J

1.2.1 Methods and Materials:

Autoradiography was performed using [^3H]UCB-J (Pharmaron Ltd., Hoddesdon, UK, molar activity 28 Ci/mmol). Radio-Thin-Layered-Chromatography (R-TLC) was performed to measure the radiochemical purity (RCP) and integrity of the parent compound. The mobile phase for [^3H]UCB-J R-TLC was Acetonitrile:Ammonium formate [25:75] (0.1 M, with 0.5% AcOH, pH 4.2).

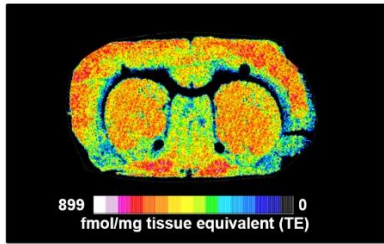
Frozen sections (containing three slices) from dopamine and sham lesioned animals ($n=4/\text{group}$) (20 μm , sectioning previously explained) were thawed to room temperature for 30–45 min before preincubating twice for 10 min in 50 mM Tris-HCl pre-incubation buffer set to 7.4 pH containing 0.5% bovine serum albumin (BSA). The sections were incubated in assay buffer containing 6 nM [^3H]UCB-J in 50 mM Tris-HCl buffer containing 5 mM MgCl_2 , 2 mM EGTA and 0.5% BSA (pH 7.4) for 1 hour. Incubation was terminated by two 10-min washes with ice-cold pre-incubation buffer followed by a rapid rinse in ice-cold deionised H_2O (dH_2O). After washing, the slides were rapidly air-dried and fixated in a paraformaldehyde vapour chamber overnight in cold storage (4 $^\circ\text{C}$). The next day, the samples were moved to an exicator for 45–60 min to remove any excess moisture and then placed in a cassette for autoradiography with tritium sensitive image plates (BAS-IP TR2040, Science Imaging, Scandinavia AB, Nacka, Sweden) along with radioactive tritium standards (ART0123B, American Radiolabelled Chemical, Inc., St. Louis, MO, USA). The image plates were exposed for two days.

After the exposure, the image plates were read using a Fujifilm BAS 1000 scanner (Fujifilm Europe, GmbH, Duesseldorf, Germany). Calibration, quantification and data evaluation was done using ImageJ software (NIH Image, Bethesda, MD, USA). The regions of interest (Supplementary Figure 2B) were hand-drawn or drawn using the wand tool and visually inspected after automated delineation. The four-parameter general curve fit (David Rodbard, NIH) of decay corrected tritium standards was used to convert mean pixel density (grayscale) to nCi/mg tissue equivalent (TE). Total binding was determined in the grey matter: cingulate cortex and motor cortex (Supplementary Figure 2B). Non-specific binding was determined in the corpus callosum (Supplementary Figure 2B). We have previously validated the use of white matter as non-specific binding in pigs (Raval et al., 2021); we have also validated this in rats (data not shown). Finally, the decay-corrected molar activity of the representative radioligand was used to convert nCi/mg TE to fmol/mg TE. Specific binding was calculated as the difference between total binding and non-specific binding.

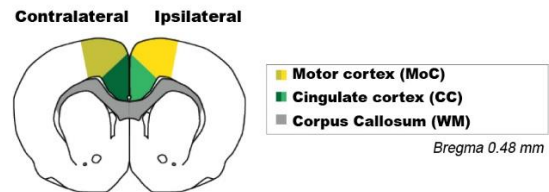
The data were analysed using Jamovi (Version 1.6, The jamovi project (2021) [Computer Software]. Retrieved from <https://www.jamovi.org>). The difference between the ipsilateral and contralateral side [^3H]UCB-J in the sham and dopamine lesioned group was calculated in Jamovi using paired t-test without correction for multiple comparisons. The difference between the two groups in the contralateral and ipsilateral hemisphere was calculated with an independent samples t-test (Mann-Whitney test). Graph-Pad Prism (v. 9.2.0; GraphPad Software, San Diego, CA, USA) was used for data visualisation. Graph-Pad Prism was also used to calculate Pearson r and perform a simple linear regression. Pearson r values between the [^3H]UCB-J fmol/mg TE and representative [^{11}C]UCB-J V_T

values from each region in the contralateral and ipsilateral hemisphere providing eight different correlation values. Values were averaged for the contralateral and ipsilateral separately to get two Pearson r values.

A) [³H]UCB-J *in-vitro* Autoradiography
Sham lesioned

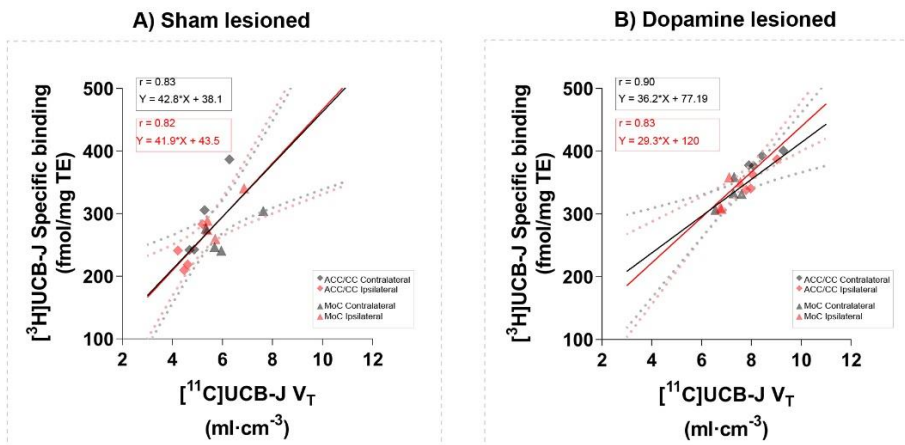


B) Region of Interests (ROI)

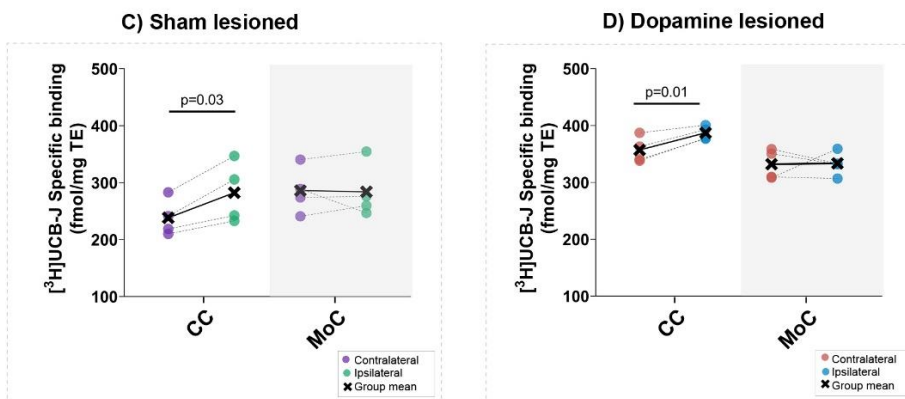


Supplementary Figure 2. Representative [³H]UCB-J *in vitro* autoradiography. A) Representative examples of [³H]UCB-J autoradiography from sham lesioned animals: section contains the cingulate cortex, motor cortex and corpus callosum B) Region of interests used in the study includes: CC = cingulate cortex (green), MoC = motor cortex (yellow) and WM = corpus callosum.

[³H]UCB-J Autoradiography vs [¹¹C]UCB-J PET



[³H]UCB-J Cortical Autoradiography



Supplementary Figure 3. Correlation between the [³H]UCB-J fmol/mg TE and representative [¹¹C]UCB-J V_T values in the sham (A) and dopamine (B) lesioned animals (n=4/group). Average Pearson r values and equation is inserted colour coded for the two linear regression. Comparison of ipsilateral and contralateral [³H]UCB-J specific binding (fmol/mg tissue equivalent [TE]) values in the cingulate and motor cortex of the sham (C) and dopamine (D) lesioned animals. Notable differences are marked with their p values. CC = cingulate cortex (green), MoC = motor cortex.

1.2.2 Results

To further validate the PET finding and verify the cortical changes detected by [¹¹C]UCB-J PET in the sham and dopamine lesioned animals, in vitro [³H]UCB-J autoradiography were performed in the cingulate cortex and motor cortex of all animals. Representative [³H]UCB-J autoradiography images from sham lesioned animals are shown in Supplementary Figure 2A. Supplementary Figure 2B shows the region of interest used in this analysis.

A correlation analysis between [³H]UCB-J fmol/mg TE and representative [¹¹C]UCB-J V_T values in both the contralateral and ipsilateral regions in the sham lesioned animals (Supplementary Figure 3A) shows a Pearson r value of 0.83 and 0.82, respectively. Similar correlation analysis in the contralateral and ipsilateral regions in the dopamine lesioned animals (Supplementary Figure 3B) shows a Pearson r value of 0.90 and 0.83, respectively. Results taken together show a high correlation between PET and autoradiography.

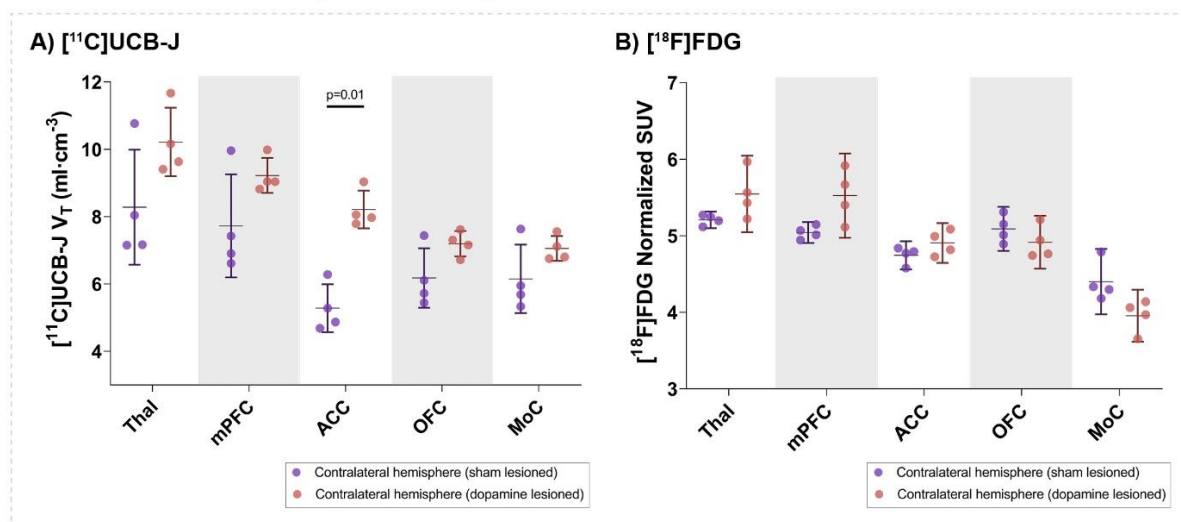
Increased specific [³H]UCB-J binding in the ipsilateral hemisphere compared to the contralateral hemisphere is seen in the cingulate cortex in sham lesioned animals (18.3%, Cohen dz = 1.84, p = 0.03) (Supplementary Figure 3C) as well as dopamine lesioned animals (8.3%, Cohen dz = 2.59, p = 0.01) (Supplementary Figure 3D). Summarised in Supplementary Table 1.

Supplementary Table 2: Summarised test in the Cingulate cortex. Notable differences are marked with *.

[³H]UCB-J Autoradiography: Cingulate Cortex			
Group	Test	% diff	p value
Sham Lesioned	Ipsilateral vs Contralateral	18.3 %	0.03*
Dopamine Lesioned	Ipsilateral vs Contralateral	8.3 %	0.01*
Dopamine vs Sham Lesioned	Contralateral	51.2 %	0.02*
Dopamine vs Sham Lesioned	Ipsilateral	40.7 %	0.02*

1.3 Changes in contralateral regions of [¹¹C]UCB-J binding and [¹⁸F]FDG uptake

Contralateral hemisphere comparison



Supplementary Figure 4. Analysis of [¹¹C]UCB-J V_T values (A) and [¹⁸F]FDG (B) uptake in the contralateral side of dopamine lesioned and sham lesioned animals. Error bar denotes the mean and the 95% confidence interval. Thal = thalamus, mPFC = medial prefrontal cortex, ACC = anterior cingulate cortex, OFC = orbitofrontal cortex, MoC = motor cortex.

A posthoc analysis of changes in the cortical regions and thalamus in the contralateral hemisphere between the dopamine lesion and sham group (Supplementary Figure 4) showed an increase in [¹¹C]UCB-J V_T values in the anterior cingulate cortex (55.5%, p = 0.01). In contrast, there is no difference in [¹⁸F]FDG uptake.

1.4 Radiosynthesis of [¹¹C]UCB-J ((R)-1-((3-(11C-methyl-11C)pyridin-4-yl)methyl)-4-(3,4,5-trifluorophenyl)pyrrolidin-2-one)

Proton irradiation of the target material (nitrogen-14 gas) is performed using the cyclotron:

Scanditronix MC-32 (Variable energy: 16-32 MeV protons) with an aluminium high-pressure gas target. Irradiations for carbon-11 are performed at 16 MeV. The target gas used is 10% hydrogen in nitrogen. Following irradiation, the target gas is transferred to the radiochemistry system through stainless steel capillaries.

Radiosynthesis is carried out using a fully automated radiochemistry system manufactured by Scansys Aps. [¹¹C]methyl iodide is synthesised from [¹¹C]methane by a standard circulation procedure.

1.4.1 Preparation of the precursor:

1 M HCl (15 μ L) and MeOH (70 μ L) is added to the precursor (1.2 mg) and reacted overnight. On the day of synthesis, the liquid is removed by a stream of nitrogen to complete dryness.

1.4.2 Preparation of the labelling mixture:

4-5 mg P-(o-tolyl)₃ was dissolved in DMF (1.8 mL) and H₂O (0.2 mL) in a capped vial and degassed with nitrogen. Pd₂dba₃ (4-5 mg) was weighed out in a capped vial and flushed with nitrogen. Right before labelling, the P-(o-tolyl)₃ solution was added to the Pd₂dba₃. From here, 350 μ L was withdrawn and added to a 0.9 ml vial containing 0.5 M K₂CO₃ (20 μ L).

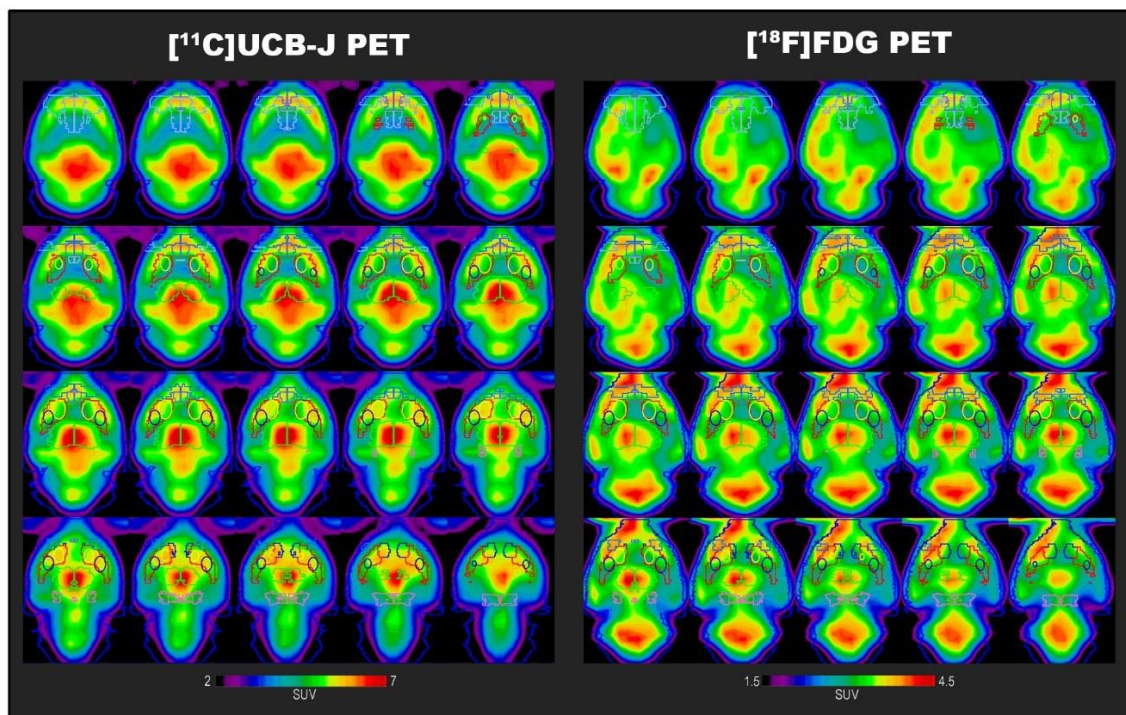
The formed [¹¹C]methyl iodide was trapped in the 0.9 ml glass vial containing the K₂CO₃/ P-(o-tolyl)₃/Pd₂dba₃ mixture. After trapping the [¹¹C]methyl iodide, the hydrolysed DM-BF₃-UCB-J precursor was re-dissolved in DMF (150 μ L) added and reacted with the mixture by heating at 100 °C for 300 seconds to give [¹¹C]UCB-J. The diluted reaction mixture was diluted with 4 ml 0.1 % H₃PO₄ and automatically injected onto a preparative HPLC column (Onyx™ Monolithic C-18, 100 \times 10 mm equipped with a SecurityGuard Cartridge Lux Cellulose-4, 4 \times 3.0 mm; flow: 6 ml/min; eluent: 12.5/80 [ethanol (96%)/0.1 M phosphoric acid]). The radioactive fraction corresponding to the radiolabelled product (retention time ca. 300 s) was collected by diverting the flow from the column outlet through a 0.22 μ m sterile filter and directly into a sterile stoppered and a capped vial containing phosphate buffer (9 ml, pH 7). The identity and molar activity of the product was determined by using a C-18 column (Kinetex 2.6 μ m, C18, 100Å, 50 \times 4.6 mm, Phenomenex) eluted with 33% acetonitrile in 25mM citrate buffer (pH 5.4); injection volume 50 μ L; flow rate 1.5 ml/min; on-line UV (261 nm) and radioactivity detection. Rt UCB-J 2.1 min.

1.4.3 Molar activity:

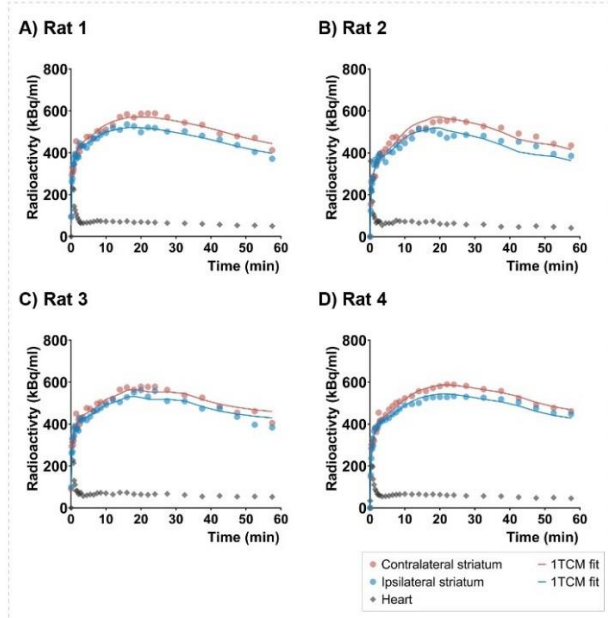
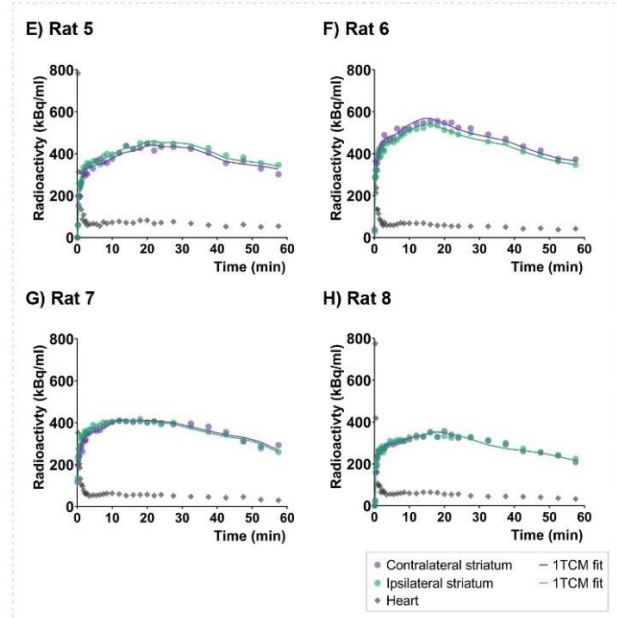
The molar activity at the time of injection for the two productions used in this 6-OHDA study was 404 and 168 GBq/ μ mol. The molar activity at the time of injection in the baseline study was 353 and 628 GBq/ μ mol.

2 Supplementary Figures and Tables

2.1 Supplementary Figures



Supplementary Figure 5. Position and fit of the select region of interests on summed PET images from the study of a single representative animal for [¹⁸F]FDG and [¹¹C]UCB-J scan. Regions include: medial prefrontal cortex (medium blue), orbitofrontal cortex (purple), motor cortex(light blue), anterior cingulate cortex (grey), striatum (red), dorsomedial striatum (yellow), dorsolateral striatum (navy blue), thalamus (green), nucleus accumbens (dark blue), and ventral midbrain (pink).

Dopamine LesionedStriatum [^{11}C]UCB-J TAC with 1TCM fit**Sham Lesioned**Striatum [^{11}C]UCB-J TAC with 1TCM fit

Supplementary Figure 6. Representative [^{11}C]UCB-J 1TCM model fit in animals within the dopamine and sham lesioned groups. Time activity curves (TAC) demonstrated are from the ipsilateral and contralateral striatum and the heart, used as image-derived input function (IDIF). 1TCM fit using the IDIF is used to extract V_T values and other modelling parameters like K_1 and k_2 values.

2.2 Supplementary Table

Supplementary Table 3: Summarised table of [¹¹C]UCB-J 1TCM modelling parameters in the ipsilateral and contralateral side of dopamine and sham lesioned animals. Mean values with standard deviation are presented for all animals (n = 4/group). Stri= striatum, DMS= dorsomedial striatum, DLS= dorsolateral striatum, NAc= nucleus accumbens, vMB= ventral midbrain, Thal= thalamus, mPFC= medial prefrontal cortex, ACC= anterior cingulate cortex, OFC= orbitofrontal cortex, MoC= motor cortex.

[¹¹C]UCB-J 1TCM modelling parameters								
Dopamine Lesioned					Sham Lesioned			
Region	Ipsilateral Side		Contralateral Side		Ipsilateral Side		Contralateral Side	
	K1	k2	K1	k2	K1	k2	K1	k2
Stri	1.18 (0.06)	0.14 (0.01)	1.18 (0.08)	0.12 (0.01)	1.16 (0.19)	0.16 (0.01)	1.14 (0.25)	0.15 (0.01)
DMS	1.23 (0.15)	0.13 (0.02)	1.3 (0.16)	0.13 (0.02)	1.21 (0.23)	0.16 (0.01)	1.17 (0.26)	0.16 (0.01)
DLS	1.25 (0.1)	0.13 (0.01)	1.26 (0.13)	0.13 (0.01)	1.18 (0.24)	0.15 (0.01)	1.16 (0.18)	0.15 (0.01)
NAc	1.04 (0.01)	0.13 (0.01)	1.05 (0.03)	0.12 (0.01)	1.02 (0.07)	0.16 (0.02)	0.96 (0.09)	0.16 (0.03)
vMB	1.45 (0.13)	0.2 (0.02)	1.5 (0.15)	0.19 (0.02)	1.3 (0.22)	0.21 (0.04)	1.29 (0.15)	0.21 (0.02)
Thal	1.55 (0.11)	0.15 (0.01)	1.5 (0.13)	0.17 (0.01)	1.42 (0.26)	0.17 (0.01)	1.37 (0.16)	0.17 (0.01)
mPFC	1.21 (0.09)	0.12 (0.01)	1.27 (0.1)	0.13 (0.01)	1.22 (0.18)	0.16 (0.01)	1.23 (0.21)	0.16 (0.01)
ACC	1.06 (0.09)	0.12 (0.01)	1.09 (0.09)	0.13 (0.01)	0.9 (0.19)	0.17 (0.01)	0.78 (0.09)	0.16 (0.01)
OFC	1.06 (0.03)	0.14 (0.01)	1.09 (0.06)	0.15 (0.007)	1.07 (0.2)	0.17 (0.01)	0.99 (0.13)	0.17 (0.01)
MoC	0.98 (0.06)	0.13 (0.01)	0.94 (0.08)	0.13 (0.01)	1.03 (0.19)	0.16 (0.01)	0.96 (0.13)	0.16 (0.01)



DECLARATION OF CO-AUTHORSHIP

The declaration is for PhD students and must be completed for each conjointly authored article. Please note that if a manuscript or published paper has ten or less co-authors, all co-authors must sign the declaration of co-authorship. If it has more than ten co-authors, declarations of co-authorship from the corresponding author(s), the senior author and the principal supervisor (if relevant) are a minimum requirement.

1. Declaration by	
Name of PhD student	Nakul Ravi Raval
E-mail	nakul.raval@nru.dk
Name of principal supervisor	Prof. Dr. Gitte Moos Knudsen
Title of the PhD thesis	Translational Positron Emission Tomography: Animal Models and In vitro Autoradiography for Radioligand Development

2. The declaration applies to the following article	
Title of article	Synaptic Density and Neuronal Metabolic Function Measured by PET in the Unilateral 6-OHDA Rat Model of Parkinson's Disease
Article status	
Published <input checked="" type="checkbox"/>	Accepted for publication <input type="checkbox"/>
Date: 18/11/21	Date:
Manuscript submitted <input type="checkbox"/>	Manuscript not submitted <input type="checkbox"/>
Date:	
If the article is published or accepted for publication, please state the name of journal, year, volume, page and DOI (if you have the information).	Front. Synaptic Neurosci. 13:715811. doi: 10.3389/fnsyn.2021.715811

3. The PhD student's contribution to the article (please use the scale A-F as benchmark)	A, B, C, D, E, F
Benchmark scale of the PhD-student's contribution to the article A. Has essentially done all the work (> 90 %) B. Has done most of the work (60-90 %) C. Has contributed considerably (30-60 %) D. Has contributed (10-30 %) E. No or little contribution (<10 %) F. Not relevant	
1. Formulation/identification of the scientific problem	B

3. The PhD student's contribution to the article (please use the scale A-F as benchmark)	
Benchmark scale of the PhD-student's contribution to the article	A, B, C, D, E, F
A. Has essentially done all the work (> 90 %) B. Has done most of the work (60-90 %) C. Has contributed considerably (30-60 %) D. Has contributed (10-30 %) E. No or little contribution (<10 %) F. Not relevant	
2. Development of the key methods	B
3. Planning of the experiments and methodology design and development	A
4. Conducting the experimental work/clinical studies/data collection/obtaining access to data	B
5. Conducting the analysis of data	D
6. Interpretation of the results	C
7. Writing of the first draft of the manuscript	A
8. Finalisation of the manuscript and submission	A
Provide a short description of the PhD student's specific contribution to the article. ⁱ	
NRR helped design the study, performed the intracranial injections, performed all PET scans and analysed one data set out of the two that are used in this study. NRR was responsible for planning and conducting data analysis with assistance from Federik Gudmundsen (shared first author). NRR was also responsible for interpretation of the results, writing the first draft and submitting the manuscript.	

4. Material from another thesis / dissertationⁱⁱ	
Does the article contain work which has also formed part of another thesis, e.g. master's thesis, PhD thesis or doctoral dissertation (the PhD student's or another person's)?	Yes: <input checked="" type="checkbox"/> No: <input type="checkbox"/>
If yes, please state name of the author and title of thesis / dissertation.	Frederik Gudmundsen Master thesis: Whole brain circuit dissection. A promising avenue for understanding the pathophysiology of OCD.
If the article is part of another author's academic degree, please describe the PhD student's and the author's contributions to the article so that the individual contributions are clearly distinguishable from one another.	This is the shared first authorship between NRR and FD. NRR performed all in vivo and in vitro experiments and analyzed one data set. At the same time, FD analyzed the other data set, which is part of his master's thesis.

5. Signatures of the co-authors ⁱⁱⁱ				
	Date	Name	Title	Signature
1.	03/01/22	Frederik Gudmundsen	MSc	
2.	03/01/22	Mikael Palner	PhD	
3.	03/02/22	Gitte Moos Knudsen	Professor	

6. Signature of the principal supervisor
I solemnly declare that the information provided in this declaration is accurate to the best of my knowledge. Date: 03/02/2022 Principal supervisor: 

7. Signature of the PhD student
I solemnly declare that the information provided in this declaration is accurate to the best of my knowledge. Date: 01/01/22 PhD student: 

Please learn more about responsible conduct of research on the [Faculty of Health and Medical Sciences' website](#).

ⁱ This can be supplemented with an additional letter if needed.

ⁱⁱ Please see Ministerial Order on the PhD Programme at the Universities and Certain Higher Artistic Educational Institutions (PhD Order) § 12 (4):

"Any articles included in the thesis may be written in cooperation with others, provided that each of the co-authors submits a written declaration stating the PhD student's or the author's contribution to the work."

ⁱⁱⁱ If more signatures are needed please add an extra sheet.

Aim II

To optimize, evaluate, and apply [¹¹C]UCB-J PET and [³H]UCB-J autoradiography for SV_{2A} quantification as a marker for synaptic density in a preclinical setting.

Study

VI

Objection II

To quantify presynaptic and 5-HT_{2A} R density in the pig brains after receiving a single dose of psilocybin.



Article

A Single Dose of Psilocybin Increases Synaptic Density and Decreases 5-HT_{2A} Receptor Density in the Pig Brain

Nakul Ravi Raval ^{1,2}, Annette Johansen ^{1,2}, Lene Lundgaard Donovan ^{1,2}, Nidia Fernandez Ros ¹, Brice Ozenne ^{1,3}, Hanne Demant Hansen ^{1,4} and Gitte Moos Knudsen ^{1,2,*}

- ¹ Neurobiology Research Unit, Copenhagen University Hospital Rigshospitalet, 2100 Copenhagen, Denmark; nakul.raval@nru.dk (N.R.R.); annette.johansen@nru.dk (A.J.); lenedonovan@nru.dk (L.L.D.); nidiafernandezros@gmail.com (N.F.R.); brice.ozenne@nru.dk (B.O.); hanne.d.hansen@nru.dk (H.D.H.)
- ² Faculty of Health and Medical Sciences, University of Copenhagen, 2200 Copenhagen, Denmark
- ³ Department of Public Health, Section of Biostatistics, Faculty of Health and Medical Sciences, University of Copenhagen, 1014 Copenhagen, Denmark
- ⁴ A. A. Martinos Center for Biomedical Imaging, Massachusetts General Hospital, Harvard Medical School, Charlestown, MA 02129, USA
- * Correspondence: gmk@nru.dk

Abstract: A single dose of psilocybin, a psychedelic and serotonin 2A receptor (5-HT_{2A}R) agonist, may be associated with antidepressant effects. The mechanism behind its antidepressant action is unknown but could be linked to increased synaptogenesis and down-regulation of cerebral 5-HT_{2A}R. Here, we investigate if a single psychedelic dose of psilocybin changes synaptic vesicle protein 2A (SV2A) and 5-HT_{2A}R density in the pig brain. Twenty-four awake pigs received either 0.08 mg/kg psilocybin or saline intravenously. Twelve pigs (n = 6/intervention) were euthanized one day post-injection, while the remaining twelve pigs were euthanized seven days post-injection (n = 6/intervention). We performed autoradiography on hippocampus and prefrontal cortex (PFC) sections with [³H]UCB-J (SV2A), [³H]MDL100907 (5-HT_{2A}R antagonist) and [³H]Cimbi-36 (5-HT_{2A}R agonist). One day post psilocybin injection, we observed 4.42% higher hippocampal SV2A density and lowered hippocampal and PFC 5-HT_{2A}R density (−15.21% to −50.19%). These differences were statistically significant in the hippocampus for all radioligands and in the PFC for [³H]Cimbi-36 only. Seven days post-intervention, there was still significantly higher SV2A density in the hippocampus (+9.24%) and the PFC (+6.10%), whereas there were no longer any differences in 5-HT_{2A}R density. Our findings suggest that psilocybin causes increased persistent synaptogenesis and an acute decrease in 5-HT_{2A}R density, which may play a role in psilocybin's antidepressant effects.



Citation: Raval, N.R.; Johansen, A.; Donovan, L.L.; Ros, N.F.; Ozenne, B.; Hansen, H.D.; Knudsen, G.M. A Single Dose of Psilocybin Increases Synaptic Density and Decreases 5-HT_{2A} Receptor Density in the Pig Brain. *Int. J. Mol. Sci.* **2021**, *22*, 835. <https://doi.org/10.3390/ijms22020835>

Received: 3 December 2020
Accepted: 12 January 2021
Published: 15 January 2021

Keywords: psilocybin; psychedelics; neuroplasticity; SV2A; 5-HT_{2A}; depression; autoradiography; functional-selectivity

Publisher's Note: MDPI stays neutral with regard to jurisdictional claims in published maps and institutional affiliations.



Copyright: © 2021 by the authors. Licensee MDPI, Basel, Switzerland. This article is an open access article distributed under the terms and conditions of the Creative Commons Attribution (CC BY) license (<https://creativecommons.org/licenses/by/4.0/>).

1. Introduction

Serotonergic psychedelic drugs have for centuries been extensively used in religious practices and also recreationally [1]. Their neurobiological and behavioral effects in mammals are mediated through stimulation of the serotonin 2A receptor (5-HT_{2A}R) as reviewed by Vollenweider et al. [2,3]. Upon ingestion of psilocybin, a tryptamine psychedelic [1], it quickly dephosphorylates to the active compound psilocin, which has a high affinity to 5-HT_{2A}R, but also to other 5-HT receptors such as 5-HT_{1A}R and 5-HT_{2C}R [1,4,5].

Psychedelic stimulation of 5-HT_{2A}R, a G-protein-coupled receptor (GPCR), has recently shown potential as an anxiolytic and antidepressant therapy. Some clinical studies suggest that a single dose of psilocybin rapidly and effectively relieves symptoms in depression and anxiety, with effects that persist long after the psychedelic experience [6–9]. Research in rodents suggests that psilocybin, lysergic acid diethylamide (LSD), 2,5-dimethoxy-4-iodoamphetamine (DOI), N,N-dimethyltryptamine (DMT), and alkaloids like harmine,

tetrahydroharmine, and harmaline (present in ayahuasca) induce structural neuroplasticity and alter the expression of important proteins like VGLUT1, BDNF, kalirin-7 and MAP2 [10–14]. The mechanism behind these synaptic changes is hypothesized to be exerted via the 5-HT_{2A}R pathway [10].

Changes in synaptic density in brain regions associated with emotional processing, i.e., the hippocampus and prefrontal cortex (PFC), may play a vital role in the pathophysiology of mood disorders, e.g., major depressive disorder. Both post-mortem human brain [15,16] and in vivo [17] studies in depressed individuals have shown a loss of synapses through the down-regulation of synaptic proteins and genes. Hence, upregulation of presynaptic proteins and an increase in synaptic density may be associated with the potential antidepressive effects of psychedelics.

Synaptic vesicle protein 2A (SV2A) is an integral 12-transmembrane domain glycoprotein expressed in synaptic vesicles throughout the brain [18], and SV2A density is thought to reflect presynaptic density [19]. The levetiracetam derivative UCB-J, which binds selectively to SV2A, has in its radiolabeled form been shown to correspond to synaptic density as measured with the well-characterized presynaptic protein synaptophysin [20–22].

Classical receptor binding assay studies have demonstrated that 5-HT_{2A}R (and other GPCRs) exist in two affinity states, a high- and a low- affinity state [23–25]. The affinity states of the receptors are considered to represent different functional states of the receptor, high-affinity being functionally active (activation of G_{αi1}-protein pathway) in contrast to the low-affinity state (activation of canonical G_{αq/11}-protein pathway) [26]. Whereas 5-HT_{2A}R antagonists bind to the total pool of 5-HT_{2A}R, 5-HT_{2A}R agonists bind to the high-affinity state GPCRs [27]. Stimulation of 5-HT_{2A}R leads to rapid receptor internalization [28]. This endosomal internalization may lead to lysosomal degradation and down-regulation of 5-HT_{2A}R, as extensively reviewed by Gray J.A. and Roth B.L [29].

In the present study, we hypothesize that a psychedelic dose of psilocybin increases presynaptic density, as reflected in SV2A protein levels in the pig brain. We also test the hypothesis that the availability of 5-HT_{2A}R is decreased after agonist stimulation with psilocybin.

Using in vitro autoradiography, we measure SV2A and 5-HT_{2A}R protein levels one and seven days post-injection of a single dose of psilocybin, known to induce 5-HT_{2A}R associated behavioral changes corresponding to psychedelic effects, in healthy pigs [30]. We investigate brain effects one day after psilocybin administration because the days following a psychedelic experience may provide a therapeutic window to treat mood disorders [6,7]. A follow-up seven days after a psilocybin intervention was done because this is when depressive scores have been reported to be the lowest [6]. To investigate if potential psilocybin-induced reductions in 5-HT_{2A}R are due to changes in the total receptor pool or confined to functionally active 5-HT_{2A}Rs, we used both an antagonist ([³H]MDL100907) and an agonist radioligand ([³H]Cimbi-36) for autoradiography.

2. Results

2.1. SV2A Autoradiography

Figure 1a,b show the SV2A protein density as determined by [³H]UCB-J autoradiography in the hippocampus and the PFC. Compared to the saline-treated group, psilocybin treatment was associated with 4.42% higher SV2A in the hippocampus ($p < 0.0001$) one day after psilocybin injection and 9.24% higher SV2A in the hippocampus ($p = 0.024$) seven days after psilocybin (Figure 1a and Table 1). One day after psilocybin, there was no difference in PFC SV2A (Figure 2b and Table 1, 0.25%, $p = 1$), but seven days after psilocybin administration there was 6.10% higher SV2A in the PFC ($p < 0.0001$).

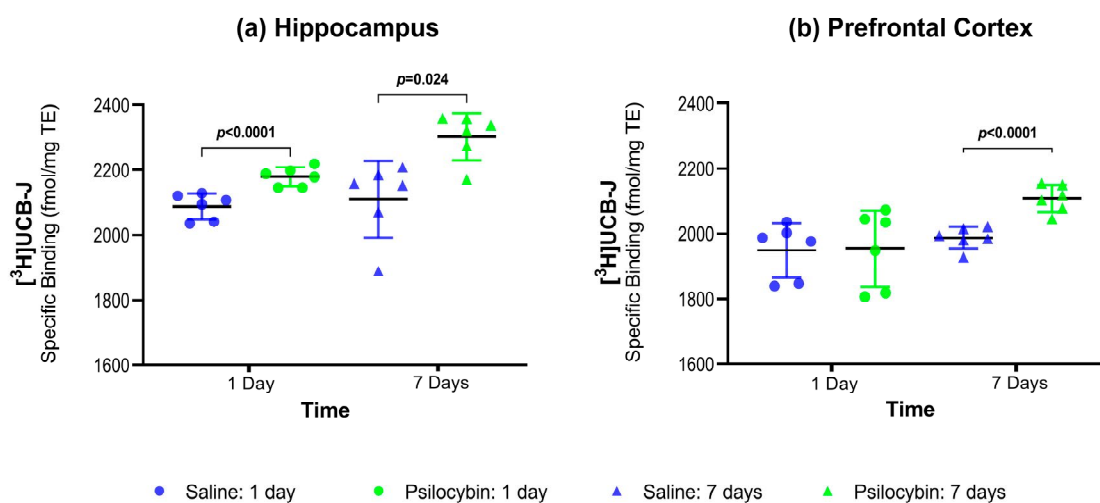


Figure 1. Group-wise comparisons of synaptic vesicle protein 2A (SV2A) density (mean \pm SD) in the hippocampus (a) and prefrontal cortex (PFC) (b) as measured with [3 H]UCB-J autoradiography.

Table 1. Group-wise summary of statistical tests performed for each radioligand. All tests show the adjusted p -values using the Holm method. NA (not applicable) indicates test was not performed.

	Hippocampus		Prefrontal Cortex	
	1 day	7 Days	1 Day	7 Days
[3 H]UCB-J (psilocybin vs. saline)	+4.42% ($p < 0.0001$)	+9.24% ($p = 0.024$)	+0.25% ($p = 1$)	+6.10% ($p < 0.0001$)
[3 H]MDL100907 (psilocybin vs. saline)	-29.60% ($p < 0.0001$)	-3.58% ($p = 1$)	-15.21% ($p = 0.162$)	+1.32% ($p = 1$)
[3 H]Cimbi-36 (psilocybin vs. saline)	-43.39% ($p = 0.013$)	+3.31% ($p = 1$)	-50.19% ($p < 0.0001$)	+2.23% ($p = 1$)
[3 H]MDL100907 vs. [3 H]Cimbi-36	NA	NA	-41.26% ($p = 0.033$)	+0.90% ($p = 0.921$)

2.2. 5-HT_{2A}R Antagonist Autoradiography

Figure 2a,b show the 5-HT_{2A}R density as measured with the antagonist radioligand [3 H]MDL100907 in hippocampus and PFC. One day after the intervention, hippocampal 5-HT_{2A}R density (Figure 2a and Table 1) was 29.60% lower ($p < 0.0001$) and PFC 5-HT_{2A}R density was similar (-15.21%, $p = 0.162$, Figure 2b and Table 1) in the psilocybin-treated group than in the saline-treated group. Seven days after the psilocybin interventions, hippocampal and PFC 5-HT_{2A}R density was not significantly different from the saline-treated animals.

2.3. 5-HT_{2A}R Agonist Autoradiography

Figure 2c,d show the 5-HT_{2A}R density as measured with the agonist radioligand [3 H]Cimbi-36 in hippocampus and PFC. One day after psilocybin intervention, hippocampal 5-HT_{2A}R/5-HT_{2C}R density (Figure 2c and Table 1) was 43.39% lower ($p = 0.013$), and PFC 5-HT_{2A}R density (Figure 2d and Table 1) was 50.19% lower ($p < 0.0001$) in the psilocybin-treated group than in the saline-treated group. With [3 H]Cimbi-36, similar to [3 H]MDL100907, 5-HT_{2A}R density was not significantly different in the hippocampus and the PFC seven days after the psilocybin intervention compared to saline.

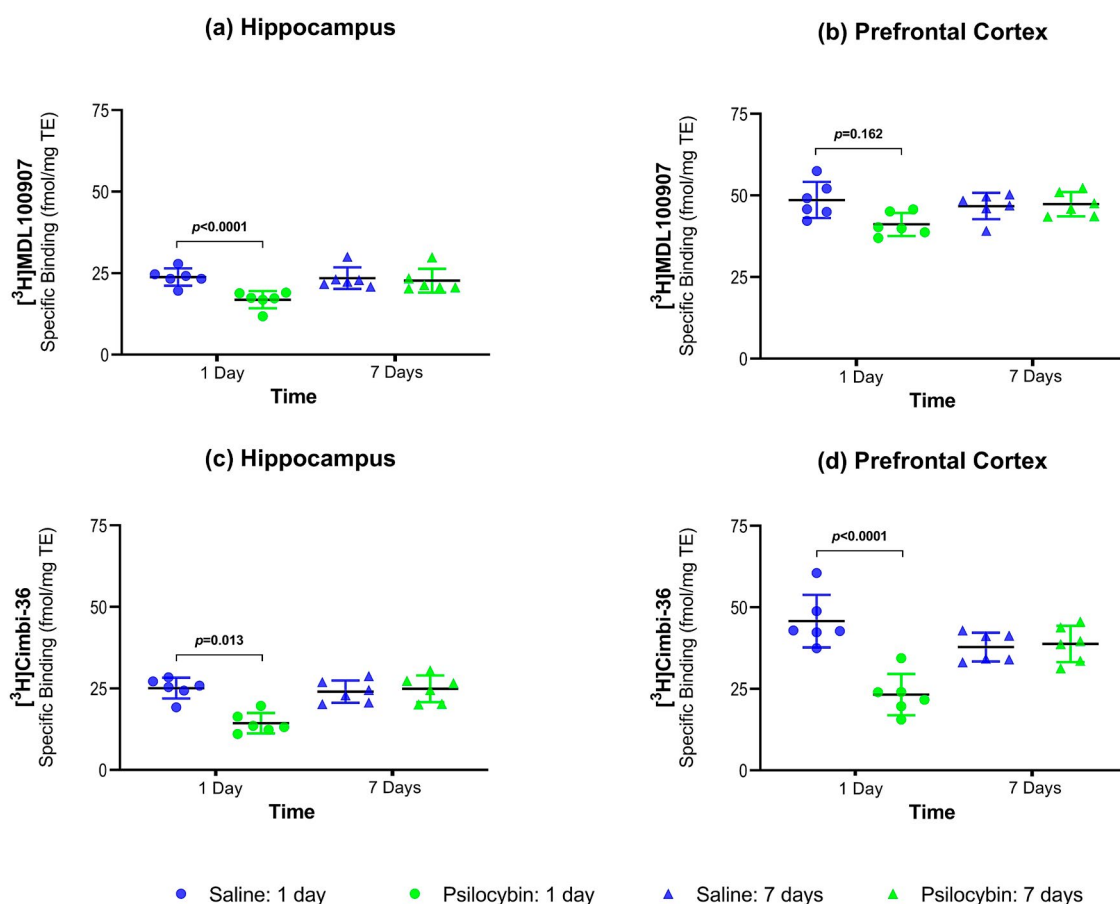


Figure 2. Group-wise comparison of 5-HT_{2A}R density (mean \pm SD) as measured with $[^3\text{H}]$ MDL100907 and $[^3\text{H}]$ Cimbi-36 in the hippocampus (a,c) and PFC (b,d) using autoradiography.

2.4. Antagonist vs. Agonist Radioligand for 5-HT_{2A}R Density

We found a more pronounced reduction of 5-HT_{2A}R density when measured with $[^3\text{H}]$ Cimbi-36 compared to $[^3\text{H}]$ MDL100907 one day after psilocybin intervention in the PFC. This difference of 41.26% was statistically significant at $p = 0.033$ (Table 1). We found no significant difference seven days after psilocybin intervention for either radioligand.

2.5. Plasma Psilocin

Plasma psilocin levels at euthanasia one and seven days after the psilocybin intervention were all below the detection limit.

3. Discussion

To the best of our knowledge, this is the first large-animal study to investigate how a single dose of psilocybin changes the key proteins SV2A and 5-HT_{2A}R in brain regions involved in emotional processing. We find that a single dose of psilocybin increases the presynaptic marker, SV2A already after one day and that it remains higher seven days after. We also show a transient reduction in the hippocampus and PFC 5-HT_{2A}R density; it is reduced one day after intervention but not seven days after.

The increase in synaptic marker SV2A may result from the stimulation of the 5-HT_{2A}R, TrkB and mTOR-signaling pathways [10]. The activation of 5-HT_{2A}R by DOI has been

shown to induce a kalirin-7-dependent increase in dendritic spine size that may play a role in regulating structural plasticity in the cortex [14]. To understand the neurobiological basis of neuroplasticity and the implication of these changes, future proteomics studies must reveal which other proteins in these pathways are changed and the temporal evolution of such changes. Our data support the notion of increased synaptogenesis following psychedelic exposure, which is hypothesized to underlie the antidepressant effects observed in humans: We find higher SV2A density in the hippocampus and the PFC, which are also regions where SV2A is reduced in patients with major depressive disorder [17]. Atypical antidepressants like ketamine are also associated with neuroplastic effects through proteins like cFos, pERK, and BDNF in the PFC and hippocampus in a social defeat stress rodent model [31]. We propose that the increase in SV2A represents an increase in presynaptic density through the same pathways. The absence of psilocybin-associated changes in mRNA for cFos, pERK, and BDNF described in Donovan et al. [30] does not, however, exclude these pathways as instrumental mediators of psilocin's effects on SV2A. This requires separate studies of protein levels or experiments where the pathways were interrupted. Together with other markers of neuroplasticity, increased levels of SV2A after intervention with a psychedelic drug adds to the scientific evidence that psychedelics enhance neuroplasticity, which may explain the mechanism of action of its antidepressant properties [32].

We have previously reported that 5-HT_{2A}R mRNA expression is unaltered in the brains of these pigs [30]. It is, however, well known that brain 5-HT_{2A}R mRNA expression does not correlate with 5-HT_{2A}R protein content [33]. Our finding of a transient decrease in 5-HT_{2A}R density, but not mRNA, one day after psilocybin is in line with results for the psychedelic substance DOI, where a significant difference in 5-HT_{2A}R protein expression was not accompanied by a change in mRNA gene expression [34].

Compared to other protein-measuring techniques such as Western blot and immunohistochemistry, autoradiography provides an added advantage of measuring receptors in the functionally active vs. total receptor pool by the use of agonist or antagonist radioligands, respectively. The use of adjacent brain sections provides the ability to directly compare receptors. We find a statistically significant reduction in 5-HT_{2A}R density in the PFC one day after psilocybin administration when measuring with [³H]Cimbi-36 compared to [³H]MDL100907. The difference between the two radioligands offers circumstantial evidence of the differential binding of antagonists versus agonists, at least when it comes to the PFC. More caution should be exerted when comparing the radioligands in the hippocampus because the hippocampus has high levels of 5-HT_{2C}R, with a density similar to 5-HT_{2A}R [35,36] and [³H]Cimbi-36 also has affinity to 5-HT_{2C}R [37,38]. That is, we cannot exclude the possibility that some of the observed reduction in [³H]Cimbi-36 in the hippocampus could be due to a down-regulation of 5-HT_{2C}R. It could be a concern that the reduction in 5-HT_{2A}R one day after psilocybin was due to partial blocking by residual psilocin. However, plasma psilocin levels at euthanasia one day after psilocybin administration were under the detection limit in all animals.

The fraction of functional 5-HT_{2A}R has to some extent been assessed in vivo in non-human primates [38] and humans [39] using [¹¹C]Cimbi-36 as an agonist and [¹¹C]MDL100907 or [¹⁸F]altanserin as antagonist radioligands, but a more precise estimate is difficult in vivo because of missing information about the free fraction of the radioligand and the radioligand affinity. A little unexpectedly, B_{max} did not differ substantially between agonist and antagonist radioligands in our study, but it should be kept in mind that uncertainties in the determination of specific activities are reflected in the calculation of B_{max}. Functional receptors can also be measured with [³⁵S]guanosine triphosphate (GTP) γ S binding stimulation mediated with DOI followed by immunoprecipitation with specific antibodies, while the complex is captured with protein A-polyvinyl toluene scintillation proximity assay. When this approach is made on post-mortem brain tissue from patients with schizophrenia, the canonical G _{α q/11}-protein pathway of 5-HT_{2A}R is found to be unaltered in the PFC, whereas the pro-hallucinogenic G _{α i1}-protein pathway is functionally overac-

tive in the PFC [40,41]. GTP γ S binding assay may be more sensitive to the measurement of functional receptors and could generate an outcome that was more straight-forward to interpret.

It is already well-known that a transient 5-HT_{2A}R down-regulation occurs upon agonist stimulation, followed by a return to baseline [42]. We have previously found that the 5-HT_{2A}R binding has normalized seven days after healthy individuals take a single psychedelic dose of psilocybin [43]. To what extent the transient down-regulation of 5-HT_{2A}R is a prerequisite for boosting the formation of new synapses is intriguing and should be examined in future studies.

Some limitations of the study should also be mentioned. We chose to investigate only two time-points and selected a few highly relevant proteins in two relevant brain regions. It would be interesting to investigate whether the synaptic density increases further beyond one week, and for how long it is maintained. Although we cannot be certain that our findings translate to humans that consume a single dose of psilocybin, the SV2A density in the hippocampus and the PFC in the saline treated pigs is in the same range as that reported in post-mortem human and non-human primates by Varnäs et al. [22]. The changes in SV2A and 5-HT_{2A}R were seen in healthy pigs; it might also be relevant to investigate changes in a psychosocial chronic-stress pig model [44]. Further, to ensure that the pigs received a well-defined dose of psilocybin, we chose to administer the drug intravenously rather than perorally. This differs from the typical approach in patients. Despite the faster pharmacokinetics after intravenous administration, the dose and administration route result in the same 5-HT_{2A}R occupancy as in humans that take it perorally [30,43].

4. Materials and Methods

4.1. Animals and Drug Dosage

The brain tissue was retrieved from pigs entering a previously published study [30] where more details are described. Briefly, female Danish slaughter pigs (Yorkshire \times Duroc \times Landrace) weighing around 20 kg (approximately nine weeks old) were used in the study. The animals were sourced from a local farm and allowed to acclimatize for at least one week before the start of the experiment. The animals were housed in individual pens with an enriched environment on a 12-h light/dark cycle, with free access to water, and weight-adjusted food twice daily. The welfare of the animals was assessed daily. After arriving in the stables, animals were trained for up to a week to allow for handling by humans.

Donovan et al. [30] identified which dose of psilocybin to give to make it comparable to a dose that elicits psychedelic effects in humans. This was based on behavioral response (headshakes, hindlimb scratches, and rubbing against the pen wall) and on Positron emission tomography (PET) studies of the 5-HT_{2A}R occupancy using the agonist radioligand [¹¹C]Cimbi-36; 67% 5-HT_{2A}R occupancy will elicit psychedelic effects in humans [43]. Intravenous injection of psilocybin was given in an ear vein catheter to the awake pigs, and the animals were under no form of external stress during the experiment. At the time of euthanasia, blood was drawn for the measurement of plasma psilocin levels, which were measured by ultra-high-performance liquid chromatography coupled to tandem mass spectrometry as previously described [43].

4.2. Ethical Statement

All animal experiments conformed to the European Commission's Directive 2010/63/EU and the ARRIVE guidelines. The Danish Council of Animal Ethics had approved all procedures (Journal no. 2016-15-0201-01149).

4.3. Study Design

Figure 3 shows the overall design of the study. Twenty-four awake pigs were given an intravenous dose of either 0.08 mg/kg psilocybin (n = 12) or saline (n = 12) through an ear vein catheter. Half of the animals in each group were euthanized one day post-injection (n = 6/intervention). The remaining 12 animals were euthanized seven days post-injection

(n = 6/intervention). That is, the animals were divided into four groups: Saline: 1 day, Psilocybin: 1 day, Saline: 7 days and Psilocybin: 7 days (Figure 3). The extracted brains were snap-frozen and stored at -80°C . From one hemisphere, 20 μm thick frozen sections were sliced on a cryostat (Leica CM1800, Leica Biosystems, Buffalo Grove, IL, USA) from the PFC and the hippocampus and mounted on Superfrost Plus™ adhesion microscope slides. Sections were stored at -20°C for the remaining period of the study.

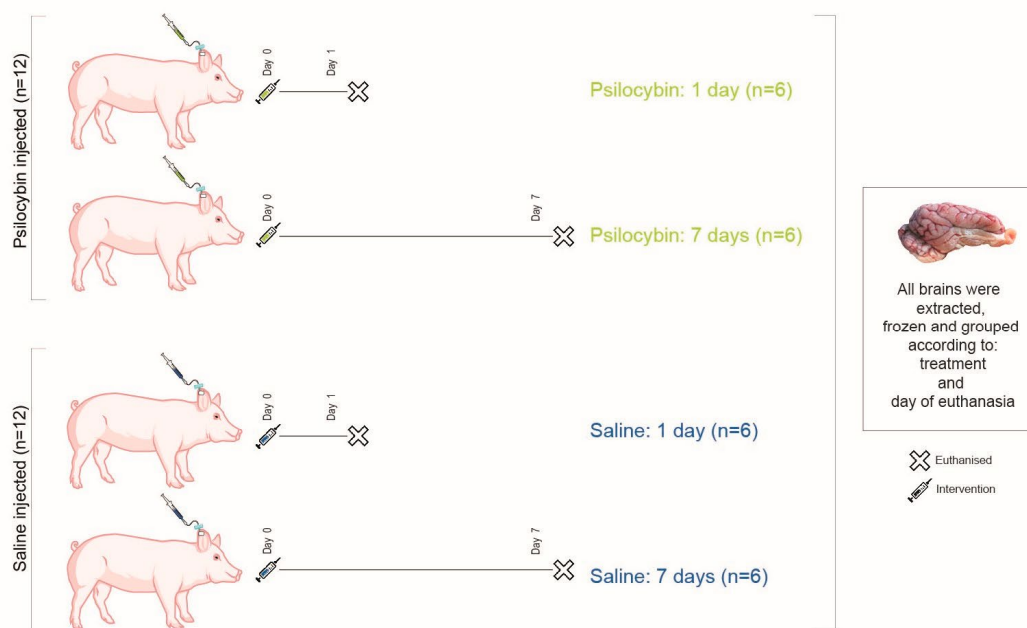


Figure 3. Study design. Twenty-four pigs received an intravenous dose of either 0.08 mg/kg psilocybin or saline. Six pigs from each type of intervention were euthanized one day or seven days post-injection. The pigs were divided into four groups, as depicted in the figure.

4.4. Autoradiography

Radioligands used for autoradiography included SV2A imaging with [^3H]UCB-J (UCB Pharma, Brussels, Belgium, specific activity 14 Ci/mmol or Pharmaron Ltd., Hoddesdon, UK, specific activity 28 Ci/mmol). [^3H]MDL100907 (ViTrax, Placentia, CA, USA, specific activity 56 Ci/mmol) was used as an antagonist radioligand for 5-HT_{2A}R and [^3H]Cimbi-36 (kindly provided by Prof. Dr C. Halldin, Department of Neuroscience, Karolinska Institute, Stockholm, Sweden, specific activity 53 Ci/mmol), as an agonist radioligand for 5-HT_{2A}R/5-HT_{2c}R. Radio-Thin-Layered-Chromatography (R-TLC) was performed for all radioligands to measure the radiochemical purity (RCP) and integrity of the parent compound. The mobile phase for [^3H]UCB-J R-TLC was Acetonitrile:Ammonium formate [25:75] (0.1 M, with 0.5% AcOH, pH 4.2). The mobile phase for [^3H]MDL100907 R-TLC was Chloroform:Methanol:Ammonia solution [90:9:1]. The mobile phase for [^3H]Cimbi-36 R-TLC was Chloroform:Methanol:Triethylamine [94:5:1]. [^3H]UCB-J and [^3H]MDL100907 had high RCP (96–98%) while [^3H]Cimbi-36 had an RCP of 52–57%. Radioactivity was corrected for RCP of [^3H]Cimbi-36 after TLC.

Sections were thawed to room temperature for 30–45 min before prewashing twice for 10 min in 50 mM Tris-HCl pre-incubation buffer set to 7.4 pH containing 0.5% bovine serum albumin (BSA) for [^3H]UCB-J or 0.01% ascorbic acid, 4 nM CaCl₂ and 0.1% BSA for [^3H]MDL100907 and [^3H]Cimbi-36.

For SV2A, the sections were incubated in assay buffer containing 60 nM [^3H]UCB-J in 50 mM Tris-HCl buffer containing 5 mM MgCl₂, 2 mM EGTA and 0.5% BSA (pH 7.4) for 1 h.

Incubation was terminated by three 5-min washes with 4 °C pre-incubation buffer followed by a rapid rinse in 4 °C deionized H₂O (dH₂O). For 5-HT_{2A}R, sections were incubated in assay buffer containing 3 nM [³H]MDL100907 or 1 nM [³H]Cimbi-36 in 50 mM Tris-HCl containing 0.01% ascorbic acid, 4 nM CaCl₂ and 0.1% BSA (pH 7.4) for 1 h. Incubation was terminated by two 10-min washes in ice-cold pre-incubation buffer followed by a rapid rinse in ice-cold dH₂O.

The assay buffer concentration of the respective radioligands was determined using $4-5 \times K_D$ values (Appendix A: Figure A1) to determine B_{max} values in the section. After washing, the slides were rapidly air-dried and fixated in a paraformaldehyde vapor chamber overnight in cold storage (4 °C). The next day, the samples were moved to an excicator for 45–60 min to remove any excess moisture and then placed in a cassette for autoradiography with tritium sensitive image plates (BAS-IP TR2040, Science Imaging Scandinavia AB, Nacka, Sweden) along with radioactive tritium standards (RPA510, Amersham Bioscience, GE Healthcare, Chicago, IL, USA) (Figure 4). The image plates were exposed for seven days. After the exposure, the image plates were read using a Fujifilm BAS 1000 scanner (Fujifilm Europe, GmbH, Duesseldorf, Germany). Calibration, quantification and data evaluation were done using ImageJ software (NIH Image, Bethesda, MD, USA) [45]. The regions of interest were hand-drawn or drawn using the wand tool and visually inspected after automated delineation, as shown in Figure 4. The four-parameter general curve fit (David Rodbard, NIH) of decay corrected tritium standards was used to convert mean pixel density (grayscale) to nCi/mg tissue equivalent (TE). Total binding was determined in the hippocampal and cortical grey matter while non-specific binding was determined in the white matter on the same slides. Finally, the decay-corrected specific activity of the representative radioligand was used to convert nCi/mg TE to fmol/mg TE. Specific binding was calculated as the difference between total binding and non-specific binding. All experiments were performed in triplicates, and experimenters were blinded.

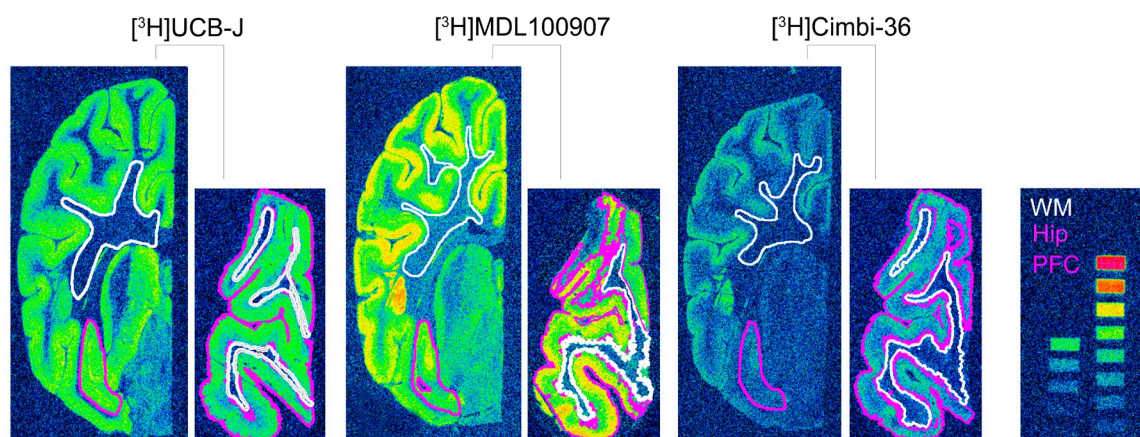


Figure 4. Representative autoradiograms of the radioligands used in this study. Half hemisphere sections of the hippocampus (larger coronal sections) and PFC (smaller coronal sections) from the same animal belonging to the Saline: 1 day group. The color-coded lines show representations of the region of interest that were either hand-drawn or drawn using the wand tool in ImageJ and visually inspected. The figure also shows the radioactive standards used in the study; approximately 16 nCi/mg to 0.2 nCi/mg decay corrected to the time of experiment and day of exposure.

4.5. Statistical Analyses

The data were analyzed using R (v. 4.0.3; R core team, Vienna, Austria), while GraphPad Prism (v. 9.0.0; GraphPad Software, San Diego, CA, USA) was used for data visualization. Comparisons between group means (\bar{X}) for the respective radioligands (Equations (1) and (2)) were done using a permutation test (with 1000 permutations) on log-transformed values and adjusted for multiple comparisons (overtime, radioligand,

and brain regions: 12 tests) using the Holm method. Comparison between the 5-HT_{2A}R radioligands, [³H]Cimbi-36 and [³H]MDL100907, was performed for the PFC using a permutation test (with 1000 permutations) on log-transformed values of treatment effect at one day and seven days (Equations (3) and (4)).

$$X (\text{Psilocybin : 1 day}) - (\bar{X}) (\text{Saline : 1 day}) \quad (1)$$

$$X (\text{Psilocybin : 7 day}) - (\bar{X}) (\text{Saline : 7 day}) \quad (2)$$

$$\frac{[{}^3\text{H}]\text{Cimbi} - 36((\bar{X}) (\text{Psilocybin : 1 day}) - (\bar{X}) (\text{Saline : 1 day})) - [{}^3\text{H}]\text{MDL100907}((\bar{X}) (\text{Psilocybin : 1 day}) - (\bar{X}) (\text{Saline : 1 day}))}{[{}^3\text{H}]\text{Cimbi} - 36((\bar{X}) (\text{Psilocybin : 7 days}) - (\bar{X}) (\text{Saline : 7 days})) - [{}^3\text{H}]\text{MDL100907}((\bar{X}) (\text{Psilocybin : 7 days}) - (\bar{X}) (\text{Saline : 7 days}))} \quad (3)$$

$$\frac{[{}^3\text{H}]\text{Cimbi} - 36((\bar{X}) (\text{Psilocybin : 7 days}) - (\bar{X}) (\text{Saline : 7 days})) - [{}^3\text{H}]\text{MDL100907}((\bar{X}) (\text{Psilocybin : 7 days}) - (\bar{X}) (\text{Saline : 7 days}))}{[{}^3\text{H}]\text{MDL100907}((\bar{X}) (\text{Psilocybin : 7 days}) - (\bar{X}) (\text{Saline : 7 days}))} \quad (4)$$

Author Contributions: Conceptualization, G.M.K., H.D.H., N.R.R., L.L.D. and A.J.; methodology, N.R.R., A.J., B.O. and N.F.R.; software, N.R.R., and B.O.; validation, N.R.R., A.J., and N.F.R.; formal analysis, N.R.R., A.J. and B.O.; investigation, N.R.R., N.F.R., A.J.; resources, L.L.D.; data curation, N.R.R., A.J., and B.O.; writing—original draft preparation, N.R.R.; writing—review and editing, N.R.R., A.J., L.L.D., B.O., H.D.H. and G.M.K.; visualization, N.R.R.; supervision, H.D.H. and G.M.K.; funding acquisition, G.M.K. All authors have read and agreed to the published version of the manuscript.

Funding: This project has received funding from the European Union’s Horizon 2020 research and innovation program under the Marie Skłodowska-Curie grant agreement No 813528. The Lundbeck Foundation supported running costs and a stipend for Lene L. Donovan. The Independent Research Fund Denmark funded Annette Johansen.

Institutional Review Board Statement: All animal experiments conformed to the European Commission’s Directive 2010/63/EU and the ARRIVE guidelines. The Danish Council of Animal Ethics had ap-proved all procedures (Journal no. 2016-15-0201-01149).

Informed Consent Statement: Not applicable.

Data Availability Statement: The data presented in this study are available on request from the corresponding author. The data are not publicly available due to other on-going studies.

Acknowledgments: The psilocybin was kindly supplied by the National Institute of Mental Health, Klecany, Czech Republic and the Forensic Laboratory of Biologically Active Compounds, Department of Chemistry of Natural Compounds, University of Chemistry and Technology Prague, Prague, Czech Republic. We would also like to acknowledge the help of Jesper Langgaard Kristensen for procuring psilocybin. The authors would like further to thank Malthe Scharff for his assistance in the experiments. The authors would also like to thank and show sincere gratitude to the veterinarians and staff at the Department of Experimental Medicine, University of Copenhagen for their continued assistance with animal experiments.

Conflicts of Interest: G.M.K.: H. Lundbeck A/S (research collaboration), Novo Nordisk/Novozymes/Chr. Hansen (stockholder), Sage Therapeutics and Sanos (Advisor). G.M.K. is currently the president of the European College of Neuropsychopharmacology. All other authors declare no conflict of interest.

Abbreviations

5-HT	5-Hydroxytryptamine (serotonin)
5-HT _{1A} R	5-Hydroxytryptamine (serotonin) 1A Receptor
5-HT _{2A} R	5-Hydroxytryptamine (serotonin) 2A Receptor
5-HT _{2C} R	5-Hydroxytryptamine (serotonin) 2C Receptor
ARRIVE	Animal Research: Reporting of In Vivo Experiments
BDNF	Brain-Derived Neurotropic Factor
B _{max}	Total density (concentration) of the receptor
BP _{ND}	Binding Potential (Non-displaceable)

BSA	Bovine Serum Albumin
DMT	N,N-dimethyltryptamine
DOI	2,5-dimethoxy-4-iodoamphetamine
GPCR	G-protein coupled receptor
K_D	Equilibrium dissociation Constant
LSD	Lysergic acid diethylamide
MAP2	Microtubule-associated protein 2
mTOR	Mammalian Target of Rapamycin
NSB	Non-specific Binding
PET	Positron Emission Tomography
pERK	Endoplasmic Reticulum Protein Kinase
PFC	Prefrontal Cortex
RCP	Radiochemical purity
R-TLC	Radio-Thin Layer Chromatography
SV2A	Synaptic Vesicular Protein 2A
TB	Total Binding
TE	Tissue Equivalent
TrkB	Tropomyosin Receptor Kinase B
VGLUT1	Vesicular Glutamate Transporter 1
\bar{X}	Mean

Appendix A

Appendix A.1. Saturation Assays

Appendix A.1.1. Methods

Two female Danish slaughter pigs' brains that were not included in this study were used to perform a saturation assay. The extracted brains were snap-frozen and stored at $-80\text{ }^{\circ}\text{C}$. From one hemisphere, $20\text{ }\mu\text{m}$ thick frozen sections were sliced on a cryostat (Leica CM1800, Leica Biosystems, Buffalo Grove, IL, USA) from the prefrontal cortex (PFC) and mounted on Superfrost Plus™ adhesion microscope slides. The sections were stored at $-80\text{ }^{\circ}\text{C}$ for the remaining period of the study.

All radioligands used for this autoradiography study were included for a saturation assay. The radioligands used are as follows: [^3H]UCB-J for SV2A (UCB pharma, Brussels, Belgium, specific activity $14\text{ Ci}/\text{mmol}$), [^3H]MDL100907 as an antagonist radioligand for $5\text{-HT}_{2A}\text{R}$ (ViTrax, Placentia, CA, USA, specific activity $56\text{ Ci}/\text{mmol}$) and [^3H]Cimbi-36 as an agonist radioligand for $5\text{-HT}_{2A}\text{R}/5\text{-HT}_{2c}\text{R}$ (kindly provided by Prof. Dr C. Halldin, Department of Neuroscience, Karolinska Institute, Stockholm, Sweden, specific activity $53\text{ Ci}/\text{mmol}$) for $5\text{-HT}_{2A}/5\text{-HT}_{2c}$. The saturation assay for [^3H]Cimbi-36 was performed in 2012, when the tracer was produced, hence high radiochemical purity was assumed.

Experimental conditions previously described were also used for the saturation assay. Briefly, after the sections were thawed to room temperature, they were prewashed twice for 10 min in 50 mM Tris-HCl pre-incubation buffer set to 7.4 pH containing 0.5% bovine serum albumin (BSA) for [^3H]UCB-J or 0.01% ascorbic acid, 4 nM CaCl_2 and 0.1% BSA for [^3H]MDL100907 and [^3H]Cimbi-36.

For SV2A, the sections ($n = 4$) were incubated in assay buffer (50 mM Tris-HCl buffer containing 5 mM MgCl_2 , 2 mM EGTA and 0.5% BSA (pH 7.4)) containing varying concentrations (0 to 100 nM) of [^3H]UCB-J for total binding (TB) and the same varying concentration of [^3H]UCB-J with 10 mM of levetiracetam (Keppra, UCB pharma, Brussels, Belgium) for non-specific binding (NSB). The sections were incubated for 60 min. Incubation was terminated by three 5-min washes with $4\text{ }^{\circ}\text{C}$ pre-incubation buffer followed by a rapid rinse in $4\text{ }^{\circ}\text{C}$ deionized H_2O (dH_2O).

For $5\text{-HT}_{2A}\text{R}$, sections ($n = 4$ for [^3H]MDL100907 and $n = 1$ for [^3H]Cimbi-36) were incubated in assay buffer (50 mM Tris-HCl containing 0.01% ascorbic acid, 4 nM CaCl_2 and 0.1% BSA (pH 7.4)) containing varying concentrations of [^3H]MDL100907 or [^3H]Cimbi-36 (0 to 4 nM) for TB and the same varying concentration of [^3H]MDL100907 or [^3H]Cimbi-36 with 10 mM ketanserin (Sigma-Aldrich, Søborg, Denmark) for NSB. The sections were

incubated for 60 min. Incubation was terminated by two 10-min washes in ice-cold pre-incubation buffer followed by a rapid rinse in ice-cold dH₂O.

After washing, the slides were rapidly air-dried and fixated in a paraformaldehyde vapor chamber overnight in cold storage (4 °C). The next day, the samples were moved to an excicator for 45–60 min to remove any excess moisture and then placed in a cassette for autoradiography with tritium sensitive image plates (BAS-IP TR2040, Science Imaging Scandinavia AB, Nacka, Sweden) along with radioactive tritium standards (ART0123B, American Radiolabelled Chemical, Inc., St. Louis, MO, USA and RPA510, Amersham Bioscience, GE Healthcare, Chicago, IL, USA) (Figure 4). The image plates were exposed for seven days. After the exposure, the image plates were read using a Fujifilm BAS 1000 scanner (Fujifilm Europe, GmbH, Duesseldorf, Germany). Calibration, quantification and data evaluation was done using ImageJ software (NIH Image, Bethesda, MD, USA) [45]. The regions of interest were hand-drawn or drawn using the wand tool and visually inspected after automated delineation, as shown in Figure 4 of the main manuscript. The four-parameter general curve fit (David Rodbard, NIH) of decay corrected tritium standards was used to convert mean pixel density (grayscale) to nCi/mg TE. TB was determined in cortical grey matter from TB slides while NSB was determined in the cortical grey matter of NSB slides, and white matter was defined on the same TB slides. Finally, the decay-corrected specific activity of the representative radioligand was used to convert nCi/mg TE to fmol/mg TE. Specific binding was calculated as the difference between TB and NSB.

The data were analyzed using GraphPad Prism (v. 9.0.0; GraphPad Software, San Diego, CA, USA). Non-linear regression analysis (One site- Fit total and non-specific binding) was used for all radioligands. The curve fitting used for saturation assays was “One site-fit total and non-specific binding”. The fitting method used was the least squared regression with no weighting.

Appendix A.1.2. Results

The saturation assay with [³H]UCB-J generated a K_D of 11.47 ± 7.8 nM and B_{max} of 1090 ± 253 fmol/mg TE. [³H]MDL100907 generated a K_D of 0.49 ± 0.1 nM and B_{max} of 44.58 ± 3.9 fmol/mg TE while [³H]Cimbi-36 shows a K_D of 0.31 ± 0.1 nM and B_{max} of 56.07 ± 3.3 fmol/mg TE. [³H]UCB-J white matter binding was lower (slope = 7.0, R² = 0.99) compared to NSB in the grey matter of levetiracetam blocked slides (slope = 10.0, R² = 0.99) but with less variation. On the other hand, white matter binding with [³H]MDL100907 (slope = 8.2, R² = 0.95) and [³H]Cimbi-36 (slope = 15.1, R² = 0.97) correlate (visually) with NSB in the grey matter of ketanserin blocked slides (slope = 8.8, R² = 0.99 and 16.4, R² = 0.99, respectively).

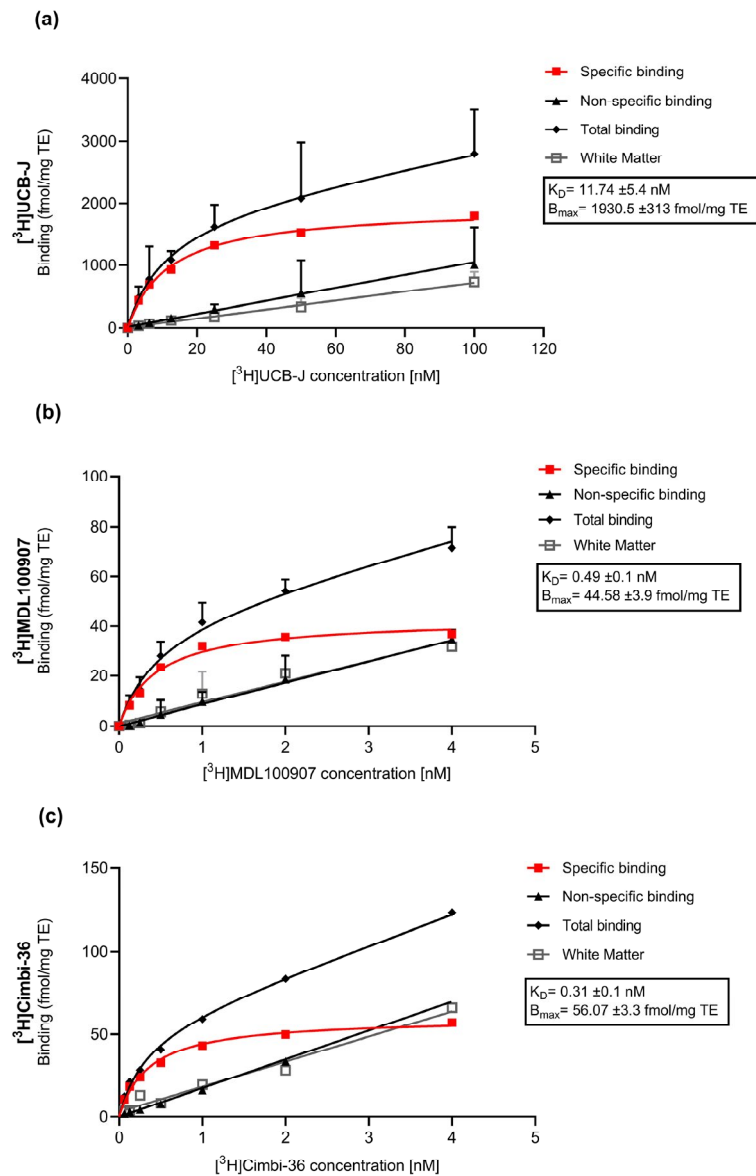


Figure A1. Saturation assay of [³H]UCB-J (a), [³H]MDL100907 (b) and [³H]Cimbi-36 (c) in the grey matter of the pig brain.

References

- Nichols, D.E. Hallucinogens. *Pharmacol. Ther.* **2004**, *101*, 131–181. [[CrossRef](#)] [[PubMed](#)]
- Vollenweider, F.X.; Kometer, M. The neurobiology of psychedelic drugs: Implications for the treatment of mood disorders. *Nat. Rev. Neurosci.* **2010**, *11*, 642–651. [[CrossRef](#)] [[PubMed](#)]
- Vollenweider, F.X.; Preller, K.H. Psychedelic drugs: Neurobiology and potential for treatment of psychiatric disorders. *Nat. Rev. Neurosci.* **2020**. [[CrossRef](#)] [[PubMed](#)]
- Rickli, A.; Moning, O.D.; Hoener, M.C.; Liechti, M.E. Receptor interaction profiles of novel psychoactive tryptamines compared with classic hallucinogens. *Eur. Neuropsychopharmacol.* **2016**, *26*, 1327–1337. [[CrossRef](#)] [[PubMed](#)]
- Blair, J.B.; Kurrasch-Orbaugh, D.; Marona-Lewicka, D.; Gumbay, M.G.; Watts, V.J.; Barker, E.L.; Nichols, D.E. Effect of ring fluorination on the pharmacology of hallucinogenic tryptamines. *J. Med. Chem.* **2000**, *43*, 4701–4710. [[CrossRef](#)]
- Carhart-Harris, R.L.; Bolstridge, M.; Rucker, J.; Day, C.M.J.J.; Erritzoe, D.; Kaelen, M.; Bloomfield, M.; Rickard, J.A.; Forbes, B.; Feilding, A.; et al. Psilocybin with psychological support for treatment-resistant depression: An open-label feasibility study. *Lancet Psychiatry* **2016**, *3*, 619–627. [[CrossRef](#)]

7. Griffiths, R.R.; Johnson, M.W.; Carducci, M.A.; Umbricht, A.; Richards, W.A.; Richards, B.D.; Cosimano, M.P.; Klinedinst, M.A. Psilocybin produces substantial and sustained decreases in depression and anxiety in patients with life-threatening cancer: A randomized double-blind trial. *J. Psychopharmacol.* **2016**, *30*, 1181–1197. [[CrossRef](#)]
8. Ross, S.; Bossis, A.; Guss, J.; Agin-Lieb, G.; Malone, T.; Cohen, B.; Mennenga, S.E.; Belser, A.; Kalliontzis, K.; Babb, J.; et al. Rapid and sustained symptom reduction following psilocybin treatment for anxiety and depression in patients with life-threatening cancer: A randomized controlled trial. *J. Psychopharmacol.* **2016**, *30*, 1165–1180. [[CrossRef](#)]
9. Davis, A.K.; Barrett, F.S.; May, D.G.; Cosimano, M.P.; Sepeda, N.D.; Johnson, M.W.; Finan, P.H.; Griffiths, R.R. Effects of Psilocybin-Assisted Therapy on Major Depressive Disorder: A Randomized Clinical Trial. *JAMA Psychiatry* **2020**. [[CrossRef](#)]
10. Ly, C.; Greb, A.C.; Cameron, L.P.; Wong, J.M.; Eden, V.; Wilson, P.C.; Burbach, K.F.; Zarandi, S.S.; Paddy, M.R.; Duim, W.C.; et al. Psychedelics Promote Structural and Functional Neural Plasticity. *Cell Rep.* **2018**, *23*, 3170–3182. [[CrossRef](#)]
11. Morales-García, J.A.; De La Fuente Revenga, M.; Alonso-Gil, S.; Rodríguez-Franco, M.L.; Feilding, A.; Pérez-Castillo, A.; Riba, J. The alkaloids of *Banisteriopsis caapi*, the plant source of the Amazonian hallucinogen Ayahuasca, stimulate adult neurogenesis in vitro. *Sci. Rep.* **2017**, *7*, 1–13. [[CrossRef](#)] [[PubMed](#)]
12. Fortunato, J.J.; Réus, G.Z.; Kirsch, T.R.; Stringari, R.B.; Fries, G.R.; Kapczinski, F.; Hallak, J.E.; Zuardi, A.W.; Crippa, J.A.; Quevedo, J. Chronic administration of harmine elicits antidepressant-like effects and increases BDNF levels in rat hippocampus. *J. Neural Transm.* **2010**, *117*, 1131–1137. [[CrossRef](#)] [[PubMed](#)]
13. Morales-García, J.A.; Calleja-Conde, J.; López-Moreno, J.A.; Alonso-Gil, S.; Sanz-SanCristobal, M.; Riba, J.; Pérez-Castillo, A. N,N-dimethyltryptamine compound found in the hallucinogenic tea ayahuasca, regulates adult neurogenesis in vitro and in vivo. *Transl. Psychiatry* **2020**, *10*, 331. [[CrossRef](#)] [[PubMed](#)]
14. Jones, K.A.; Srivastava, D.P.; Allen, J.A.; Strachan, R.T.; Roth, B.L.; Penzes, P. Rapid modulation of spine morphology by the 5-HT_{2A} serotonin receptor through kalirin-7 signaling. *Proc. Natl. Acad. Sci. USA* **2009**, *106*, 19575–19580. [[CrossRef](#)]
15. Duric, V.; Banasr, M.; Stockmeier, C.A.; Simen, A.A.; Newton, S.S.; Overholser, J.C.; Jurjus, G.J.; Dieter, L.; Duman, R.S. Altered expression of synapse and glutamate related genes in post-mortem hippocampus of depressed subjects. *Int. J. Neuropsychopharmacol.* **2013**, *16*, 69–82. [[CrossRef](#)]
16. Kang, H.J.; Voleti, B.; Hajsan, T.; Rajkowska, G.; Stockmeier, C.A.; Licznarski, P.; Lepack, A.; Majik, M.S.; Jeong, L.S.; Banasr, M.; et al. Decreased expression of synapse-related genes and loss of synapses in major depressive disorder. *Nat. Med.* **2012**, *18*, 1413–1417. [[CrossRef](#)]
17. Holmes, S.E.; Scheinost, D.; Finnema, S.J.; Naganawa, M.; Davis, M.T.; DellaGioia, N.; Nabulsi, N.; Matuskey, D.; Angarita, G.A.; Pietrzak, R.H.; et al. Lower synaptic density is associated with depression severity and network alterations. *Nat. Commun.* **2019**, *10*. [[CrossRef](#)]
18. Bartholome, O.; Van den Ackerveken, P.; Sánchez Gil, J.; de la Brassinne Bonardeaux, O.; Leprince, P.; Franzen, R.; Rogister, B.; Surguchov, A.; Conti, F.; Haucke, V.; et al. Puzzling Out Synaptic Vesicle 2 Family Members Functions. *Front. Mol. Neurosci* **2017**, *10*, 148. [[CrossRef](#)]
19. Heurling, K.; Ashton, N.J.; Leuzy, A.; Zimmer, E.R.; Blennow, K.; Zetterberg, H.; Eriksson, J.; Lubberink, M.; Schöll, M. Synaptic vesicle protein 2A as a potential biomarker in synaptopathies. *Mol. Cell. Neurosci.* **2019**, *97*, 34–42. [[CrossRef](#)]
20. Nowack, A.; Yao, J.; Custer, K.L.; Bajjalieh, S.M. SV2 regulates neurotransmitter release via multiple mechanisms. *Am. J. Physiol. Cell Physiol.* **2010**, *299*, 960–967. [[CrossRef](#)]
21. Finnema, S.J.; Nabulsi, N.B.; Eid, T.; Detyniecki, K.; Lin, S.F.; Chen, M.K.; Dhaher, R.; Matuskey, D.; Baum, E.; Holden, D.; et al. Imaging synaptic density in the living human brain. *Sci. Transl. Med.* **2016**, *8*. [[CrossRef](#)] [[PubMed](#)]
22. Varnäs, K.; Stepanov, V.; Halldin, C. Autoradiographic mapping of synaptic vesicle glycoprotein 2A in non-human primate and human brain. *Synapse* **2020**. [[CrossRef](#)] [[PubMed](#)]
23. López-Giménez, J.F.; Villazón, M.; Brea, J.; Loza, M.I.; Palacios, J.M.; Mengod, G.; Vilaró, M.T. Multiple conformations of native and recombinant human 5-hydroxytryptamine_{2A} receptors are labeled by agonists and discriminated by antagonists. *Mol. Pharmacol.* **2001**, *60*, 690–699. [[PubMed](#)]
24. Song, J.; Hanniford, D.; Doucette, C.; Graham, E.; Poole, M.F.; Ting, A.; Sherf, B.; Harrington, J.; Brunden, K.; Stricker-Krongrad, A. Development of homogenous high-affinity agonist binding assays for 5-HT₂ receptor subtypes. *Assay Drug Dev. Technol.* **2005**, *3*, 649–659. [[CrossRef](#)] [[PubMed](#)]
25. Shalgunov, V.; van Waarde, A.; Booij, J.; Michel, M.C.; Dierckx, R.A.J.O.; Elsinga, P.H. Hunting for the high-affinity state of G-protein-coupled receptors with agonist tracers: Theoretical and practical considerations for positron emission tomography imaging. *Med. Res. Rev.* **2019**, *39*, 1014–1052. [[CrossRef](#)]
26. Kent, R.S.; De Lean, A.; Lefkowitz, R.J. A quantitative analysis of beta-adrenergic receptor interactions: Resolution of high and low affinity states of the receptor by computer modeling of ligand binding data. *Mol. Pharmacol.* **1980**, *17*, 14–23.
27. López-Giménez, J.F.; Vilaró, M.T.; Palacios, J.M.; Mengod, G. Multiple conformations of 5-HT_{2A} and 5-HT_{2C} receptors in rat brain: An autoradiographic study with [¹²⁵I](±)DOI. *Exp. Brain Res.* **2013**, *230*, 395–406. [[CrossRef](#)]
28. Berry, S.A.; Shah, M.C.; Khan, N.; Roth, B.L. Rapid agonist-induced internalization of the 5-hydroxytryptamine(2A) receptor occurs via the endosome pathway in vitro. *Mol. Pharmacol.* **1996**, *50*, 306–313.
29. Gray, J.A.; Roth, B.L. Paradoxical trafficking and regulation of 5-HT_{2A} receptors by agonists and antagonists. *Brain Res. Bull.* **2001**, *56*, 441–451. [[CrossRef](#)]

30. Donovan, L.L.; Johansen, J.V.; Ros, N.F.; Jaber, E.; Johansen, S.S.; Ozenne, B.; Issazadeh-Navikas, S.; Hansen, H.D.; Knudsen, G.M. Effects of a single dose of psilocybin on behaviour, brain 5-HT_{2A} receptor occupancy and gene expression in the pig. *Eur. Neuropsychopharmacol.* **2021**, *42*, 1–11. [[CrossRef](#)]
31. Zhang, M.; Radford, K.D.; Driscoll, M.; Purnomo, S.; Kim, J.; Choi, K.H. Effects of subanesthetic intravenous ketamine infusion on neuroplasticity-related proteins in the prefrontal cortex, amygdala, and hippocampus of Sprague-Dawley rats. *IBRO Rep.* **2019**, *6*, 87–94. [[CrossRef](#)] [[PubMed](#)]
32. Hutten, N.R.P.W.; Mason, N.L.; Dolder, P.C.; Theunissen, E.L.; Holze, F.; Liechti, M.E.; Varghese, N.; Eckert, A.; Feilding, A.; Ramaekers, J.G.; et al. Low Doses of LSD Acutely Increase BDNF Blood Plasma Levels in Healthy Volunteers. *ACS Pharmacol. Trans. Sci.* **2020**, acsptsci.0c00099. [[CrossRef](#)]
33. Beliveau, V.; Ganz, M.; Feng, L.; Ozenne, B.; Højgaard, L.; Fisher, P.M.; Svarer, C.; Greve, D.N.; Knudsen, G.M. A high-resolution in vivo atlas of the human brain's serotonin system. *J. Neurosci.* **2017**, *37*, 120–128. [[CrossRef](#)] [[PubMed](#)]
34. Anji, A.; Kumari, M.; Sullivan Hanley, N.R.; Bryan, G.L.; Hensler, J.G. Regulation of 5-HT_{2A} receptor mRNA levels and binding sites in rat frontal cortex by the agonist DOI and the antagonist mianserin. *Neuropharmacology* **2000**, *39*, 1996–2005. [[CrossRef](#)]
35. Pompeiano, M.; Palacios, J.M.; Mengod, G. Distribution of the serotonin 5-HT₂ receptor family mRNAs: Comparison between 5-HT_{2A} and 5-HT_{2C} receptors. *Mol. Brain Res.* **1994**, *23*, 163–178. [[CrossRef](#)]
36. Marazziti, D.; Rossi, A.; Giannaccini, G.; Zavaglia, K.M.; Dell'Osso, L.; Lucacchini, A.; Cassano, G.B. Distribution and characterization of [³H]mesulergine binding in human brain postmortem. *Eur. Neuropsychopharmacol.* **1999**, *10*, 21–26. [[CrossRef](#)]
37. Ettrup, A.; Holm, S.; Hansen, M.; Wasim, M.; Santini, M.A.; Palner, M.; Madsen, J.; Svarer, C.; Kristensen, J.L.; Knudsen, G.M. Preclinical safety assessment of the 5-HT_{2A} receptor agonist PET radioligand [¹¹C]cimbi-36. *Mol. Imaging Biol.* **2013**, *15*, 376–383. [[CrossRef](#)]
38. Finnema, S.J.; Stepanov, V.; Ettrup, A.; Nakao, R.; Amini, N.; Svedberg, M.; Lehmann, C.; Hansen, M.; Knudsen, G.M.; Halldin, C. Characterization of [¹¹C]Cimbi-36 as an agonist PET radioligand for the 5-HT_{2A} and 5-HT_{2C} receptors in the nonhuman primate brain. *Neuroimage* **2014**, *84*, 342–353. [[CrossRef](#)]
39. Ettrup, A.; Svarer, C.; McMahon, B.; da Cunha-Bang, S.; Lehel, S.; Møller, K.; Dyssegaard, A.; Ganz, M.; Beliveau, V.; Jørgensen, L.M.; et al. Serotonin 2A receptor agonist binding in the human brain with [¹¹C]Cimbi-36: Test–retest reproducibility and head-to-head comparison with the antagonist [¹⁸F]altanserin. *Neuroimage* **2016**, *130*, 167–174. [[CrossRef](#)]
40. García-Bea, A.; Miranda-Azpiazu, P.; Muguruza, C.; Marmolejo-Martinez-Artesero, S.; Diez-Alarcia, R.; Gabilondo, A.M.; Callado, L.F.; Morentin, B.; González-Maeso, J.; Meana, J.J. Serotonin 5-HT_{2A} receptor expression and functionality in postmortem frontal cortex of subjects with schizophrenia: Selective biased agonism via G α i1-proteins. *Eur. Neuropsychopharmacol.* **2019**, *29*, 1453–1463. [[CrossRef](#)]
41. Miranda-Azpiazu, P.; Díez-Alarcia, R.; García-Bea, A.; González-Maeso, J.; Morentin, B.; Meana, J.J. P.1.g.022 Hallucinogenic and non-hallucinogenic 5-HT_{2A} receptor agonists induce distinct patterns of G protein coupling in postmortem human brain. *Eur. Neuropsychopharmacol.* **2013**, *23*, S201. [[CrossRef](#)]
42. Buckholtz, N.S.; Zhou, D.; Freedman, D.X. Serotonin₂ agonist administration down-regulates rat brain serotonin₂ receptors. *Life Sci.* **1988**, *42*, 2439–2445. [[CrossRef](#)]
43. Madsen, M.K.; Fisher, P.M.; Burmester, D.; Dyssegaard, A.; Stenbæk, D.S.; Kristiansen, S.; Johansen, S.S.; Lehel, S.; Linnet, K.; Svarer, C.; et al. Psychedelic effects of psilocybin correlate with serotonin 2A receptor occupancy and plasma psilocin levels. *Neuropsychopharmacology* **2019**, *44*, 1328–1334. [[CrossRef](#)] [[PubMed](#)]
44. Menneson, S.; Ménicot, S.; Ferret-Bernard, S.; Guérin, S.; Romé, V.; Le Normand, L.; Randuineau, G.; Gambarota, G.; Noirot, V.; Etienne, P.; et al. Validation of a psychosocial chronic stress model in the pig using a multidisciplinary approach at the gut-brain and behavior levels. *Front. Behav. Neurosci.* **2019**, *13*, 161. [[CrossRef](#)] [[PubMed](#)]
45. Schneider, C.A.; Rasband, W.S.; Eliceiri, K.W. NIH Image to ImageJ: 25 Years of Image Analysis HHS Public Access. *Nat. Methods* **2012**, *9*, 671–675. [[CrossRef](#)] [[PubMed](#)]



DECLARATION OF CO-AUTHORSHIP

The declaration is for PhD students and must be completed for each conjointly authored article. Please note that if a manuscript or published paper has ten or less co-authors, all co-authors must sign the declaration of co-authorship. If it has more than ten co-authors, declarations of co-authorship from the corresponding author(s), the senior author and the principal supervisor (if relevant) are a minimum requirement.

1. Declaration by	
Name of PhD student	Nakul Ravi Raval
E-mail	nakul.raval@nru.dk
Name of principal supervisor	Prof. Dr. Gitte Moos Knudsen
Title of the PhD thesis	Translational Positron Emission Tomography: Animal Models and In vitro Autoradiography for Radioligand Development

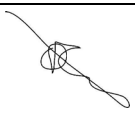
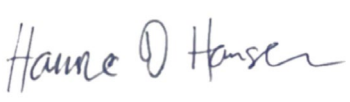
2. The declaration applies to the following article	
Title of article	A Single Dose of Psilocybin Increases Synaptic Density and Decreases 5-HT _{2A} Receptor Density in the Pig Brain
Article status	
Published <input checked="" type="checkbox"/>	Accepted for publication <input type="checkbox"/>
Date: 15/01/21	Date:
Manuscript submitted <input type="checkbox"/>	Manuscript not submitted <input type="checkbox"/>
Date:	
If the article is published or accepted for publication, please state the name of journal, year, volume, page and DOI (if you have the information).	Int. J. Mol. Sci. 2021, 22(2), 835 doi: 10.3390/ijms22020835

3. The PhD student's contribution to the article <i>(please use the scale A-F as benchmark)</i> Benchmark scale of the PhD-student's contribution to the article	A, B, C, D, E, F
A. Has essentially done all the work (> 90 %) B. Has done most of the work (60-90 %) C. Has contributed considerably (30-60 %) D. Has contributed (10-30 %) E. No or little contribution (<10 %) F. Not relevant	
1. Formulation/identification of the scientific problem	B
2. Development of the key methods	A

3. The PhD student's contribution to the article (please use the scale A-F as benchmark) Benchmark scale of the PhD-student's contribution to the article		A, B, C, D, E, F
A. Has essentially done all the work (> 90 %) B. Has done most of the work (60-90 %) C. Has contributed considerably (30-60 %) D. Has contributed (10-30 %) E. No or little contribution (<10 %) F. Not relevant		
3. Planning of the experiments and methodology design and development		B
4. Conducting the experimental work/clinical studies/data collection/obtaining access to data		B
5. Conducting the analysis of data		B
6. Interpretation of the results		B
7. Writing of the first draft of the manuscript		A
8. Finalisation of the manuscript and submission		A
Provide a short description of the PhD student's specific contribution to the article. ⁱ		
NRR performed the optimization of the ligands used in the study. Previous study was conducted by LLD and the brains from that study were used in the current study. With the laboratory assistance of AJO and NFR, NRR performed the experiments required for the study. NRR was responsible for planning and conducting data analysis, interpretation of results as well as writing the first draft and submitting the manuscript.		

4. Material from another thesis / dissertationⁱⁱ	
Does the article contain work which has also formed part of another thesis, e.g. master's thesis, PhD thesis or doctoral dissertation (the PhD student's or another person's)?	Yes: <input type="checkbox"/> No: <input checked="" type="checkbox"/>
If yes, please state name of the author and title of thesis / dissertation.	
If the article is part of another author's academic degree, please describe the PhD student's and the author's contributions to the article so that the individual contributions are clearly distinguishable from one another.	

5. Signatures of the co-authorsⁱⁱⁱ				
	Date	Name	Title	Signature
1.	07/01/22	Annette Johansen	MD	

5. Signatures of the co-authors ⁱⁱⁱ				
2.	05/01/22	Lene Lundgaard Donovan	PhD	
3.	07/01/22	Nídia Fernandez Ros	BSc	
4.	03/01/22	Brice Ozenne	PhD	
5.	05/01/22	Hanne Demant Hansen	PhD	
6.	03/02/22	Gitte Moos Knudsen	Professor	

6. Signature of the principal supervisor
I solemnly declare that the information provided in this declaration is accurate to the best of my knowledge.
Date: 03/02/2022
Principal supervisor: 

7. Signature of the PhD student
I solemnly declare that the information provided in this declaration is accurate to the best of my knowledge.
Date: 01/01/22
PhD student: 

Please learn more about responsible conduct of research on the [Faculty of Health and Medical Sciences' website](#).

ⁱ This can be supplemented with an additional letter if needed.

ⁱⁱ Please see Ministerial Order on the PhD Programme at the Universities and Certain Higher Artistic Educational Institutions (PhD Order) § 12 (4):

"Any articles included in the thesis may be written in cooperation with others, provided that each of the co-authors submits a written declaration stating the PhD student's or the author's contribution to the work."

ⁱⁱⁱ If more signatures are needed please add an extra sheet.